UNIVERSITY OF LIVERPOOL

Characterisation and Surface Modification of Graphitic Felts

By

Robert Smith

January 2018

Thesis submitted in accordance with the requirements of the University of Liverpool for the degree of Doctor in Philosophy

Table of Contents

Chapter 5: The Electrochemical Characterisation of Graphite Felts.

Chapter 6: Investigation into the Electrochemical Modification of Carbon Surfaces via an Aryl Radical Mechanism.

Acknowledgements:

Writing my acknowledgements page feels like the first time in 4 years that I've been able to stop and think back over the adventure I've had. Trying to name everyone who has helped and supported me over the years in a single page does not do justice to how thankful I am to them, and I can't help but feel extremely fortunate to have so many amazing people in my life. There are so many people I'd love to make a special mention to that a significantly reduced font size would be required, but I could in no way make their support seem small. To all of my friends, old, very old and new, thank you, I honestly could not have done this without you.

There are still a few people who I do need to mention. Firstly, I'd like to thank my supervisor Professor Richard Nichols, for always being there to help whenever I needed it and for giving me this opportunity, along with the Centre for Global Eco-Innovation, the ERDF and ACAL Energy for their support and funding. A very special thank you to Trevor Davies, I really wouldn't have got here without you and I honestly can't thank you enough for all your support and encouragement.

To my parents Dave and Sue, thank you, so very much. I would not be the man I am today without the unrelenting love and support you have given me. It's definitely all your fault. Thank you for believing I could do it, even when you weren't entirely certain what it is. What more could a son ask for. Finally, to Caitlin, thank you for showing me all the love I could ever ask for, for holding me up when I was down and for always believing in me, I love you.

“I mean, yes idealism, yes the dignity of pure research, yes, the pursuit of truth in all its forms, but there comes a point I'm afraid where you begin to suspect that if there's any real truth it's that the entire multi-dimensional infinity of the Universe is almost certainly being run by a bunch of maniacs; and if it comes to a choice between spending another ten million years finding that out and on the other hand just taking the money and running, I for one could do with the exercise”

Douglas Adams

The Hitchhiker’s Guide to the Galaxy

1952-2001

Abstract:

Carbon materials are used as electrode in a wide range of scientific and engineering applications. In many cases, the surface properties of the carbon electrode play an important role in the effectiveness of the material for a particular application. The ability to produce a carbon electrode with a particular desired surface could be of great use. This thesis reports on initial work on producing such bespoke carbon surfaces, with a view of real industrial applications.

Graphitic felts are the bulk electrode material of choice in many fuel cell systems. However, to rapidly prototype different surface modifications, a simpler experimental set-up was required. Before these materials could be employed within a still, 3 electrode cell, further fundamental characterisation work was needed. This involved the development of novel sample preparation techniques to ensure the surface of the GF was fully wetted, an area previous literature has not sufficiently addressed, as well the use of simulations to probe the pore sizes of the material. Also, whilst reducing the analyte concentration to minimise the signal interference from solution resistance, it was noted that the GFs were able to detect very low quantities of analyte while still producing a significant signal. This revelation led to a further investigation into the potential application of GFs in electrochemical sensory applications.

The development of techniques for the electrochemical modification of graphite felts with protected diazonium compounds has also been demonstrated, and groundwork laid for the future functionalisation of this surface layer has begun. Initial work focussed on controlling the deposition of unprotected diazonium compounds, such as 4-nitroanaline, onto a planar carbon surface, using electrochemical control to deposit a monolayer. Due to the highly reactive nature of the aryl diazonium, by which C-C bonding, and therefore surface grafting is achieved, forming a single monolayer was difficult and the surface was coated in a multilayer of material. Moving from planar carbon and armed with a clearer understanding of GFs as electrode materials, investigations began into using protected diazonium compounds, i.e. ones with large terminal groups to sterically reduce

the likelihood of multilayer formation, as a route to grafting a single monolayer of material to a GF. The additional benefit of these materials was the potential to remove the bulky, protecting group, post-grafting, to allow functionalisation of the surface layer with a desired terminal group. The use of STM and Raman spectroscopy confirmed the success of this post-grafting functionalisation when applied to a gold substrate, whilst electrochemical and SEM techniques suggest equal success for the GF. Whilst the grafting of a single monolayer has not been shown by this study, it has laid the foundation for further work to continue in this area, as well as opening other opportunities to investigate further applications of GF electrodes, particularly as a sensor material.

Symbols and Abbreviations:

Symbol	Units	Meanings
A_{elec}	cm^2	Area of electrode
a_i	none	Activity of species i
C_d	F cm^{-2}	Differential capacitance of the double layer
C^o	F cm^{-2}	Specific capacitance
c^*	Mol	Concentration of bulk solution
D_i	cm s^{-1}	Diffusion coefficient of species i
d	cm	Distance
E	V	Electrode potential versus a reference
E_{Fermi}	eV	Fermi level
E_f	V	Formal potential
E^o	V	Standard potential
E_p	V	Peak potential
ΔE_p	V	Difference between peak potential of anodic and cathodic processes
$E_p{}^a / E_p{}^c$	V	Anodic / Cathodic peak potential respectively
F	C	Faraday's constant
f_e	none	Fraction of edge plane
G	kj mol^{-1}	Gibbs free energy
ΔG	kj mol^{-1}	Change in Gibbs free energy
$\Delta G^{\ddagger}$	kj mol^{-1}	Standard Gibbs energy of activation
$\Delta_r G$	kj mol^{-1}	Change in reaction Gibbs free energy
I	A	Current flow
I_a / I_c	A	Anodic / Cathodic peak current respectively
I_p	A	Peak current
I_o	A	Exchange current
J	A cm^{-2}	Current density
J_o	A cm^{-2}	Exchange current density
j	mol cm^{-2} s^{-1}	Flux
k	order dependant	Rate constant for a heterogeneous reaction
k^o	cm s^{-1}	Standard heterogeneous rate constant
L_{cf}	Cm	Carbon fibre length
m	G	Mass of electrode
n	None	Stoichiometric number of electrons involved in a reaction
N	Mol	Stoichiometric number of mols involved in a reaction
Q	C	Charge passed in electrolysis
Q	none	Reaction quotient
Q_F	C	Faradaic current
R	J mol^{-1} K^{-1}	Molar gas constant
r	Cm	Radius
R_p	cm	Pore radius
R_s	Ω	Solution Resistance
T	K	Absolute temperature
t	s	Time
v	V s^{-1}	Linear potential scan rate
V_{cf}	cm^3	Carbon fibre volume
x	none	Coordinate of diffusing ions
x	cm	Unit cell dimensions

z	C	Charge

Symbol	Units	Meanings
α	none	Transfer coefficient
γ	none	Activity coefficient of species i
δ	cm	Diffusion layer thickness at the electrode surface
η	V	Overpotential
$\Phi_в$	V	Potential
Φ	none	Porosity of graphite felt
μ_i	kj mol^{-1}	Chemical potential of species i
ρ_{cf}	g cm^{-3}	Density of graphite felt
χ	none	Dimensionless parameter
ψ	none	Dimensionless current

Abbreviation	Meaning
BET	*Brunauer–Emmett–Teller*
BPPG	Basal plane pyrolytic graphite
CVD	Chemical vapour deposition
DOS	Density of states
EPPG	Edge plane pyrolytic graphite
GC	Glassy carbon
GF	Graphite felt
HOPG	Highly orientated pyrolytic graphite
IHP	Inner Helmholtz plane
LoD	Limit of detection
LoQ	Limit of quantification
NP	Nanoparticle
OHP	Outer Helmholtz plane
PAN	Polyacrylonitrile
PEEK	Polyether ether ketone
PEM	Proton exchange membrane
PFCE	Plastic formed carbon electrode
POM	Polyoxometalate
SCE	Saturate calomel electrode
SECCM	Scanning electrochemical cell microscopy
SEM	Scanning electron microscopy
SHE	Standard hydrogen electrode
SHINERS	shell-isolated nanoparticle-enhanced Raman ***s****pectroscopy*
STM	Scanning tunnelling microscopy
TBAP	Tetrabutlyammonium perchlorate

Chapter 1:

Introduction to Flow Cells.

Table of Contents

1.1 Introduction

Fossil fuels currently account for over 80% of the world's energy production [3, 4]. Taking millions of years to form, fossil fuels are not a sustainable source of power generation [4, 5]. There is uncertainty on exactly when fossil fuels will run out as new deposits are found and new removal techniques allow more effective use of existing reserves [3]. Despite this, the annual usage of fossil fuels continues to increase, which is a significant problem with a finite resource [6]. This is not the only issue currently facing the world in terms of fossil fuel usage. The burning of fossil fuels releases large amounts of 'greenhouse' gases, such as CO_2, N_2O and CH_4 into the atmosphere [7, 8]. These have a proven link to global warming, a rise in the temperature of Earth's climate [9]. One of the most common fossil fuel burning systems is the internal combustion engine found in vehicles the world over. With continuous rises in the cost of oil, finding an alternative method of powering vehicles would have major economic benefits. If the technology that can replace the internal combustion engine is also less polluting, then the environmental impact of vehicles is lessened, whilst increasing the quality of life in urban centres (for example, by decreasing the cases of respiratory illness caused by poor air quality) [10, 11]. Fuel cells may be one such technology that can achieve these aims.

Fuel cells are energy conversion devices, converting chemical energy to electrical energy. There are various types of fuel cell but they all work on the general principle of electrical power generation through a chemical reaction. While different types of fuel cell operate slightly differently, the basic principle is that the fuel H_2 gas is catalytically oxidised at the anode into protons and electrons. The electrons are conducted away from the anode and pass through an external circuit to the cathode. Protons carry the ionic current across the membrane to the cathode, where they are involved in the direct reduction of oxygen (from air) forming water.

Fuel cells are generally a much environmentally cleaner alternative to traditional fossil fuel methods of power generation, providing solutions across many energy sectors. Using fuel cells for

transportation applications will lead to an improvement in air quality by reducing the CO_2, NO_x and hydrocarbon emission of combustion engines. They can be used in stationary power applications, both industrial and domestic, as well as providing energy storage, with some governments already looking to implement hydrogen infrastructure. Germany, for example, is aiming to install 400 hydrogen refuelling depots by 2023 [12]. Excess electricity could be used to electrolyse water, generating H_2 for later use as a fuel. Whilst for some applications, financial viability still remains an issue, in others fuel cells are already economical alternatives to existing power sources. Fuel cells are already in use in materials handling applications with companies such as Walmart investing in fuel cell materials handling vehicles for use in warehouses, whilst numerous fuel cell bus programs are currently underway globally [13-15].

1.2 Fuel Cell Types:

There are several types of fuel cell. The most common include the solid oxide, molten carbonate, phosphoric acid, alkaline and polymer electrolyte fuel cells (PEFC). Their main characteristics are summarised in the table below [1].

Table 1: Summary of differences between fuel cell types [1].

Type	Solid Oxide	Molten Carbonate	Phosphoric Acid	Alkaline	Proton Exchange Membrane
Operating Temperature	600-1000°C	650°C	205°C	65-220°C	80°C
Electrolyte	Ceramic	Molten Carbonate	Phosphoric Acid	Potassium Hydroxide	Ionically conductive membrane
Charge Carrier	O^{-2}	CO_3^{-2}	H^+	OH^-	H^+
Catalyst	Ceramic Oxide	Ceramic + Nickel	Platinum	Platinum	Platinum

Solid oxide fuel cells (SOFCs) consist of a ceramic, porous anode, a porous cathode and a solid, ceramic electrolyte [16]. The cathode reduces O_2 to O^{2-} which then diffuses through the membrane to the anode and oxidises the fuel. The fuel most commonly associated with SOFCs is H_2 gas, but light hydrocarbons such as methanol/methane can be reformed within the fuel cell to produce H_2. In order for the ceramic material to be conductive, both electronically and ionically, the solid oxide fuel cell operates between 500°C and 1000°C. Due to the temperature range and the weight of the ceramic materials, this type of fuel cell is not suitable for use in automobiles, but has found use as stationary power generation units. The reaction mechanism is as follows [1, 17-19]:

Anode: $H_2 + O_2 \rightarrow H_2O + 2e^-$ (1.1)

Cathode: $\frac{1}{2}O_2 + 2e^- \rightarrow O^{2-}$ (1.2)

Overall: $H_2 + ½O_2 \rightarrow H_2O$ (1.3)

Molten carbonate fuel cells operate at similar temperatures to solid oxide fuel cells, but instead of a ceramic electrolyte they typically use a lithium potassium carbonate salt [20]. H_2 gas or reformate produced from light hydrocarbons, is reduced at the anode to produce electrons and protons. O_2 and CO_2 are brought together at the cathode to form CO_3^{-2} which is ionically conducted by the electrolyte to the anode to reform CO_2 and produce H_2O. Again, the high temperature couple with the liquid electrolyte makes molten carbonate fuel cells more suitable for static installations [1, 17-19].

Anode: $2H_2 + 2CO_3^{2-} \rightarrow 2H_2O + 2CO_2 + 4e^-$ (1.4)

Cathode: $2CO_2 + O_2 + 4e^- \rightarrow 2CO_3^{2-}$ (1.5)

Overall: $2H_2 + O_2 \rightarrow 2\ H_2O$ (1.6)

Alkaline fuel cells have been heavily developed and were used by NASA during the 1960's, for the Apollo series of missions. H_2 gas is used as the fuel, oxidised at the anode forming protons and electrons. An aqueous alkaline electrolyte transports hydroxyl ions from the cathode to the anode to form H_2O [21]. This type of fuel cell is more attractive for use in automobiles due to the lower operating temperature, typically 100°C, but the poor power density associated with this cell prevents this application. The disadvantages are the requirement for pure O_2 gas, which adds additional expense, as the electrolyte can be easily poisoned by CO_2 [18, 19].

Anode: $2H_2 + 4OH^- \rightarrow 4H_2O + 4e^-$ (1.7)

Cathode: $O_2 + 2H_20 + 4e^- \rightarrow 4OH^-$ (1.8)

Overall: $2\ H_2 + O_2 \rightarrow 2\ H_2O$ (1.9)

1.2.1 Polymer Electrolyte Fuel Cell (PEFC).

By far the most appropriate for use in automobiles, whilst also being suitable for static and portable electricity generators, is the polymer electrolyte fuel cell (PEFC), represented in Figure 1.1 [22, 23].

This type of fuel cell can operate in the relatively low temperature range of 50-80°C. The mechanism for the PEFC reaction is as follows [1, 17]:

Anode: $H_2 \rightarrow 2\ H^+ + 2e^-$ ($E°$ = 0 V vs. SHE) (1.10)

Cathode: $O_2 + 4\ H^+ + 4e^- \rightarrow 2\ H_2O$ ($E°$ = 1.23 V vs SHE) (1.11)

Overall: $2\ H_2 + O_2 \rightarrow 2\ H_2O$ ($E°_{(cell)}$ = 1.23 V vs SHE) (1.12)

$E°_{(cell)}$ is the standard potential of the fuel cell from the potentials of the anodic and cathodic processes, where:

$$E°_{(cell)} = E°_{reduction} - E°_{oxidation} \quad (1.13)$$

In this process, $E°_{(cell)}$ is positive 1.23 V vs SHE. The Gibbs free energy ($\Delta G°$) of a system shows how thermodynamically spontaneous a process is, and relates to the $E°_{(cell)}$ by:

$$\Delta G° = -nFE°_{(cell)} \quad (1.14)$$

Where F is the faraday constant and n is the number of transferred electrons. As the value for $E°_{(cell)}$ is positive, the value for $\Delta G°$ is negative which shows that overall reaction is thermodynamically spontaneous.

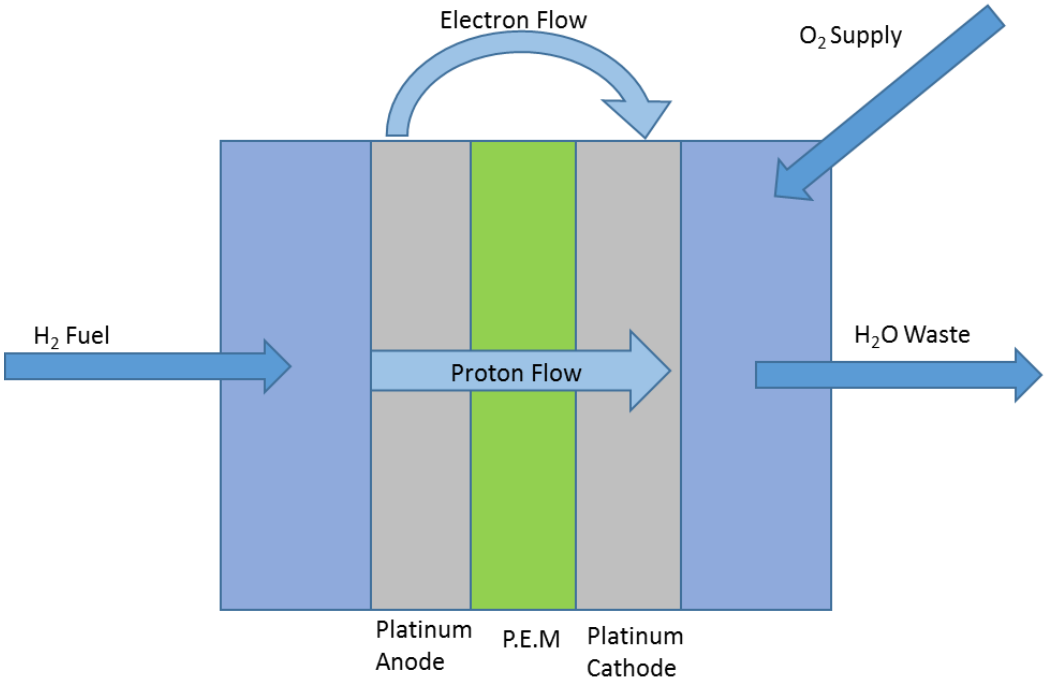

Figure 1.1: Diagram of PEFC processes, where PEM is the proton exchange membrane, typically an ionically conductive polymer, such as Nafion®.

Typically, the anode and the cathode both contain a catalyst which is often nano-disperse to improve surface area. Platinum is the optimum elemental catalyst, but other elements or compound can be used (such as Ru or Pd). Platinum catalyses the hydrogen oxidation reaction with high activity and good durability [24]. For the cathode, much higher platinum loadings are required due to the slow rate of the oxygen reduction reaction [23, 25]. The electrolyte is a thin membrane that is ionically conductive but electrically insulating. Typically, this membrane is a material called Nafion® or a variation of it (polyfluorinated sulphonic acid, PFSA). Nafion® is a super-acid, with sulfonic acid groups attached to a Teflon-like polymer backbone. The sulfonic acid groups generate an environment which promotes ionic conductivity, providing the membrane remains moist. 80°C is generally regarded as the upper range of PEFC, above this temperature it becomes too difficult to maintain the hydration of the membrane, resulting in an increase in the ohmic resistance, resulting in a loss of performance.

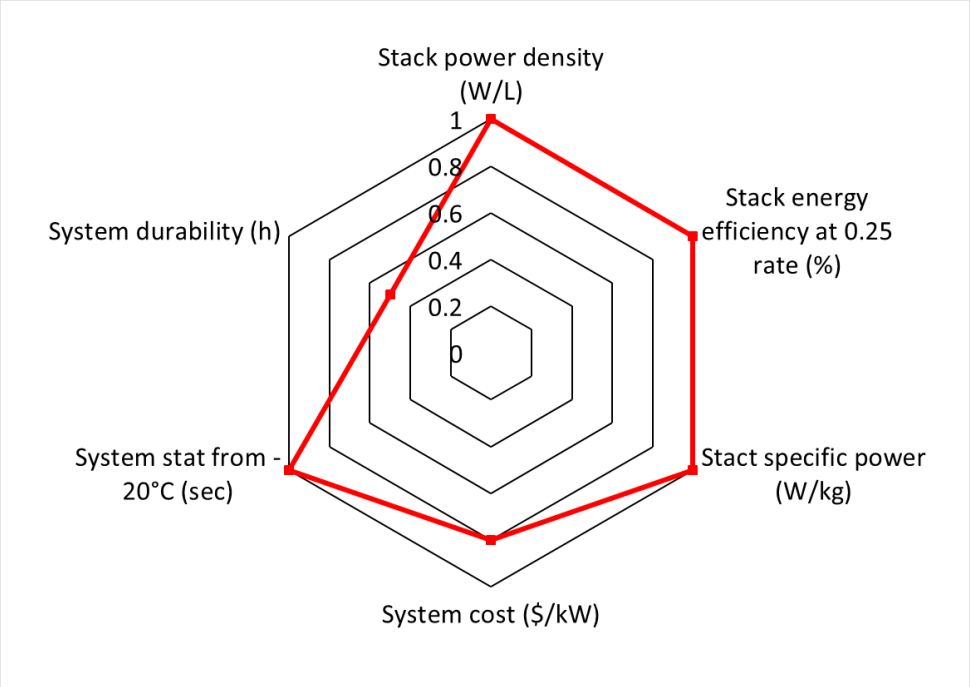

Figure 1.2: Web chart showing PEM fuel cell targets against current status [10].

PEFC have certain challenges to overcome before they can be considered as a replacement to the internal combustion engine. The diagram above (Figure 1.2) shows the state of technological advancement required as of 2013 by the US Drive: Fuel Cell Technical Team [10]. In the diagram the technical requirements for fuel cells are given a score between 0 and 1, with 1 being the minimum target required. Currently the cost and durability of the cell is the major limitation to bringing PEFC into the wider market. The target system cost is around $40/kW within the next 5 years. The cost of the precious metal catalyst is particularly high and any system that can reduce the amount required will significantly lessen this hurdle [24]. For durability, the target is 5000 hours of operation with a performance loss of less than 10%. This must also cover the wide range of environmental conditions (like temperature and humidity) as well as driving situations (bumpy surfaces, city/motorway driving). During the lifetime of the fuel cell the total surface area of the platinum catalyst is significantly reduced, affecting the durability of the system. The direct reduction of oxygen on platinum within the fuel cell is a difficult reaction and requires a large surface area of platinum to run the cell efficiently.

Due to the selectivity of the 4 e^- reduction of O_2 at the cathode, alternative reactions can occur, resulting in peroxide and free radical production which can damage cell components.

As mentioned previously, fuel cells can require extreme temperatures, whilst PEFCs run at lower temperatures of around 50-80°C, this is still hot enough to cause further engineering challenges. Like all fuel cells, the temperature of PEFC must be regulated to reach optimal performance; this is usually achieved through the use of a liquid cooling system around the fuel cell. Furthermore; the proton exchange membrane itself must be prevented from drying out. If membrane drying occurs the ionic resistance increases, which negatively impacts the fuel cell performance. Even at the lower end of the PEFC operating temperatures membrane drying is a common problem and may lead to durability issues.

1.2.2 Chemically Regenerative Redox Cathode (CRRC) PEFC:

An alternative approach to the traditional PEFC cathode reaction is via the indirect reduction of O_2. ACAL Energy has been developing a novel fuel cell that replaces up to 80% of the platinum from a typical PEFC, by employing a liquid catalyst system for the indirect reduction of oxygen [2, 26], described in Figure 1.3. Referred to as a 'catholyte', this aqueous solution significantly reduces the cost, due to the reduction in required platinum and is not susceptible to poisoning on the cathode greatly increasing the durability of the fuel cell.

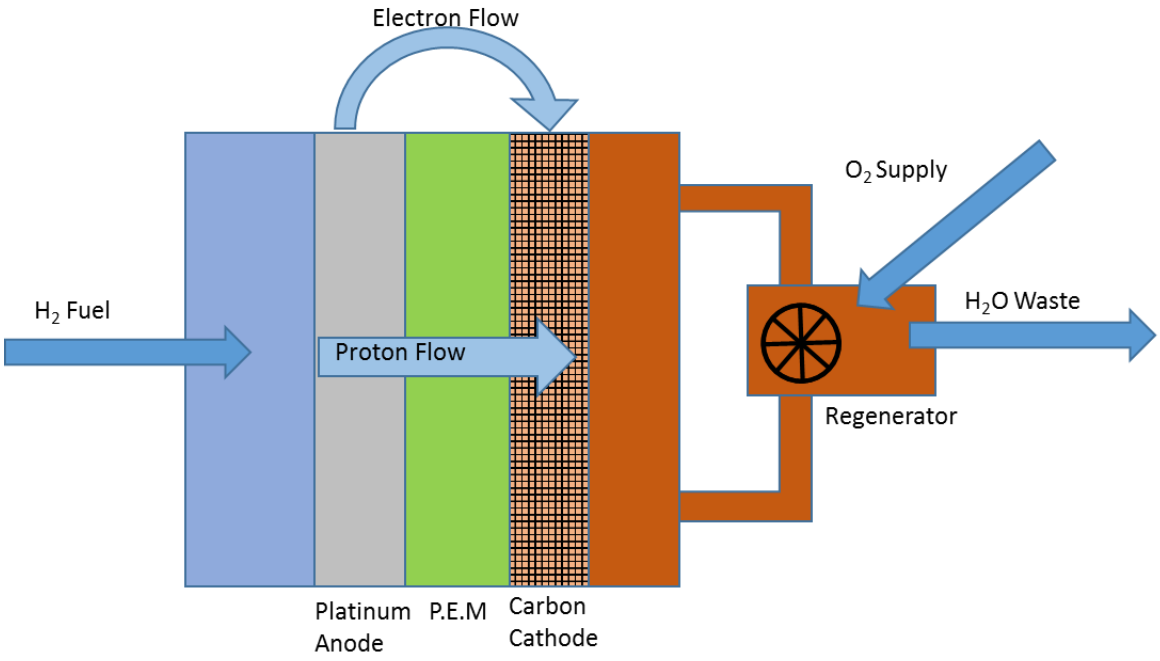

Figure 1.3: Diagram of ACAL's CRRC PEFC processes including liquid catholyte and regenerator. Where PEM is the proton exchange membrane.

Much like traditional fuel cells, the novel fuel cell uses H_2 gas as a fuel, which is oxidised at the platinum anode to protons and electrons. The protons pass through the Nafion® membrane whilst the electrons pass through the circuit providing electrical work. At the cathode side of the membrane protons pass into the aqueous solution and the electrons reduce the catholyte molecule. The solution is pumped around to a regenerator where the reduced catholyte undergo a chemical reaction producing H_2O and oxidised catholyte. Whilst there are challenges to overcome engineering a fuel cell for such a novel system, there are additional benefits. The aqueous catholyte is ideal for preventing membrane drying, as it is in constant contact with the membrane and maintained at a constant concentration. The liquid catholyte system also aids with heat management of the CRRC. Traditional PEFCs usually run at a maximum temperate of 80°C as anything above this can lead to drying of the membrane. The membrane in the CRRC is in constant contact with the liquid catholyte, allowing for a higher maximum temperature, improving the electrode kinetics. Whereas a traditional PEFC requires an external cooling system, increasing both the cost and complexity, in the CRRC the higher heat capacity of the

catholyte means it is able to transfer the heat from the system to an in-line heat exchanger. This removes the need for an external system, reducing cost and size of the cell.

A key component of a CRRC PEFC system is the catholyte. To date, the most promising catholytes have been based on a polyoxometalate (POM) molecule, with formula $H_xNa_yPMo_{12-z}V_zO_{40}$, where x + y = z + 3, and z is between 1 and 4 [26, 27]. POMs are inorganic molecules whose 3D structure is self-assembled from 2 or more oxyanions in an acidic solution [28, 29]. POMs consist of transition metals, often of different elements, connected by linking oxygen atoms. These large compounds are generally anionic and can take on a number of different framework depending on the particular elemental makeup and conditions in which they are formed (temperature, pH and concentration).

The metal atoms that make up the shell are referred to as the addenda atoms and are normally V, W or Mo. Many POMs also contain a central hetero atom with coordination numbers between 4 and 12 depending on the structure of the POM. The POM used in ACAL's CRRC catholyte are of the Keggin structure depicted in Figure 1.4 [2, 28].

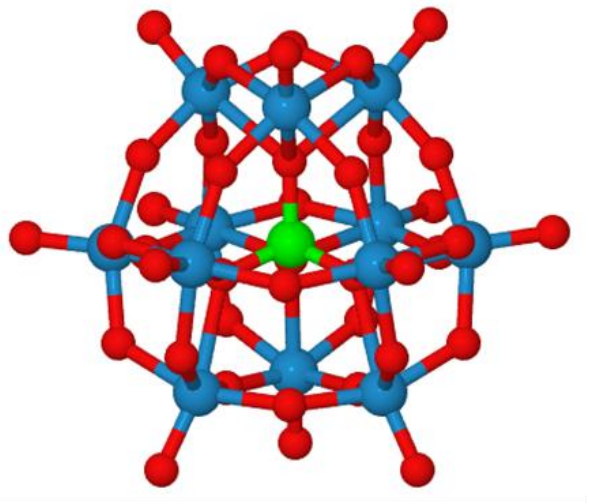

Figure 1.4: Structure of the α-keggin polyoxometalate molecule $[PMo_{12}O_{40}]^{3-}$, where Mo is blue, P is green, and O is red. In the $H_xNa_yPMo_{12-z}V_zO_{40}$ structure V will replace Mo. For clarity, the hydrogens have been excluded. Reproduced from ref. [2].

Unlike the traditional PEFC, where the thermodynamics are dependent on the reduction of oxygen to form water with an open cell voltage (OCV) of 1.23 V vs SHE, this flow cell's OCV is controlled by the catalyst used within the catholyte solution, which is usually less [30]. The anode reaction resembles that of a conventional PEFC with H_2 oxidised to H^+ and electrons. The overall reaction for the CRRC is identical to that of a standard PEFC, with water vapour as the only product. The cathodic reaction is noticeably different as it involves the of V(V) to V(IV).

Anode:	$H_2 \rightarrow 2\ H^+ + 2\ e^-$	(1.15)
Liquid cathode:	$2\ V^{5+} + 2\ e^- \rightarrow 2\ V^{4+}$	(1.16)
Regenerator:	$2\ V^{4+} + 2\ H^+ + ½\ O_2 = 2\ V^{5+} + H_2O$	(1.17)
Overall:	$H_2 + ½\ O_2 \rightarrow H_2O$	(1.18)

However, the regeneration reaction requires a lower redox potential than that for the reduction of O_2, which typically limits the open circuit voltage (OCV) to <1 V (as the reduced liquid cathode must be oxidised by the O_2) [30, 31]. Whilst this maximum OCV could appear low when compared with

standard PEFCs, the faster kinetics of the O_2 reduction of the catholyte more than make up for the difference [2, 32, 33].

The cathode used in the CRRC is a form of graphitic carbon fibre formed into an unordered felt material. It is a commercially available felt, called GFD2.5, supplied by SGL Group (Germany), with a nominal thickness of 2.8 mm (measured under a slight compressive force). Despite its commercial availability, there are many unknown factors regarding the felt, such as how its structure relates to its electrochemical activity. Previously; a collaborative research project between ACAL and Dr Ben Alston at the University of Liverpool, investigated how concentration of POM affected current flow. It was found that increasing concentration did not increase current flow to the magnitude expected, but resulted is a reduced current flow. One possible cause could be deposition of POM and related material onto the electrode surface, which has previously been discussed in literature [34, 35].

1.3 Aims and Objectives

The focus of this thesis is to investigate methods of chemical surface engineering of carbon materials, with the aim to improve the efficiency of the advanced CRRC fuel cell. The main goals of this work are to characterise the porous graphitic carbon felt currently used as the cathode material within most advanced CRRC fuel cells and to investigate the grafting, and characterisation of, a surface layer to a carbon electrode. In order to better understand their fuel cell, ACAL requires an in-depth investigation into the structure and properties of the carbon felt materials. This thesis will aim to examine the use of this graphitic felt as an electrode material, to develop a suitable method for the repeatable trialling of different porous electrodes and surface modifications. This method will need to both cost effective and rapid, preferably without the need to build a fuel cell for each iteration, using a conventional glass cell instead for example. Once this has been achieved, the surface modification experimentation can begin, generating a reliable technique for the creation and functionalisation of a stable surface layer, without inhibiting the electrochemical activity of the graphitic felt.

Note: ACAL Energy Ltd ceased trading in July 2017.

1.4 References

[1] Fuel Cell Handbook, EG&G Services Parsons Inc, Science Applications International Corporation, October (2000).

[2] N.L. Gunn, D.B. Ward, C. Menelaou, M.A. Herbert, T.J. Davies, Investigation of a chemically regenerative redox cathode polymer electrolyte fuel cell using a phosphomolybdovanadate polyoxoanion catholyte, Journal of Power Sources 348 (2017) 107-117.

[3] United States Energy Information Administration, International Energy Outlook 2017, https://www.eia.gov/outlooks/ieo/ (2017).

[4] F. Barbir, PEM fuel cells: theory and practice, Academic Press (2012).

[5] G. Miller, S. Spoolman, Environmental science: problems, connections and solutions, Cengage Learning (2007).

[6] C.J. McNerney, M. Cheek, Clean energy nation: freeing America from the tyranny of fossil fuels, AMACOM Div American Mgmt Assn (2011).

[7] Intergovernmental Panel on Climate Change (IPCC), Variations in atmospheric CO2 concentration on different time-scales. http://www.grida.no/publications/other/ipcc_tar/?src=/climate/ipcc_tar/wg1/fig3-2.htm (2001).

[8] Intergovernmental Panel on Climate Change (IPCC), Climate Change 2013: The Physical Science Basis, (2013).

[9] Advancing the Science of Climate Change, The National Academies Press (2010).

[10] United States Drive Partnership, Fuel Cell Technical Team Roadmap. http://energy.gov/sites/prod/files/2014/02/f8/fctt_roadmap_june2013.pdf, (2013).

[11] S.H. Yim, S.R. Barrett, Public health impacts of combustion emissions in the United Kingdom, Environmental science & technology 46(8) (2012) 4291-4296.

[12] Hydrogen Mobility Europe. http://h2me.eu/2016/05/05/germany-h2-mobility-targets-400-hydrogen-fueling-stations-by-2023/

[13] Modern Materials Handling. http://www.mmh.com/article/plug_power_announces_expanded_collaboration_with_walmart

[14] United States Depatment of Energy. https://energy.gov/sites/prod/files/2016/12/f34/fcto_early_markets_mhe_fact_sheet.pdf

[15] E. Energy, Commercialisation of hydrogen fuel cell buses. http://www.fuelcellbuses.eu/sites/default/files/documents/FC%20bus%20commercialisation%20-%20White%20Paper_October%202017.pdf

[16] R.M. Ormerod, Solid oxide fuel cells, Chemical Society Reviews 32(1) (2003) 17-28.

[17] A. Appleby, F.F.F.C. Handbook, van Nostrand Reinhold, New York 18 (1989).

[18] J. Larminie, A. Dicks, M.S. McDonald, Fuel cell systems explained, J. Wiley Chichester, UK (2003).

[19] R. O'hayre, S.-W. Cha, F.B. Prinz, W. Colella, Fuel cell fundamentals, John Wiley & Sons (2016).

[20] A. Kulkarni, S. Giddey, Materials issues and recent developments in molten carbonate fuel cells, Journal of Solid State Electrochemistry 16(10) (2012) 3123-3146.

[21] Y.J. Wang, J.L. Qiao, R. Baker, J.J. Zhang, Alkaline polymer electrolyte membranes for fuel cell applications, Chemical Society Reviews 42(13) (2013) 5768-5787.

[22] M.F. Mathias, R. Makharia, H.A. Gasteiger, J.J. Conley, T.J. Fuller, C.J. Gittleman, S.S. Kocha, D.P. Miller, C.K. Mittelsteadt, T. Xie, Two fuel cell cars in every garage, Electrochem. Soc. Interface 14(3) (2005) 24-35.

[23] H.A. Gasteiger, N.M. Marković, Just a dream—or future reality?, Science 324(5923) (2009) 48-49.

[24] O.T. Holton, J.W. Stevenson, The role of platinum in proton exchange membrane fuel cells, Platinum Metals Review 57(4) (2013) 259-271.

[25] F.T. Wagner, B. Lakshmanan, M.F. Mathias, Electrochemistry and the future of the automobile, J. Phys. Chem. Lett 1(14) (2010) 2204-2219.

[26] A.M. Creeth, A.R. Potter, K. Knuckey, Redox fuel cell, Google Patents, (2015).

[27] B.R. Limoges, R.J. Stanis, J.A. Turner, A.M. Herring, Electrocatalyst materials for fuel cells based on the polyoxometalates PMo(12-n)VnO40 ((3+n)-) (n=0-3), Electrochimica Acta 50(5) (2005) 1169-1179.

[28] I.V. Kozhevnikov, Catalysis by heteropoly acids and multicomponent polyoxometalates in liquid-phase reactions, Chemical Reviews 98(1) (1998) 171-198.

[29] J.J. Borrás-Almenar, E. Coronado, A. Müller, M. Pope, Polyoxometalate molecular science, Springer Science & Business Media (2003).

[30] R. Pattabiraman, V. Venkatesan, H. Udupa, Applications of redox systems on fuel-cells, Journal of Scientific & Industrial Research 40(7) (1981) 432-447.

[31] J. Zhang, Y. Tang, C. Song, J. Zhang, H. Wang, PEM fuel cell open circuit voltage (OCV) in the temperature range of 23 C to 120 C, Journal of power sources 163(1) (2006) 532-537.

[32] K.T. Cho, P. Albertus, V. Battaglia, A. Kojic, V. Srinivasan, A.Z. Weber, Optimization and analysis of high-power hydrogen/bromine-flow batteries for grid-scale energy storage, Energy Technology 1(10) (2013) 596-608.

[33] A. Creeth, PEM fuel cells can now rival diesel engines on performance, Fuel Cells Bulletin 2013(7) (2013) 12-14.

[34] S. Choi, J. Kim, Adsorption Properties of Keggin-type Polyoxometalates on Carbon Based Electrode Surfaces and Their Electrocatalytic Activities, Bulletin of the Korean Chemical Society 30(4) (2009) 810-816.

[35] I. Kovacs, Spontaneous and artificial structures of thin, Keggin-like polyoxometallate arrays on graphite, International Conference on Nanoscience and Technology, Basel, SWITZERLAND, (2006) 623-627.

Chapter 2:

Electrochemical Theory and Methods.

Contents

2.1 Thermodynamic considerations

The thermodynamics of a system can show which direction a chemical process will take. The chemical potential of each species in a chemical system is a key parameter in the explanation of a systems thermodynamics. The following homogenous system describes the reversible change of species A to species B:

$$\mathrm{A} \rightleftharpoons \mathrm{B} \tag{2.1}$$

Using this simple reaction, a chemical potential μ_i, is applied to each species, *i*, leading to the equation:

$$\mu_i = \mu_i^o + RT \ln a_i \tag{2.2}$$

Where μ_i^o is the standard chemical potential of species *i*, *R* is the molar gas constant, *T* is temperature and a_i is the activity of species *i* [2]. When the reaction is at equilibrium, the chemical potential of reactant and product species, μ_A and μ_B, must be equal.

$$\mu_A = \mu_B \tag{2.3}$$

Moving from a chemical reaction, to an electrochemical reaction at the electrode-solution interface, the laws of thermodynamics are maintained, but additional factors must be taken into consideration.

2.1.1 Electron Transfer at the Solution-Electrode Interface

To better describe the heterogeneous reaction, we can consider the following electron transfer reaction between an electrode and species A and B.

$$\mathrm{A}^{n+} + e^- \rightleftharpoons \mathrm{B}^{(n-1)+} \tag{2.4}$$

In the above equation species A and B exist in the solution phase and the solid phase electrode is the electron source for the reaction. Due to the presence of an electric field, the energy of the charge species is adjusted by $n_i z_i F \phi_\beta$. Where z_i is the charge of species *i*, *F* is the Faraday Constant, ϕ_β is the

potential of phase β within which species *i* is found [3-5]. Therefore, the molar Gibbs energy for these species is described by the electrochemical potential, $\overline{\mu}_i$, as follows.

$$\overline{\mu_i} = \mu_i^\circ + z_i F \phi_\beta + RT \ln a_i \tag{2.5}$$

When the above reaction is at equilibrium, we obtain the condition:

$$\left(\mu_{\mathrm{A}}^\circ + nF\phi_{\mathrm{S}} + RT\ln a_{\mathrm{A}}\right) + \left(\mu_e^\circ - F\phi_{\mathrm{M}} + RT\ln a_e\right) = \left(\mu_{\mathrm{B}}^\circ + (n-1)F\phi_{\mathrm{S}} + RT\ln a_{\mathrm{B}}\right) \tag{2.6}$$

Where ϕ_S refers to the potential in solution phase and ϕ_M refers to the potential of the solid, electrode phase. This equation can be rearranged to obtain:

$$(\phi_M - \phi_S) = \frac{1}{F}(\mu_A^\circ + \mu_e - \mu_B^\circ) - \frac{RT}{F} ln\left(\frac{a_B}{a_A}\right) \tag{2.7}$$

This gives us the interfacial potential of the half-cell, (ϕ_{M}-ϕ_S), at the electrode surface. This equation is an alternative form of the Nernst equation, which is generally expressed as:

$$E = E^\circ - \frac{RT}{nF}\ln Q_{\mathrm{R}} \tag{2.8}$$

Where *E* is the electrode potential, *E*° is the standard electrode potential, *n* is the number of transferred electrons and Q_R is the reaction quotient. If the A-B half-cell was measured with respect to with the standard hydrogen electrode (SHE), the electrode potential of the whole cell would be described by the Nernst equation [1-6]. In this particular case the electrode potential, *E*, would be equivalent to the potential of the A-B system (by definition the SHE potential is zero) and the reaction quotient would be given by:

$$Q = \frac{\gamma_B[B]}{\gamma_A[A]} \tag{2.9}$$

Where γ_i is the activity coefficient of species A or B and [4]:

$$a_A = \gamma_A \frac{[A]}{C^o} \quad (2.10)$$

$$a_B = \gamma_B \frac{[B]}{C^o} \quad (2.11)$$

Where C^o is the standard concentration (1 M). The Nernst equation describes the relationship between the actual cell potential and the standard potential and reaction quotient. It can be simplified by the addition of the formal potential E_f in place of the standard potential $E°$:

$$E = E_f - \frac{RT}{nF} ln \frac{[B]}{[A]} \quad (2.12)$$

where:

$$E_f = E^o - \frac{RT}{F} ln \left(\frac{\gamma_B}{\gamma_A}\right) \quad (2.13)$$

The formal potential is the measured potential of the half-cell when concentrations of A and B are equal, and includes the activity coefficient of the species [3-5]. From equation 2.12 we can see that any change in the interfacial potential will cause the position of equilibrium to shift, resulting in a change of species A and B concentrations within the interfacial region. This allows us to understand how the application of an external voltage across the electrode-solution interface affects the thermodynamics of an electron transfer reaction. How quickly this response occurs can be determined through the study of electrode kinetics.

2.2 The Electrochemical Cell

Electrochemical cells are commonly divided into two groups, electrolytic cells and galvanic cells. Galvanic cells are comprised of two electrodes, and like any cell, have an oxidation process occurring at one electrode and reduction at the other [4]. These two simultaneous processes represent two half-cell reactions required for a complete cell. The Daniell cell is the classic example of a Galvanic cell where zinc and copper electrodes are place in zinc and copper sulphate solutions, respectively. The two half-cells must connect through an ionically conducting medium, for example, by a porous

membrane. The transport of ions across this membrane will be balanced by the electron flow around the connecting external circuit. For spontaneous reaction to occur, and current to flow, the cell potential, $E^o_{(cell)}$, must be positive:

$$E^o_{(cell)} = E^o_{red} - E^o_{ox} \quad (2.14)$$

The spontaneity of a reaction is determined by the reaction Gibbs free energy, ΔrG [2]. For the case above, when $E^o_{(cell)}$ is positive the related Gibbs energy will be negative, allowing the reaction to proceed:

$$\Delta rG^o = -nFE^o_{(cell)} \quad (2.15)$$

For electrolytic cells it is not possible to directly measure the interfacial potential (ϕ_M-ϕ_S), the difference between two half-cell electrode reactions is measured instead [4]. The redox active species of interest makes up the first of the two half-cell reactions and a reference electrode or reference cell makes up the other half. A reference electrode works on the principle of an ideal nonpolarizable electrode, one where there is no change in potential when current passes through it. In practice, an extremely small amount of current passes through the reference electrode of an electrochemical cell, allowing it to maintain a near constant potential. This constant interfacial potential allows the potential difference to be determined by:

$$E = (\phi_M - \phi_S)_{AB} + IR_S + (\phi_S - \phi_M)_{red} \quad (2.16)$$

Where $(\phi_M\text{-}\phi_S)_{AB}$ is the interfacial potential for the redox couple of interest, I is the current flow, R_s is the solution resistance and $(\phi_S\text{-}\phi_M)_{ref}$ is the interfacial potential of the reference electrode. For electrochemical reactions where there is current flow, the IR_s term can either be compensated for via electronic or computational methods, or reduced experimentally by minimising the distance between the reference and working electrodes, reducing electrolyte concentration and/or using smaller electrodes to reduce I [7, 8]. The fundamental reason for using a reference electrode is that it maintains a constant potential, allowing equation 2.16 to be re-expressed as:

$$E = \left(\phi_{\mathrm{M}} - \phi_{\mathrm{S}}\right)_{\mathrm{AB}} + constant \qquad (2.17)$$

The reference electrode used in Figure 2.1 is the SHE, which by definition has a potential of zero, at zero current, leading to $E = (\phi_M - \phi_S)_{AB}$.

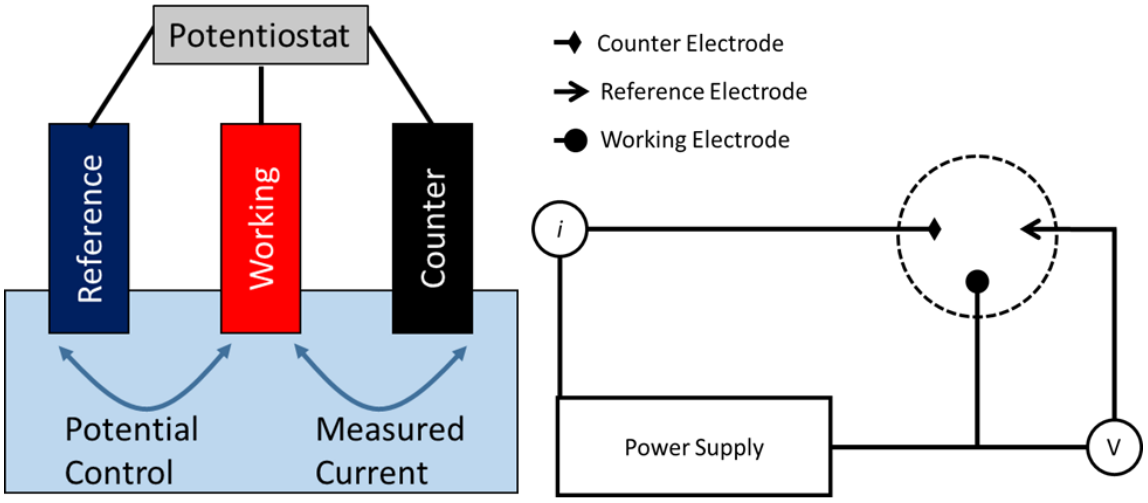

Figure 2.1: Diagram of a 3 electrode cell in solution where the reference electrode is the SHE and equivalent circuit diagram.

Ensuring that $(\phi_S - \phi_M)_{ref}$ remains constant is a key requirement of a potentiostat for a current/potential experiment, along with ensuring it changes in the desired way for dynamic potential experiments. In order to achieve this a counter electrode is employed, creating a three-electrode system. The potentiostat is designed such that current flows between the counter and working electrode, with negligible current through the reference. The potential difference is then measured between the reference and working electrode.

2.2.1 Structure of the Solution-Electrode interface

Adjacent to the electrode surface the electroneutrality of the electrolyte solution is not preserved, generating a potential across the solution-electrode interface [9]. The first model proposed to describe this region was by Helmholtz. The interface is described as a capacitor, where the solution must

balance the charge at the electrode with an opposing layer of oppositely charged and solvated ions parallel to the surface, at the Outer Helmholtz Plane (OHP) [10].

The Gouy-Chapman description of this region includes a diffuse double layer to overcome the limitation of the Helmholtz model that did not account for the dependence of the double layer capacitance on either the electrode potential or solution concentration. Whilst this model is able to show that the excess charge is not rigidly parallel to the electrode surface but decays away from the surface and into the bulk solution [10-12].

The Stern model essentially combines the previous two models; it includes both the rigid layer of solvated ions parallel to the surface with additional excess charge contained within a diffuse layer extending into the bulk solution, this gives reasonably good agreement with experimental capacitance measurements. The drop in potential is borne across both the inner and diffuse layers, which for electrolyte concentrations greater than 0.01 M, extends less than ~100 Å from the electrode into the bulk [10, 13]. A further adaptation was introduced by Grahame, which describes the occurrence of ions losing their solvation shell and directly adsorbing (specific adsorption) to the electrode surface [14]. This layer is called the Inner Helmholtz Plane (IHP).

Electron transfer reactions occur via electron tunnelling across the solution-electrode interface. In general, this happens within a few nm's of the electrode surface. As the distance between the redox active species and the electrode increases the probability of tunnelling decreases exponentially. In order to provide an accurate quantitative analysis of the redox active species in question, it is imperative that the majority, if not all, of the potential drop occurs within the region where electron tunnelling is most probable [3, 4, 10]. The addition of a background electrolyte to the solution ensures most of the potential drop occurs within a few nm's of the electrode surface [4].

As discussed above, the electrode-solution interface acts like a capacitor, with current flowing without the transfer of electrons as the capacitor is charged [3-6]. Thus, two types of current are recorded,

which must be clearly distinguished, when investigating a redox process. Currents originating from heterogeneous electron transfer reactions, resulting in a reduction or oxidation of an electroactive species across the electrode-solution interface are known as faradaic currents. The total faradaic contribution is described by Faraday's law;

$$I_F = \frac{dQ_F}{dt} \tag{2.18}$$

$$Q_F = nFN \tag{2.19}$$

Where I_F is the total faradaic current, N is the number of moles of analyte undergoing electron transfer reactions, n is the number of electrons transferred per reaction, t is time and Q_F is charge transferred due to the faradaic process.

The second type of current present, known as non-faradaic currents, occurs when the applied potential, or solution composition causes a change in the solution-electrode interface, due to an applied potential [3-5]. This interface can be thought of as a capacitor, and if considered as potential independent, can be described as having a capacitance, C_d of:

$$C_d = \frac{Q}{E} \tag{2.20}$$

$$I = C_d \frac{dv(t)}{dt} \tag{2.21}$$

where t is time, v is scan rate and Q is the charge on the capacitor.

2.3 Electrode Kinetics

The study of the thermodynamics of a system is only able to predict the equilibrium position of that system, when the system is controlled by the rate of electron transfer, the electrode kinetics are able to describe what affects perturbation of the equilibrium have on the system. Considering the redox reaction below, two new terms are introduced, k_{red} *and* k_{ox}, corresponding to the rate of reduction and oxidation.

$$A + e^- \underset{k_{ox}}{\overset{k_{red}}{\rightleftharpoons}} B \quad (2.22)$$

Over the course of a reaction, the faradaic current recorded, *I*, is a combination of the negative contribution from the reduction of A, the cathodic reaction I_c, and a positive contribution from the anodic reaction, I_a, the oxidation of B. This is given by the following:

$$I = I_a + I_c \quad (2.23)$$

To produce an electrical current, the ionic charge carrier must diffuse to within 10-20 Å of the electrode surface in order for electron tunnelling to occur [3]. The transfer of an electron between the species in solution and the electrode produces the electric current and so both currents directly depend upon the flux, *j*, of species A and B to the electrode surface. This flux is itself dependent on the respective rate of the two reactions mentioned above. If the electrode is assumed to be uniformly accessible:

$$I_a = F\, A_{elec}\, k_{ox}[B]_o \quad (2.24)$$

$$I_c = -F\, A_{elec}\, k_{red}[A]_o \quad (2.25)$$

Where $[A]_o$ is the surface concentration. The total current can then be written as a function of the net flux, *j*:

$$I = FA_{elec}j \quad (2.26)$$

where:

$$j = k_{ox}[B]_o - k_{red}[A]_o \quad (2.27)$$

Where $[A]_o$ and $[B]_o$ are the surface concentrations of the electroactive species. The heterogeneous rate constant for the redox process is also dependent on conditions such as the temperature, potential, transition state and pressure [1, 3-6].

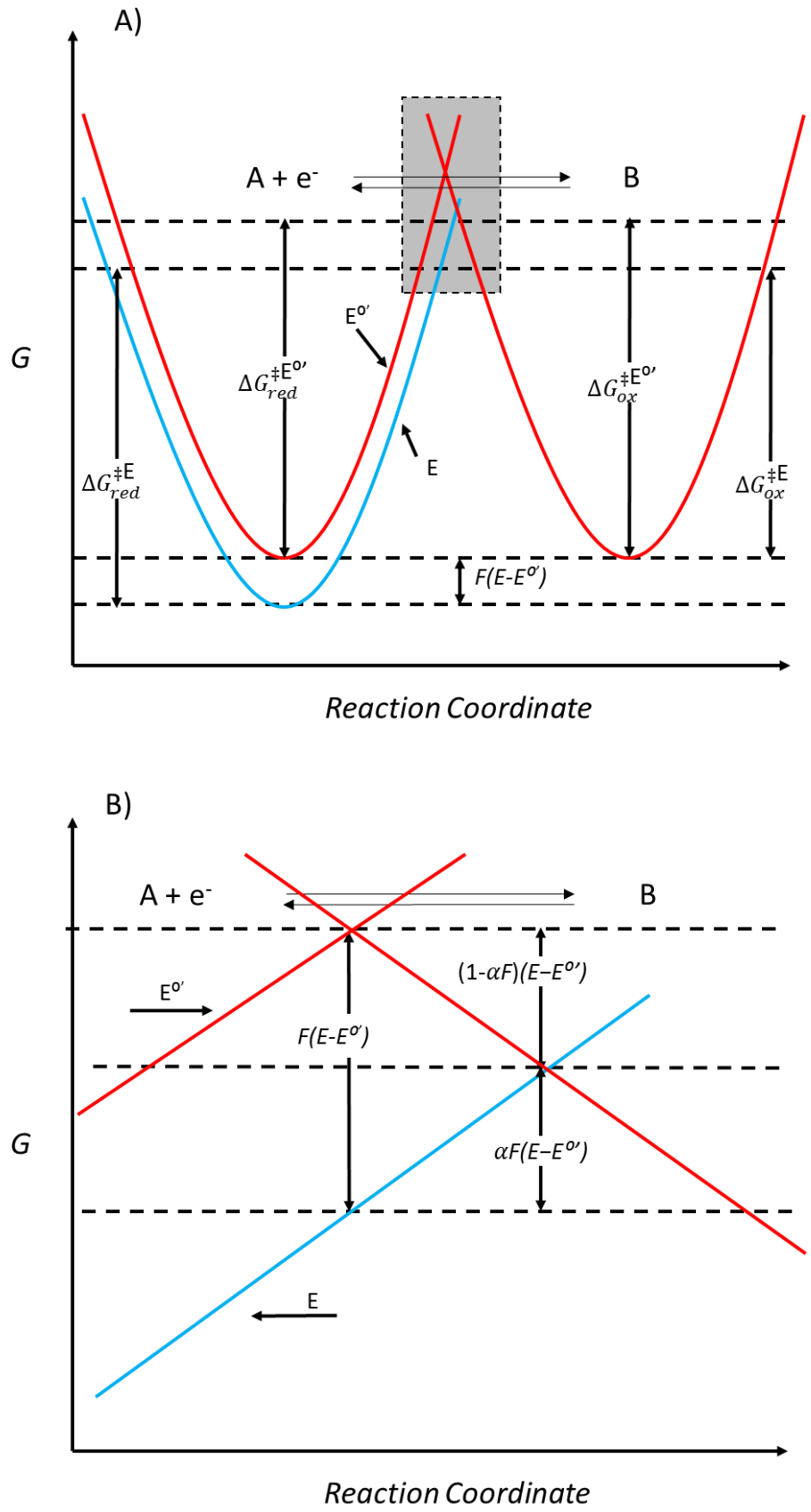

Figure 2.2: Diagram of A) the redox reaction profile for the reaction in equation 1.22, and B) a close-up of the highlighted area from diagram A.

Figure 2.2 A) illustrates the reaction profile for the one electron reaction at two potentials, $E^{o\prime}$ and E. At the potential, $E^{o\prime}$, there is no net reaction as the change in Gibbs energy for the reaction, ΔrG, is zero. If the potential is increased to the value E, the Gibbs energy of the electron is in turn decreased by $F(E-E^{o\prime})$. All other species are unaffected by this change as ϕ_M is increased while ϕ_S remains the same. By increasing the potential from $E^{o\prime}$ to E, ΔrG for the oxidation of B decreases by the value of $F(E-E^{o\prime})$, while the activation energy for the oxidation state transition phase $\Delta G_{ox}^{\ddagger E^{o\prime}}$ decreases in magnitude, $\Delta G_{ox}^{\ddagger E}$. This decrease in $\Delta G_{ox}^{\ddagger E^{o\prime}}$ is related to the symmetry of the reaction profile and affects the magnitude of the Gibbs energy of the transition ($F(E-E^{o\prime})$). For an oxidative process, the fraction is given as (1-α), where α is the symmetry coefficient, with a value between one and zero [1, 3, 4, 15-17]. Therefore:

$$\Delta G_{ox}^{\ddagger E} = \Delta G_{ox}^{\ddagger E^{o\prime}} - (1-\alpha)F(E - E^{0\prime}) \tag{2.28}$$

This also results in an increase to the energy barrier of reduction:

$$\Delta G_{red}^{\ddagger E} = \Delta G_{red}^{\ddagger E^{o\prime}} + \alpha F(E - E^{0\prime}) \tag{2.29}$$

In reality, the electrons within an electrode do not have individual energy levels, but a continuum of energy levels, or bands, from overlapping electronic fields of closely packed atoms [3, 4, 18]. The energy bands are occupied by electrons, with the lowest energy bands occupied first. In a metal or semi-metal structure, the Femi level, E_{fermi}, is the highest energy band that contains electrons, with bands above this level having a high probability of being empty.

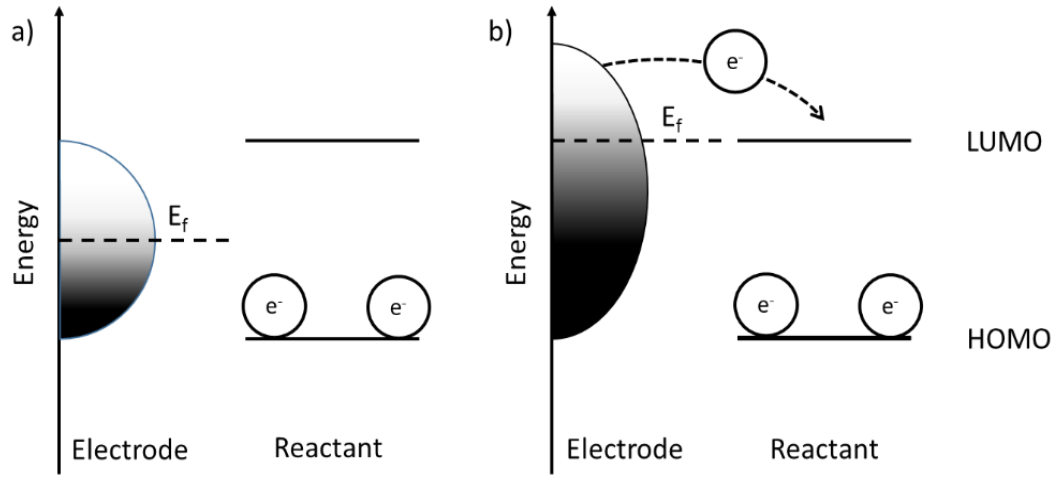

Figure 2.3: Diagram representing the electron transfer from an electrode to a redox couple solution A) before and B) after, raising the E_{fermi} high enough to allow electron transfer into the redox species LUMO.

Figure 2.3 depicts the effect of increasing the E_{fermi} of a metal/semi-metal electrode on the highest occupied molecular orbital, HOMO, and lowest unoccupied molecular orbital, LUMO, of the reactant. Electron transfer from the electrode to the reactant becomes more likely when the E_{fermi} approaches or exceeds the LUMO energy. When the difference in energy levels, between E_{fermi} and LUMO is larger, as in Figure 2.3 a), the electron transfer is energetically unfavourable. Once the potential difference between the electrode and LUMO is reduced, shown in Figure 2.3 b) as an increase in electrode potential, the electron has a higher probability of undergoing electron transfer to the reactant [1, 3, 4]. By assuming the rate constants for the reactions discussed take an Arrhenius form, they can be given as:

$$k_{ox} = A_{ox} e^{\frac{-\Delta G_{ox}^{\ddagger}}{RT}} \tag{2.30}$$

$$k_{red} = A_{red} e^{\frac{-\Delta G_{red}^{\ddagger}}{RT}} \tag{2.31}$$

Where A_{red} and A_{ox} are the pre-exponential factors for the respective oxidation and reduction reactions [2, 4]. If these equations, 2.28 and 2.29, are substituted into equations 2.30 and 2.31:

$$k_{ox} = A_{ox} e^{\frac{-\Delta G^{\ddagger}_{E^{o\prime}_{ox}}}{RT}} e^{\frac{(1-\alpha)F(E-E^{0\prime})}{RT}} \quad (2.32)$$

$$k_{red} = A_{red} e^{\frac{-\Delta G^{\ddagger}_{E^{o\prime}_{red}}}{RT}} e^{\frac{\alpha F(E-E^{0\prime})}{RT}} \quad (2.33)$$

By considering the reaction at $E^{o\prime}$ where $\Delta_r G = 0$, then $k_{red} = k_{ox}$, we can define the standard electron transfer rate constant, k^o:

$$k^o = A_{ox} e^{\frac{-\Delta G^{\ddagger}_{ox}}{RT}} = A_{red} e^{\frac{-\Delta G^{\ddagger}_{red}}{RT}} \quad (2.34)$$

From equation 2.34 it can be seen that k^o is independent of potential but is strongly influenced by the transition state, which in turn means we can write:

$$k_{ox} = k^o e^{\frac{(1-\alpha)F(E-E^{0\prime})}{RT}} \quad (2.35)$$

$$k_{red} = k^o e^{\frac{-\alpha F(E-E^{0\prime})}{RT}} \quad (2.36)$$

If these equations, 2.35 and 2.36, are substituted into equations 2.27 we are able to derive the Butler-Volmer equation, which represents the potential-current relationship [16, 17].

$$I = FAk^o \left\{ [B]_0 e^{\frac{(1-\alpha)F(E-E^{0\prime})}{RT}} - [A]_0 e^{\frac{-\alpha F(E-E^{0\prime})}{RT}} \right\} \quad (2.37)$$

The value of k^o for coventional redox reactions tends to be in the range of 1 cm s^{-1} to 1x10^{-4} cm s^{-1} [19, 20]. The lower the value of k^o the more sluggishly the system will react to a change in potential and higher overpotentials, η, are required to drive the reaction, where:

$$\eta = E - E_{ocp} \quad (2.38)$$

and E_{ocp} is the open circuit potential of the system. Whilst the Butler-Volmer equation is able to describe the complete current-potential relationship, it is important to note that the concentrations

terms refer to concentrations of the redox species directly at the electrode surface, and that these may be different to the concentrations in the bulk solution.

When considering the transfer of electrons, it is also vital to consider if the transfer occurs via an *inner* or *outer sphere* pathway. While these terms apply to both homogeneous and heterogeneous reactions, here only heterogeneous reactions will be discussed. An *outer sphere* electron transfer occurs when the reactant and product have a relatively undisturbed solvent layer during the transfer and the outer Helmholtz plane is the plane of closest approach for the solvated ion/molecule. Common examples for *outer sphere* electron transfer species include the redox of hexachloroiridate(II)/(III) and hexaammineruthenium(II)/(III). In contrast, *inner sphere* electron transfers occur when the solvent layer is disturbed to a level where the reactant, intermediates or products interact strongly with the electrode surface, or are adsorbed to it. Whilst the *outer sphere* pathway is significantly less dependent on the electrode material, compared to the *inner sphere* pathway, there can still be a dependence on electrode material in relation to the electronic states within the material, or the materials effect on the double layer. Two of the most famous examples of an *inner sphere* reaction are the oxygen reduction reaction and the oxidation of hydrogen. Both of these are of particular interest as they occur on the cathode and anode of fuel cells, respectively.

2.3.1 Mass Transport

The mass transport of electroactive species from the bulk solution to the electrode surface are described by three main processes; diffusion, migration and convection, with each having an effect on the observed current.

2.3.2 Diffusion

The movement of electroactive species due to a concentration gradient is called diffusion. This is described by Fick's two laws. Ficks first law describes how a change in concentration affects the flux of molecules along a specified coordinate:

$$j_A(x,t) = -D_A(\frac{\partial[A](x,t)}{\partial x}) \quad (2.39)$$

Where j_A is the flux of species A, D_A is the diffusion coefficient of species A, and x is the coordinate that diffusing ions travel along [4, 21].

$$\frac{\partial[A](x,t)}{\partial x} = D_A\left(\frac{\partial^2[A](x,t)}{\partial x^2}\right) \quad (2.40)$$

Fick's second law, above, describes the change in concentration with respect to time at a specified coordinate. These equations only consider diffusion in one dimension in Cartesian coordinates. Other geometries such as spherical or cylindrical require other coordinate systems, for which the Laplace or del operator are commonly used. When a reaction produces or depletes species at the electrode surface, a concentration gradient is developed. This concentration gradient at the electrode surface is directly proportional to the current:

$$j = -D\frac{d[A]_{x=0}}{dx} \quad (2.41)$$

Where j is the diffusion flux and D the diffusion coefficient. The depletion zone essentially defines the diffusion layer between the electrode surface and the bulk solution. Nernst estimated the thickness of the diffusion layer, δ_N, by extrapolating the linear region in Figure 2.4 below, to a concentration equal to the bulk solution, given by the equation [1-3]:

$$\frac{\partial[A]_0}{\partial x} = \frac{[A]_{bulk}-[A]_0}{\delta_N} \quad (2.42)$$

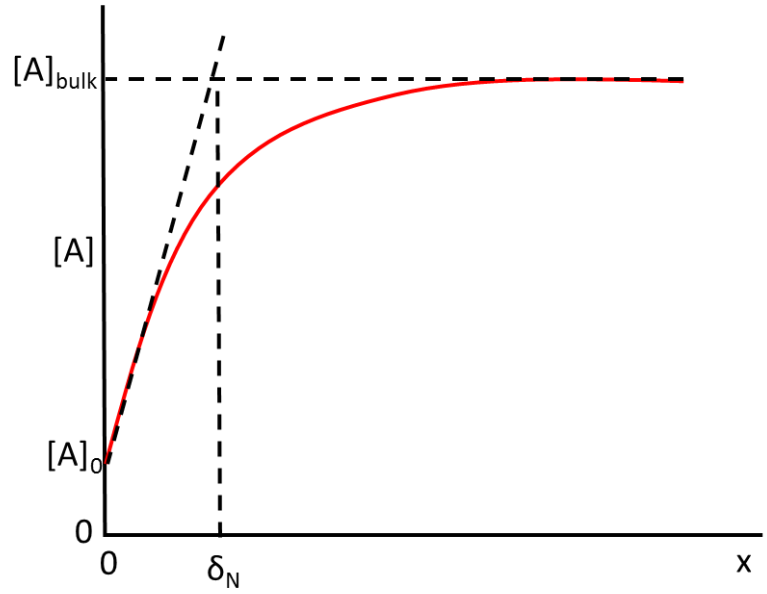

Figure 2.4: Diagram of the diffusion profile for a diffusion layer adjacent to the surface of an electrode.

The current from the reaction of species *A*, is related to the diffusion layer by:

$$I_A = nFAj_a = nFAD_A \frac{[A]_{bulk} - [A]_0}{\partial_N} \quad (2.43)$$

2.3.3 Migration

Migration is the movement of species, *i*, with charge, z_i, due to a potential gradient [1-3].

$$j_{A_m} = -\frac{z_A F}{RT} D_A [A] \frac{\partial \phi}{\partial x} \quad (2.44)$$

Where j_{A_m} is the flux due to migration of species A, z_A is the charge on species A and ϕ is potential. When considering the mathematical treatments of electrochemical systems, it is possible to simplify the contribution of migration by reducing j_{A_m} to a negligible value. This can be achieved by introducing an excess of inert background electrolyte to the solution, typically ≥0.1 M [4]. The background electrolyte at these concentrations is able to carry the majority of the current in the bulk solution, reducing the migration of the electroactive species of interest. There are several other benefits to introducing the background electrolyte. A clear, well defined and thin double layer is maintained. This

allows for the majority of the potential drop occurs across the double layer rather than as *iR* drop in solution [5]. The solution resistance is reduced, causing a smaller ohmic drop, which would otherwise lead to a distortion of the voltage-current response to the reaction of the electroactive species [1-3]. A fixed ionic strength is maintained across the whole solution, causing the activity coefficients of all species to be constant, allowing electrode potentials to be given as formal potentials.

2.3.4 Convection

Convection is the movement of molecules from an imbalance of force, either forced or natural. Forced convection occurs when an external force is applied to the solution, such as bubbling, stirring or pumping the solution, such as in the case of a flow cell or a rotating disc electrode [22, 23]. The introduction of convection can be used to deliberately dominate the mass transport to the electrode. Natural convection is usually due to gradients in temperature, surface charge or solution density and is random in nature, making it difficult to model [24, 25]. Over short time periods (<10 s) it can be considered insignificant [4].

2.4 Cyclic Voltammetry

Galvanostatic and potentiometric experiments are two typical approaches to the study of heterogeneous electron transfer reactions at the solid-electrolyte interface. For galvanostatic experiments, the current is controlled and the resulting potential is measured. In potentiometric experiments the reverse occurs, with a controlled potential and a measured current. While both methods produce quantitative data, in this thesis potentiometric experiments are used exclusively [1-3]. There are many possible techniques available for potentiometric experiments, but cyclic voltammetry is often the preferred technique due to its ease of experimental set-up and quantitative results.

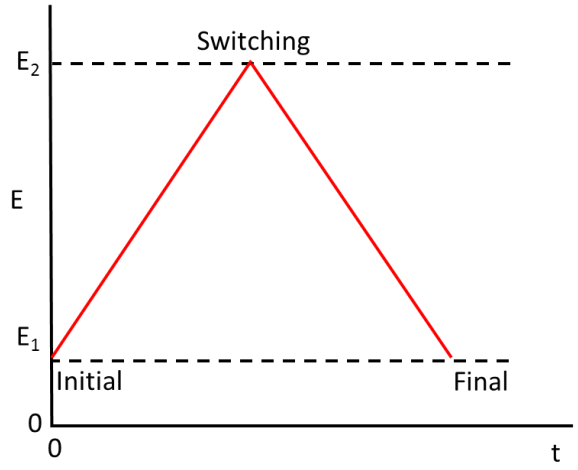

Figure 2.5: Diagram of voltage change vs time for a cyclic voltammetry experiment.

Figure 2.5 shows the triangular wave form representing a cyclic voltammetry experiment following the change of voltage over time. An external potential is applied to the working electrode (E_1). This gradual change from E_1 to E_2 will occur at a chosen potential where the analyte will not undergo a redox process. The potential is swept, at a rate of *v*, to the switching potential (E_2). This change in potential gives rise to faradaic currents as the analyte undergoes a redox process. If the experiment was to stop at E_2 it would be a linear sweep experiment. By reversing the direction of the potential sweep from E_2 back to E_1 at rate *v*, the experiment is now cyclic. The value of *v* is usually set between a few millivolts per second to a megavolt per second [26]. If *v* is too large, charging effects across the double layer, coupled with solution resistance leads to a distorted voltammogram. Similarly, if *v* is too small, leading to greater time periods between measurements, natural convection is no longer negligible and this undesired mass transport can cause distortion [4]. The current is measured at set increments across the scan and can be plotted as a function of applied potential to give the recognisable cyclic voltammogram.

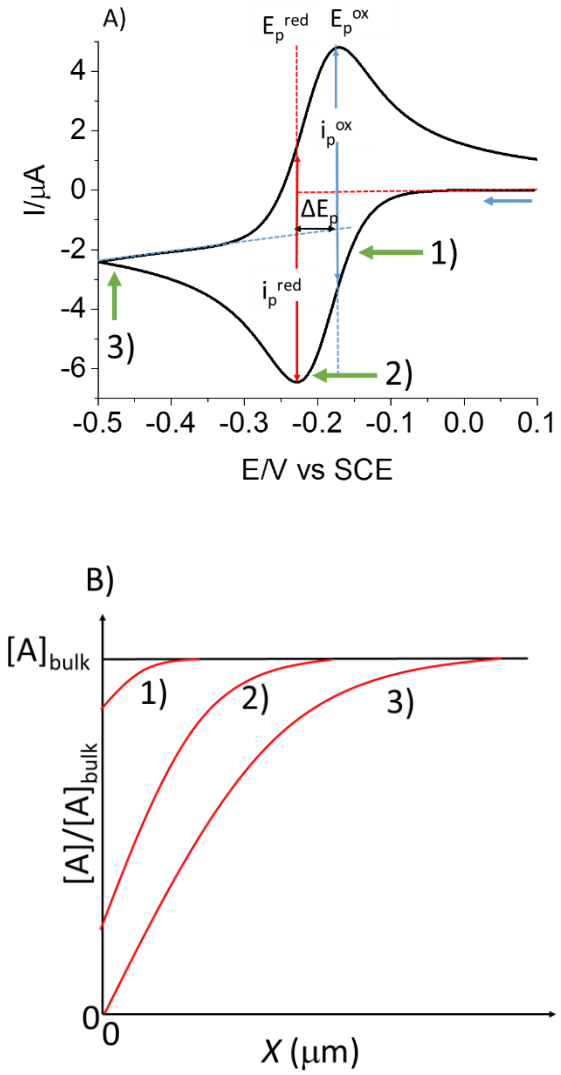

Figure 2.6: A) The cyclic voltammogram for a reversible one electron reaction where $E^{o'}$ = -0.2 V, α = 0.5, k^o = 0.1 cm s^{-1}, [A] = 1 x10^{-3} mols, D^o = 1 x10^{-6} cm^2 s^{-1}, v = 0.1 V s^{-1}, and A_{elec} = 0.076 cm^2. B) The change in concentration at the three labelled points from Figure 1.6 A)

Figure 2.6 A) illustrates a cyclic voltammogram for a reversible redox process following equation 2.22, where $E^{o'}$ = 0.22 V and **[**$A]_{bulk}$ = 1 mM, and **[**B] = 0 immediately before the reaction. As the current is swept from its initial potential the reduction of species A begins to occur, with the corresponding current increasing. At this point the solution in close proximity of the electrode surface has become depleted of species A, causing a concentration gradient. The reaction continues as the potential

increases; however, the current is limited by the flux of species A to the electrode surface. Diffusion is no longer enough to support the continued increase in current and a peak current I_p^{red}, is reached. As the diffusion layer continues to grow in size, the concentration gradient at the surface decreases, this means the flux of species A to the electrode surface decreases and therefore a reduction in j_A is seen.

Figure 2.6 B) shows the concentration profiles, with respect to species A, at different stages across the reduction sweep. At the first stage of the reaction, a small amount of species A has been reduced at the electrode surface and so only a small amount of species B has built up. At the second stage, the flux of species A to the electrode surface via diffusion is no longer sufficient to continue the increase in current, this leads to a peak current I_P^{red}. The diffusion layer will now be thicker. At the third stage, the concentration of species A will be approaching zero and the reduction of species A is now diffusion controlled. The diffusion layer growth, now 10s of μm thick, around the electrodes is large enough to cause lower currents. Once the potential reaches E_2, and the direction of the scan is reversed, the concentration of B which has accumulated at the electrode surface is oxidised, resulting in an anodic current. The concentration of species B, decreases in the same way as described for species A, and results in a peak oxidation current of I_P^{ox}. Each peak occurs at a characteristic potential of E_p^{red} and E_p^{ox} respectively, with the peak separation, ΔE_p, being the difference between these two potentials.

The change in applied potential over time is referred to as the scan rate, *v*. Each cyclic voltammogram will have a specific scan rate, and by varying this scan rate significant changes in the voltammetry can be observed, Figure 2.7.

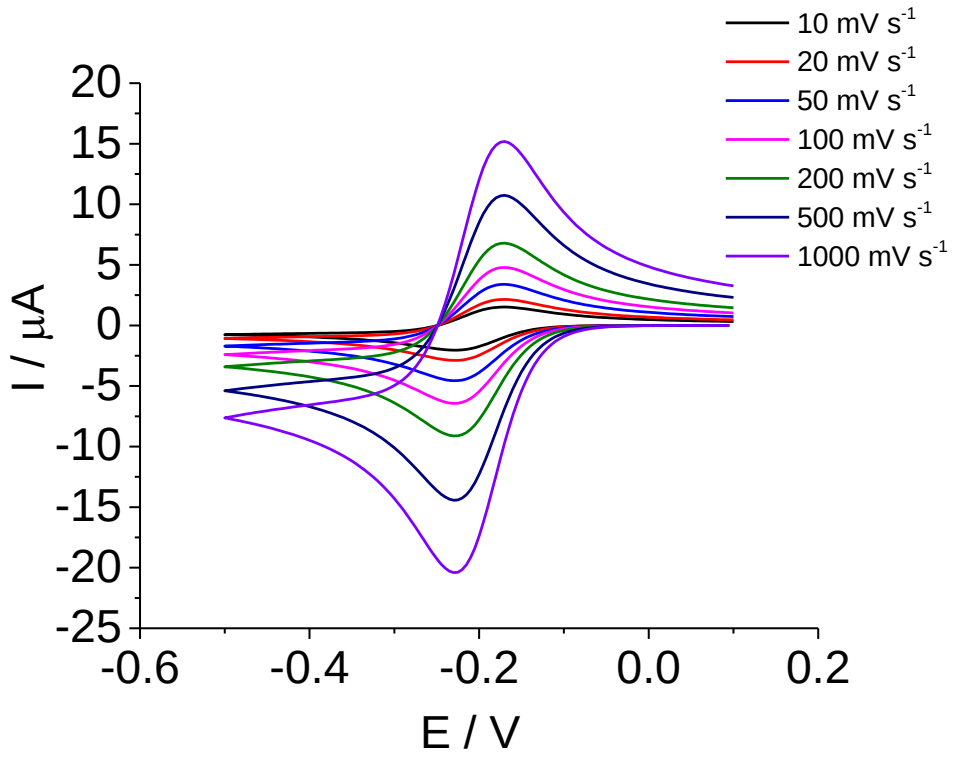

Figure 2.7: The cyclic voltammogram for a reversible one electron reaction at a range of scan rates as labelled, where $E^{o'}$ = -0.2 V, α = 0.5, k^o = 0.1 cm s^{-1}, [A] = 1 x10^{-3} mols, D^o = 1 x10^{-6} cm^2 s^{-1}, and A_{elec} = 0.076 cm^2.

$$\delta = \sqrt{2Dt} \tag{2.45}$$

The relationship shown between time, *t*, and the Nernst diffusion layer thickness, δ is described the equation above. Using this premise, it can be predicted that as the scan rate is increased, the electrochemical reaction, and therefore the diffusion layer thickness is reduced, whilst current increases. Figure 2.6 B) also shows that as *v* increases, the magnitude of the current also increases. The resulting concentration gradient is steeper, leading to a greater rates of mass transport of material to the electrode, causing an increase in faradaic current. The increase in faradaic current with scan rate will clearly lead to a change in the shape of the cyclic voltammogram, this change is observable in Figure 2.7. The response of the observed current (I_p) to the applied scan rate is described by the Randles- Ševćik equation:

$$I_p = \pm\psi nFAC\left(\frac{nFvD}{RT}\right)^{1/2} \quad (2.46)$$

$$I_p = \pm 0.4463nFAC\left(\frac{nFvD}{RT}\right)^{1/2} \quad (2.47)$$

Where *A* is the area of the electrode and *C* is the concentration of the species undergoing the redox reaction and ψ is the dimensionless current. By solving ψ for each point during a CV, the value of *E* vs ψ can be determined, which defines the shape of the cyclic voltammograms *I-E* curve. For reversible systems, the values of *E* vs ψ are always the same, where ψ_{max} = 0.4463 (where α = 0.5). The ± sign relates to the initial direction, oxidative or reductive, of the scan.

When discussing the kinetics at the electrode solution interface, the reversibility of a system may lie between electrochemically reversible and electrochemically irreversible. In an electrochemically reversible system the electrode-solution electron transfer rate is greater than the rate of diffusion to the electrode surface such that the electrode-solution interface is at equilibrium for the whole of the potential sweep [3, 4]. When this is the case, the concentration of both reactants and products is maintained to ensure the Nernst equation is satisfied. Thus, it is not possible to extract a value for k^o, with an inequality being the only qualitative result i.e. $k^o \geq 0.1$ cm s^{-1}. The required conditions for a reaction to be electrochemically reversible are given in table 2.1 [1].

Table 2.1: The diagnostic tests for an electrochemically reversible, irreversible and electrochemically quasi-reversible system at 298 K [1]. *Reverse peak may not be observed if outside the potential window of interest.

Reversible System	Quasi-Reversible System	Electrochemically Irreversible System
$\Delta E_p = \lvert E_p^c - E_p^a \rvert = 57$ mV n^{-1}	$\Delta E_p \geq 57$ mV n^{-1} and increases with increasing v	$\Delta E_p >> 57$ mV n^{-1} and increases with increasing v *
$\lvert I_p^c - I_p^a \rvert = 1$	$\lvert I_p^c - I_p^a \rvert = 1$ provided $\alpha = 0.5$	No reverse peak
E_p^c independent of v	E_p^c shifts negatively with increasing v	$E_p^c - \frac{30}{\alpha C^{n\alpha}}$ mV shifts for each decade increase in v
$\lvert I_p \rvert \propto v^{1/2}$	$\lvert I_p \rvert$ increases but is not proportional to $v^{1/2}$	$\lvert I_p \rvert \propto v^{1/2}$

At the other end of the spectrum lies electrochemically irreversible systems, where the electrode kinetics are slower than the rate of diffusion. In this case the equilibrium is not maintained during the cyclic voltammetry experiment, and the Nernst equation is not satisfied at the electrode-solution interface. An example of an electrochemically irreversible system is given in Figure 2.8 where k^o = 5 x10^{-5} cm^2 s^{-1}.

This irreversible cyclic voltammogram has a ΔE_p of significantly more than 57 mV, and when observing a limited potential range, it is not uncommon to only view a single peak due to the larger peak-to-peak separation. The principle attribute in determining electrochemical reversibility, $k°$, is also greatly reduced relative to the value in a reversible system and a larger overpotential is required to achieve a sizable electrochemical reaction current.

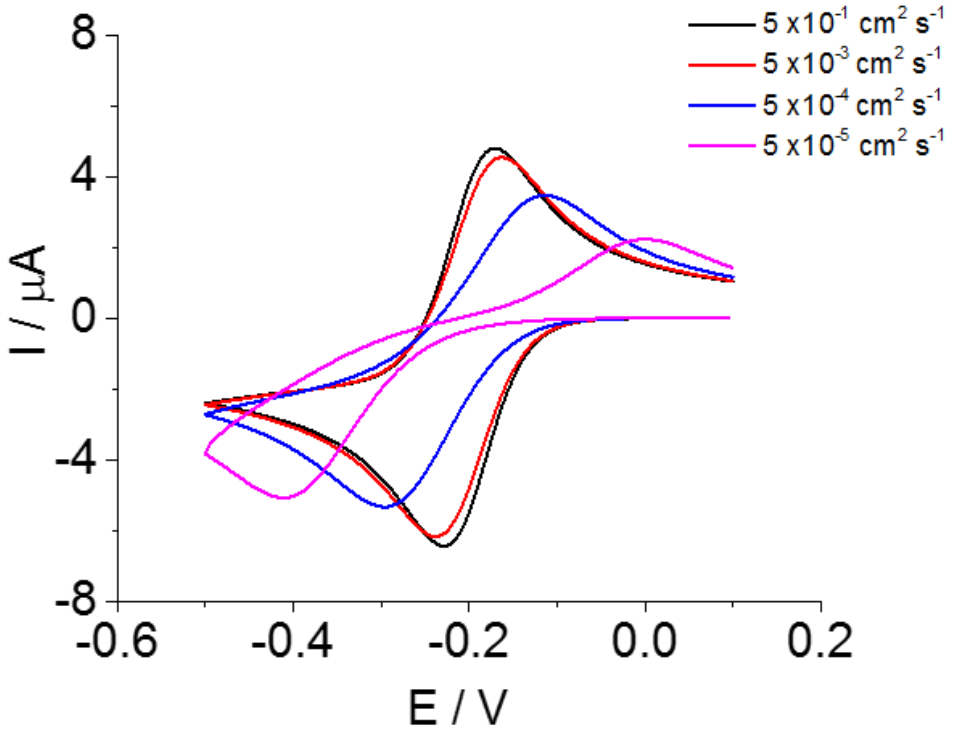

Figure 2.8: The simulated cyclic voltammogram for a one electron reaction at a range of k^o values as labelled, where $E^{o'}$ = -0.2 V, α = 0.5, v = 0.1 V s^{-1}, [A] = 1 x10^{-3} mols, D^o = 1 x10^{-6} cm^2 s^{-1}, and A_{elec} = 0.076 cm^2.

Any electrochemical process that lies between the two extremes of reversibility is known as an electrochemically quasi-reversible system. Previously it was shown (Figure 2.7) that ΔE_{p} is not affected by an increase in scan rate, v, however if the scan rate is further increased, ΔE_{p} would also increase showing a shift from reversible to quasi-reversible behaviour. In this case the rate of electrode kinetics is not great enough to maintain equilibrium at the electrode-solution interface and limits the resulting current. At this point it is possible to make appraisals of electrode kinetics parameters as they are now the limiting factor. Figure 2.8 shows the result of varying $k°$, leading to the transition from reversible, to quasi-reversible, to an irreversible system, clearly stating the importance of $k°$ for determining the reversibility of a system.

The Randles-Ševćik equation given in 2.47 is only valid for a reversible redox reaction, for an irreversible system, ψ_{max} is found to be 0.3506 (where α = 0.5) [27, 28]. In Figure 2.9, simulated cyclic voltammograms have been plotted showing ψ vs. E for different values of $k°$. The maximum values for the reversible and irreversible values of ψ are the peaks of the simulated CVs.

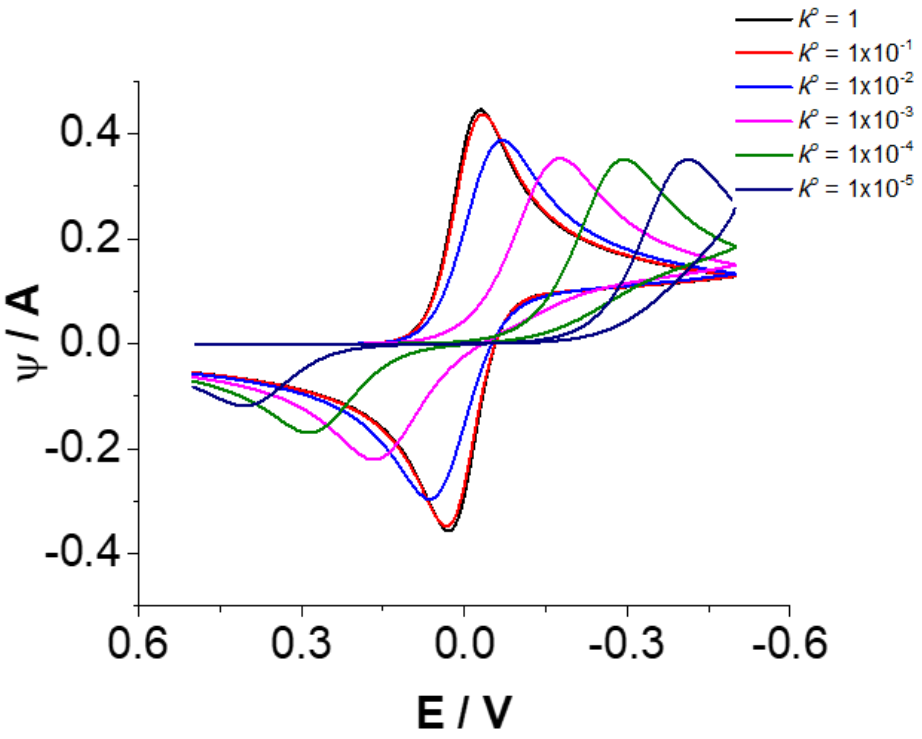

Figure 2.9: A plot of ψ vs. E for simulated cyclic voltammogram for a one electron reaction at a range of k^o values as labelled, where $E^{o'}$ = -0.2 V, α = 0.5, v = 0.1 V s^{-1}, [A] = 1 x10^{-3} mols, D^o = 1 x10^{-6} cm^2 s^{-1}, and A_{elec} = 0.076 cm^2.

It is also possible to determine $k°$ for quasi-reversible voltammograms, as shown by Nicholson, who found that ΔE_p could be expressed as a function of χ (a dimensionless parameter), where χ is given as [29]:

$$\chi = \frac{\left(\frac{D_A}{D_B}\right)^{\alpha/2} k^\circ}{\left(\frac{\pi D_A F v}{RT}\right)^{1/2}} \qquad (2.47)$$

Where D_A and D_B are the diffusion coefficients of species A and B. A simpler method for determining not only k°, but also D and α is to simulate a 1-dimensional reaction using commercially available software, such as DigiElch or DigiSim [30]. By matching an experimental voltammogram as closely as possible to a simulated one, by varying these parameters, their value is in turn revealed. This is the technique used within this thesis for determining values of k° and D.

2.4.1 Electrochemistry of Coupled Reactions

In this thesis, several of the electrochemical experiments are proceeded by an additional chemical reaction, for example reducing an organic molecule by one electron to for a radical anion, which is highly active and goes on to create an irreversible, covalent attachment to the electrode surface. In this case the reaction is described as an 'EC reaction', a notation system set out by Testa and Reinmuth, where E is the electrochemical electron transfer and C is the homogeneous chemical reaction [31]:

$$\begin{aligned} &\mathrm{A} + e^- \underset{k_{\mathrm{ox}}}{\overset{k_{\mathrm{red}}}{\rightleftharpoons}} \mathrm{B} \\ &\mathrm{B} \xrightarrow{k_{\mathrm{EC}}} \mathrm{C} \end{aligned} \qquad (2.48)$$

Fortunately, cyclic voltammetry can be effectively used to investigate these reactions, with a reduced reverse scan, depending on the magnitude of k_{EC}. As k_{EC} increases the reduction of the reverse peak will also increase, allowing the value of k_{EC} to be calculated, in cases where $k_{EC} >> k_{ox}$ there may be no visible peak at all.

2.4.2 Macro versus Micro Electrodes

The size of the electrodes active surface area also has a significant impact on its electrochemistry, the convention is to class electrodes as either micro or macro. Microelectrodes, are conventionally defined as those with a surface area on the scale of micrometres and below, can have significantly different behaviours when compared to their macroelectrode counterparts [32]. Due to the much smaller currents, as a smaller electrode results in smaller currents passed, the effect of solution resistance on the electrochemical signal is also much smaller (see equation 2.46),. Microelectrodes

also have a non-planar, or convergent diffusion regime, allowing for greater rates of mass transport. The hemi-spherical diffusion around the microelectrode is described in Figure 2.10. The edge of the electrode, where it meets the insulating material around it, the diffusion has an 'edge effect' where the mass transport becomes greater for the edge, leading to a greater current density. Micro (or even nano) electrodes are effectively dominated by the edge sites leading to a loss of peak signal (at low scan rates) and steady state voltammetry, shown in Figure 2.10 b). The steady state current, for a disc electrode is given by:

$$I = 4nFDc^*r \tag{2.49}$$

Where r is the radius of the disc electrode and c^* is the concentration of the bulk solution. This results in an increased rate of mass transport (per unit area) and therefore larger current densities, reducing the background 'noise' of non-faradaic processes. Microelectrodes also have a lower double-layer capacitance (*C*) as this is directly proportional to the area of the electrode surface. For macroelectrodes, electrodes with a surface area on the scale of millimetres, the proportion of edge is small enough to make this increase negligible. The planar diffusion associated with macroelectrode voltammetry leads to a traditional CV for a 1 electron reaction, as shown in Figure 2.10 a) [32]. The larger surface area also equates to a larger double-layer capactiance, which in turn leads to a lower potential scan rate maximum, before the charging current obsures the Faradaic current. Thus a smaller surface area will reduce the capactiance and lead to a higher possible scan rate. Combining all of these factors, microelectrodes are more adept for use in systems where a fast scan speed is required.

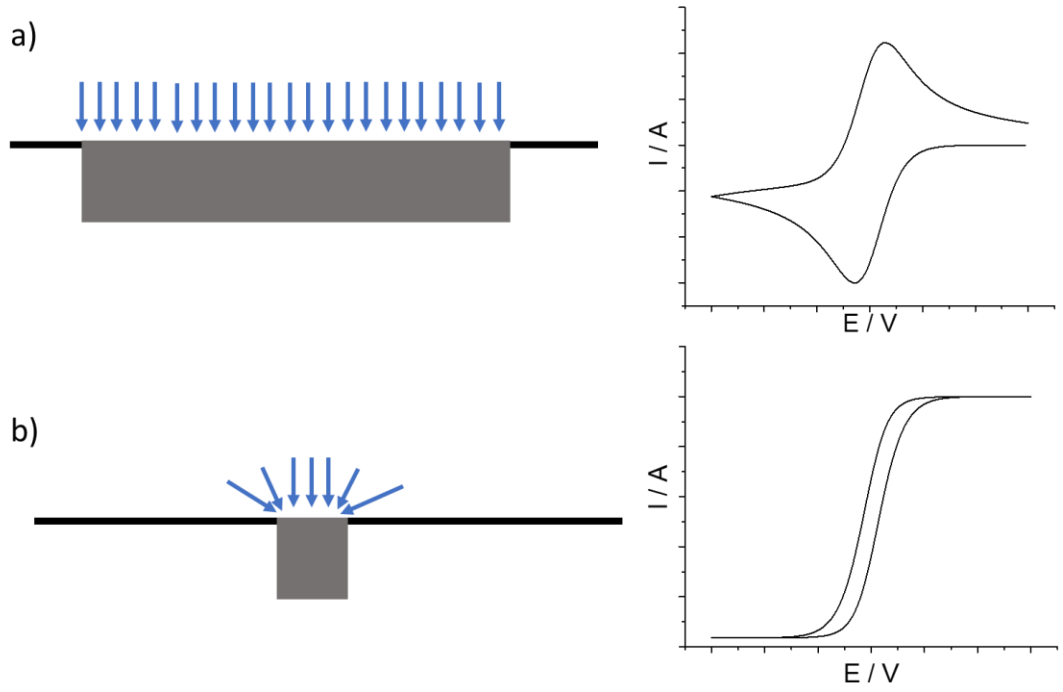

Figure 2.10: Comparison of a) planar diffusion at a macro electrode and its simulated cyclic voltammetric response for a one electron reaction and b) convergent diffusion at a micro electrode and its simulated cyclic voltammetric response for a one electron reaction [32].

2.4.3 Semi Infinite vs Thin Layer

In addition to the effects discussed so far, the structure of the electrode used also has a significant influence on the electrochemistry. In this thesis, many experiments use a porous, carbon fibre felt electrode. In this type of electrode (or any that contains small pores), the diffusion is split between two regimes. Across the external surface of the electrode, 'semi-infinite' diffusion takes place, representing the type of electrochemical response described previously. Within the pores 'thin layer' electrochemistry is the dominating factor, leading to a change in voltammetric response. This is discussed further in chapter 5 where the difference in thin layer vs semi-infinite diffusion is digitally simulated to characterise a porous felt electrode.

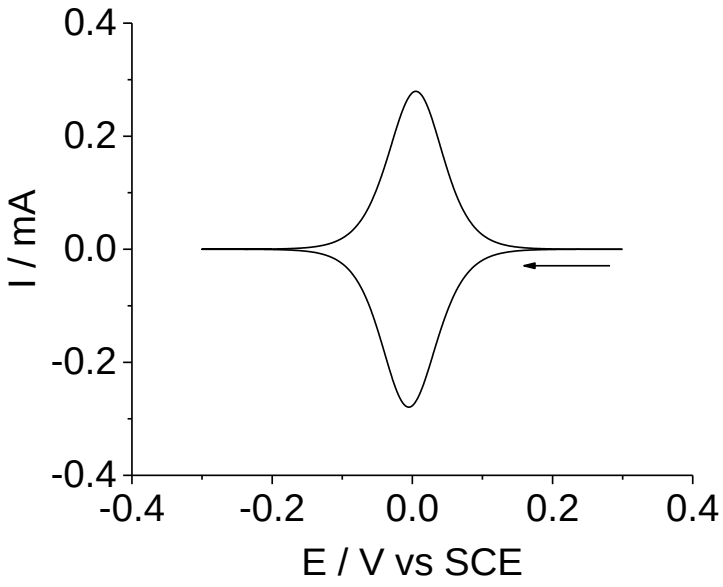

Figure 2.11: Simulated cyclic voltammograms for thin layer voltammetry at a scan rate of 0.01 V s^{-1}.

Thin layer electrochemistry occurs when the diffusion layer for an electrode is greater than the distance to cell boundary and increases the rate of depletion next to the electrode surface as mass transfer to the surface from the bulk cannot occur. In the extreme example the solution between the electrode surface and the cell boundary becomes fully depleted, as seen in a CV by the signal returning to the baseline, as shown in Figure 2.11. This is often characterised by the peak to peak distance in a cyclic voltammogram being significantly less than 57 mV (for a reversible reaction), even down to 0 mV difference, this effect is shown in Figure 2.11. A similar CV can be produced when the electroactive species is bound to the electrode surface, as mass transport is again negligible.

2.5 References

[1] D. Pletcher, Instrumental Methods in Electrochemistry, Horwood Pub Limited (2000).

[2] P. Atkins, J. De Paula, Physical Chemistry, Oxford University Press (2006).

[3] C. Banks, R. Compton, Understanding Voltammetry, World Scientific Publishing, (2007).

[4] A. Bard, L. Faulkner, Electrochemical Methods: Fundamentals and applications, 2nd ed., Wiley, New York, (2000).

[5] J. Koryta, J. Dvorak, L. Kavan, Principles of Electrochemistry, John Wiley & Sons Inc (1992).

[6] A. Fisher, Electrode Dynamics (Oxford Chemistry Primers), 1st ed., Oxford University Press (1996).

[7] C. Zoski, Handbook of Electrochemistry, 1st ed., Elsevier Science Limited (2007).

[8] I. Rubinstein, Physical Electrochemistry, CRC Press Llc (1994).

[9] E.J.F. Dickinson, J.G. Limon-Petersen, R.G. Compton, The electroneutrality approximation in electrochemistry, Journal of Solid State Electrochemistry 15(7-8) (2011) 1335-1345.

[10] S. Srinivasan, Fuel Cells: From Fundamentals to Applications, Springer US (2006).

[11] D.L. Chapman, LI. A contribution to the theory of electrocapillarity, Philosophical Magazine Series 6 25(148) (1913) 475-481.

[12] M. Gouy, Sur la constitution de la charge électrique à la surface d'un électrolyte, J. Phys. Theor. Appl. 9(1) (1910) 457-468.

[13] O. Stern, Zur theorie der elektrolytischen doppelschicht, Zeitschrift für Elektrochemie und angewandte physikalische Chemie 30(21-22) (1924) 508-516.

[14] D.C. Grahame, The electrical double layer and the theory of electrocapillarity, Chemical reviews 41(3) (1947) 441-501.

[15] J.A.V. Butler, Studies in heterogeneous equilibria. Part I. Conditions at the boundary surface of crystalline solids and liquids and the application of statistical mechanics, Transactions of the Faraday Society 19(March) (1924) 659-665.

[16] J. Butler, Studies in heterogeneous equilibria. Part II.—The kinetic interpretation of the nernst theory of electromotive force, Transactions of the Faraday Society 19(March) (1924) 729-733.

[17] J. Butler, Studies in heterogeneous equilibria. Part III. A kinetic theory of reversible oxidation potentials at inert electrodes, Transactions of the Faraday Society 19(March) (1924) 734-739.

[18] H. Gerischer, W. Ekardt, Fermi levels in electrolytes and the absolute scale of redox potentials, Applied Physics Letters 43(4) (1983) 393-395.

[19] R. Marcus, Electron transfer past and future, Advances in Chemical Physics: Electron Transfer-from Isolated Molecules to Biomolecules. Part 1, Volume 106 (1999) 1-6.

[20] R. Marcus, Tutorial on rate constants and reorganization energies, Journal of Electroanalytical Chemistry 483(1) (2000) 2-6.

[21] A. Fick, V. On liquid diffusion, The London, Edinburgh, and Dublin Philosophical Magazine and Journal of Science 10(63) (1855) 30-39.

[22] J. Jordan, R.A. Javick, Electrode kinetics by hydrodynamic voltammetry—study of ferrous-ferric, ferrocyanide-ferricyanide and iodide-iodine systems, Electrochimica Acta 6(1-4) (1962) 23-33.

[23] K. Tokuda, K. Aoki, H. Matsuda, Hydrodynamic voltammetry at channel electrodes: Part III. Theory of kinetic currents, Journal of Electroanalytical Chemistry and Interfacial Electrochemistry 80(2) (1977) 211-222.

[24] J.L. Taylor, T.J. Hanratty, Influence of natural convection on mass transfer rates for the electrolysis of ferricyanide ions, Electrochimica Acta 19(8) (1974) 529-533.

[25] W.M. Kays, M.E. Crawford, B. Weigand, Convective heat and mass transfer, Tata McGraw-Hill Education (2012).

[26] C. Amatore, E. Maisonhaute, G. Simonneau, Ultrafast cyclic voltammetry: performing in the few megavolts per second range without ohmic drop, Electrochemistry communications 2(2) (2000) 81-84.

[27] J. Randles, A cathode ray polarograph, Transactions of the Faraday Society 44 (1948) 322-327.

[28] A. Ševčik, Oscillographic polarography with periodical triangular voltage, Collection of Czechoslovak Chemical Communications 13 (1948) 349-377.

[29] R.S. Nicholson, Theory and Application of Cyclic Voltammetry for Measurement of Electrode Reaction Kinetics, Analytical chemistry 37(11) (1965) 1351-1355.

[30] M. Rudolph, D.P. Reddy, S.W. Feldberg, A simulator for cyclic voltammetric responses, Analytical chemistry 66(10) (1994) 589A-600A.

[31] A. Testa, W. Reinmuth, Stepwise reactions in chronopotentiometry, Analytical Chemistry 33(10) (1961) 1320-1324.

[32] M.C. Henstridge, R.G. Compton, Mass Transport to micro- and nanoelectrodes and their arrays: a review, Chemical Record 12(1) (2012) 63-71.

Chapter 3:

Carbon Materials as Electrodes.

Contents

3.1 Introduction

Carbon has been employed in electrochemical experiments in a huge variety of forms for decades and has been essential in the growth of the electrochemical discipline. Carbon electrodes boast many desirable traits over noble metal (Au, Pt) electrodes making them a popular choice for a wide variety of experiments. Unlike noble metal electrodes, carbon electrodes are relatively less costly to produce, usually have wider potential windows and can be modified in a variety of ways. The many forms of carbon electrodes have each become a subject of electrochemical research, ranging from carbon paste, to boron doped diamond, to the varying faces of graphite layers, to the structures of graphene such as nanotubes and graphene sheets. Each has a particular set of properties making 'carbon electrodes' a huge and versatile field.

3.2 Graphite

Graphite is an inexpensive and abundant material which can be manufactured into a wide variety of forms, making it a popular choice as an electrode material. It has an sp^2 hybridisation where planar hexagonal structures form from the combination of each carbon atoms sp^2 hybridised orbitals, in turn these layers stack to produce graphite. The one free electron on each carbon atom (2p orbital) lies perpendicular to the planar structure, creating a delocalised orbital system. This allows electrons to move perpendicular to the planar structure with relative ease, whilst moving between layers is much more difficult. A singular layer of this carbon material is known as graphene, which can be thought of as an infinitely large polyaromatic carbon compound, whilst multiple stacked layers are graphite.

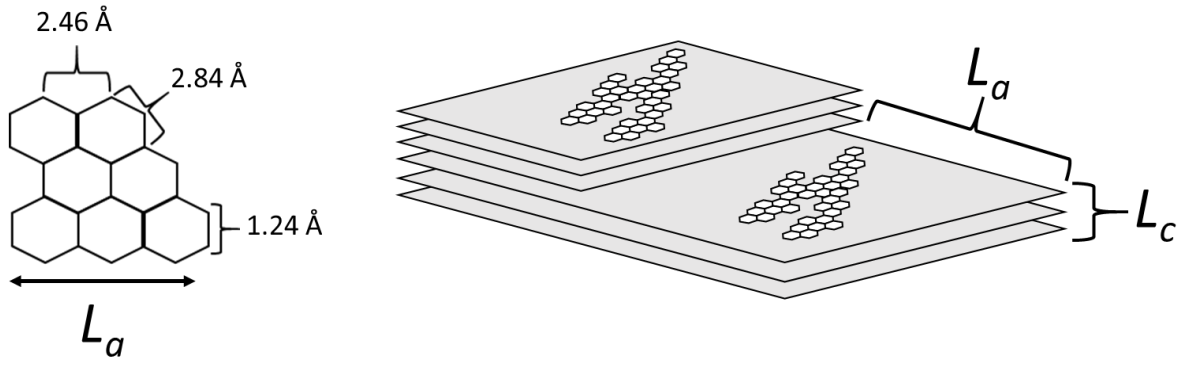

Figure 3.1: Diagram of the top-down view of a graphite sheet with C-C distances and lateral crystalline length (L_a) labelled (reproduced from ref [3]), and of the side view of HOPG, with the crystal planes labelled.

All the carbon atoms within a pristine graphite sheet are sp^2 hybridized with an intraplanar c-c distance of 1.42 Å and an interplanar separation of 3.35 Å (often described as '*d002*' from the X-ray diffraction peak). Pristine graphite has a density of between 2.09-2.23 g cm^{-3} [7]. Graphitic materials can be characterised using Raman spectroscopy and X-ray diffraction to determine the crystalline dimensions, with lateral length (L_a) referring to the layer plane width and L_c for crystalline stacking height as shown in Figure 3.1 [8-12]. Highly Orientated Pyrolytic Graphite (HOPG) is, the most highly ordered of these graphite materials. For high quality HOPG the values for L_a and L_c are in the micrometre range, for polycrystalline materials, such as carbon fibre this value would be in the nanometre range (Figure 3.2).

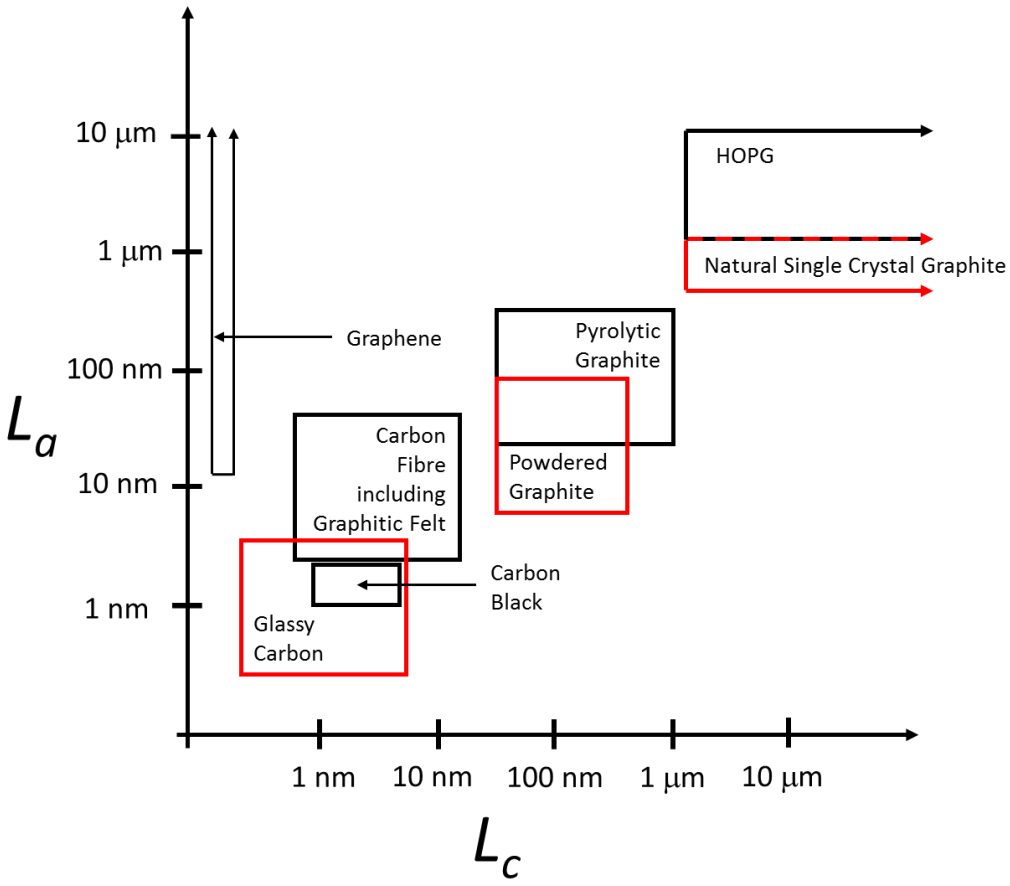

Figure 3.2: Chart of the approximate ranges of L_a and L_c for several sp^2 carbon materials.

Graphite is commonly stacked using a hexagonal ABA sequence, shown in Figure 3.3, although heat treatment >1300°C can cause rearrangement to the more thermodynamically stable, rhombohedral ABC stacking [1]. The hexagonal plane consists of two axes, the highly atomically ordered basal plane contains the a-axis while the irregular, termination sites at the end of the basal plane, parallel to the c-axis is the edge plane, these are shown in Figure 3.4.

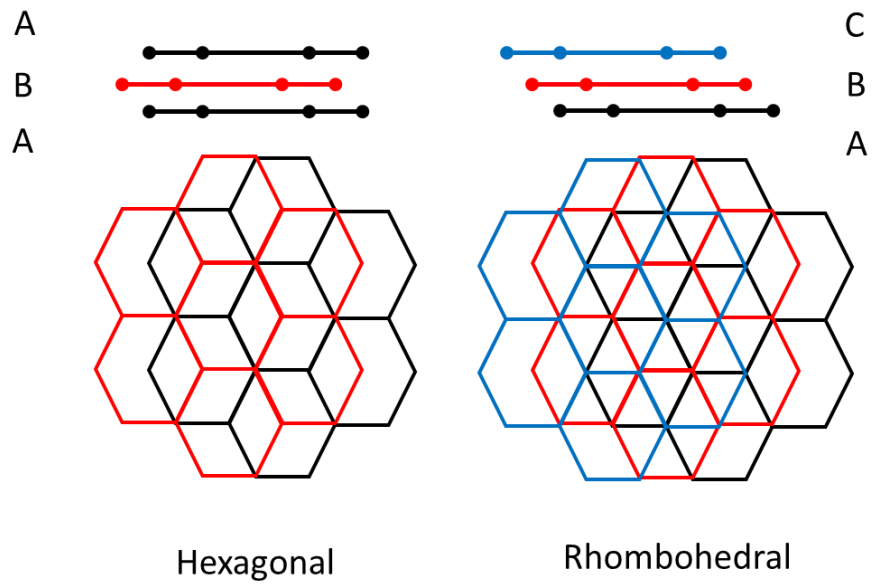

Figure 3.3: Diagram of the hexagonal and rhombohedral arrangement of bulk graphite.

3.2.1 Edge and Basal plane sites

The surface structure of carbon materials can be more complex than their metal counterparts. Similar to metal electrodes, the surface of these materials are exposed to the air and are able to react with gases present, leading to the production of surface oxide groups. In the case of graphite, the two planes will react with their surroundings in very different ways. The basal plane is highly ordered and smooth at the nanometre scale, but over a larger distance (micrometre range) the basal surface will contain many grain boundaries and step edges, and imperfections (such as missing carbon atoms), leaving the 'edge' of the basal plane exposed [13-15].

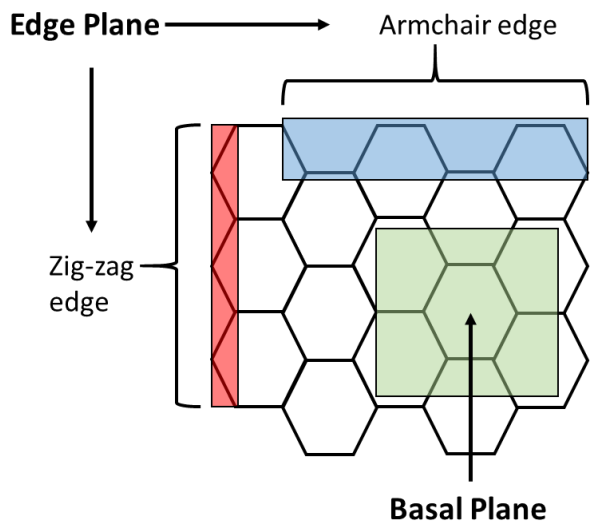

Figure 3.4: Diagram of the edge and basal planes of a graphite sheet with the 'zig-zag' and 'armchair' structural variations labelled.

At these defects there will be a reaction with ambient gasses, leading to surface oxide formation. The two most common crystal formations of the edge-plane are zig-zag and Armchair, shown in Figure 3.4. The two sites, edge and basal, are very different electrochemically and play a large role in the assessment of carbon electrode types. When a graphite surface is initially formed, any carbons with unsatisfied valence electrons will react with their surroundings. In the case of air or water, this will form a wide variety of oxide surface functionalities. The most common of these are ethers, carbonyls carboxylates and phenolic OH groups. A great deal of work is required to remove or prevent these groups from developing on a carbon surface, so for most lab work their presence must simply be accepted.

3.2.2 Edge vs Basal properties

Graphite's edge and basal plane sites appear to have significantly different reaction rates, related to their surface energies. The edge plane sites surface energy of 5 J m^{-2} is much greater than the basal plane's of 0.11 J m^{-2}, resulting in the reactions taking place at the edge plane to be much faster [16]. Electron transfer for the oxidation of ferrocyanide, a common redox probe, at the basal surface has been measured to be as low as 10^{-9} cm s^{-1} and in many cases the basal plane can be considered inert

[6, 17, 18]. The capacitance of the edge and basal planes also greatly differs. The basal plane has been measured to as low as 1.9 μF cm^{-2} to 3.0 μF cm^{-2}, by comparison the edge plane has shown a much higher specific capacitance of 60 μF cm^{-2}, but this is very dependant on the surface chemistry [3]. The Compton group have provided a lot of experimental evidence on the differences between edge and basal plane sites and show that the major contribution to any basal plane electrochemical activity is due to edge plane sites seen at defects and basal plate edges [19]. Figure 3.5 shows a schematic representation of a one electron transfer reaction occurring at the edge and basal plane sites of a single electrode [18]. The electrochemical activity of these sites will differ from one another and therefore, different α and Butler-Volmer terms.

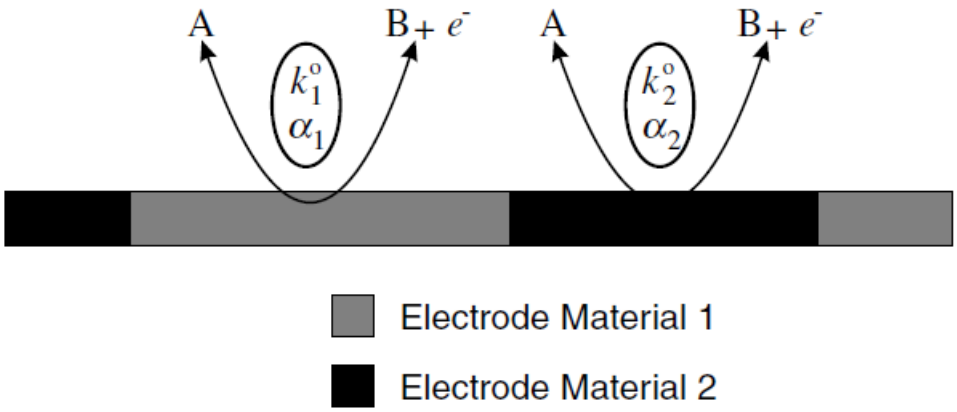

Figure 3.5: (**A**) Schematic representation of an electrochemical reaction occurring at two electrode materials on the same electrode. Reproduced from ref. [18].

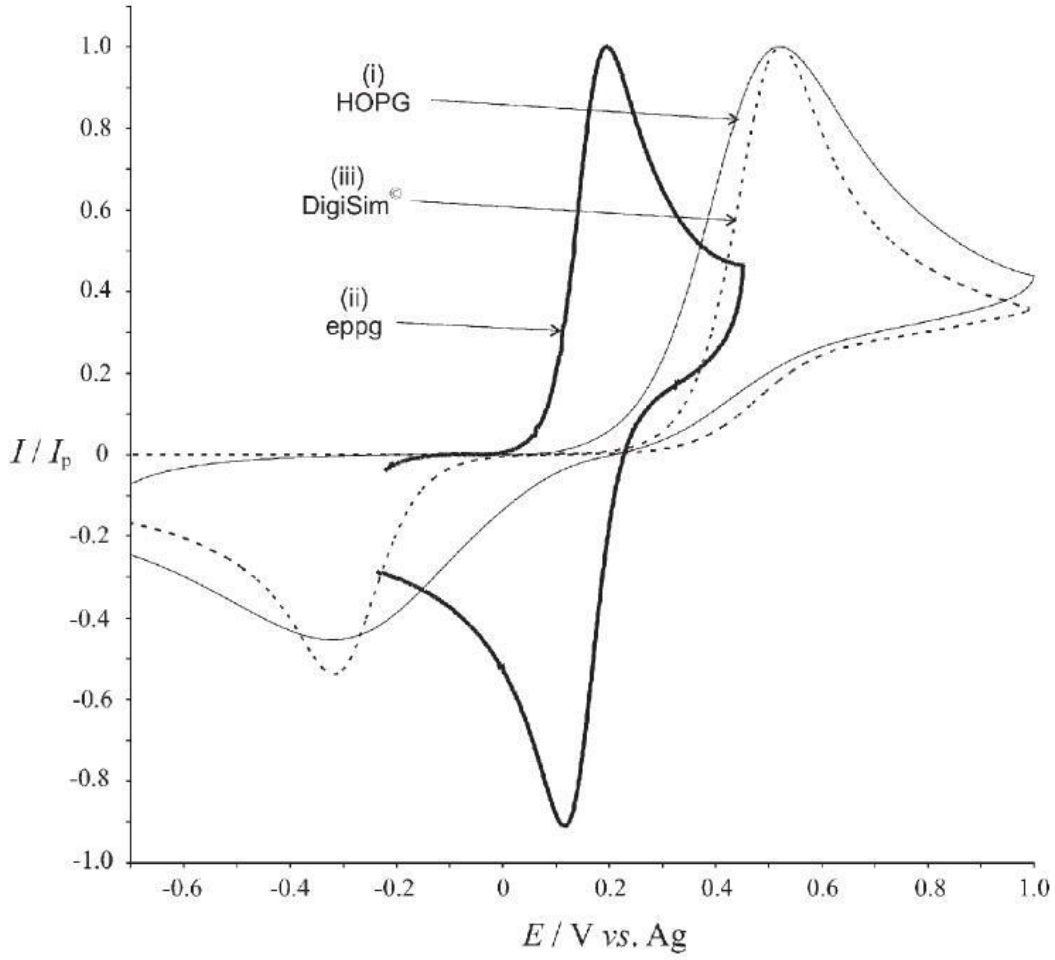

Figure 3.6: Cyclic voltammograms for (i) HOPG (basal orientation) and (ii) EPPG electrodes in a solution of 1 mM ferrocyanide in 1 M KCl. Overlaid is (iii) the Digisim© simulated cyclic voltammogram using a linear diffusion model. Reproduced from ref. [6].

The cyclic voltammograms in Figure 3.6 shows both the experimental results for a HOPG and EPPG electrode, but also the simulated response from the DigiSim© program using a purely linear diffusion model, when assuming that all parts of the surface are equally electrochemically active. It is important to note that the simulated response shows a greater peak to peak separation (ΔE_p) than for the experimental EPPG results, but also a greater expected reductive peak current than is observed from the HOPG experimental results

In order to accurately model the observed experimental voltammograms, the HOPG surface must be considered as a heterogeneous surface, with 'islands' of electrochemically inert basal plane, bordered by electrochemically active edge plane as shown in Figure 3.7 A). Both the basal disc and the boundary

edge plane will have a separate diffusion profile, which is modelled as shown in Figure 3.7 B) by a band of edge plane related diffusion encircling the basal plane related diffusion in a cylinder. Each of these diffusion cylinders is essentially independent of those cylinders surrounding it, resulting in no net flux between domains [6]. This technique is referred to as the diffusion domain model, with the voltammetric signal of the HOPG electrode being the total of all domains across the surface.

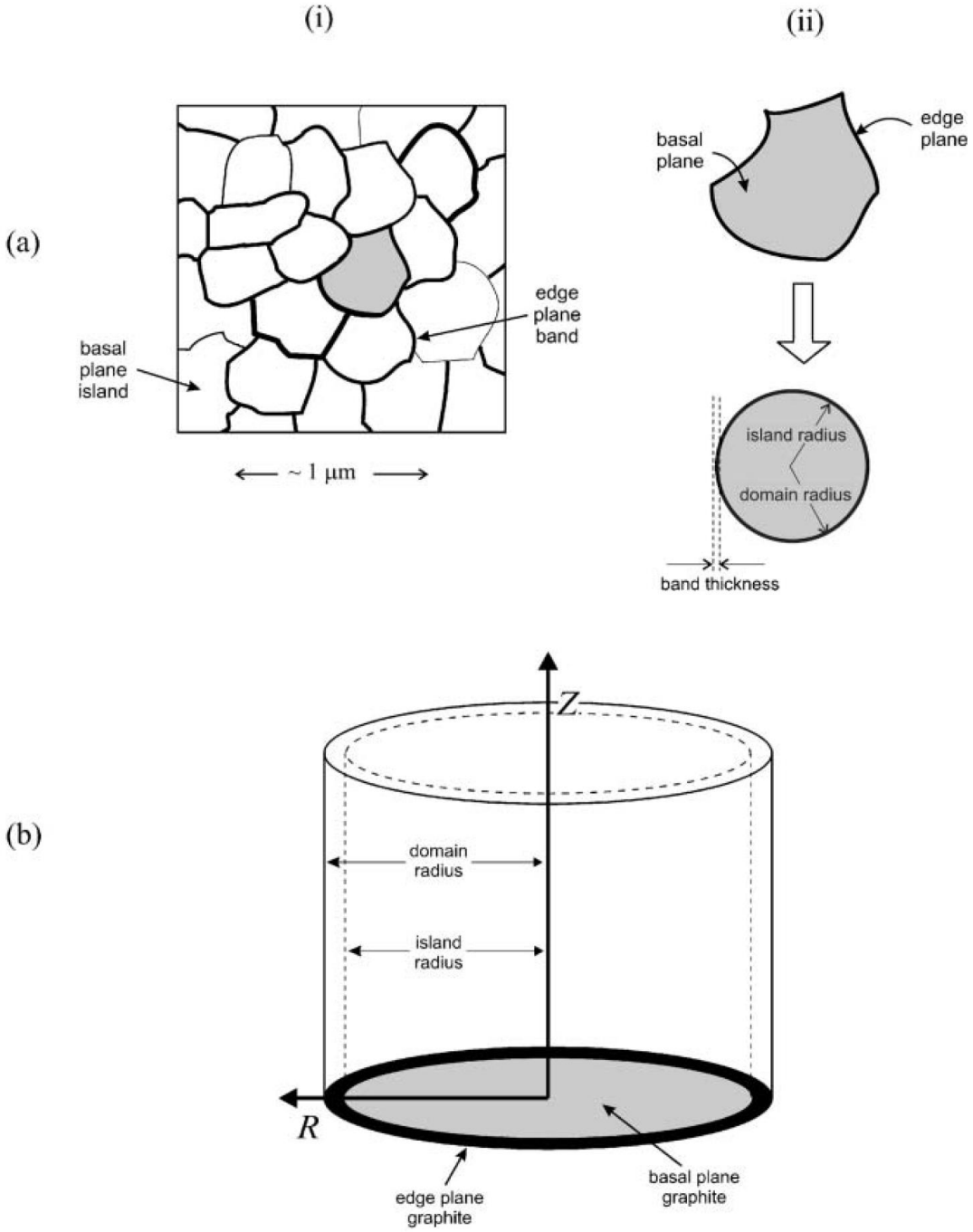

Figure 3.7: Diagrams of (a), (i) the top-down view of the basal plane of a HOPG, (ii) the translation from a 'island' to a circular disc and (b) the diffusion domain resulting from the disc shown in (a) (ii) with related diffusion cylinder. Reproduced from ref [6].

Shown in Figure 3.8 is the simulated curves of increasing diffusion domain radius. It can be seen that as the radius increases (and the proportion of edge plane decreases), the ΔE_p also increases. From this it can plausibly be presumed that the oxidation reaction modelled takes place entirely at the edge plane and that the basal plane is effectively inert.

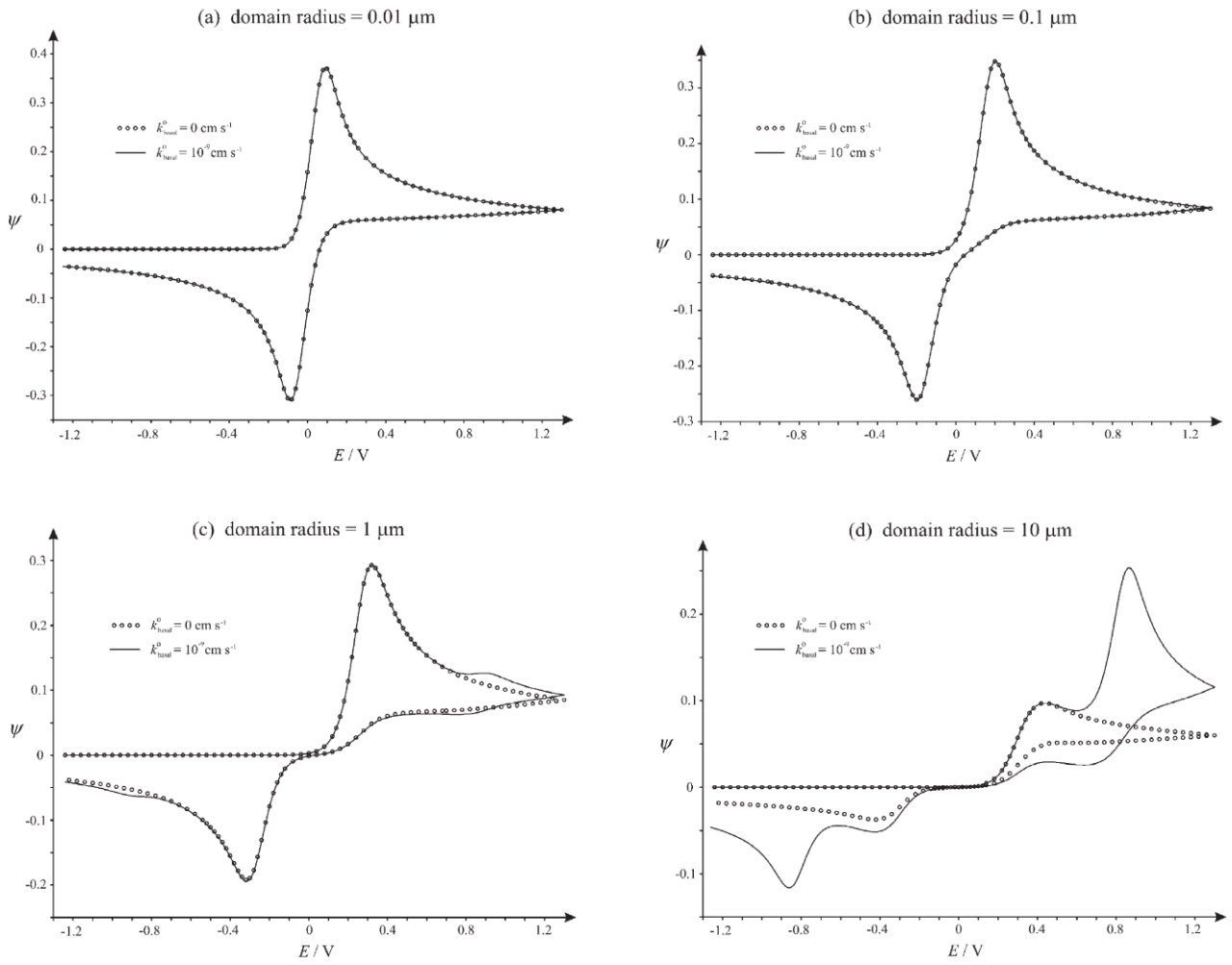

Figure 3.8: Simulated cyclic voltammograms (solid curve) of dimensionless current for increasing domain radius. Where α = 0.5, dα/dE = 0, D = 6.1 x 10^{-6} cm^2s^{-1}, kE$_{basal}$ = 10^{-9} cm s^{-1}, kE$_{edge}$ = 0.022 cm s^{-1} and a band thickness of 1.005 x 10^{-9} m. With the simulated inert basal domain (kE$_{basal}$ = 0 cm s^{-1}) overlaid (dotted curve). Reproduced from ref. [6].

Another example is the use of a polymer to selectively block the basal plane sites of HOPG, while the edge planes are left exposed and active. Figure 3.9 shows the process by which this experiment was achieved. Beginning with a freshly cleaved HOPG surface at stage 1, in stage 2 MoO_2 nanowires are formed along the edge plane sites leaving the basal plane exposed. These exposed areas are covered by a layer of 4-nitrobenzenediazonium through an aryl radical mechanism in stage 3 (this reaction is covered in greater depth in chapter 4). In stage 4 the MoO_2 nanowires are removed by washing with HCl, leaving the edge plane sites exposed.

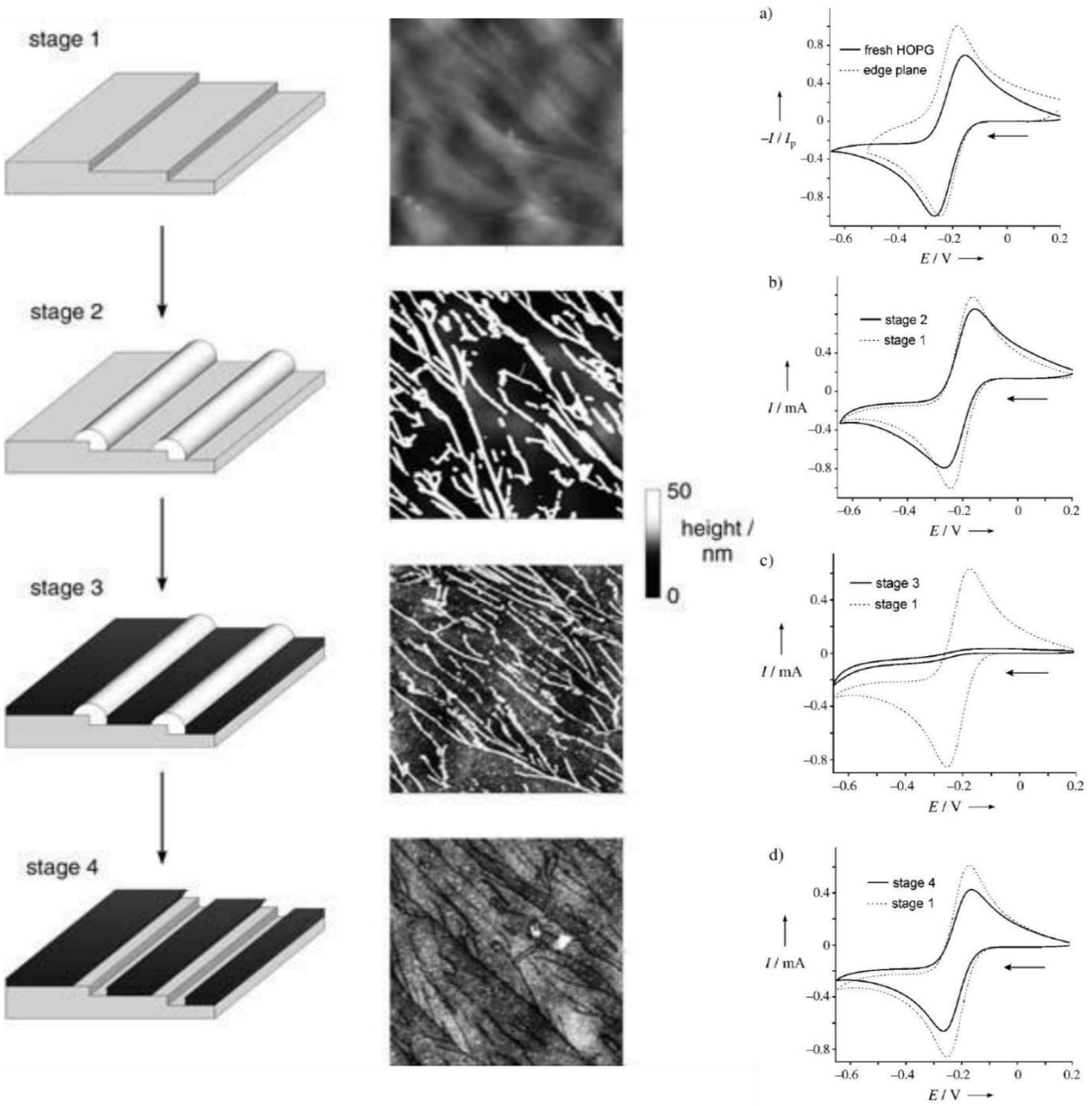

Figure 3.9: Stages 1-4 of deposition of the edge and basal plane coverage, on a freshly cleaved HOPG surface, with related cyclic voltammetry response a-d) in 1.1 mM $[Ru(NH_3)_6]^{3+}$ solution. CV a) used an EPPG electrode as a comparison to the fresh HOPG, whereas b-d) use the CV obtained from the stage 1 surface as a comparison. Reproduced from ref. [5].

At each stage the surface is assessed by measuring the cyclic voltammetry of 1.1 mM $[Ru(NH_3)_6]^{3+}$, the resulting voltammograms are displayed next to the appropriate stage in Figure 3.9. From these voltammograms it is clear that the basal plane has negligible contribution to the reduction of the $[Ru(NH_3)_6]^{3+}$, and all the electrochemical processes occur at the edge plane sites.

Work conducted by the Unwin group has attempted to show electrochemical activity at the basal plane site using an nano-scale droplet electrode technique (scanning electrochemical microscopy, SECM), on freshly cleaved HOPG and graphene [20-22]. The study suggests that the macroscopic scale of the electrodes commonly used in research, combined with the defects commonly found in the basal plane, means that any study of the surface electrochemically invariably leads to both basal and some step/edge plane being measured. Instead, by using a microscale electrode, the basal plane can be studied exclusively, avoiding step and edge sites. The work also shows that freshly cleaved basal plane in common redox probes can yield fast, almost reversible, electron transfer [21]. However it is also noted that over time the basal plane activity decreases significantly, as it reacts with the environment. More recent work by Compton et al has shown that the temperature distribution across the microscopic basal plane could explain the perceived increase in electrochemical activity. When these minute variations in localised temperature are not properley accounted for they can lead to misleading interpretation of results [23]. This allows the conclusion that electrochemical activity on basal electrodes is entirely due to the presence of edge plane sites at grain boundaries and defects.

3.3 Graphitic Electrode Electronic Properties

When considering any electrode, metallic or graphitic, one key element is the density of electronic states (DOS). The DOS is a measure of the number of electronic states available to be occupied, with a higher DOS relating to an increased possibility that an electron will have the necessary energy required to move to the electroactive species [8]. This results in a direct relation between the value of DOS and the heterogeneous electron transfer rate. For metallic species, the high conductivity is due to the high number of atomic orbitals forming energy bands with a high DOS. Gold is a commonly used metallic electrode and has a DOS of 0.28 states $atom^{-1}$ eV^{-1}, in comparison pristine HOPG has a much lower DOS at 0.0022 states $atom^{-1}$ eV^{-1} [24, 25]. The consequences of the low DOS of graphitic materials are their lower conductivity, relative to metals. Whereas the DOS in metals is usually high

and has a low energy dependence, the DOS in graphitic materials is very different, with the shape and value of DOS strongly dependant on the particular graphitic structure. The value of DOS can be increased with increased disorder in the graphitic material, hence the low value for pristine HOPG, whilst glassy carbon and EPPG electrodes, with their lower degree of crystalline ordering, have much higher DOS and therefore improved electron transfer rates [26].

3.4 Types of Graphite Electrode

As mentioned previously there is a great diversity of carbon electrodes commercially available and used across a wide range of applications. In this thesis the carbon electrodes used have been selected for their physical and chemical properties, and their relevance for use in fuel cells and flow batteries, such as graphitic felts (GFs), and for their significance to carbon electrode types used commonly in the literature, such as glassy carbon (GC), basal and edge plane pyrolytic graphite (BPPG / EPPG respectively). BPPG is very similar in structure to the common Highly Orientated Pyrolytic Graphite (HOPG) electrodes, although it is less highly orientated making it much less expensive. These materials, along with all other sp^2 hybridised carbon materials, share a similar crystalline graphite structure. Yet it is the lateral size of this graphite crystal (L_a) that determines the overall structure of the material. As shown in Figure 3.2, for electrode materials this can range from nm values in amorphous carbon materials, such as GC to tens of μm for HOPG electrodes. The fibres of GFs and EPPG/BPPG electrodes lie somewhere between these values, and can depend on the conditions used for the production of the electrodes.

3.4.1 Edge and Basal Plane Pyrolytic Graphite

EPPG and BPPG electrodes are cut from larger pieces of pyrolytic graphite which in turn is formed by the thermal decomposition of carbonaceous gas, such as methane and propane, on a hot substrate surface [3, 27]. This process is known as chemical vapour deposition (CVD), with the structural control based upon several factors, including: the precursor gas used, the density of the gas at the substrate

surface, the temperature and pressure at deposition and the contact time between gas and substrate. In general, higher temperatures and longer deposition times reduce the number of defects in the pyrolytic graphite allowing for greater ordering, whereas higher pressures can lead to an increase of incompletely combusted carbon particles, also known as 'carbon black' particles [1, 28]. For example; a high density pyrolytic carbon material formed from methane at 1400 °C to 2000 °C would require a low pressure (1.7×10^{-2} mbar), with any pressure over 4 mbar leading to low density pyrolytic materials due to the inclusion of carbon black particles [1]. The EPPG and BPPG electrodes are usually embedded in an inactive material such as glass or polyether ether ketone (PEEK) with the desired plane exposed as the electrode area. To prepare a fresh surface for use in electrochemical experiments a different approach is required based on the surface exposed. EPPG is usually polished on a microfiber pad using particles (such as diamond) of decreasing size, from ~10 μm to 0.1 μm in diameter. The layered structure of BPPG requires a more gentle technique, with the fresh surface exposed by exfoliating the top graphite layers, often through the use of adhesive tape, revealing the clean layers below. In either case the electrode will require rinsing with water and/or solvent (such as ethanol), to remove any small particles or adhesive left behind by these methods [28].

3.4.2 Graphene

In recent years the carbon material graphene has seen a surge in interest across a vast range of applications [2, 29-31]. Whilst not employed in this thesis it is worth outlining the basics of this popular material. Graphene is a single layer of graphite, essentially an infinitely large polycyclic aromatic hydrocarbon. Unlike graphite, pristine graphene is a purely two dimensional material, with sp2 carbons each bound to three neighbours in a hexagonal lattice [2, 30, 32]. Whilst pristine graphene is only a single sheet of material, stacks of graphene are not considered graphite until they number 8 sheets or more, with the a range of quasi-graphene materials numbering between 2 and 7 sheets with properties depending on the stack number [33-35]. Graphene is also the base material for other graphitic forms such as stacking into graphite, (single or multi-walled) carbon nanotubes (CNTs) and

fullerene C60 'buckyballs', as illustrated in Figure 3.10, each with their own distinctive electrochemical properties [2].

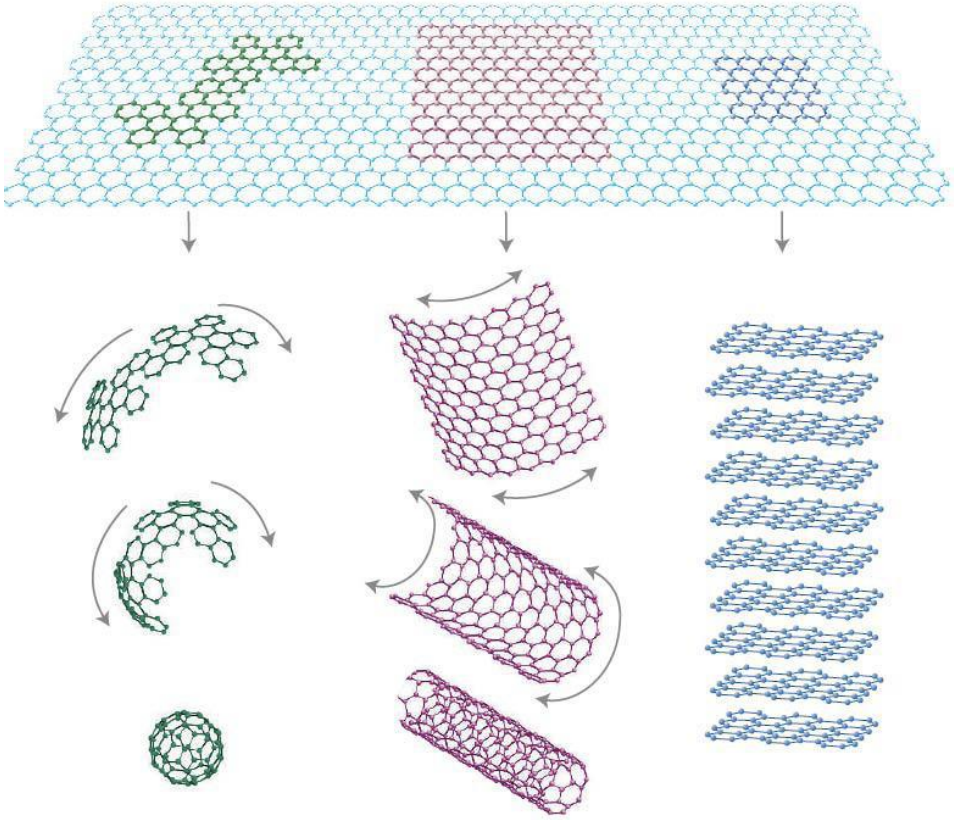

Figure 3.10: Graphical representation of graphene as a building material for fullerenes (left), single walled CNT (centre) and graphite (right). Reproduced from ref. [2]

Graphene can be formed via a vast range of techniques such as chemical vapour deposition (CVD), chemical or mechanical exfoliation of graphite or even synthesised from sugars, for example [36-39]. Each technique will produce graphene of varying purity and quantity, making different techniques suitable for different applications [30, 36]. In respect to electrochemistry, graphene has several properties that make it an advantageous electrode material. Firstly the theoretical surface area of pristine graphene sheet is significantly larger than that of graphite's, which is beneficial to applications such as sensors or energy storage [40]. Secondly, the particular electronic structure of means that it has excellent conductivity, capable of carrying charge significantly faster, than either graphite or CNTs,

allowing for greatly increased electron transfer rates [29, 31, 41]. These properties continue to make graphene a material of intense interest.

3.4.3 Carbon Fibres

Carbon fibre electrodes are used in a wide variety of applications, from in vivo biological measurements to flow batteries and fuel cells [42-44]. Carbon fibres can be used singularly or as part of a larger structure such as carbon felts and papers. The structure of a carbon fibre, and hence its chemical and physical properties are closely tied to its manufacturing conditions and precursor material. While most fibres tend to have diameters similar to a human hair, ~10 micrometres, with varying crystalline order and preparation technique, they can be better classified by their cross-sectional structure. Fibres can have an irregular orientation of graphite, or be structured, typically in either radial or layered forms. In the layered form the graphite planes form concentric rings, also known as an 'onion' structure. This contrasts the radial form, where the graphite planes radiate from the centre, similar to the spokes on a bicycle wheel, as shown in Figure 3.11. The onion and, to some degree, the random structure of carbon fibres, have a high ratio of basal plane graphite on the fibre sides than on the ends. Considering the different properties of edge and basal planes discussed previously, the side of a carbon fibre will have different electrochemical properties to the end of the fibre, if the ratio of edge to basal between the fibre side and end is also different. The literature shows the capacitance of a fresh carbon fibre's cylindrical surface to be 6.8 $\mu F\ cm^{-2}$, whereas for the fibre end this value is much greater at 23 $\mu F\ cm^{-2}$ [45]. The low capacitance value for the fibre sides is likely due to the higher fraction of basal plane graphite found there, with the pristine basal plane capacitance between 2-3 $\mu F\ cm^{-2}$, it would suggest that the structure is linked to its electrochemical properties [3]. The type of fibre, along with degree of order is highly dependent on the preparation conditions and precursor material.

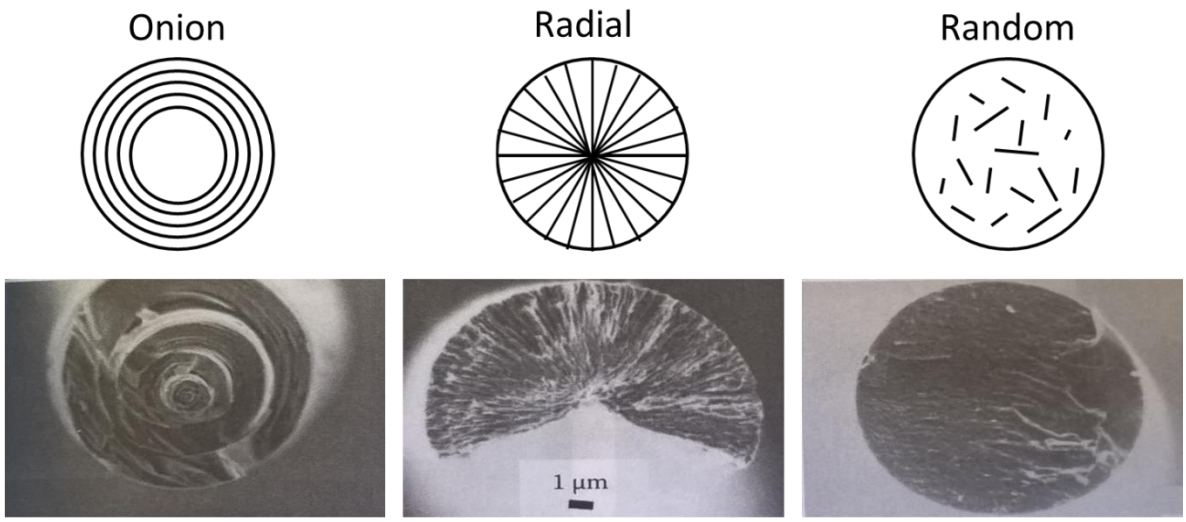

Figure 3.11: Scanning Electron Microscopy (SEM) images and related diagrams of carbon fibres with different structural forms. SEM images reproduced from ref [1].

The three most common commercial carbon fibre precursors are polyacrylonitrile (PAN), Pitch and Rayon, while the graphite felts used in this thesis are produced from PAN. The manufacturing process is broadly similar for each precursor and can be divided into three distinct steps. Firstly, heat stabilisation of the precursor in air at ~300 °C, leading to oxidation of the material to prevent the fibres melting or fusing together. Secondly carbonisation of the felt occurs at >1000 °C in an inert atmosphere. The process only lasts a few minutes but ensures that almost all non-carbon elements are removed from the material. At this stage it is possible to use the fibre, but it has a high degree of electrical resistance. The final stage, graphitisation, is also carried out in an inert atmosphere at between 2000-3000 °C and leads to three-dimensional ordering of the carbons, forming a graphitic structure. The precise nature of this final structure is dependent on the precursor and the exact conditions used during these three steps.

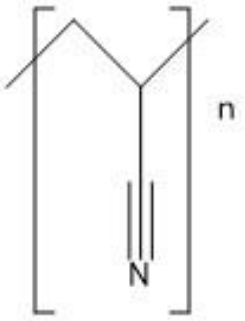

Figure 3.12: Structure of PAN monomer.

PAN (Figure 3.12) is used as a precursor for ~90% of the world's carbon fibre production [46]. The manufacturing of PAN based fibres is very similar to the steps provided in the overview, but often requires lower temperatures for carbonisation (1000 °C) and graphitisation (1500-3000 °C), reducing the manufacturing cost compared to the other precursors [46]. PAN based fibres generally form the concentric 'onion' ringed structure. In comparison, pitch is a much less expensive precursor material, but the more harsh conditions required during manufacturing, lead to an increased cost. Pitch based carbon fibre are most commonly found in the radial form. Rayon is derived from regenerated cellulose fibre and requires many additional processes to form, compared to the PAN fibre. It requires graphitisation under pressure to produce a known orientation of graphitic layering, which adds additional cost to the material. The yield of the manufacturing process of rayon is much lower than that of the other two precursors, at only 10-30 %. Graphite felts are often used as supplied with only rinsing with water/solvent as further cleaning, this is discussed further in chapter 4 [47].

3.4.4 Glassy Carbons

Glass-like carbons, more commonly known as vitreous or glassy carbon (GC) was discovered by Bernard Redfern in the mid 1950's. It is a non-graphitising form of carbon that combines elements of both ceramic and graphitic materials, with a combination of sp^2 and sp^3 hybridisation, and used across a wide range of electrochemical areas due to a few key properties [48-50]. Firstly, with the lack of any

long range crystalline ordering, low L_a, these materials are essentially non-porous, reducing the risk of contamination between experiments. This amorphous structure is derived from the carbonisation of organic polymer, usually PAN, at high temperatures and pressures until only the carbon atoms remain [51].

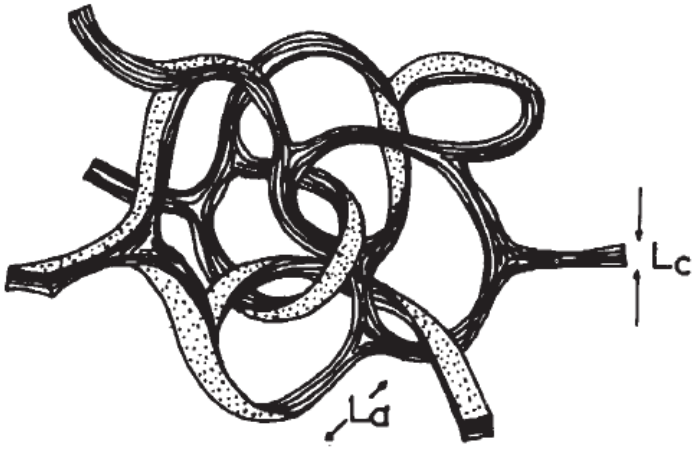

Figure 3.13: Diagram describing the interlinking ribbon structure of GC, reproduced from ref. [4].

This results in the interlinking ribbon structure of GC, first proposed by G.M. Jenkins and K. Kawamura in 1971 [4], shown in Figure 3.13, although this random structure causes a large degree of ambiguity in the microstructure [14, 52]. Secondly the sp^3 hybridisation leads to a degree of diamond crystalline ordering, which could lend to the high strength and resistance to chemical attack. Glassy carbon is only around 60% as dense a material as HOPG, with a larger interplanar spacing (*d002*) of around 3.6 Å and the intertwined ribbon structure leading to voids within the material. The L_c and L_a values for glassy carbon are much smaller than that of HOPG, at around 30-70 Å due to the restrictive nature of the structure to form longer ranged graphite sheets. Both GC and the plastic formed carbon electrode mentioned below are cleaned using the polishing method described in section 2.4.1.

3.4.4.1 Plastic Formed Carbon

Plastic formed carbon (PFC) electrodes are also employed within this thesis. Developed by the Mitsubishi Pencil Company in the 1990's; PFCE is a glass-like carbon material, but rather than being

randomly arranged like GC, the graphite crystals have been grown with the same orientation, giving the electrode surface a greater degree of edge plane characteristic [53, 54].

The production of PFC electrodes is illustrated by Figure 3.14 [55]. The initial material is a mix of graphite powder, chlorinated polyvinyl chloride and di-allyl phthalate monomer, which is mixed and extruded into a thin rod. This then undergoes thermal before undergoing thermal treatment. The initial thermal treatment (150-300 °C) in air is followed by a carbonisation process at 1000 °C under a N_2 atmosphere. The carbonised material impregnated with silicon oil before being insulated within a resin. This process allows the creation of PFC rods with diameters down to 10 μM allowing the use of this material as a microelectrode.

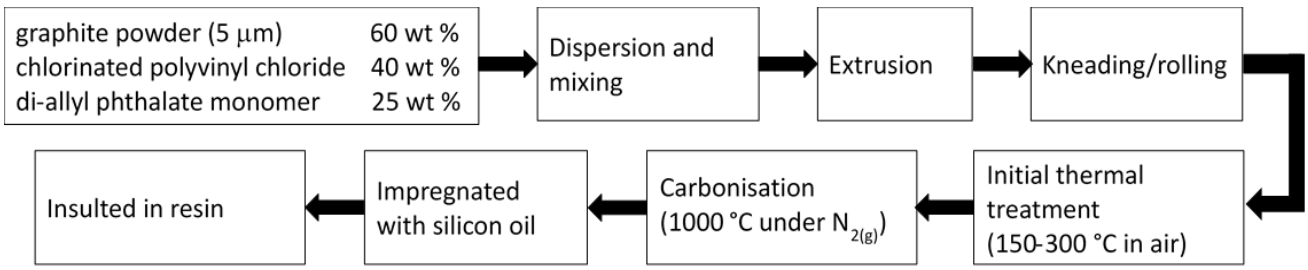

Figure 3.14: Diagram of the plastic formed carbon manufacturing process [55].

3.5 References

[1] F. Béguin, E. Frackowiak, Carbons for electrochemical energy storage and conversion systems, CRC Press2009.

[2] A.K. Geim, K.S. Novoselov, The rise of graphene, Nature materials 6(3) (2007) 183-191.

[3] R.L. McCreery, Carbon Electrodes: Structural Effects on Electron Transfer Kinetics, in: A.J. Bard (Ed.), Electroanalytical Chemistry: A Series of Advances, CRC Press (1990).

[4] G.M. Jenkins, K. Kawamura, Structure of glassy carbon, Nature 231(5299) (1971) 175-6.

[5] T.J. Davies, M.E. Hyde, R.G. Compton, Nanotrench arrays reveal insight into graphite electrochemistry, Angewandte Chemie-International Edition 44(32) (2005) 5121-5126.

[6] C.E. Banks, T.J. Davies, G.G. Wildgoose, R.G. Compton, Electrocatalysis at graphite and carbon nanotube modified electrodes: edge-plane sites and tube ends are the reactive sites, Chemical Communications (7) (2005) 829-841.

[7] J.W. Anthony, R.A. Bideaux, K.W. Bladh, M.C. Nichols, Graphite, PDF). Handbook of Mineralogy. I (Elements, Sulfides, Sulfosalts). Chantilly, VA, US: Mineralogical Society of America. ISBN 962209708 (1990).

[8] R.L. McCreery, Advanced carbon electrode materials for molecular electrochemistry, Chemical Reviews 108(7) (2008) 2646-2687.

[9] M.J. Matthews, M.A. Pimenta, G. Dresselhaus, M.S. Dresselhaus, M. Endo, Origin of dispersive effects of the Raman D band in carbon materials, Physical Review B 59(10) (1999) R6585-R6588.

[10] Y. Wang, D.C. Alsmeyer, R.L. McCreery, Raman-spectroscopy of carbon materials – structural basis of observed spectra, Chemistry of Materials 2(5) (1990) 557-563.

[11] R. Aljishi, G. Dresselhaus, Lattice-dynamical model for graphite, Physical Review B 26(8) (1982) 4514-4522.

[12] J.S. Speck, J. Steinbeck, M.S. Dresselhaus, Microstructual studies of laser irradiated graphite surfaces, Journal of Materials Research 5(5) (1990) 980-988.

[13] M.T. McDermott, K. Kneten, R.L. McCreery, Antraquinonedisulfonate adsorption, electron-transfer kinetics, and capacitance of ordered graphite-electrodes – The important role of surface-defects, Journal of Physical Chemistry 96(7) (1992) 3124-3130.

[14] M.T. McDermott, C.A. McDermott, R.L. McCreery, Scanning tunneling microscopy of carbon surfaces – relationships between electrode-kinetics, capacitance, and morphology for glassy-carbon electrodes, Analytical Chemistry 65(7) (1993) 937-944.

[15] H.P. Chang, A.J. Bard, Observation and characterization by scanning tunelling microscopy of structures generated by cleaving highly oriented pyrolytic-graphiteE, Langmuir 7(6) (1991) 1143-1153.

[16] R. Sharma, J.H. Baik, C.J. Perera, M.S. Strano, Anomalously Large Reactivity of Single Graphene Layers and Edges toward Electron Transfer Chemistries, Nano Letters 10(2) (2010) 398-405.

[17] C.E. Banks, R.G. Compton, New electrodes for old: from carbon nanotubes to edge plane pyrolytic graphite, Analyst 131(1) (2006) 15-21.

[18] T.J. Davies, R.R. Moore, C.E. Banks, R.G. Compton, The cyclic voltammetric response of electrochemically heterogeneous surfaces, Journal of Electroanalytical Chemistry 574(1) (2004) 123-152.

[19] M.E. Hyde, T.J. Davies, R.G. Compton, Fabrication of random assemblies of metal nanobands: A general method, Angewandte Chemie-International Edition 44(40) (2005) 6491-6496.

[20] M.A. Edwards, P. Bertoncello, P.R. Unwin, Slow Diffusion Reveals the Intrinsic Electrochemical Activity of Basal Plane Highly Oriented Pyrolytic Graphite Electrodes, Journal of Physical Chemistry C 113(21) (2009) 9218-9223.

[21] S.C. Lai, A.N. Patel, K. McKelvey, P.R. Unwin, Definitive evidence for fast electron transfer at pristine basal plane graphite from high-resolution electrochemical imaging, Angew Chem Int Ed Engl 51(22) (2012) 5405-8.
[22] C.G. Williams, M.A. Edwards, A.L. Colley, J.V. Macpherson, P.R. Unwin, Scanning Micropipet Contact Method for High-Resolution Imaging of Electrode Surface Redox Activity, Analytical Chemistry 81(7) (2009) 2486-2495.
[23] J.K. Novev, R.G. Compton, Thermal convection in electrochemical cells. Boundaries with heterogeneous thermal conductivity and implications for scanning electrochemical microscopy, Physical Chemistry Chemical Physics 19(20) (2017) 12759-12775.
[24] H. Gerischer, R. McIntyre, D. Scherson, W. Storck, Density of the electronic states of graphite – derivation from differential capacitance measurements, Journal of Physical Chemistry 91(7) (1987) 1930-1935.
[25] K. Kokko, E. Ojala, K. Mansikka, Fermi level density of states in Ag-Au alloys – Nuclear magnetic spin-lattice relaxation rate and low-temperature specific-heat, Physica Status Solidi B-Basic Research 153(1) (1989) 235-241.
[26] D.A.C. Brownson, D.K. Kampouris, C.E. Banks, Graphene electrochemistry: fundamental concepts through to prominent applications, Chemical Society Reviews 41(21) (2012) 6944-6976.
[27] F. Rodriguez-Reinoso, A. Linares-Solano, In Chemistry and Physics of Carbon; Thrower, PA, Ed, Marcel Dekker, New York, (1988).
[28] R. Diefendorf, The deposition of pyrolytic graphite, DTIC Document, (1960).
[29] X. Wang, L. Zhi, K. Müllen, Transparent, conductive graphene electrodes for dye-sensitized solar cells, Nano letters 8(1) (2008) 323-327.
[30] D.A. Brownson, C.E. Banks, Graphene electrochemistry: an overview of potential applications, Analyst 135(11) (2010) 2768-2778.
[31] S. Sato, N. Harada, D. Kondo, M. Ohfuchi, Graphene—Novel material for nanoelectronics, Sci Tech 46(1) (2010) 103-110.
[32] E. Fitzer, K. H. Kochling, H. Boehm, H. Marsh, Recommended terminology for the description of carbon as a solid (IUPAC Recommendations 1995), Pure and Applied Chemistry 67(3) (1995) 473-506.
[33] D. Yoon, H. Moon, H. Cheong, J.S. Choi, J.A. Choi, B.H. Park, Variations in the Raman Spectrum as a Function of the Number of Graphene Layers, J. Korean Phys. Soc 55(3) (2009) 1299-1303.
[34] D.A. Brownson, L.C. Figueiredo-Filho, X. Ji, M. Gómez-Mingot, J. Iniesta, O. Fatibello-Filho, D.K. Kampouris, C.E. Banks, Freestanding three-dimensional graphene foam gives rise to beneficial

electrochemical signatures within non-aqueous media, Journal of Materials Chemistry A 1(19) (2013) 5962-5972.

[35] D. Graf, F. Molitor, K. Ensslin, C. Stampfer, A. Jungen, C. Hierold, L. Wirtz, Spatially resolved Raman spectroscopy of single-and few-layer graphene, Nano letters 7(2) (2007) 238-242.

[36] C. Soldano, A. Mahmood, E. Dujardin, Production, properties and potential of graphene, Carbon 48(8) (2010) 2127-2150.

[37] L. Tang, X. Li, R. Ji, K.S. Teng, G. Tai, J. Ye, C. Wei, S.P. Lau, Bottom-up synthesis of large-scale graphene oxide nanosheets, Journal of Materials Chemistry 22(12) (2012) 5676-5683.

[38] S. Park, R.S. Ruoff, Chemical methods for the production of graphenes, Nature nanotechnology 4(4) (2009) 217-224.

[39] M.H. Rümmeli, C.G. Rocha, F. Ortmann, I. Ibrahim, H. Sevincli, F. Börrnert, J. Kunstmann, A. Bachmatiuk, M. Pötschke, M. Shiraishi, Graphene: piecing it together, Advanced Materials 23(39) (2011) 4471-4490.

[40] M. Pumera, Electrochemistry of graphene: new horizons for sensing and energy storage, The Chemical Record 9(4) (2009) 211-223.

[41] C. Liu, S. Alwarappan, Z. Chen, X. Kong, C.-Z. Li, Membraneless enzymatic biofuel cells based on graphene nanosheets, Biosensors and bioelectronics 25(7) (2010) 1829-1833.

[42] M. Heien, M.A. Johnson, R.M. Wightman, Resolving neurotransmitters detected by fast-scan cyclic voltammetry, Analytical Chemistry 76(19) (2004) 5697-5704.

[43] A. Hermans, A.T. Seipel, C.E. Miller, R.M. Wightman, Carbon-fiber microelectrodes modified with 4-sulfobenzene have increased sensitivity and selectivity for catecholamines, Langmuir 22(5) (2006) 1964-1969.

[44] R.M. Wightman, Probing cellular chemistry in biological systems with microelectrodes, Science 311(5767) (2006) 1570-1574.

[45] J.X. Feng, M. Brazell, K. Renner, R. Kasser, R.N. Adams, Electrochemical pretreatment of carbon fibers for in vivo electrochemistry: effects on sensitivity and response time, Analytical chemistry 59(14) (1987) 1863-1867.

[46] M.S.A. Rahaman, A.F. Ismail, A. Mustafa, A review of heat treatment on polyacrylonitrile fiber, Polymer Degradation and Stability 92(8) (2007) 1421-1432.

[47] R.E.G. Smith, T.J. Davies, N.D. Baynes, R.J. Nichols, The electrochemical characterisation of graphite felts, Journal of Electroanalytical Chemistry 747 (2015) 29-38.

[48] S. Ranganathan, T.C. Kuo, R.L. McCreery, Facile preparation of active glassy carbon electrodes with activated carbon and organic solvents, Analytical Chemistry 71(16) (1999) 3574-3580.

[49] R.J. Rice, N.M. Pontikos, R.L. McCreery, Quantitative correlations of heterogeneous electron-transfer kinetics with surface-properties of glassy-carbon electrodes, Journal of the American Chemical Society 112(12) (1990) 4617-4622.

[50] I.F. Hu, D.H. Karweik, T. Kuwana, activation and deactivation of glassy-carbon electrodes, Journal of Electroanalytical Chemistry 188(1-2) (1985) 59-72.

[51] G.M. Jenkins, Polymeric carbons--carbon fibre, glass and char, Cambridge University Press, Cambridge ; New York, (1976).

[52] M.T. McDermott, R.L. McCreery, Scanning-tunneling-microscopy of ordered glassy-carbon surfaces – electronic control of quinone adsorption, Langmuir 10(11) (1994) 4307-4314.

[53] H. Kinoshita, Y. Suda, T. Kawakubo, K. Takayama, T. Ikeda, Electroanalysis of NADH using a new electrode prepared from plastic formed carbon, Microchemical journal 49(2-3) (1994) 226-234.

[54] H. Kaneko, A. Negishi, Y. Suda, T. Kawakubo, Fabrication and evaluation of PFC (plastic formed carbon) electrodes for voltammetric use, Denki Kagaku 61(7) (1993) 920-921.

[55] T. Kawakubo, Y. Suda, H. Kaneko, A. Negishi, M. Yamada, Electrochemical Behavior of Carbon Microelectrodes Prepared by Using Graphite/Carbon Composite, Tanso 1992(152) (1992) 106-114.

Chapter 4:

Equipment and Experimental Methods.

Contents

4.1 Equipment

All chemicals were used as received from Sigma Aldrich without further purification unless stated otherwise. Solutions of ferricyanide with KNO_3 supporting electrolyte, ferrocyanide with KCl supporting electrolyte and vanadium(V)oxide in sulphuric acid were prepared using ultrapure water (18 MΩ cm^{-1}, Milli-Q®). Non-aqueous solutions of ferrocene with tetrabutylammonium perchlorate (TBAP) in acetonitrile were also prepared. Two potentiostats were used for electrochemical experimentation, a Metrohm Autolab PGSTAT 128N potentiostat and a CH Instruments 1100B potentiostat. Solution resistance was measured and compensated for via an in-built method on the CH instruments potentiostat and a manual, stepped-increase method on the Autolab potentiostat.
A standard three electrode configuration was employed for all electrochemical measurements. Four, 3 mm diameter carbon electrodes (ALS Co. Ltd, Japan); edge plane pyrolytic graphite (EPPG), basal plane pyrolytic graphite (BPPG), glassy carbon (GC) and plastic formed carbon (PFC), were used, Figure 4.1. The EPPG and BPPG electrodes contain graphite with a purity of >99.99% surrounded by a polyether ether ketone (PEEK) insulating layer. Also note the BPPG is not highly orientated pyrolytic graphite (HOPG), but contains >60% basal orientation.

Measurements of peak current and charge were achieved through the use of the Peak Analyser function found in the data analysis and graphics software, OriginPro 9. This allowed for simultaneous baseline correction of the forward voltammetric scan and the integration of the area under the peaks found in said scan. The surface area of each GF electrode was estimated from the weight of the sample as discussed in chapter 5, but was typically in the range of 50-60 cm^2 for a 1 cm x 1 cm sample.

4.2 Electrode Preparation

4.2.1 Macro disc electrodes

The BPPG electrode was prepared by polishing the electrode with a 1 µm polycrystalline diamond suspension (Buehler) on a silk-type cloth pad (Kemet International) before washing the surface in

ultrapure water and briefly sonicating. The electrode surface was then refreshed by removing excess graphite with sellotape. This was repeated multiple times before washing the electrode in acetone to remove any residue. The PFC, GC and EPPG electrodes were prepared by polishing with diamond slurries of decreasing particle size (9 µm, 3 µm and 1 µm) on a silk-type cloth pad before washing the surface in ultrapure water and briefly sonicating. A bright platinum wire with attached platinum wire mesh (Metrohm UK) was used as the counter electrode and a saturated calomel electrode (ALS Co. Ltd, Japan) was used as the reference. In non-aqueous solutions a double junction (ALS Co. Ltd, Japan) was used to reduce contamination of the reference.

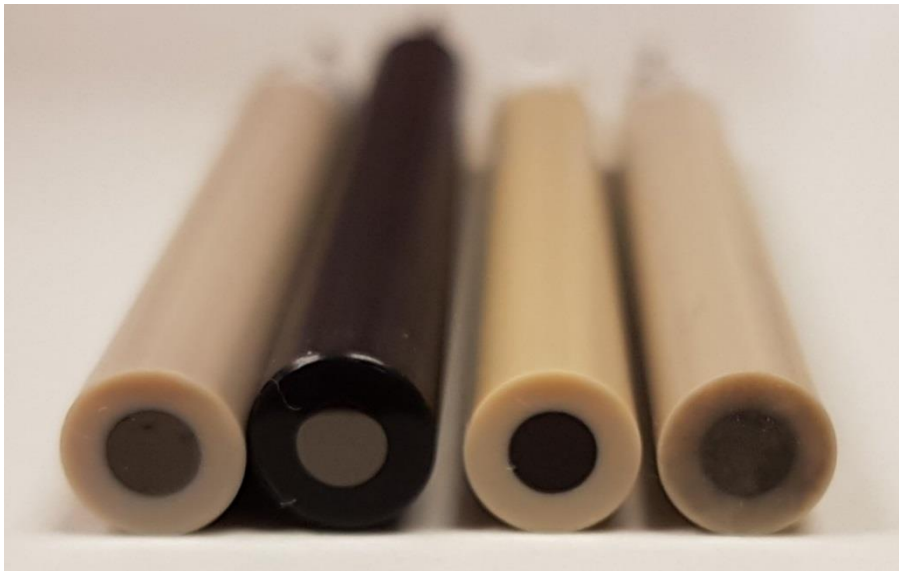

Figure 4.1: Image of from left to right; PFC, GC, EPPG and BPPG electrodes, with 3 mm diameter.

4.2.2 GF electrodes

The GF used was GFD 2.5, a commercially available felt supplied by SGL Group, with a nominal thickness of 2.8 mm (measured under a slight compressive force). A 1 cm^2 piece of GF was cut from a clean roll of the felt using a bespoke 'cookie cutter' tool. After weighing the GF using a 4 point balance (Sartorius, TE214S), a 0.5 mm (diameter) platinum wire 'fish hook' was passed through the felt to secure it and provide a good electrical connection to the whole of the felt piece. This is shown in the photographs in Figure 4.2. In all of the redox solutions, cyclic voltammetry was also conducted with

the bare platinum fish hook submerged in solution. The size of the voltammetric signal from the platinum wire fish hook was negligible compared to the signal from the GF electrode.

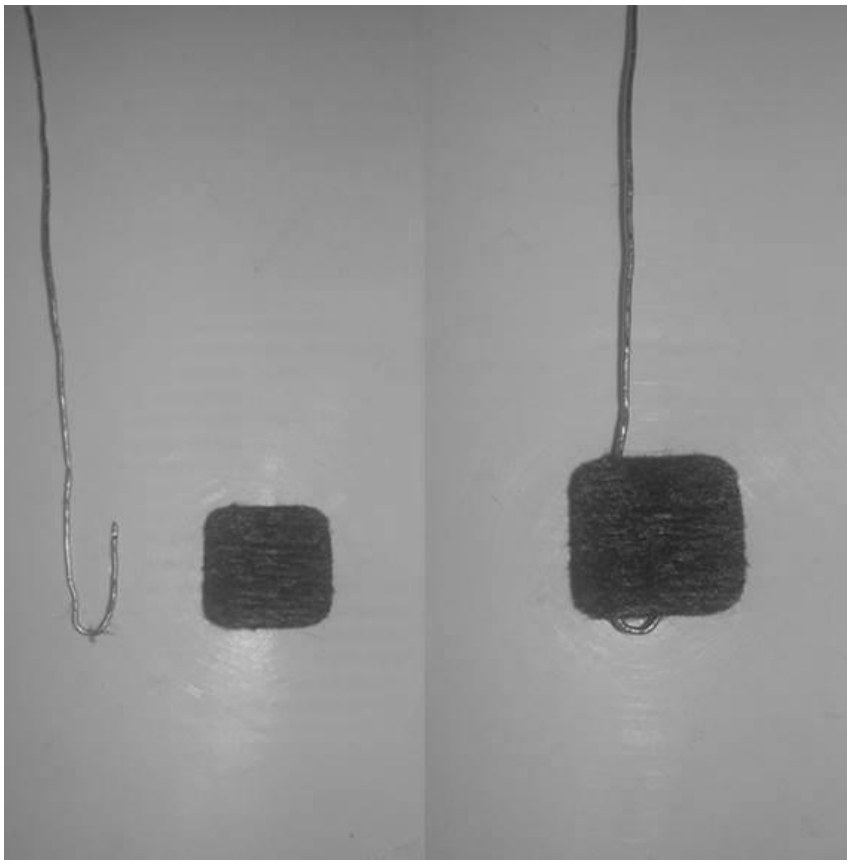

Figure 4.1: Image of GF electrode with platinum 'Fishhook' before and after attachment.

Prior to taking measurements, the GF electrode was initially washed in ethanol before being rinsed with ultrapure water. It was then agitated in a sacrificial sample of the electrochemical solution before being transferred to the electrochemical cell. This ensured full wetting of the interior surface of the GF with the redox solution under investigation. The electrochemical simulation software employed was DigiElch (v7.FD) from ElchSoft, Germany. SEM (Quanta 250 FEG, FEI) was used to determine the diameter of the fibres within the carbon felt. The fibres were found to have an average diameter of 8 µm from a range of measurements. Typical SEM images are shown in Figure 4.3 for a range of magnifications.

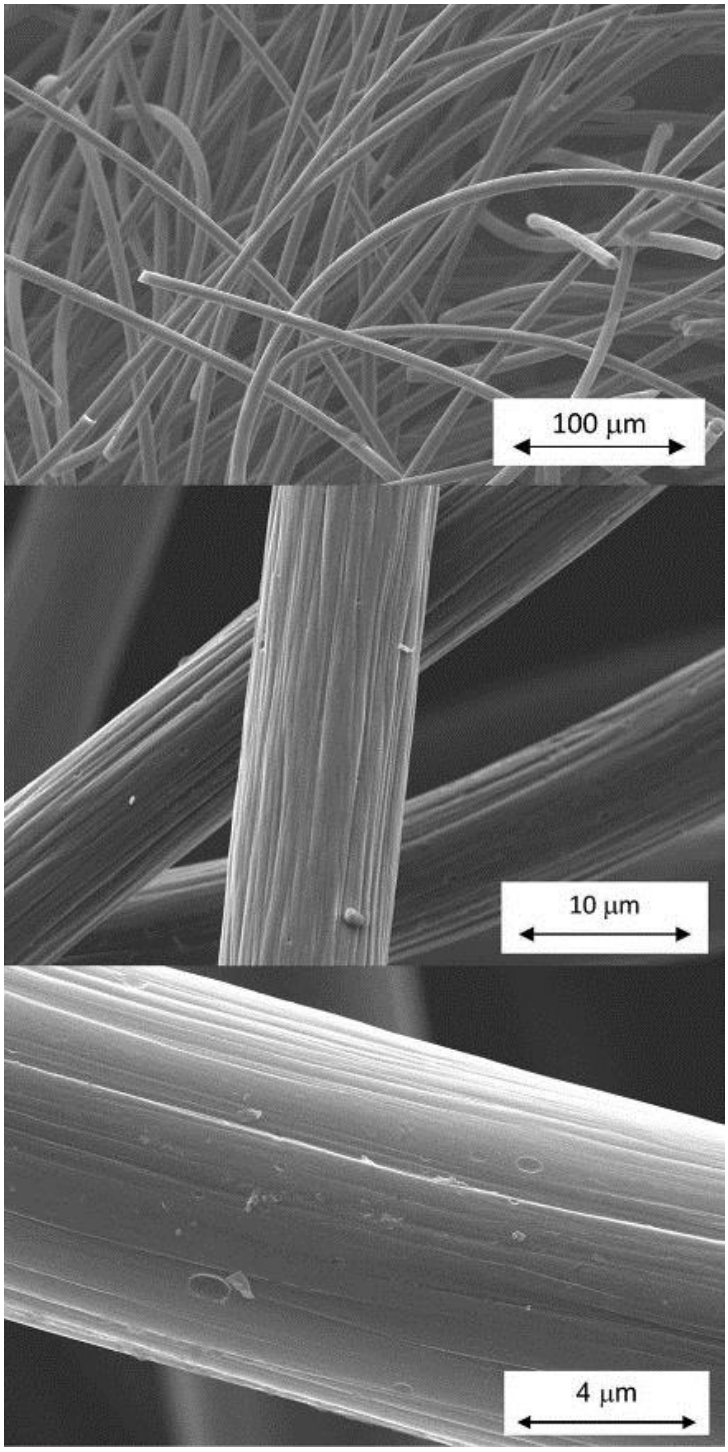

Figure 4.3: SEM images of GF fibres after washing in ethanol and drying at 80°C.

4.3 Limit of Detection Measurements

A Metrohm Autolab PGSTAT 128N potentiostat was used for electrochemical experimentation. A standard three electrode configuration was employed for all electrochemical measurements (cyclic

voltammetry). The graphite felt used was GFD 2.5, which was cleaned and prepared as stated previously. All chemicals were used as received from Sigma Aldrich without further purification unless stated otherwise. Solutions of ferrocyanide with KCl supporting electrolyte were prepared using ultrapure water (18 MΩ cm^{-1}, Milli-Q®). Non-aqueous solutions of ferrocene with 0.1 M tetrabutylammonium perchlorate (TBAP) in acetonitrile were also prepared. For the non-aqueous solutions, the concentration of ferrocene was increased from 0.1 nM to 0.1 mM over 22 concentrations. For the aqueous solution, the concentration of ferrocene was increased from 10 nM to 10 μM

4.4 Surface Grafting and Functionalisation of Carbon Electrodes

4.4.1 Diazonium Grafting to macro disc electrode

4.4.1.1 Equipment

12 M HCl, 0.1 M $NaNO_2$, 4-aminophenol, 4-nitroanaline, 4-aminopyridine, 4-aminobenzoic acid, potassium ferricyanide, 1 M KCl were all purchased from Sigma Aldrich and used as supplied. V1 ($H_3Na_1PW_{11}VO_{40}$) polyoxometalate (POM) solution was supplied by ACAL Energy. All electrochemical techniques were carried on an Autolab potentiostat (using the Autolab GPES software) with a standard 3 electrode cell. The potassium ferricyanide solution used as a redox probe consisted of 10 mM $K_3[Fe(CN)_6]$ in 1 M KCl. This was acidified from approximately pH 5.1 to pH 1.0 using 12 M HCl to closer match the conditions of the POM solutions. The V1 POM solutions were used as supplied (0.3 M) as well as being diluted to 1 mM using a 0.1 M perchloric acid solution as the background electrolyte.

4.4.1.2 Procedure

In the grafting solution; the sodium nitrite with HCl generates nitrous acid, which reacts with the amino group of the aniline (referred to as the “diazonium precursor”), leaving the diazonium group, Figure 4.4. The diazonium group undergoes a one electron reduction at the electrode surface forming N_2 gas and a phenyl radical. This radical is then able to attack the carbon surface forming the

strong C-C bond. In this report two methods are used to supply current to the grafting solution, one at a constant potential the other a cyclic method. This one-pot method was chosen over other method, such as the one presented by Savéant et al [2], in order to avoid the direct handling of diazonium salts, due to their explosive nature.

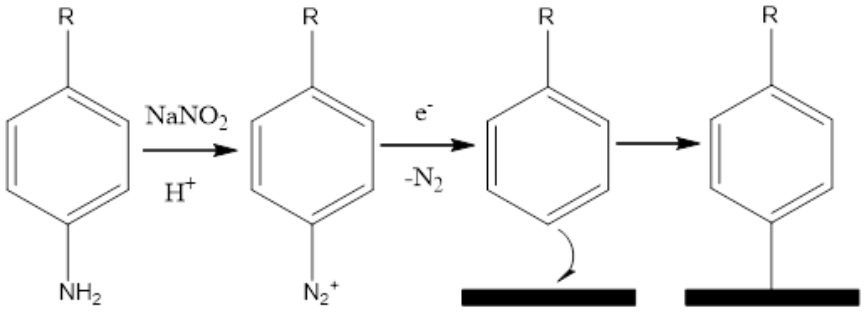

Figure 4.4: Diazonium grafting to carbon surface reaction scheme.

4.4.1.2.1 Potentiostatic deposition

The electrodes are held at a set potential in a solution of 2.24 ml diazonium precursor (5 mM), 0.24 ml sodium nitrite (0.1 M), 0.51 ml hydrochloric acid (12 M) and 8.85 ml Milli-Q water for a set amount of time (10 minutes unless otherwise stated). After grafting, the electrodes are thoroughly rinsed with Milli-Q water.

4.4.1.2.2 Cyclic deposition

The electrodes are cycled across a potential range in a solution of 2.24 ml diazonium precursor (5 mM), 0.24 ml sodium nitrite (0.1 M), 0.51 ml hydrochloric acid (12 M) and 8.85 ml Milli-Q water at a set scan rate (10 mV s^{-1} unless otherwise stated). After grafting, the electrodes are thoroughly rinsed with Milli-Q water.

4.4.2 Grafting to graphite felts

4.4.2.1 Equipment

All chemicals were used as received from Sigma Aldrich without further purification. The grafting solutions were prepared using a modified method of the 'one-pot' procedure set forth by Y. Leroux Figure 4.5 [3]. For a 25 ml solution, 10 mM (27 μL) of perchloric acid (60%) was added to 15 ml of acetonitrile, followed by 5 mM of the protected diazonium (~0.3 g). 0.1 M (~0.8 g) tetrabutylammonium tetrafluoroborate (TBAB) was then dissolved in the solution and then 5 mM of sodium nitrite (1.25 mL) was added and the solution made up to 25 ml with acetonitrile.

For the electrochemical experimentation a Metrohm Autolab PGSTAT 128N potentiostat was used. A standard three electrode configuration was employed for all electrochemical measurements. A bright platinum wire with attached platinum wire mesh (Metrohm UK) was used as the counter electrode and a saturated calomel electrode (ALS Co. Ltd, Japan) was used as the reference with a double junction (ALS Co. Ltd, Japan) to reduce contamination of the reference. The graphite felt used was GFD 2.5, which was cleaned and prepared as stated previously. A cyclic voltammetry experiment was used to graft the protected diazonium to the GF surface, the potential was swept between 0.7 V and -0.7 V at a rate of 30 mV s^{-1}. Once the CV had finished, the samples were agitated in ethanol, followed by ultra-pure water to remove any additional material.

4.4.2.2 Functionalisation of surface layer

To remove the protecting group from the monolayer, the felt was stirred in 3 ml of 0.1 M Tetrabutylammonium fluoride (TBAF) in tetrahydrofuran (THF) under an argon atmosphere for 30 minutes. It was then washed and agitated in acetonitrile to remove any remaining TBAF, Figure 4.5.

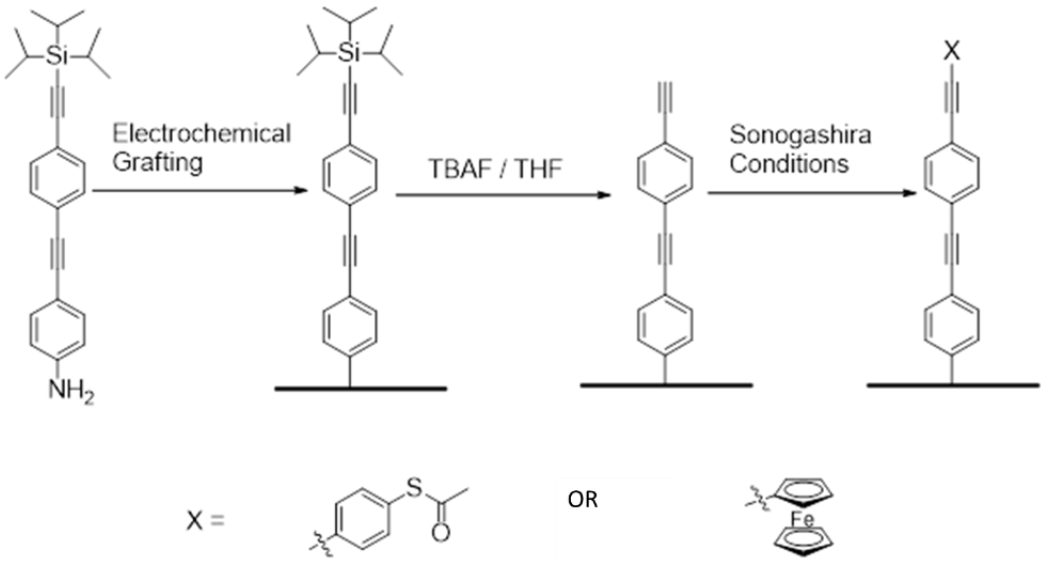

Figure 4.5: Reaction diagram for the deprotection of grafted diazonium layer and the attachment of new terminal moieties. Reproduced from ref. [5].

The felt is then dried under vacuum and transferred to a solution of 45 ml diisopropylamine (DIPA), 5 mg copper iodide, 45 mg PPh_3, 15 mg $PdCl_2(MeCN)_2$ and either 0.17 g Iodothiolacetate or 0.15 g of bromoferrocene, depending on the required terminal moiety to attach. The solution is stirred under argon at 55 °C for 3 hours, Figure 4.5. The GF is then removed from the solution and repeatedly washed and agitated in acetonitrile, removing any remaining solution, before being dried under vacuum.

This method described above, for attaching a functionality, through the creation of a covalent C-C bond between the electrochemically grafted layer and the selected functionalisation precursor, is called a Sonogashira coupling reaction. The Sonogashira cross-coupling reaction was discovered by Kenkichi Sonogashira et al, and subsequently reported in their publication [1]. It follows the previous work of Dieck, Cassa and Heck which produce the same products from reaction, but require much harsher conditions for synthesis. While both reaction mechanisms use a palladium catalyst, the Sonogashira reaction uses a copper co-catalyst to allow the reaction to be carried out under less harsh conditions, notably at room temperature. While the true reaction mechanism is still debated, the most widely accepted mechanism works via the following route.

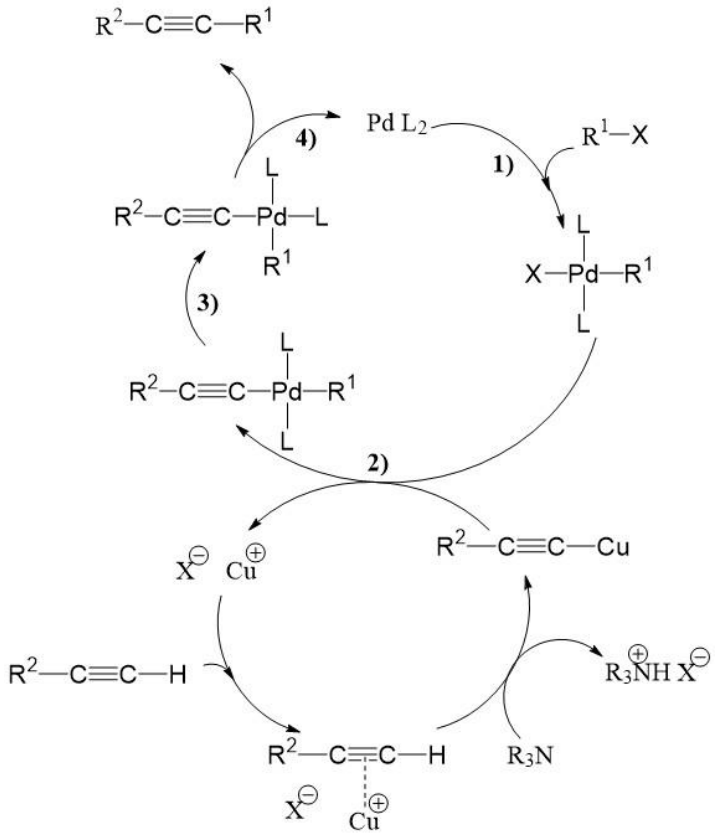

Figure 4.6: Reaction diagram for the Sonogashira reaction used to attach new functionalities to terminal alkyne on surface grafted layer [1].

Studies have shown that the catalytic cycle shown in Figure 4.6 could be the preferred reaction pathway, but that exact reaction conditions could affect the intermediary structures [4]. The two catalysts required for the coupling reaction are a palladium (0) complex and a copper (I) halide salt. Phosphine ligands are often used to create the Pd(0) complex, both monodentate ligands like $Pd(PPH_3)_2Cl_2$ and bidentate ligands such as Pd(dppe)Cl can be used. Problems can arise from Pd(0)s instability in air, this can be problematic when storing these compounds over extended time periods. To counter this, a Pd(II) pre-catalyst, reduced in situ, is often used. This method is used in the experimental work detailed below, where $Pd(MeCN)_2Cl_2$ is reduced to Pd(0) by triphenylphosphine (PPh_3). The Cu(I) salts, such as the copper iodide used below, forms a acetylide by reacting with a terminal alkyne. This terminal alkyne is produced by removing the protecting group from the grafted surface layer. As mentioned previously, the Pd(0) complex is unstable in air, so the reaction is

required to be oxygen free, experimentally this is achieved by deaerating the solution with argon. An amine based solvent, like diisopropylaminine is used as a solvent for the reaction to prevent H-X halide formation.

4.5 References

[1] K. Sonogashira, Y. Tohda, N. Hagihara, A convenient synthesis of acetylenes: catalytic substitutions of acetylenic hydrogen with bromoalkenes, iodoarenes and bromopyridines, Tetrahedron Letters 16(50) (1975) 4467-4470.

[2] P. Allongue, M. Delamar, B. Desbat, O. Fagebaume, R. Hitmi, J. Pinson, J.M. Saveant, Covalent modification of carbon surfaces by aryl radicals generated from the electrochemical reduction of diazonium salts, Journal of the American Chemical Society 119(1) (1997) 201-207.

[3] Y.R. Leroux, H. Fei, J.M. Noel, C. Roux, P. Hapiot, Efficient Covalent Modification of a Carbon Surface: Use of a Silyl Protecting Group To Form an Active Monolayer, Journal of the American Chemical Society 132(40) (2010) 14039-14041.

[4] R. Chinchilla, C. Najera, Recent advances in Sonogashira reactions, Chemical Society Reviews 40(10) (2011) 5084-5121.

[5] J. Liang, R.E.G. Smith, A. Vezzoli, L. Xie, D.C. Milan, R. Davidson, A. Beeby, P.J. Low, S.J. Higgins, B. Mao, R.J. Nichols, Electrochemically grafted single molecule junctions exploiting a chemical protection strategy, Electrochimica Acta Publication (2016).

Chapter 5:

The Electrochemical Characterisation of Graphite Felts.

Contents

5.1 Introduction

Graphite felts (GFs) are the electrode material of choice for redox flow batteries (RFBs) [1-4]. These materials remain more popular than other carbon based materials, such as carbon paper, a result of their favourable liquid permeability and high surface area [5, 6]. Due to the popularity of these materials and the rapidly growing RFB market, a large amount of research has been conducted on their physical and electrochemical properties, where the main objective is to improve cell performance, i.e. obtain higher current densities whilst maintaining the required operating efficiency. A common objective of GF research has been the measurement of mass transport coefficients in miniaturized flow cells [7-9]. Although these experiments provide useful property data, they can be difficult to set up and require specialized/bespoke equipment. In an attempt to simplify experimental requirements, some researchers have made stationary electrodes from graphite felts and studied the material with classical 3 electrode cyclic voltammetry [10-12]. However, as Figure 5.1 shows, many GFs are hydrophobic and difficult to wet. The apparent high contact angle suggests a hydrophobic surface, similar to that reported by Banks et al. for graphene foam [13]. As a result, the amount of the interior surface in contact with electrolyte is difficult to control and can generate misleading results, especially if electrodes of different surface wettability are being compared.

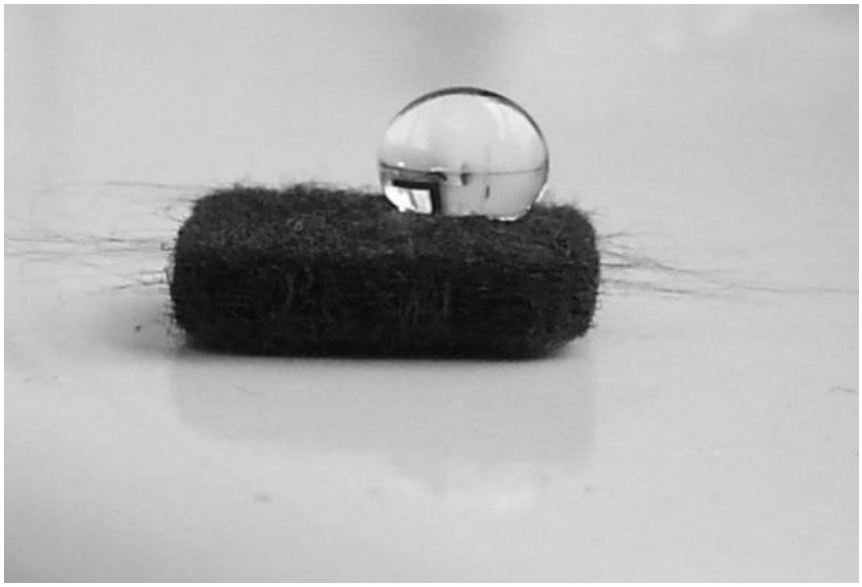

Figure 5.2: Image of water droplet on graphite felt (SGL GFD2.5), taken 30 s after the water drop was deposited on the felt surface.

The development of an elegant technique that allows GFs to be used as electrodes in quiescent voltammetry experiments is described in this chapter. This involves a felt pre-treatment to allow for homogeneous wetting through the GF sample, followed by cyclic voltammetry in a redox system of interest. Using simple voltammetric techniques combined with a commercially available simulation package, key properties such as capacitance, electrode kinetics, average pore size and electrochemical surface area can be determined. This is of particular interest for examining multiple or modified GFs quickly, without the need for a complicated experimental set up. The developments reported in this chapter pave the way for the rapid screening of electrode materials and electrode treatments for redox flow batteries and other applications.

The "smooth" surface area of the felt can be estimated by approximating the felt as one cylindrical carbon fibre. The mass of the felt electrode, m, can be used to determine the total volume of the carbon fibres, V_{cf}, via the simple density relationship:

$$V_{\mathrm{cf}} = \frac{m}{\rho_{\mathrm{cf}}} \qquad (5.1)$$

Where ρ_{cf} is the density of carbon fibres and is generally considered to be around 1.8 g cm^{-3}.[14, 15] The equivalent length of the carbon fibre, L_{cf}, is then deduced using the equation for the volume of a cylinder:

$$\pi r^2 L_{\mathrm{cf}} = V_{\mathrm{cf}} \qquad (5.2)$$

Where *r* is the radius of the carbon fibres in the felt, determined to be 4 µm for the particular felt used in this investigation. The surface area of the fibre (and hence the whole electrode), A_{cf}, is then determined using:

$$A_{\mathrm{cf}} = 2\pi r L_{\mathrm{cf}} \qquad (5.3)$$

The average pore size within the felt proved to be a difficult quantity to measure. Initially, fifty SEM images were analysed using the method reported for carbon fibre papers in reference [16]. Unfortunately, the 3-dimensional structure of the GF samples resulted in meaningless results from the image analysis (the method works well for carbon papers, which are considered to possess a 2-dimensional structure). Mercury porosimetry and BET were also unable to give meaningful pore size distribution data for this material. Therefore, a conceptual approach to estimate the average pore radius was developed.

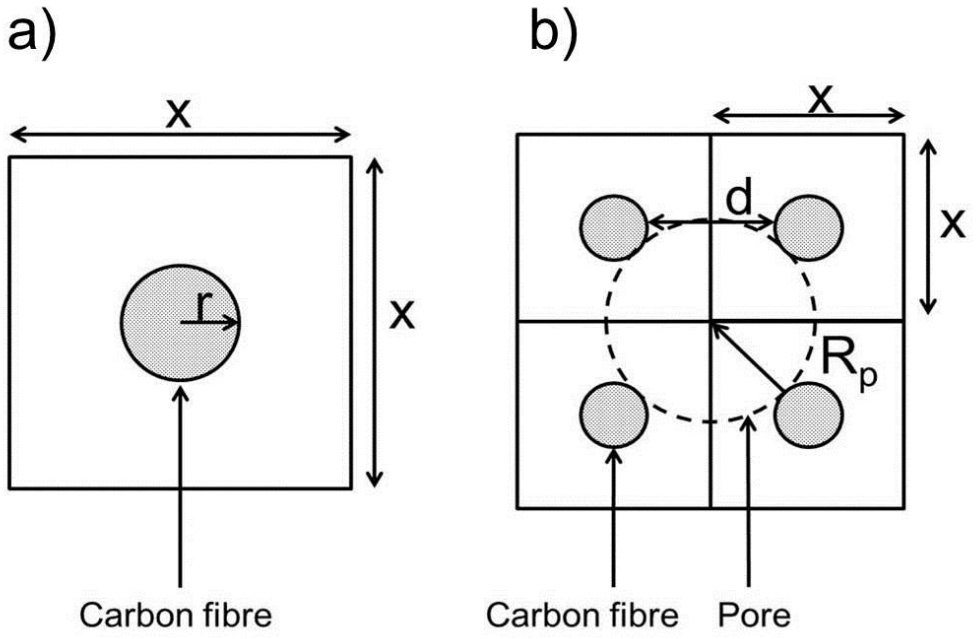

Figure 5.5: Illustration of a theoretical unit cell (a) for evaluating pore radius, R_p, and fibre to fibre distance, *d*. (b).

The square unit cell model in figure 5.5(a) represents an idealized view of the GF structure and provides an estimation of the average distance between fibres, which can be used to approximate the average pore size. For the cubic unit cell to be representative of the material, the area of the empty space, divided by the area of the unit cell should equal the porosity, of the felt, ϕ:

$$\phi = 1 - \left(\frac{\pi r^2}{x^2} \right) \tag{5.4}$$

Where *x* is the dimension of the unit cell, as labelled in Figure 5.5. The porosity of the felt can be determined using the total volume of the felt, V_{Tot}, and the equation:

$$\phi = 1 - \left(\frac{m}{V_{\text{Tot}} \rho_{\text{cf}}} \right) \tag{5.5}$$

The shortest fibre surface to fibre surface distance, *d*, is then simply given by:

$$d = x - r = \sqrt{\left[\frac{\pi r^2 V_{\text{Tot}} \rho_{\text{cf}}}{m} \right]} - 2r \tag{5.6}$$

where the parameters r, m, V_{Tot} and ρ_{cf} are all known.

In terms of evaluating a pore radius, R_p, to compare with experimental results and subsequent model, an approximation is shown in Figure 5.5 (b), where four unit cells are drawn together. In this case, R_p resembles the pore radius and is given by:

$$R_p = \left(\frac{x}{\sqrt{2}}\right) - r = \sqrt{\left(\left[\frac{\pi r^2 V_{\mathrm{Tot}} \rho_{\mathrm{cf}}}{m}\right]\Big/_2\right)} - r \qquad (5.7)$$

In the case of a hexagonally packed unit cell, the equation for R_p is also given by equation 5.7.

5.3 Simulations

Dr Trevor Davies suggested that by using simulations in combination with experimental GF voltammograms, electrochemical and physical properties of the GF electrodes could be extracted. The following section describes the model used to simulate the cyclic voltammetry of GF (and other porous) electrodes.

Consider the schematic diagram in Figure 5.6. The porous GF electrode can be approximated as an ensemble of pores that mimic tube electrodes, with the interior surface being the active area. Each pore of radius R_p and length L can be approximated as two parallel plate electrodes separated by a distance $2R_p$ where the area of each plate is $\pi(2R_p)L/2$. Note that for planar diffusion where the pore radius is comfortably greater than the diffusion layer thickness, the voltammetric response of the tube and parallel plates should be the same (assuming planar diffusion). However, as R_p becomes similar to the diffusion layer thickness and the depletion zone extends into the pore, the voltammetric signals for the two electrodes will start to differ as the parallel plates have an enclosed electrolyte volume of $\pi(2R_p)^2L/2$, whereas the tube has an enclosed electrolyte volume of $\pi(2R_p)^2L/4$. This represents a source of error in the simulation approach but is acceptable as a first attempt, allowing the use of commercially available cyclic voltammetry software.

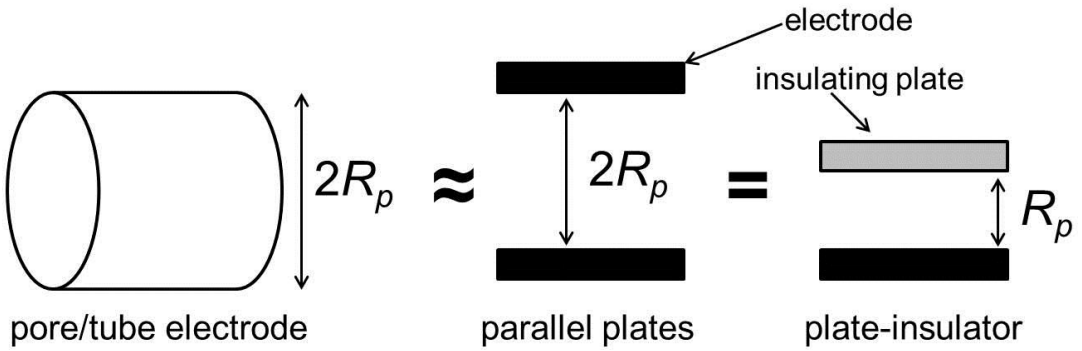

Figure 5.6: Schematic diagram approximating a pore as a tube electrode, which can be approximated as a parallel plate electrode assembly, which is mathematically identical to a planar electrode below an insulating plate.

Due to a region of zero flux between the parallel electrodes in Figure 5.6, the situation can be considered as, and is mathematically identical to, the situation where an insulating plate is placed above an electrode at a height of R_p [17]. In this situation the total area of the parallel plate electrodes is equal to the area of the single plate electrode in the plate-insulator model. The cyclic voltammetry of the latter can be simulated with commercially available software, such as DigiElch or DigiSim, using the finite diffusion package intended for thin layer voltammetry [18, 19]. In the final step of the model, the whole porous electrode is approximated as a plate electrode, separated from an insulating plate by a distance of R_p.

In the following description, the redox system is a simple one electron reduction of species A to B:

$$\mathrm{A} + e^- \rightarrow \mathrm{B} \qquad (5.8)$$

Where the initial concentration of A, [A], is 1 mM, initial [B] is 0 mM, the formal potential, E_f, is 0 V, the diffusion coefficients of A and B, D, are equal to 1 x 10^{-6} cm^2 s^{-1} and the standard electron transfer rate constant, k^o, is 0.01 cm s^{-1}. The value of D can be obtained via separate experiments with traditional macroelectrodes, whereas k^o can be initially estimated then refined once conditions of semi-infinite diffusion are known (see later).

The objective of the simulation method is to determine the two unknowns of electrochemical surface area and average pore size from the experimental cyclic voltammetry response of the porous electrode. Consider the example where the porous electrode can be described as the plate electrode in Figure 5.6 with a surface area of 10 cm^2 and a pore radius, R_p, of 30 µm. Figure 5.7 illustrates cyclic voltammograms (simulated) for the electrode in the given redox solution at scan rates of 0.01, 0.1 and 1 V s^{-1}. At low scan rates, thin layer voltammetry is observed, with well-defined forward and reverse peaks with almost identical peak potentials [19]. As the scan rate increases, the mass transport changes to semi-infinite diffusion and "classically shaped" voltammograms are observed. The transition from thin layer to semi-infinite diffusion voltammetry can be seen in plots of cathodic peak current, I_p^c vs. scan rate, v, and I_p^c vs. $v^{0.5}$ (Figure 5.9). The changing shape of the voltammograms and I_p^c-v relationship is predominantly affected by diffusion layer overlap. At low scan rates, the diffusion layer thickness is larger than R_p, leading to heavily overlapping diffusion layers within the pore and consequently thin layer voltammetry. At the highest scan rates, the diffusion layer is comfortably smaller than R_p leading to little or no diffusion layer overlap and voltammetry where mass transport is described by semi-infinite diffusion. Compton and co-workers have previously shown diffusion layer overlap can be used to determine the size of individual electrodes in microelectrode arrays and the size of blocking particles on electrode surfaces [20-23]. Using the same principle, diffusion layer overlap can be used to determine the size of pores in porous electrodes. A direct method is to compare simulated voltammograms with experimental voltammograms and vary the parameters to find the best fit. However, a more elegant and relatively faster method is now described.

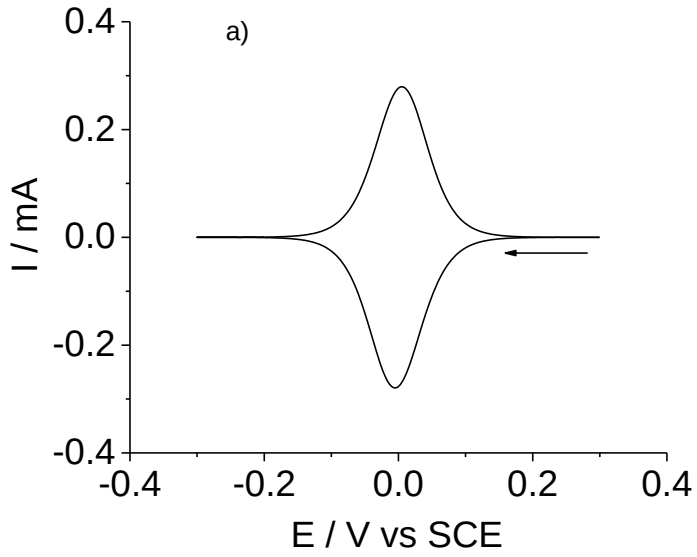
a)
0.4
0.2
0.0
-0.2
-0.4
I / mA
-0.4
-0.2
0.0
0.2
0.4
E / V vs SCE

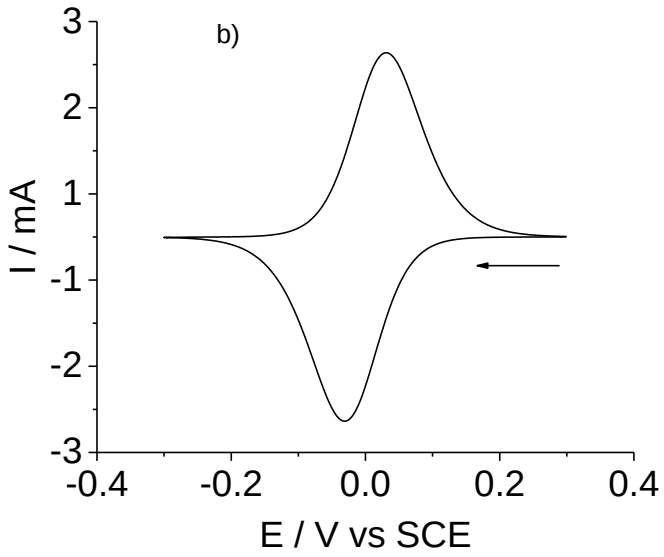
b)
3
2
1
-1
-2
-3
I / mA
-0.4
-0.2
0.0
0.2
0.4
E / V vs SCE

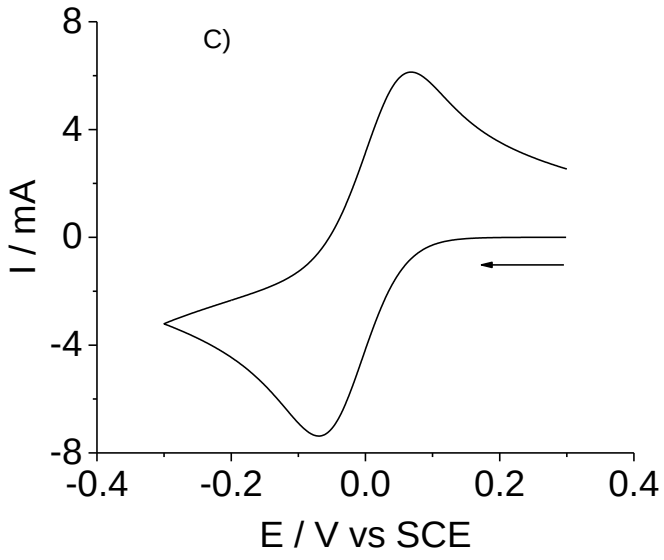

Figure 5.7: Simulated cyclic voltammograms for the porous electrode of total surface area 10 cm^2 and average pore radius of 30 µm in the A-B redox system discussed in the text at scan rates of (a) 0.01 V s^{-1}, (b) 0.1 V s^{-1} and (c) 1 V s^{-1}.

Imagine the voltammograms in Figure 5.7 are actually real experimental voltammograms for a GF electrode of unknown surface area and average pore size. Using the previously determined values of D and k^o and the known value of [A], the cyclic voltammetry response of an electrode of surface area 1 cm^2 can be simulated (using the finite diffusion facility) for a range of R_p values at each scan rate. For each value of R_p, a corresponding value of I_p^c can be determined. Because the simulation is for an electrode area of 1 cm^2, dividing the experimental I_p^c by the simulated I_p^c gives a ratio that is equal in magnitude to the equivalent area in cm^2. For example, in the case of R_p = 10 µm and v = 0.1 V s^{-1} the simulated peak cathodic current is 0.092 mA. The corresponding experimental voltammogram is Figure 5.7(b). Dividing the experimental peak current (2.14 mA) by 0.092 mA gives the number 23.3. Therefore, if the porous electrode had an average pore radius size of 10 µm, it would require a total surface area of 23.3 cm^2 to generate a peak current of 2.14 mA at 0.1 V s^{-1} in the given redox system. Using this approach, a plot of equivalent area vs. pore size can be produced for each scan rate, as shown by the curves in Figure 5.8, each curve corresponding to a different scan rate. At high values of R_p, diffusion layer overlap does not occur. In this case mass transport is described by semi-infinite

diffusion and the peak current is independent of pore size, so a horizontal line is observed in the equivalent area vs. pore size plot. As the pore size decreases, a transition to finite diffusion occurs, resulting in increasing amounts of diffusion layer overlap. The equivalent area increases as the peak currents are smaller than those obtained under semi-infinite diffusion. Because scan rate directly affects diffusion layer thickness, the equivalent area vs. pore size plots change with scan rate. As such, the surface area and average pore size of the experimental electrode are determined by where the curves intersect in Figure 5.8. This is the only point unique to all scan rates for the individual felt employed as the electrode, in this case 10 cm^2 and 30 µm respectively. Thus, using a simple approximation for pores and a rapid simulation method in commercially available software, estimates for the electrode surface area and average pore size can be determined from cyclic voltammetry experiments with a known redox couple.

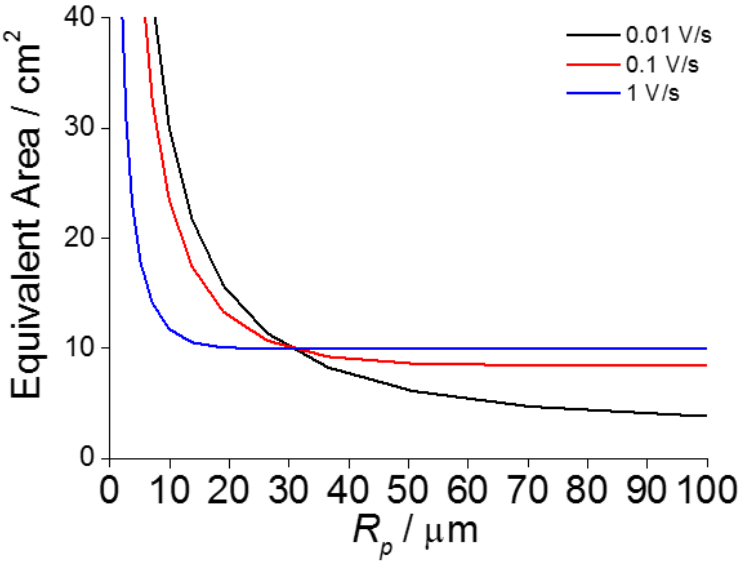

Figure 5.8: Simulated curves of equivalent surface area vs. pore radius using the cathodic peak current results from the porous electrode with total surface area 10 cm^2 and average pore radius 30 µm.

Figure 5.9 illustrates plots of peak cathodic current, I_p^c, vs. scan rate, v, and I_p^c vs. $v^{0.5}$ for the porous electrode. At low scan rates the peak current is proportional to scan rate, indicative of thin layer

voltammetry and finite diffusion, whereas at high scan rates the peak current is proportional to the square root of scan rate, indicative of semi-infinite diffusion.

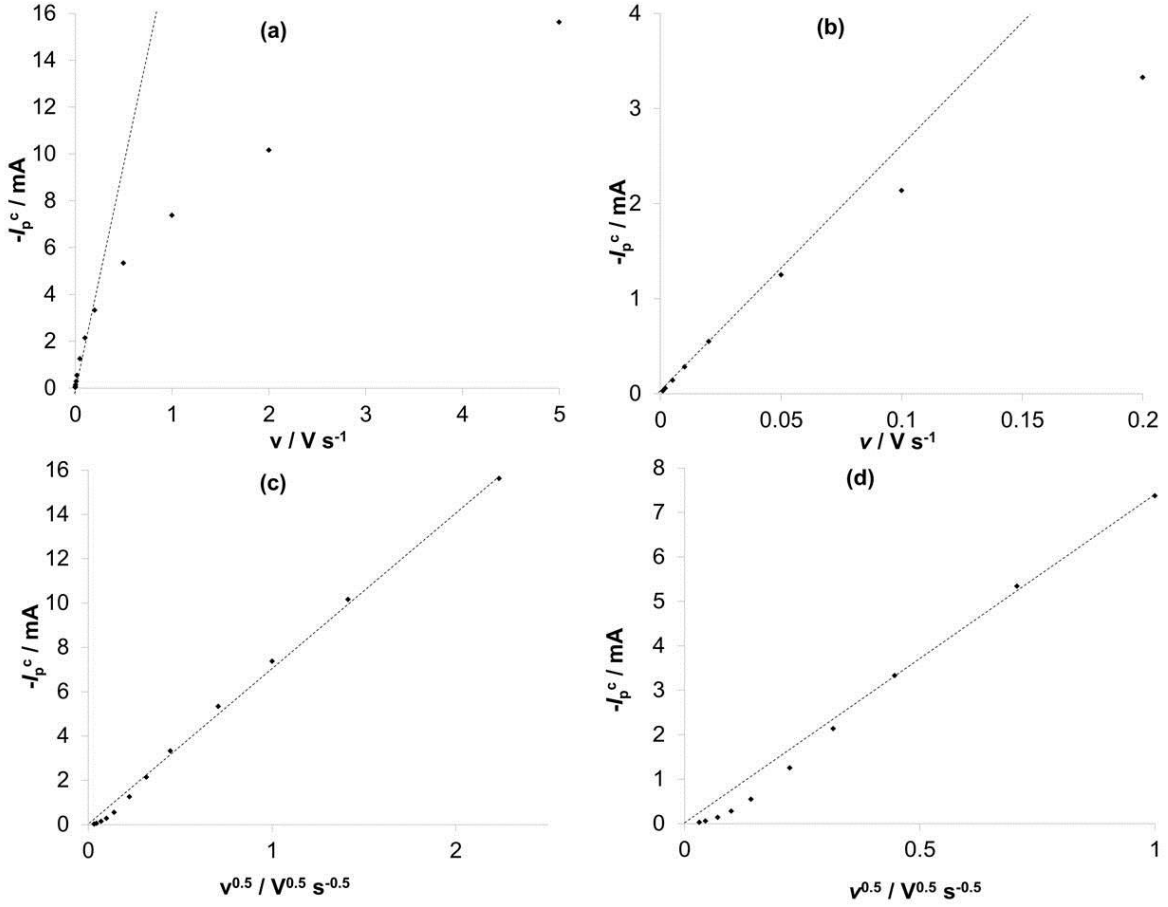

Figure 5.9: (a) Cathodic peak current vs. scan rate for the porous electrode of total area 10 cm^2 and average pore radius of 30 µm. (b) Magnification of the linear region in (a). (c) Cathodic peak current vs. square root of scan rate for the porous electrode of total area 10 cm^2 and average pore radius of 30 µm. (d) Magnification of the non-linear region in (c).

5.4. Results and Discussion

The large surface area of the GF electrodes (~60 cm^2 per electrode) resulted in currents of magnitude ~10 mA when solutions of mM concentrations of redox species were used. This caused distortions in

the voltammetry due to uncompensated solution resistance. Two methods were used to correct for this. In some cases the "*IR*-compensation" feature in the potentiostat was used to automatically compensate the potential signal for solution resistance (where *I* is the current and *R* is the solution resistance between the reference and working electrodes). In other cases the concentration of redox species was reduced 10-100 times to decrease the current magnitude and eliminate the requirement for *IR*-compensation (i.e. the value of *IR* became insignificant).

Figure 5.3(a) illustrates cyclic voltammograms recorded at 0.1 V s^{-1} with a GF electrode in 0.1 mM ferrocene/0.1 M TBAP. The dashed curve corresponds to the uncompensated cyclic voltammogram whereas the solid curve is the voltammogram with 85 % compensation of solution resistance. The measured solution resistance in the cell was 15 Ohm. The magnitude of the current signal is ~10 mA, producing an "*IR* drop" value of ~150 mV (where *I* is the current and *R* is the solution resistance). This is large enough to distort the signal, which is illustrated by the difference between the compensated and uncompensated voltammograms in Figure 5.3(a). An alternative to electronically compensating for solution resistance is to reduce the concentration of the redox system, thus reducing the magnitude of the current and associated "*IR* drop". This is illustrated in figure 5.3(b) where applying electronic *IR* compensation for solution resistance had little to no effect for the 10 µM ferrocene solution which is ten times more dilute that in Figure 5.3(a). Both IR compensation and redox species dilution were used to obtain voltammograms suitable for data analysis.

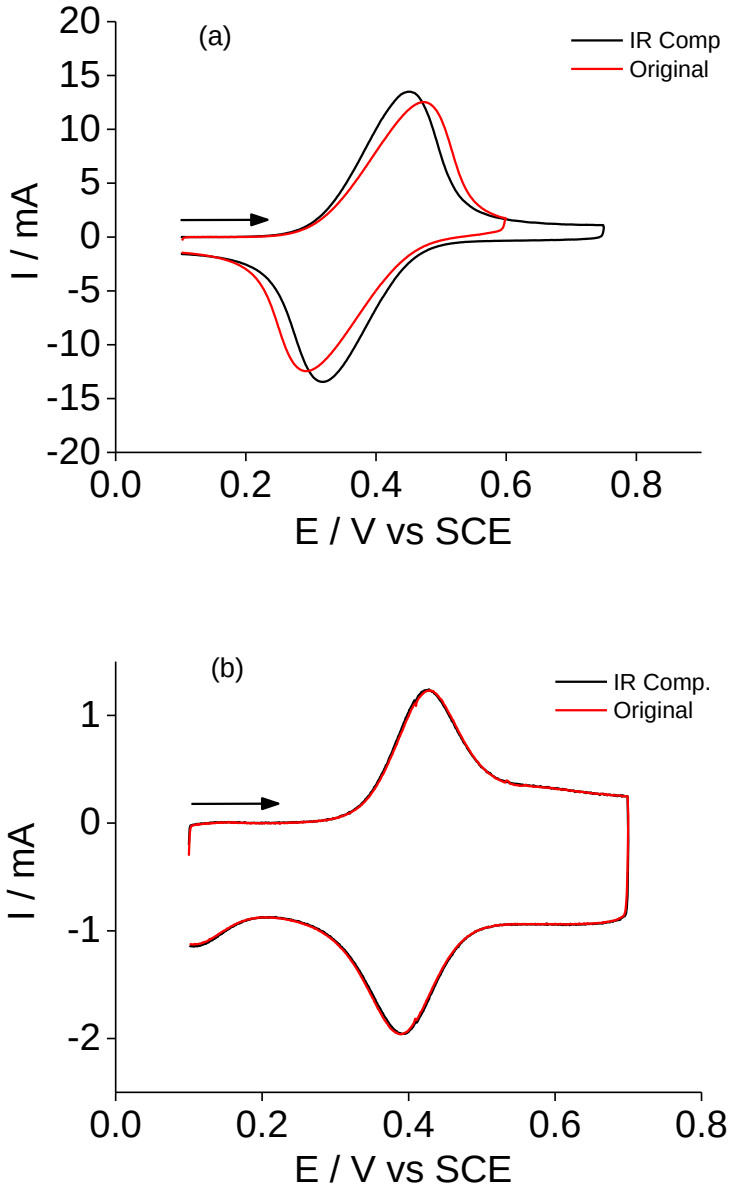

Figure 5.3: Cyclic voltammetry of a GF electrode in (a) 0.1 mM and (b) 10 µM ferrocene solution, before and after automatic solution resistance compensation. Scan rate = 0.1 V s^{-1}

The cyclic voltammetry of four redox systems were studied: ferricyanide in 0.1 M KNO_3; ferrocyanide in 1 M KCl(aq), vanadium(V) oxide in 4 M H_2SO_4(aq) and ferrocene in 0.1 M TBAP / acetonitrile. By comparing the voltammograms from experiments using 3 mm carbon electrodes (EPPG, BPPG and PFCE) with simulations produced using the DigiElch© software; it was possible to determine both *D* and k^o for each redox system studied. Values for both *D* and k^o were obtained for a range of scan rates

between 10 mV s^{-1} and 1 V s^{-1}. Average values are given in Table 5.1 and compare well with values previously reported (the values of k^o for the GF electrodes in Table 5.1 are discussed later) **[**25-27].

Table 5.1. Rate constants (k^o and diffusion coefficients (D) for EPPG, PFC and GF electrodes.

Redox System	**k^o of different electrodes (cm s^{-1})**			**D (cm^2 s^{-1})**
	EPPG	**PFC**	**GF**	
Ferricyanide (aqueous)	2.3 ±0.3 x 10^{-3}	3.0 ±0.5 x 10^{-3}	2.2 ±0.5 x 10^{-3}	7.5 ±0.3 x 10^{-6}
Ferrocyanide (aqueous)	7.5 ±0.4 x 10^{-3}	-	7.0 ±0.5 x 10^{-3}	6.0 ±0.2 x 10^{-6}
Ferrocene (non-aqueous)	2.2 ±0.3 x 10^{-2}	3.5 ±0.4 x 10^{-4}	2.0 ±0.4 x 10^{-2}	2.4 ±0.2 x 10^{-5}
Vanadium(V) (aqueous)	1.7 ±0.3 x 10^{-5}	2.0 ±0.6 x 10^{-5}	4.1 ±0.7 x 10^{-6}	1.9 ±0.5 x 10^{-6}

5.4.1 Ferricyanide Voltammetry

Figure 5.10(a) illustrates cyclic voltammograms at 0.05 V s^{-1} for the PFC and EPPG electrodes in an aqueous solution of 1.0 mM ferricyanide and 0.1 M KNO_3. Figure 5.10(b) illustrates the corresponding voltammogram for a graphite felt electrode under the same conditions but where the ferricyanide concentration is 0.1 mM. The lower concentration was used to avoid the requirement for *IR* compensation as discussed previously. There are two main differences between the felt and disc voltammetry. First, the currents recorded with the felt electrode are much higher in magnitude than for the traditional carbon disc electrodes. This is to be expected as the surface area is much larger for the felt electrode. Second, the peaks in the felt voltammogram are better defined, with the current almost returning to the baseline after the peak, resembling thin layer voltammetry [19].

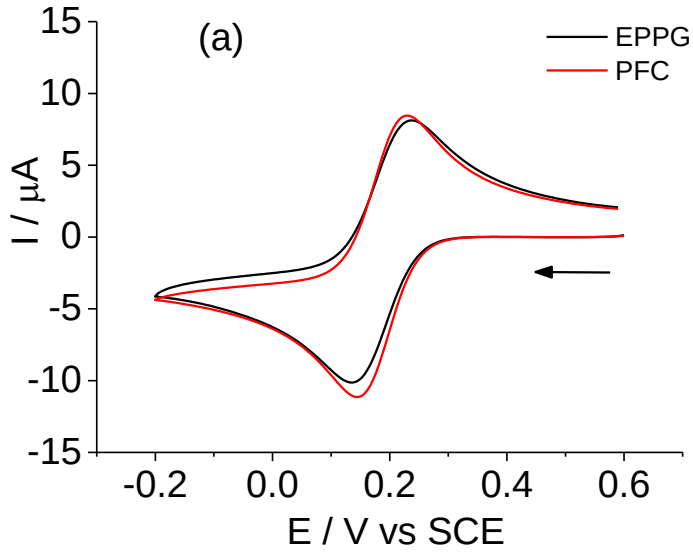
(a)
EPPG
PFC
I / µA
15
10
5
0
-5
-10
-15
-0.2
0.0
0.2
0.4
0.6
E / V vs SCE

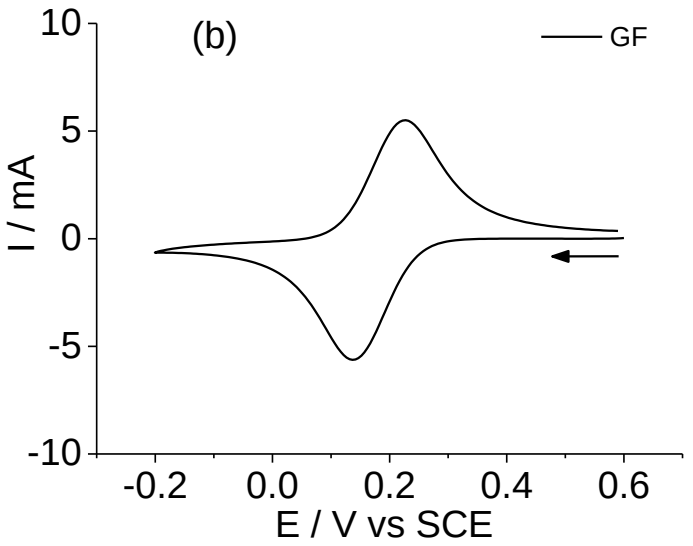
(b)
GF
I / mA
10
5
0
-5
-10
-0.2
0.0
0.2
0.4
0.6
E / V vs SCE

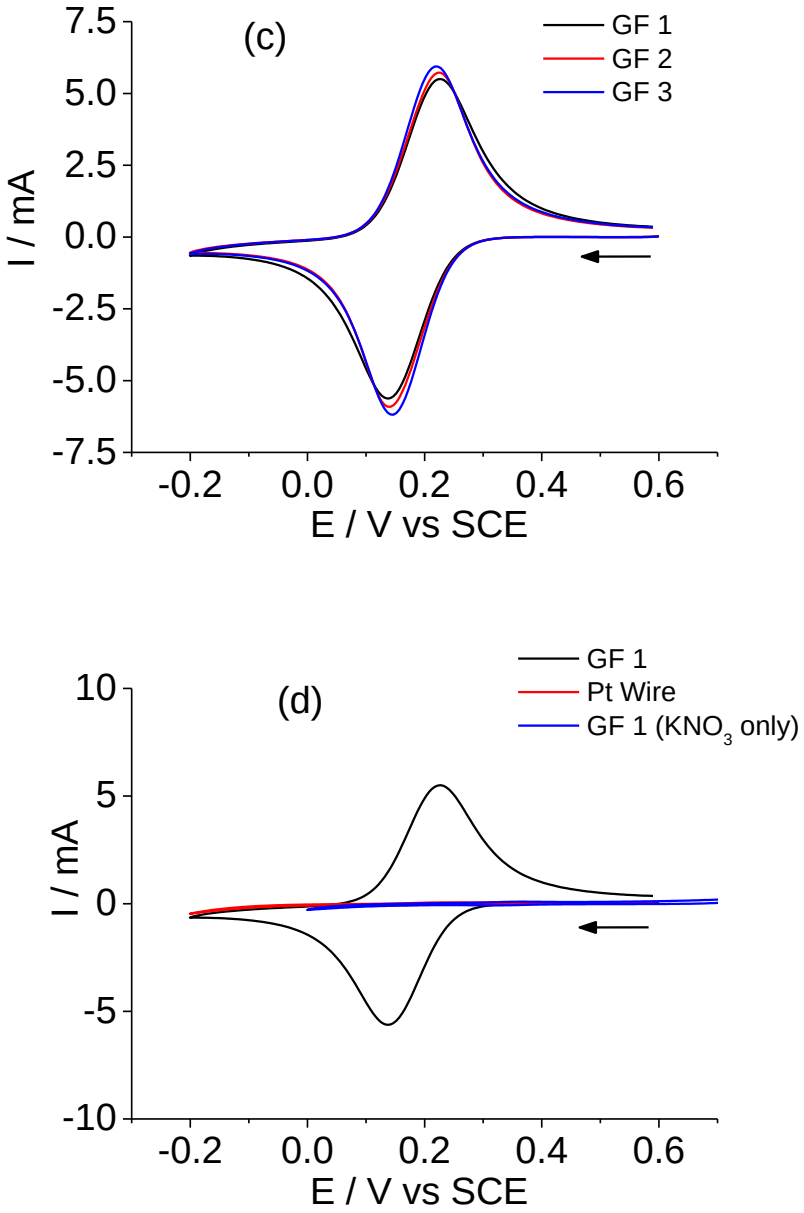

Figure 5.10: Cyclic voltammograms of (a) EPPG and PFC type electrodes in 1.0 mM ferricyanide/0.1 M KNO_3(aq.) solution and (b) GF electrode in 0.1 mM ferricyanide/0.1 M KNO_3(aq.) solution. Scan rate = 0.05 V s^{-1}. (c) Cyclic voltammograms of three different GF electrodes in a 0.1 mM ferricyanide / 0.1 M KNO_3(aq.) solution. Scan rate = 0.05 V s^{-1}. (d) Cyclic voltammograms of the platinum wire fish hook in 0.1 mM ferricyanide / 0.1 M KNO_3(aq.) solution and a GF electrode in 0.1 M KNO_3(aq.) solution. Scan rate = 0.05 V s^{-1}.

Figure 5.10(c) illustrates cyclic voltammograms recorded at 0.05 V s^{-1} in an aqueous solution of 0.1 mM ferricyanide and 0.1 M KNO_3 with 3 different GF electrodes. As observed, the GF electrodes demonstrate good repeatability in terms of the shape and magnitude of the signal. This is a result of

the GF preparation method, specifically the 3 step pre-wetting of the electrode. Without the pre-treatment, the GF electrodes produce signals with a reduced magnitude (compared to Figure 5.10(c)) and poor repeatability. Figure 5.10(d) illustrates a cyclic voltammogram recorded at 0.05 V s^{-1} in an aqueous solution of 0.1 mM ferricyanide and 0.1 M KNO_3 with just the platinum wire fish hook as the working electrode (i.e. no GF). Also shown is the corresponding voltammogram for a GF electrode immersed in supporting electrolyte only. These two voltammograms show the signal observed in Figures 5.10(b) and (c) are predominantly due to ferricyanide redox reactions occurring on GF. On increasing the scan rate, the expected transition in voltammetry characteristics from thin-layer to semi-infinite diffusion was observed.

Figure 5.11(a-d) illustrates plots of peak cathodic current, I_p^c, vs. scan rate, v, and I_p^c vs. $v^{0.5}$ for a GF electrode in 0.1 mM ferricyanide solution. The results are very similar to the simulated plots in Figure 5.7, and indicate a transition from finite diffusion/thin layer voltammetry at low scan rates to semi-infinite diffusion at high scan rates. The amount of diffusion layer overlap inside the porous electrode changes with scan rate, which suggests the simulation method proposed in the previous section can be used in combination with these experimental results to simultaneously determine the total (smooth) surface area and average pore size for this GF electrode.

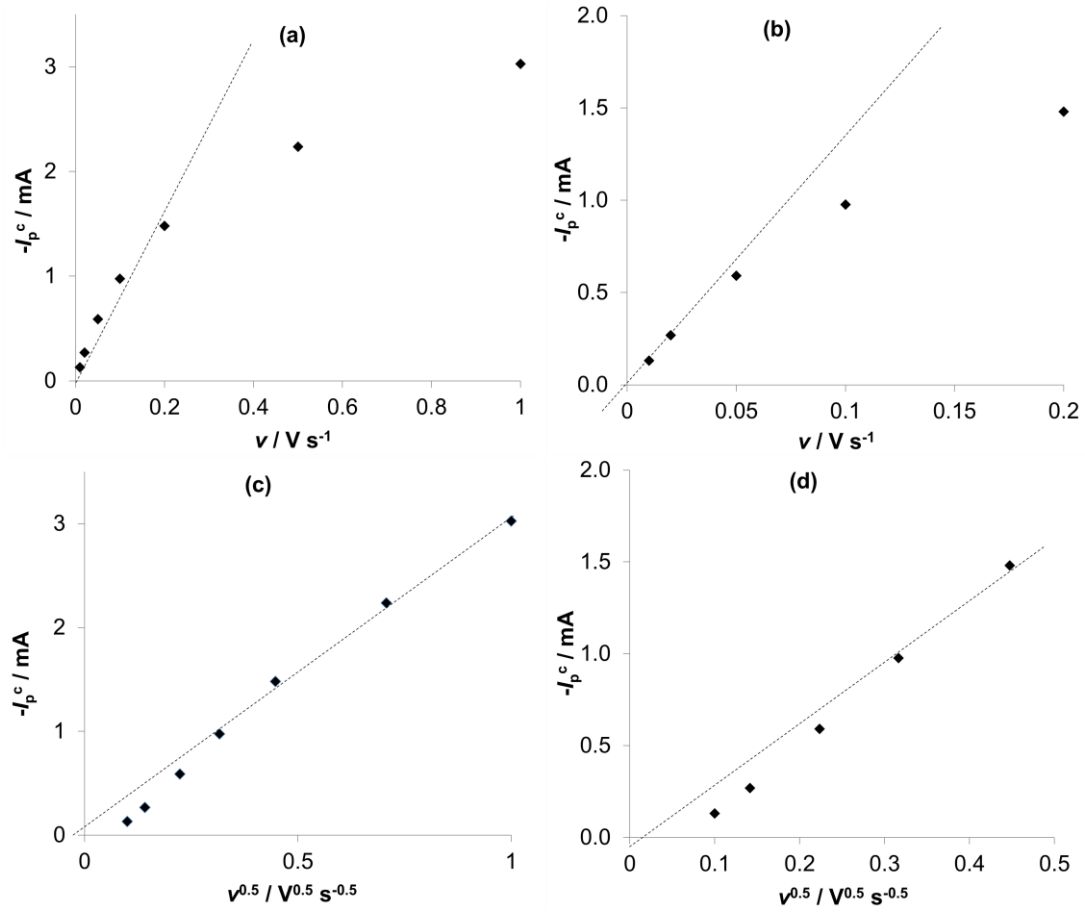

Figure 5.113: (a) Cathodic peak current vs. scan rate for a GF electrode in 0.1 mM ferricyanide solution. (b) Magnification of the linear region in (a). (c) Cathodic peak current vs. square root of scan rate for a GF electrode in 0.1 mM ferricyanide solution. (d) Magnification of the non-linear region in (c).

The simulation method described in the previous section was combined with the experimental peak currents (at multiple scan rates) and used to generate plots of equivalent surface area vs. average pore size, as shown in Figure 5.12. Initially, the simulations used the D and k^o values for the PFC electrode/ferricyanide system in Table 5.1. This generated a similar plot to Figure 5.8, and suggested the 0.5 V s^{-1} and 1 V s^{-1} experimental scans corresponded to semi-infinite diffusion mass transport (i.e. the 0.5 V s^{-1} and 1 V s^{-1} curves were horizontal at the curve crossing point). Therefore, an average k^o value of 2.2 x 10^{-3} cm s^{-1} was obtained by fitting the peak to peak separation values for the 0.5 V s^{-1} and 1 V s^{-1} GF experimental voltammograms to simulated semi-infinite diffusion cyclic voltammograms using DigiElch. This is another benefit of the simulation method – the identification of experimental data where mass transport is described by semi-infinite diffusion. Figure 5.12 was then generated

using values of D = 7.5 x 10^{-6} cm^2 s^{-1} and k^o = 2.2 x 10^{-3} cm s^{-1}. As observed, the curves (representing different scan rates) intersect at around 50 cm^2 and 30 µm in Figure 5.12, implying these are the values of electrochemical surface area and average pore radius for the particular GF tested.

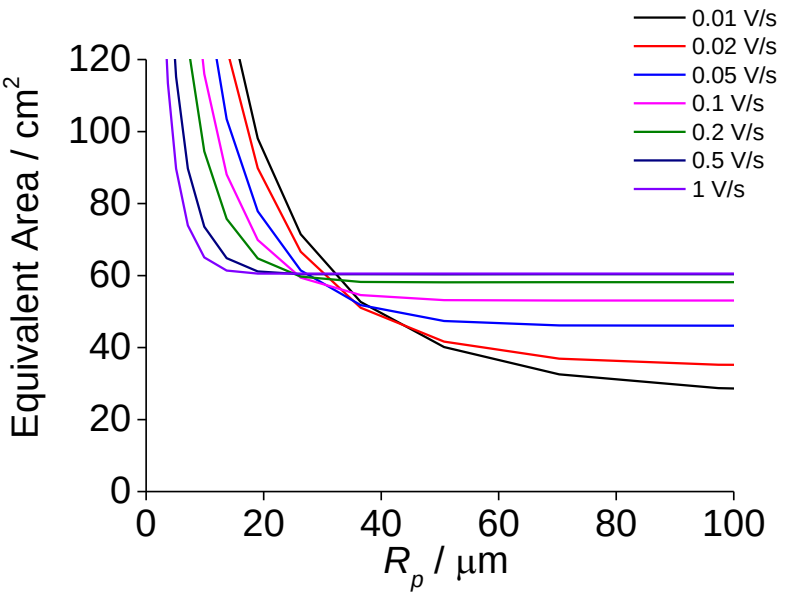

Figure 5.12: Simulated curves of equivalent surface area vs. pore radius using the cathodic peak current results from a GF electrode in a 0.1 mM ferricyanide solution.

Table 5.2: Summary of experimentally determined equivalent surface area and pore radius and theoretical pore radius and surface area.

Redox system	GF electrode number	Equivalent pore radius (μm)	Equivalent surface area (cm^2)	Theoretical average pore radius (μm)	Theoretical single fibre surface area (cm^2)
Ferricyanide (aqueous)	1	26 – 38	47 – 51	20.4	58.9
	2	24 – 42	52 – 56	20.4	59.8
	3	24 – 42	51 – 64	19.9	61.4
Ferrocyanide (aqueous)	1	25 – 30	57 – 61	20.7	57.5
	2	26 – 29	59 – 56	21.3	54.9
	3	27 – 30	57 – 61	20.7	57.6
Vanadium(V) (aqueous)	1	12 – 34	44 – 68	20.9	56.7
	2	21 – 39	43 – 53	19.9	61.7
	3	30 – 40	38 – 46	22.2	51.4
Ferrocene (non-aqueous)	1	24 – 47	48 – 64	22.3	48.3
	2	22 – 40	40 – 50	22.0	51.9
	3	24 – 43	40 – 55	22.1	51.7

A more precise range for the cross-over region is given in Table 5.2, along with the surface area calculated from the cylinder approximation and the corresponding approximate pore radius. Also given are the results for 2 other GF electrodes in the same electrolyte. It is clear from Table 5.2 that there is good agreement between experimentally determined and theoretically predicted surface areas, suggesting the approximations used in the model are a good first attempt at describing the complex electrode surface arrangement inside the porous electrode. Regarding the experimental pore sizes, these are similar to the theoretical pore sizes but the theoretical pore sizes tend to be consistently smaller than the experimental values. This is to be expected as the experimental result is a summation of an ensemble of pores where the larger pores have a disproportionally larger contribution to the peak current (as they have less thin layer and more semi-infinite diffusion-type voltammetry). Assuming the pore size distribution follows a Gaussian curve, the experimental result represents a pore size that is larger than the median whereas the theoretical result represents the median (or a size closer to the median if the distribution isn't symmetrical). Further work will address this issue, where the GF electrode will be modelled as an ensemble of tubular pores.

5.4.2 Other Redox Systems

In addition to ferricyanide, 3 other redox systems were investigated: ferrocyanide in 1 M KCl(aq); vanadium(V) oxide in 4 M H_2SO_4(aq); and ferrocene in 0.1 M TBAP / acetonitrile. Following the same procedure in the previous section, cyclic voltammograms were recorded with GF working electrodes at different scan rates. The results were then analysed using the simulation method discussed previously. This generated experimental values for the equivalent pore radius and surface area, which are reported in Table 5.2.

5.4.2.1 Ferrocyanide Voltammetry

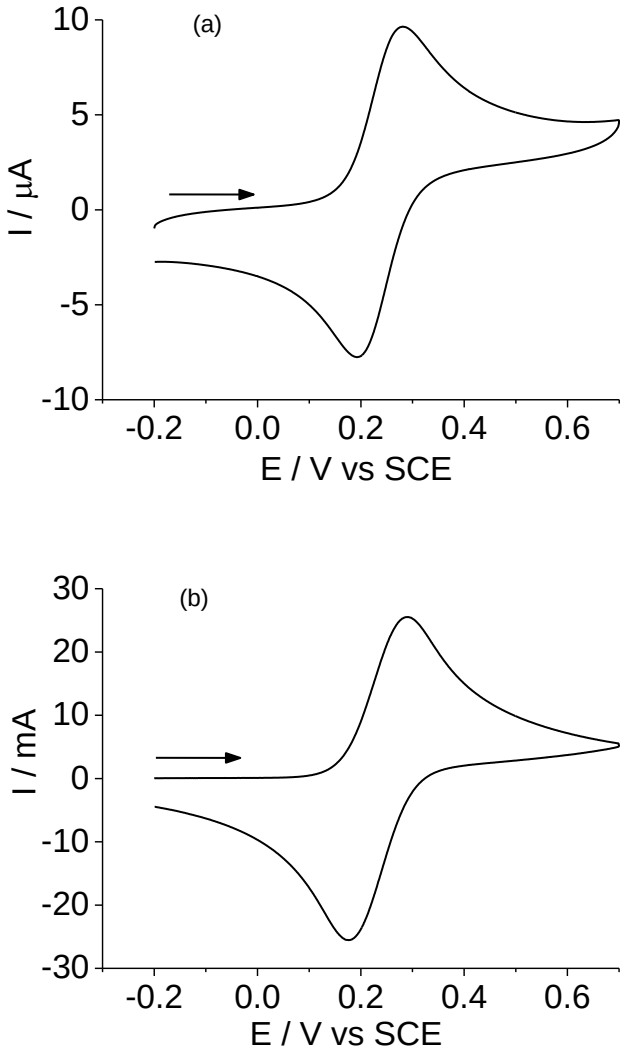

Figure 5.13: Cyclic voltammetry of (a) an EPPG and (b) a GF electrode in 1.0 mM ferrocyanide/1.0 M KCl(aq.) solution. Scan rate = 0.05 V s^{-1}.

In addition to the ferricyanide, the ferrocyanide redox system was also investigated with GF electrodes. However as a higher concentration was used it was necessary to apply solution resistance compensation. For the GF electrode in 1.0 mM ferrocyanide solution, Figure 5.13(b), 85% of the measured 6.6 Ohm solution resistance was compensated for. The ferrocyanide system is in excellent agreement with the ferricyanide system in terms of both voltammetric characteristics and the deduced felt properties (e.g. pore radius and surface area) in Table 5.2. The same relationship between scan rate, the square root of scan rate and peak anodic current, as shown previously, Figure 5.11(a-d), is also seen for ferrocyanide Figure 5.14(a-d).

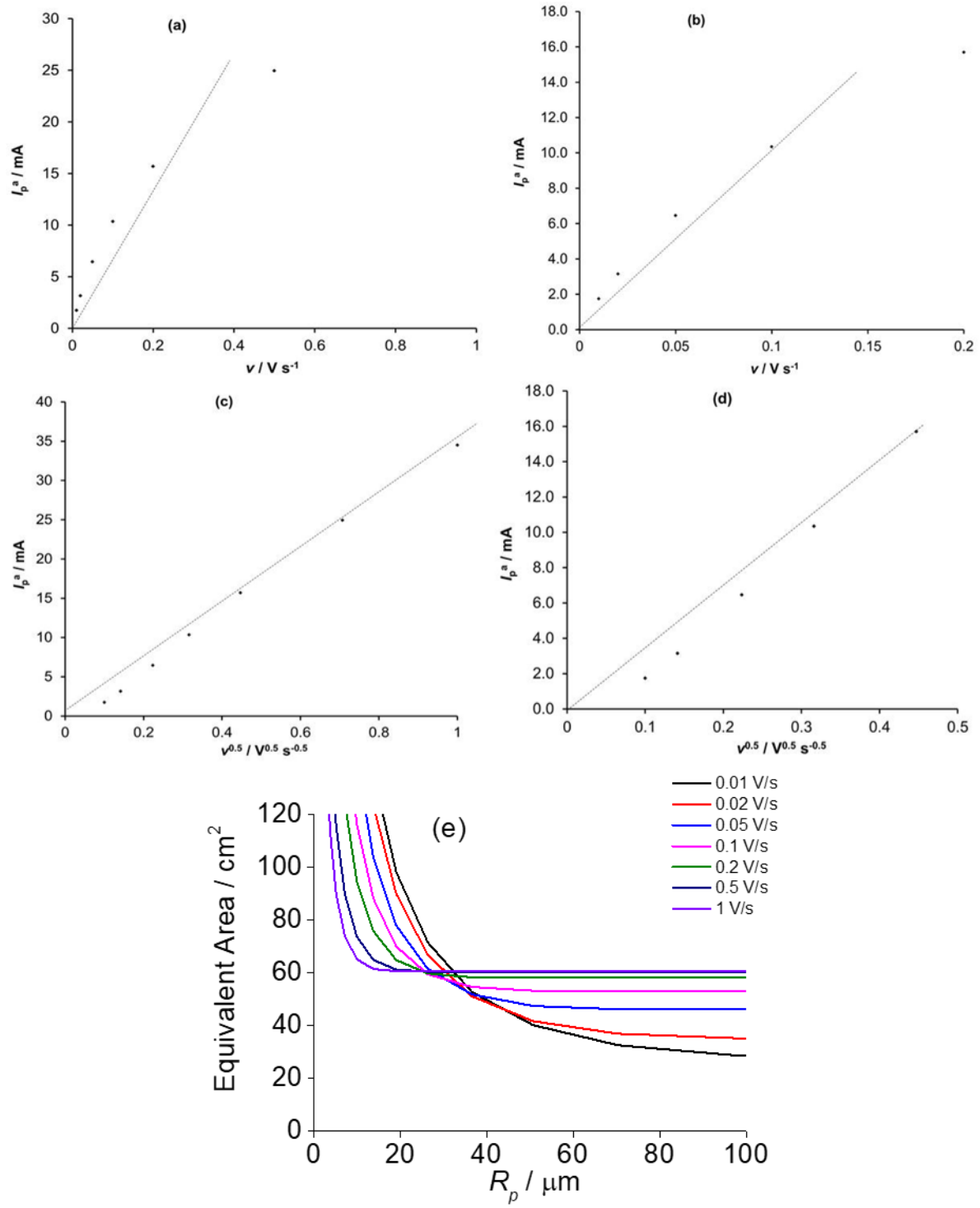

Figure 5.14: (a) Anodic peak current vs. scan rate for a GF electrode in 0.1 mM ferrocyanide solution. (b) Magnification of the linear region in (a). (c) Anodic peak current vs. square root of scan rate for a GF electrode in 0.1 mM ferrocyanide solution. (d) Magnification of the non-linear region in (c). (e) Simulated curves of equivalent surface area vs. pore radius using the anodic peak current results from a GF electrode in a 1.0 mM ferrocyanide solution.

The equivalent area vs. R_p plot shown in Figure 5.14 (e) is comparable to both the initial simulated plot and that of ferricyanide (Figures 5.8 and 5.12). However, the crossover region is more diffuse than previously. Whilst this produces a larger range for both pore size and equivalent area, the low scan rate results are more likely to have the largest error due to the issues discussed in the previous section. The higher scan rate results suggest values of R_p = 30 µm and area = 60 cm^2. This agrees well with the theoretical surface area given in Table 5.2.

The voltammetry and analysis followed the same trends as shown above for the ferricyanide system. For all the systems there was good agreement between the experimental and theoretical surface area, generating more confidence in the simulation method (especially given the diverse selection of redox systems). As before, the experimental average pore radius values were similar to but consistently larger than their theoretical analogues.

5.4.2.2 Vanadium(V) Voltammetry

Of particular interest was the vanadium(V) oxide redox system, described by equation 5.9:

$$VO_2^+{}_{(aq)} + e^- + 2H^+{}_{(aq)} \rightleftharpoons VO^{2+}{}_{(aq)} + H_2O \qquad (5.9)$$

This system is well known to be electrochemically irreversible and produce poor quality voltammograms with traditional carbon disc working electrodes and offers an excellent opportunity to showcase the ability of the GF electrodes.[37] Figure 5.16(a) shows the cyclic voltammogram for 1.6 mM vanadium(V) oxide in 4 M H_2SO_4(aq) with a PFC working electrode at 50 mV s^{-1}. In comparison Figure 5.16 (b) shows the cyclic voltammogram for the same solution but with a GF electrode. The GF is clearly superior at both resolving the redox peaks and improving the profile of the voltammogram. The GF felt was also able to distinguish the redox peaks of a 32 µM solution of the vanadium(V), shown in Figure 5.16(c). It was not possible to distinguish these redox peaks with the 3 carbon disc electrodes at this low concentration. Given the challenging nature of this redox system, the ability of the GF electrode to distinguish peaks at such minute concentrations is particularly impressive.

Vanadium redox flow batteries (VRFBs) are of ever increasing industrial and academic interest. With the growing global demand for long lasting, stable energy storage systems the VRFB has been extensively studied and is widely discussed in literature [38]. A large amount of research on this system has used either flow cell or rotating disc experiments. Whilst these techniques provide a host of useful information, especially regarding the systems use within flow batteries, they can be both difficult to set up and costly in terms of both expenditure and time. By following the techniques set out in this work, the vanadium(V) oxide system can be studied effectively, even at minute concentrations and with very little effort. This makes rapid screening of electrode modifications possible and could significantly enhance the development of more efficient VRFBs.

A solution of 1.6 mM vanadium(V) in 4 M H_2SO_4(aq.) was produced and investigated using the above voltammetric method. Again values for both *D* and *k* were determined from cyclic voltammetry using the standard 3 mm diameter carbon electrodes, Table 5.1, and these compare well with literature values [39]. The difficulties in measuring this system with standard carbon electrodes, such as the poor peak definition shown in Figure 5.15(a), give an excellent opportunity to showcase the ability of the GF electrodes. Figure 5.15(a) shows the cyclic voltammogram for 1.6 mM vanadium(V) with a PFC working electrode at 50 mV s^{-1}. In comparison Figure 5.15 (b) shows the cyclic voltammogram for the same solution but with a GF electrode. The GF is clearly superior at both resolving the redox peaks and improving the profile of the voltammogram. The GF felt was also able to distinguish the redox peaks of a 32 µM solution of the vanadium(V), shown in Figure 5.15(c). It was not possible to distinguish these redox peaks with the 3 carbon disc electrodes at this low concentration. Given the challenging nature of this redox system, the ability of the GF electrode to distinguish peaks at such minute concentrations is particularly impressive. The equivalent surface area vs. R_p plot for the 1.6 mM vanadium system is shown in Figure 5.15(d). The range of equivalent surface area and pore sizes are much greater than for the previous redox systems. Despite this they still compare well to the predicted values, shown in Table 5.2, as well as the two previous systems.

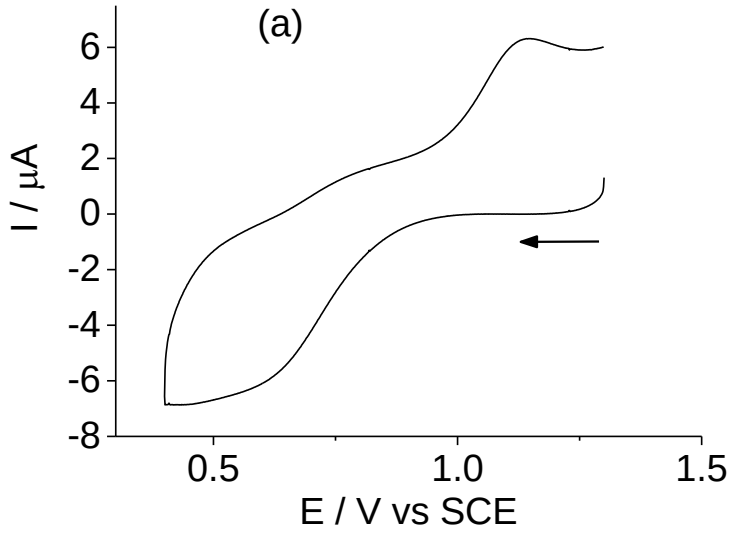
(a)
I / µA
6
4
2
0
-2
-4
-6
-8
0.5
1.0
1.5
E / V vs SCE

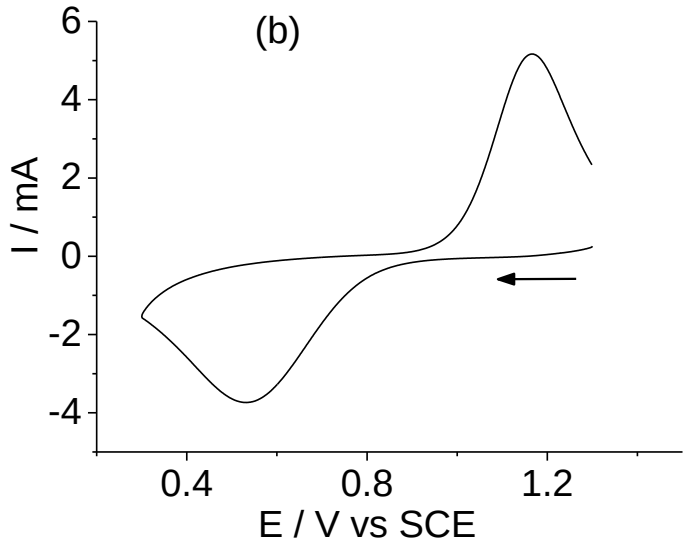
(b)
I / mA
6
4
2
0
-2
-4
0.4
0.8
1.2
E / V vs SCE

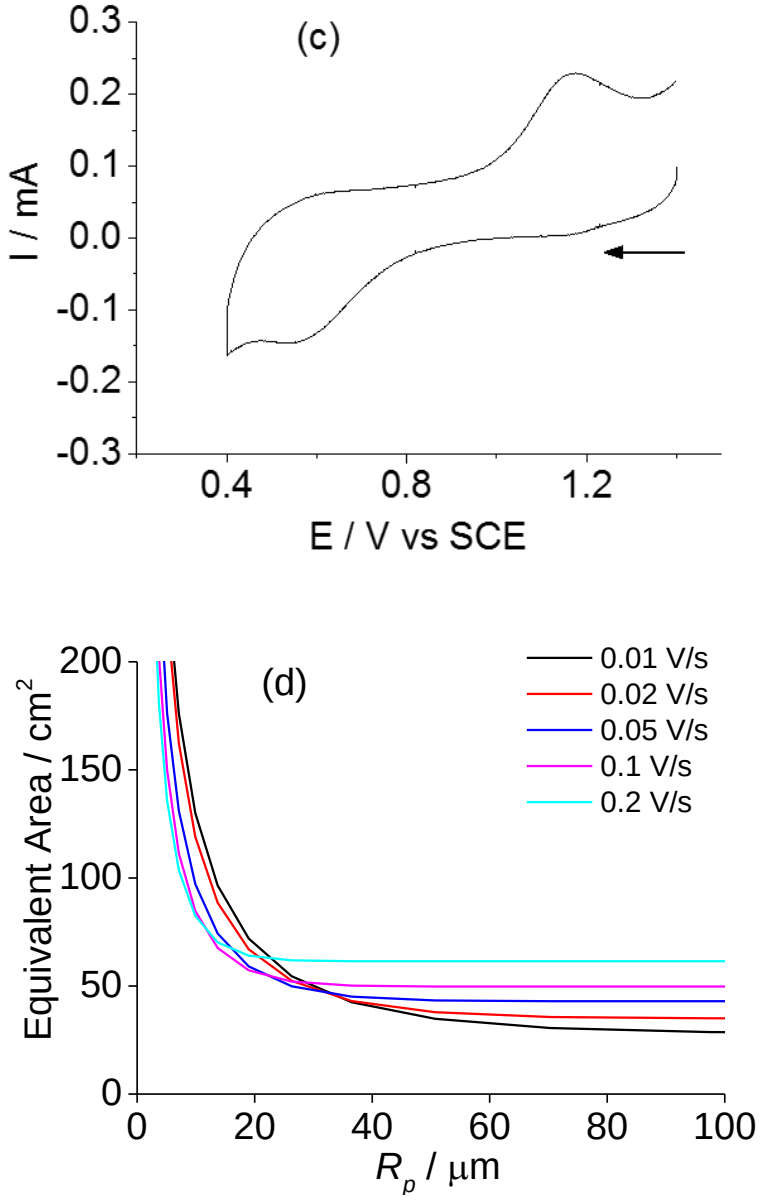

Figure 5.15: Cyclic voltammetry of (a) EEPG electrode, (b) GF electrode in 1.6 mM vanadium(V) / 4 M H_2SO_4(aq.) solution and (c) GF electrode in 32 µM vanadium(V) / 4 M H_2SO_4(aq.) solution. Scan rate = 0.05 V s^{-1}. (d) Simulated curves of equivalent surface area vs. pore radius using the cathodic peak current results from a GF electrode in a 1.6 mM vanadium(V) solution.

5.4.2.2 Ferrocene Voltammetry

To further examine the ability of the GF electrodes, a non-aqueous redox system was also investigated. A solution of 0.1 mM ferrocene in 0.1 M TBAP/acetonitrile was used for the standard carbon disc electrodes, whereas 10 µM ferrocene in 0.1 M TBAP/acetonitrile was used for the GF samples. The

non-aqueous nature of the ferrocene solution eliminated the wettability issue of the GF and therefore removed the requirement for the ethanol pre-treatment step. Values of D and k^o were again determined using the traditional carbon disc electrodes, Table 5.1, and are within the range of previous literature values [40]. Figure 5.16 shows a comparison between the EPPG and GF electrodes in the ferrocene solution.

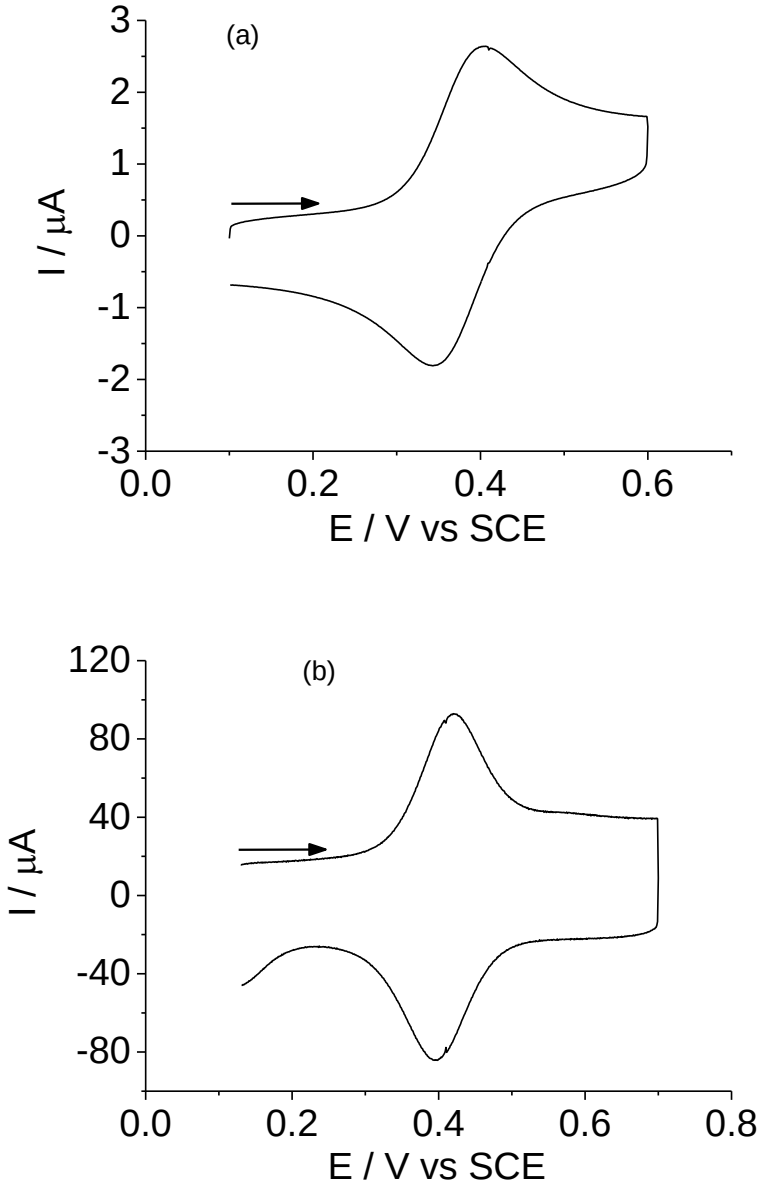

Figure 5.16: Cyclic voltammetry of (a) an EPPG electrode in 0.1 mM ferrocene solution and (b) a GF electrode in 10 µM ferrocene solution. Scan rate = 0.05 V s^{-1}.

The results for GF electrodes in ferrocene/acetonitrile solution follow the same trends seen in the previous aqueous systems, as shown in Figure 5.17(a-d). The equivalent area vs. average pore radius plot determined using the simulation method is shown for one of the GF electrodes in the ferrocene/acetonitrile system in Figure 5.17(d). As observed, the cross over region is much more diffuse for this system compared to the aqueous systems. The cause could be the higher diffusion coefficient of ferrocene in acetonitrile, making the lower scan rate results even more prone to the simulation error discussed in the previous section. Discarding the 0.01 and 0.02 V s^{-1} data, the results agree well with the other systems.

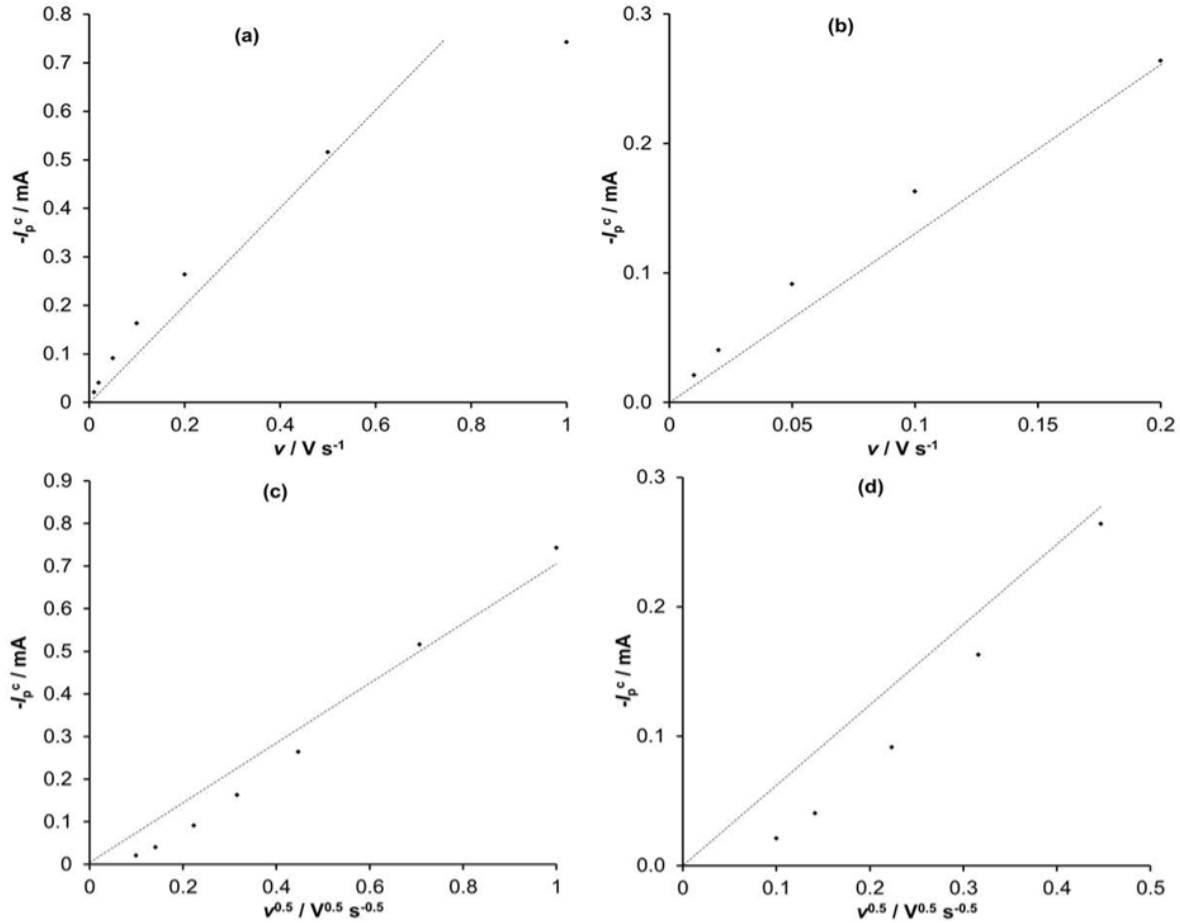
(a)
$-I_p^c$ / mA
v / V s^{-1}
(b)
$-I_p^c$ / mA
v / V s^{-1}
(c)
$-I_p^c$ / mA
$v^{0.5}$ / V$^{0.5}$ s$^{-0.5}$
(d)
$-I_p^c$ / mA
$v^{0.5}$ / V$^{0.5}$ s$^{-0.5}$

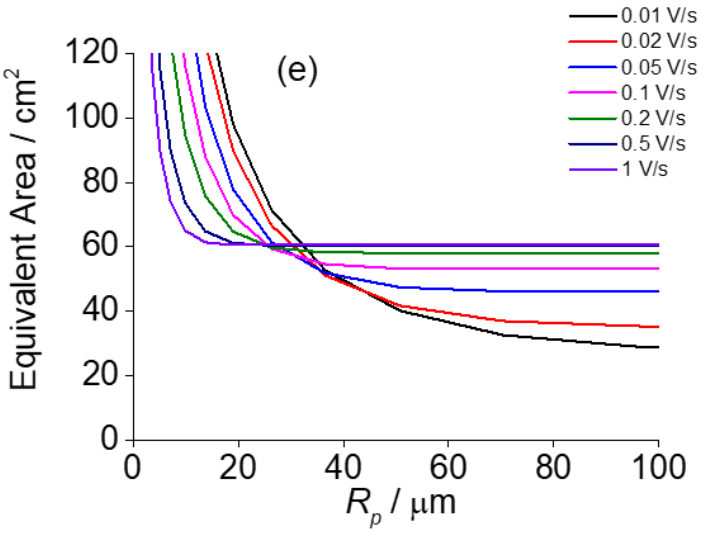
(e)
0.01 V/s
0.02 V/s
0.05 V/s
0.1 V/s
0.2 V/s
0.5 V/s
1 V/s
Equivalent Area / cm^2
R_p / μm

Figure 5.17: (a) Anodic peak current vs. scan rate for a GF electrode in 10 µM ferrocene solution. (b) Magnification of the linear region in (a). (c) Anodic peak current vs. square root of scan rate for a GF electrode in 10 µM ferrocene solution. (d) Magnification of the non-linear region in (c). (e) Simulated curves of equivalent surface area vs. pore radius using the anodic peak current results from a GF electrode in a 10 µM ferrocene solution.

5.4.3 Fibre Surface Structure

The capacitance of an electrode surface can be determined via cyclic voltammetry within a potential window where no faradaic reactions occur. Once the capacitance, C, of the GF electrode is determined, the specific capacitance, C^o, can be evaluated by dividing the capacitance value by the total area of the electrode, these are listed in Table 5.3 where the theoretical surface area was used. The results provide an insight into the nature of the carbon fibre surfaces with the graphite felt. Previous studies with highly ordered pyrolytic graphite, found graphite with a predominantly basal plane surface has a specific capacitance of around 1-2 µF cm^{-2}, whereas for edge plane surfaces the figure is a lot higher, around 70 µF cm^{-2} [28]. In addition when a carbon surface is comprised of both edge and basal plane, the total specific capacitance, C^o, is a weighted average of the edge and basal plane contributions:

$$C^o = C^o_e f_e + C^o_b (1-f_e) \qquad (5.10)$$

where C^o_e and C^o_b are the specific capacitance values for the edge and basal plane surfaces, and f_e is the fraction of edge plane on the graphite surface.

Table 3.3: Average specific capacitance measurements for GF in a range of redox systems at various scan speeds (0.1-5 V s^{-1}).

Redox System	**Average Specific Capacitance (μF cm^{-2})**
Ferricyanide (aqueous)	20
Ferrocyanide (aqueous)	4.2
Vanadium(V) (aqueous)	14
Ferrocene (non-aqueous)	7.8

The results from Table 5.3 indicate the average specific capacitance of the GF electrode is relatively low, around 10 μF cm^{-2} over the four systems studied in this work. Using equation 5.10 and values of 70 μF cm^{-2} and 1 μF cm^{-2} for C^{o}_{e} and C^{o}_{b}, respectively, this corresponds to an approximate basal/edge ratio of 87/13 (i.e. 87% basal plane, 13% edge plane) and suggests that basal plane carbon is the dominant surface structure in the GFs studied in this work. This agrees well with the 'onion ring' structure observed in highly graphitized carbon fibres derived from polyacrylonitrile [28]29].

The capacitance of an electrode surface can be determined via cyclic voltammetry within a potential window where no faradaic reactions occur. Figure 5.18 illustrates an example of the capacitance scans recorded in the ferrocene systems. These are typical results with the capacitive current, I, increasing linearly with scan rate, ν. For these voltammograms the capacitance, C, of the surface can be calculated using equation 5.11;

$$I = C\nu \qquad (5.11)$$

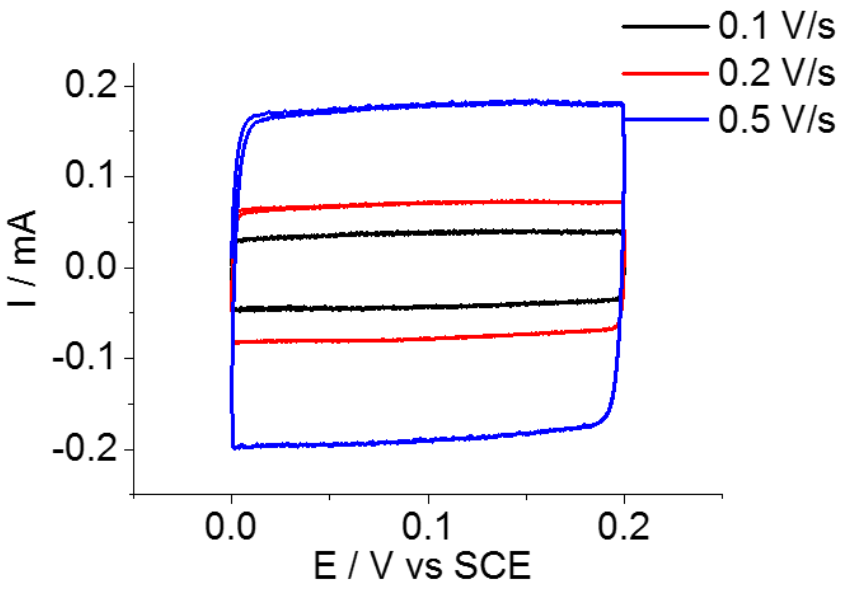

Figure 5.18: Capacitance measurements using cyclic voltammetry of GF in 10 µM ferrocene solution at the shown scan rates.

5.5. Limit of Detection

In order to further examine the properties of the GF materials and their application as electrodes, a study into their limit of detection was performed. For many electroanalytical applications, electrodes are often required to detect increasingly low concentrations of analyte. Decreasing the limit of detection (LoD) of electrodes is therefore a continuing goal of the electrochemical community. Whilst the type of electrochemical experiment used can provide an increase in signal size and quality, for example the use of differential pulse voltammetry over cyclic voltammetry, it is often the physical characteristics of the electrode that play the largest part in increasing the current signal to noise ratio, thereby decreasing the LoD. Conventional thinking lends to the approach of reducing electrode size to improve the LoD, by increasing the rate of mass transport, which leads to increased current densities and improvements in the signal to noise ratio. This ratio of analyte to capacitive background current signal is very important when discussing voltammetric techniques for electroanalysis. While the voltammetric techniques employed in electroanalysis are very sensitive to the currents produced by even a small amount of analyte, the LoD is significantly higher due to the

background capacitive charging of the double layer, causing interference [24]. On metal electrodes, such as Hg, this capacitive current has been used to investigate the structure of the double layer and its effect on electrode kinetics [25]. In the case of carbon electrodes, this is increasingly more difficult due to the additional factors such as the range of surface groups and surface roughness adding complications to the observation of the background current. Often an unfortunate side effect of reduced surface area is an increase in either cost of the electrode or difficulty in preparation. Both of these conditions reduce the throughput of experiments due to the preparation and care requirements of these electrodes and reduce the variety of experiments for risk of damaging expensive equipment. Furthermore, small electrodes generate small currents that required sophisticated potentiostats to detect and "ideal" lab conditions to reduce electrical noise [26-28].

Previous work on the electrochemical characterization of graphite felt electrode suggested graphitic felts were able to detect lower concentrations of analyte better than their planar disc counterparts. Due to the high surface area of the felts, when using cyclic voltammetry in a redox solution of ~1 mM analyte concentration, the corresponding peak currents were very high, in the milliamp and above range. This in turn led to an increased uncompensated solution resistance (IR drop) which consequently effected the voltammetry. To counter this there were two options; either electronically compensate for the resistance or reduce the concentration of the analyte to a point where the corresponding value of IR is below 0.1 mV. It was while reducing the analyte concentration that it was noted the felts outperformed the planar disc carbon, even when working with analytes below 10 µM concentration, the quality of the signal appeared to be unaffected by the reduced concentration [29].

Using GFs as "mega-macro" electrode materials for studying low concentrations moves against the trend for smaller surface area electrodes. Previous literature has reported the use of macro carbon electrodes for use in quiescent electrochemical experiments, but as reported in chapter 3 these have suffered from wettability issues, making LoD studies difficult to control. The GFs used here have physical surface areas of approximately 27.5 m^2 g^{-1}, dimensions of 1 cm x 1 cm x 0.28 cm and an

electrochemical surface area of approximately 60 cm^2 [29]. Furthermore, due to the mass production of this material for redox flow battery applications, each 0.28 cm^3 piece of electrode material costs less than 0.01 GBP. In addition, graphite felt electrodes are relatively easy to prepare and require no polishing. This chapter investigates to what degree these low-cost, robust GF electrodes are able to detect analyte signals in both aqueous and non-aqueous solutions.

5.5.1. Results and Discussion

The electrochemistry of the felt differs from that of the macro disc electrode in two key respects. Firstly; due to the large surface area of the felt, higher currents are recorded, compared to the traditional disc electrodes. At a given concentration, the analyte signal is typically 100 times greater for a 1 cm x 1 cm GF electrode than for a 3 mm diameter EPPG electrode. Secondly; the thin layer voltammetry exhibited by the felt at low scan rates (due to its porous structure) allows for better defined peaks, with the current almost returning to the baseline after the peak.

The limit of detection is the smallest concentration that can be detected with a reasonable level of certainty, while the limit of quantification (LoQ) is the smallest concentration which can be reliably quantitatively analysed [30]. The 3σ method was used for each solution to provide a statistical value for the LoD [31]. Measurements were carried out in both aqueous and non-aqueous, background electrolyte, with no added analyte to determine the validity of the measurements.

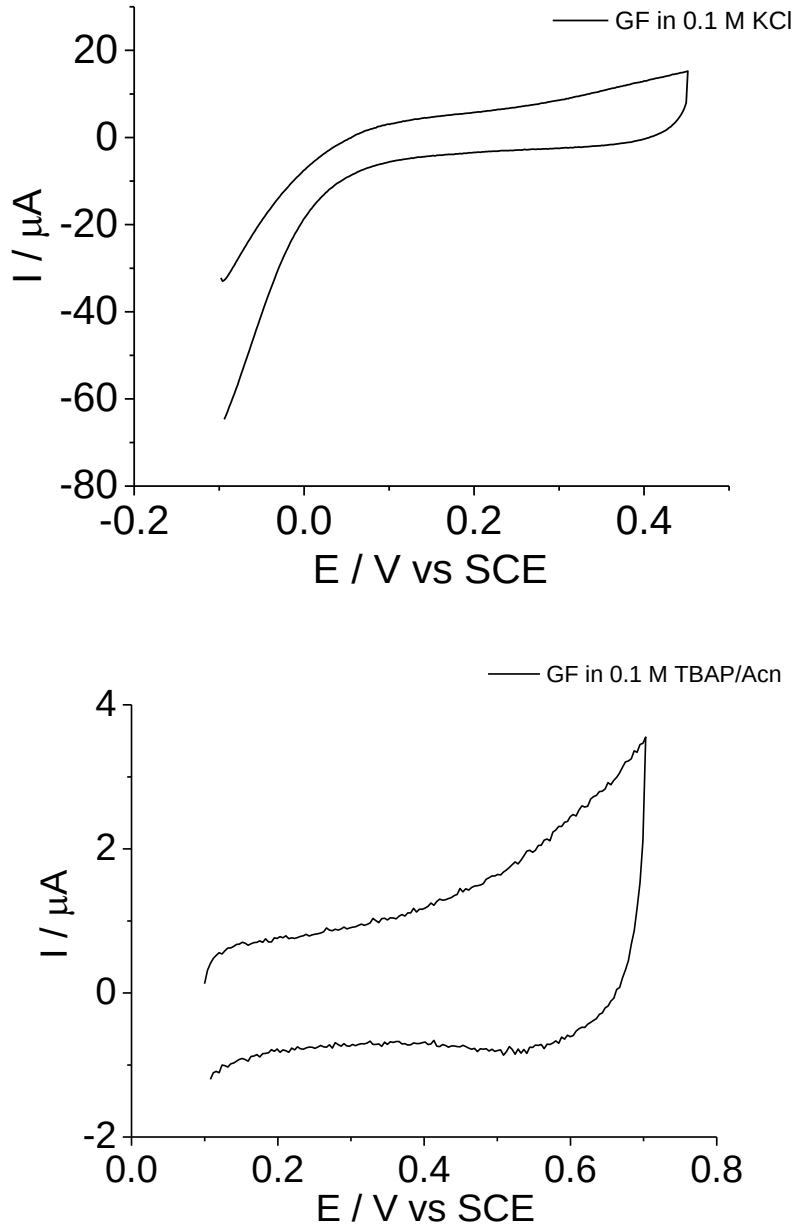

Figure 5.19: Cyclic voltammograms of GFs in background electrolyte solutions of a) 0.1 M KCl and b) 0.1 M TBAP/acn, at 50 mV s^{-1}.

5.5.1.1 Ferrocene electrochemistry

Figure 5.20c shows the comparison between an EPPG electrode, in red and GF, in blue in a 1 µM ferrocene solution. This is a much lower concentration than the millimolar concentrations usually employed for electrochemical measurements on planar disc electrodes. Despite this the GF provides a much clearer signal. The EPPG electrodes' oxidation peak is extremely broad, almost

indistinguishable from the baseline, while the reduction peak is non-existent. By comparison the graphitic felt has a clearly flatter baseline with discernible redox peaks. For a 3 mm carbon disc electrode in a 1 μM ferrocene solution, simulations give an expected peak current of 13.5 nA, which is too small to be reliably measured using the standard experimental set-up, thereby requiring more a more advanced, and expensive, potentiostat. These peaks are characterised by their minimal peak to peak separation, again indicating the difference in diffusion model between the felt and the planar disc. This along with the comparably lower current density of the felt, is an effect of the thin layer type electrochemistry seen with the felts (at low scan rates) rather than the semi-infinite diffusion of the disc electrode.

Figure 5.20 shows the voltammogram for a graphitic felt and an EPPG electrode in a non-aqueous 1 μM ferrocene solution. In the case of the GF, the flat baseline, 'perky' peaks and small peak to peak potential, characteristic of the thin layer voltammetry are clearly visible. Notice how well the graphitic felt performed in a low concentration solution relative to the EPPG. The magnitude of the analyte peak current for the GF sample versus the blank baseline is significantly higher than that of the EPPG, this is the key principle of investigating the detection limits of GFs. The graphitic felt was then evaluated with a much lower concentration to investigate to what level these materials are able to perform. Figure 5.21 b) shows the graphitic felt in a 25 nM ferrocene solution. Even at such a low concentration the redox peaks of the ferrocene are still clearly distinguishable.

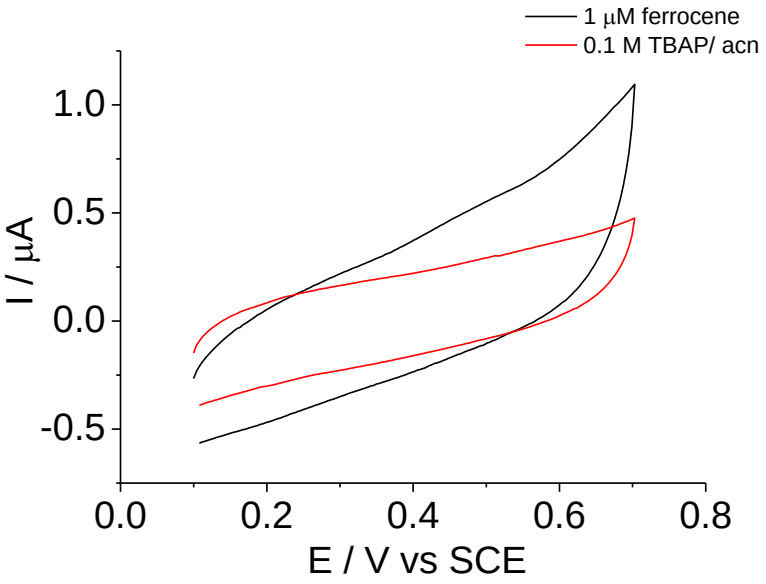
1 μM ferrocene
0.1 M TBAP/ acn
1.0
0.5
0.0
-0.5
I / μA
0.0
0.2
0.4
0.6
0.8
E / V vs SCE

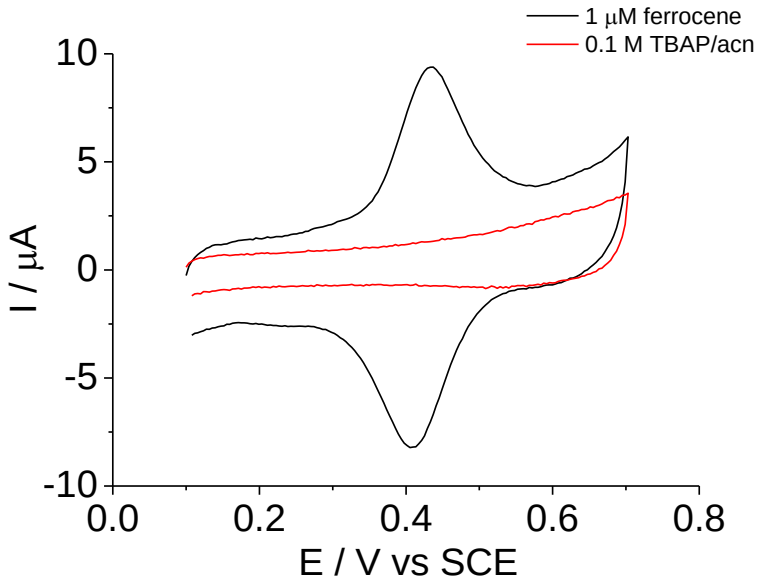
1 μM ferrocene
0.1 M TBAP/acn
10
5
0
-5
-10
I / μA
0.0
0.2
0.4
0.6
0.8
E / V vs SCE

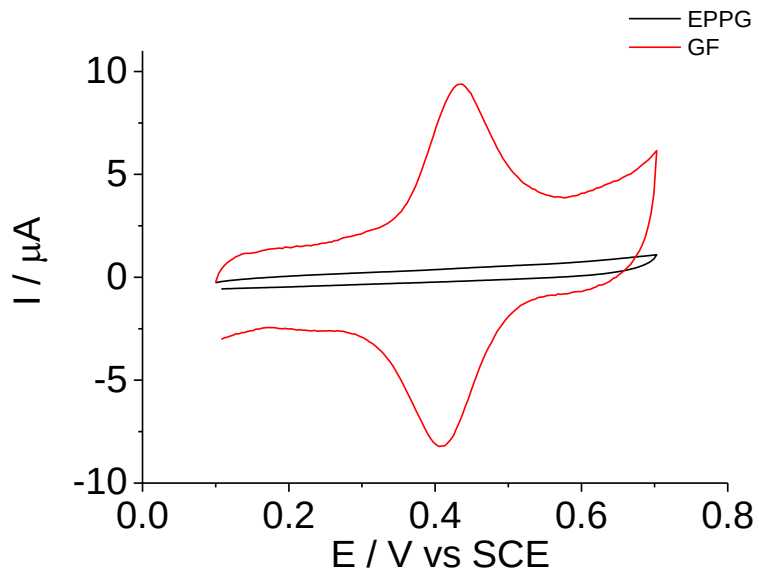

Figure 5.20: Cyclic voltammograms of a) an EPPG electrode and b) a GF electrode, in 1.0 µM ferrocene in 0.1 M TBAP/acn solution and with the background electrolyte control of 0.1 M TBAP/acn, and c) the overlaid cyclic voltammograms of both the EPPG and GF in in 1.0 µM ferrocene in 0.1 M TBAP/acn solution. All cyclic voltammograms measured at 50 mV s^{-1}.

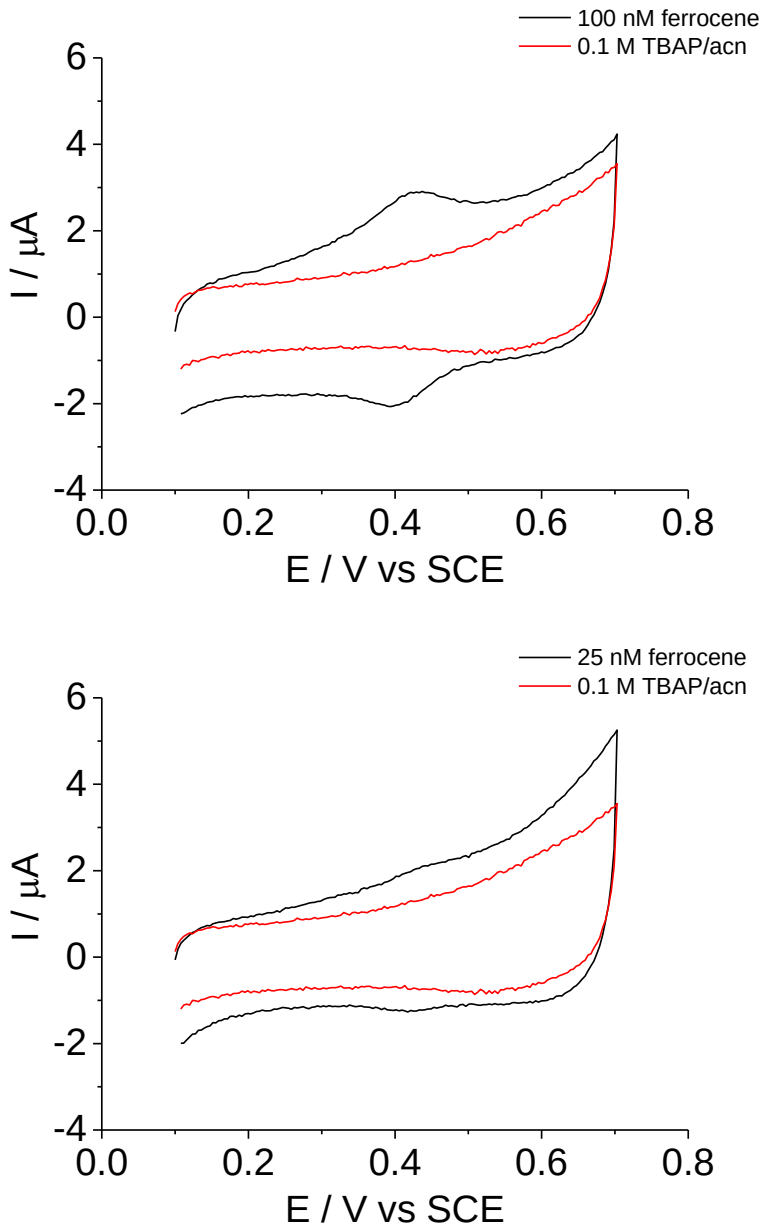

Figure 5.21: Cyclic voltammograms of a GF in a) 100 nM and b) 25 nM ferrocene in 0.1 M TBAP/acn solution, versus the GF in 0.1 M TBAP/acn background electrolyte solution. All cyclic voltammograms measured at 50 mV s^{-1}.

Both the GF electrodes and an EPPG electrode were measured in ferrocene solutions of increasing concentration from 10 nM to 0.1 mM. The resulting cyclic voltammograms were evaluated using the peak integration software from Origin Pro, with the associated charge of the ferrocene oxidation peak determined across the range of solution concentrations. Figure 5.22 shows the results for the graphitic felts and EPPG electrode determined using this method. As observed between 1 µM and 60 nM there

is a clear linear relationship between concentration and charge density for the GFs, but with both felts. Despite being able to measure the redox signal of ferrocene at concentrations below 60 nM there is no longer a clear relationship between charge density and concentration. So a simple observation of the data suggests the LoD is down to as low as ~20 nM, the LoQ is ~60 nM. Using the 3σ method to give a statistical value a LoD of 156 nM is achieved, while the 10σ value is 0.52 µM, while these values are higher than simple observation may suggest, they are still noteworthy, showing the impressive range of concentrations the GF electrode can measure. In comparison, we see that the EPPG electrode has an excellent stability from 0.1 mM down to around 3 µM. Although there is a good linear relationship across the whole of this region, below 3 µM it is impossible to determine redox peaks on the voltammogram. As expected the GF shows a linear relationship across this whole concentration region. By comparing the charge/concentration relationship across the entire range of concentrations, it is clear to see the performance of the GFs. The GFs have a distinctive linear relationship across the 0.1 mM to 60 nM region. The felt electrodes are clearly able to measure across a wide range of ferrocene concentrations and to a much lower concentration than the disc electrodes in non-aqueous solutions.

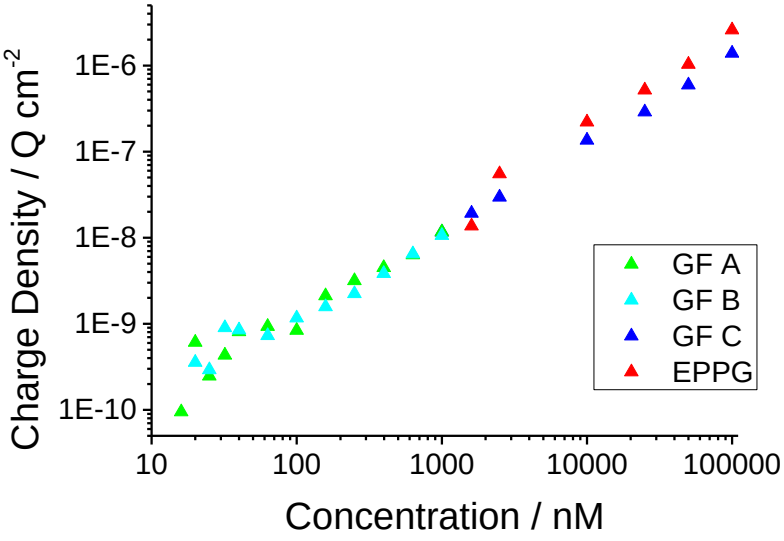

Figure 5.22: Charge density versus ferrocene concentration for GFs electrodes and an EPPG electrode.

By using the known dimensions of the GF electrode, it is possible to estimate a maximum and minimum value for the ferrocene oxidation charge. The minimum charge is based upon the concentration of the ferrocene and the volume of the GF electrode. The maximum takes this value and adds the amount of charge gained from treating the external surface area of the felt as a planar electrode. The dimensions of the felt (2.8 mm x 10 mm x 10 mm) and the felt porosity, ϕ can be determined from the mass measurement as shown previously in this chapter. Therefore, complete oxidation of ferrocene within the GF would require n_{Fc} moles of ferrocene within the felt, where n_{Fc} is given by:

$$n_{Fc} = [Fc^{+}]_{bulk}\phi V_{GF} \qquad (5.12)$$

Where $[Fc^{+}]_{bulk}$ is the concentration of the initial solution and V_{GF} is the volume of the GF electrode. Determining the minimum charge is then simply a case of multiplying the internal surface, Q_{int}, area by Faraday's constant:

$$Q_{int} = Fn_{Fc} \qquad (5.13)$$

If the external surface area of the GF is considered as a planar electrode, where surface area, A, is 3.12cm^2, and D and k^0 are found from the work in chapter 4, the charge relating to purely the external surface, Q_{ext}, can be approximated by simulating the reaction and measuring the resulting charge. Combining the internal (Q_{int}) with the external (Q_{ext}) charge, a value for total theoretical charge can be estimated.

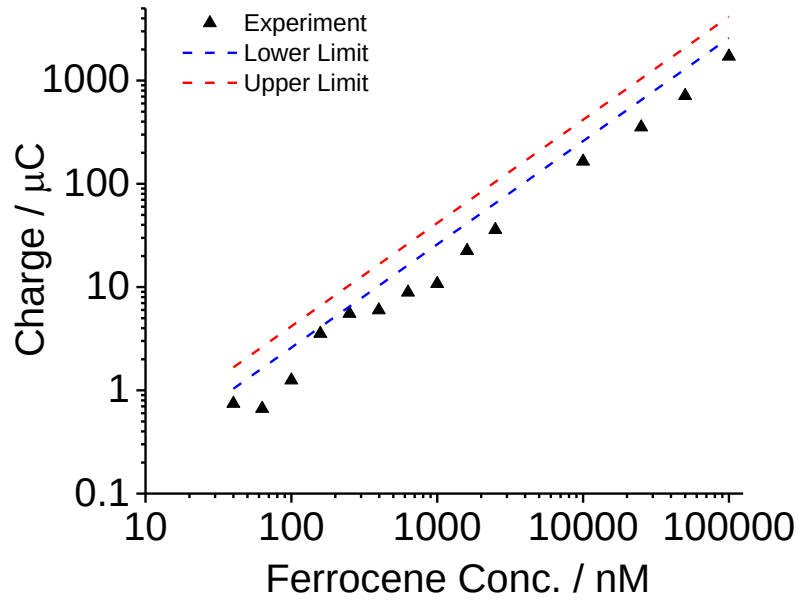

Figure 5.23: Charge density versus ferrocene concentration for a GF electrode. Also shown at the theoretical upper and lower charge limits.

Figure 5.23 plots the charge from the oxidation of ferrocene against the concentration of ferrocene. The upper and lower limits are calculated as described above. Interestingly, the experimental result is not between the upper and lower limits, as might be expected, but follows a linear range at a value of roughly half the expected lower limit. This is likely a product of the scan speed (50 mV s^{-1}) that the experimental results were taken, and only around half of the ferrocene concentration was oxidised. To ensure full oxidation of the felt contents a slower scan speed (≤10 mV s^{-1}) would be required. This result again highlights the ability of the GF electrode to detect concentrations across a wide range of concentrations, whilst suggesting the lowest limits of both detection and quantification, could potentially be even lower than shown in this chapter.

5.5.1.2 Ferrocyanide Electrochemistry

Aqueous solutions provide additional challenges for graphitic felt electrochemistry. One of the key aspects to the graphitic felts performance is its large surface area, around 800 times larger than that of the 3-mm diameter, planar disc electrodes. The structure of the felt, however, makes ensuring wettability throughout the entire electrode especially important. The fibrous nature of the felt combined with the hydrophobicity of the carbon surface dominates the wetting of the felt interior. Aqueous solutions invariably suffer in this respect when compared to the non-aqueous solutions, for example acetonitrile, due to the higher surface tension of water. For these reasons, it is essential to ensure the interior of the felt is fully wetted as this is a major factor in the magnitude of the analyte signal in aqueous solutions.

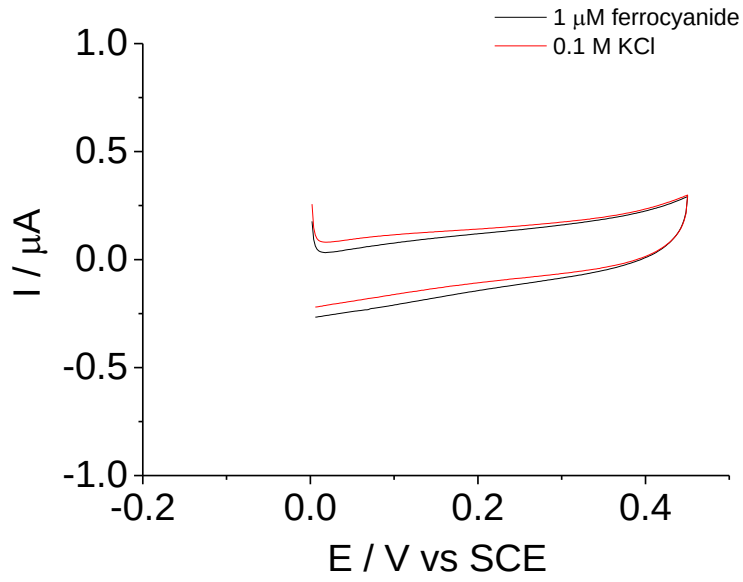

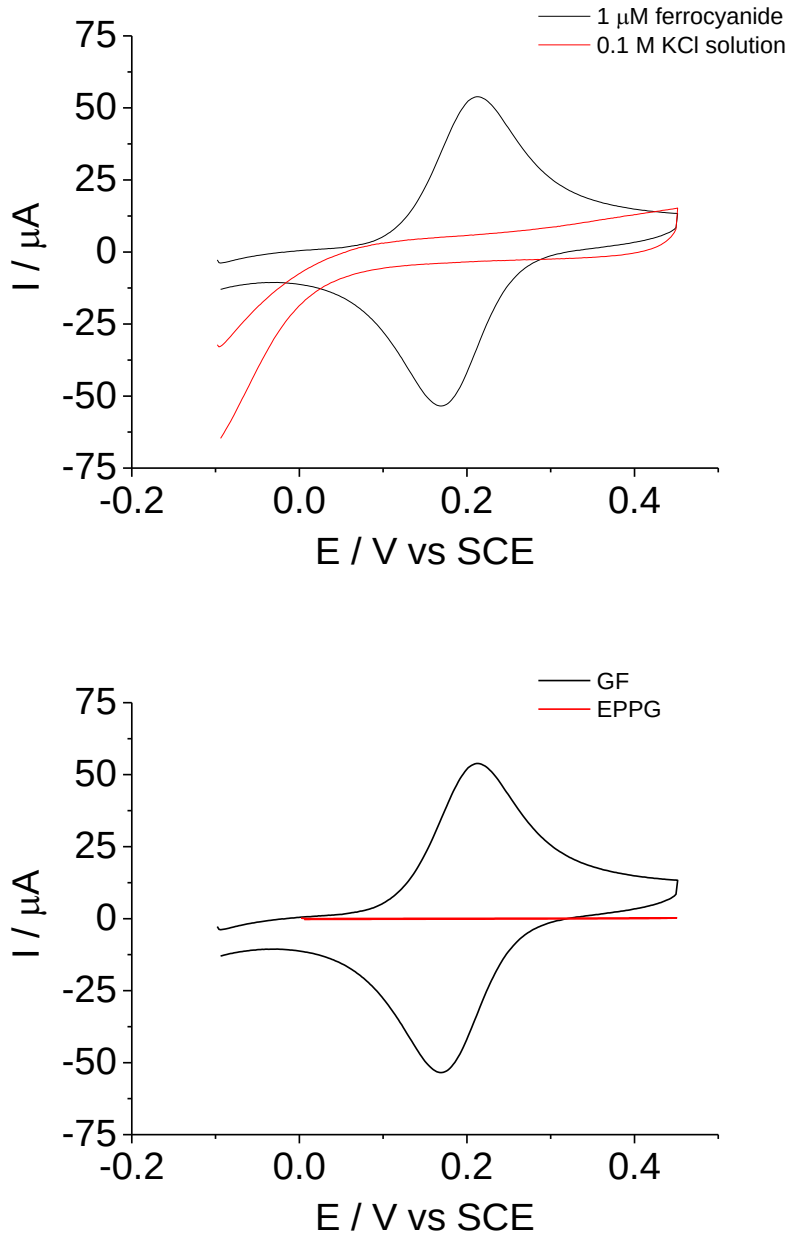

Figure 5.24: Cyclic voltammograms of a) an EPPG electrode and b) a GF electrode, in 1.0 μM ferrocyanide in 0.1 M KCl solution and with the background electrolyte control of 0.1 M KCl, and c) the overlaid cyclic voltammograms of both the EPPG and GF in in 1.0 μM ferrocyanide in 0.1 M KCl solution. All cyclic voltammograms measured at 50 mV s^{-1}.

Figure 5.24 c) show again a comparison between a planar EPPG electrode and a graphitic felt electrode in a 1 μM ferrocyanide solution in 0.1 M KCl background electrolyte. Much like in the previous example for non-aqueous electrochemistry (Figure 5.20), the EPPG electrode has barely visible redox peaks,

whereas the GF has comparatively well-defined peaks and a much flatter baseline. As with the previous non-aqueous example, the graphitic felt is able to give distinct redox peaks across a wide range of concentrations. Figure 5.25 a) displays the voltammograms for a GF in 100 nM ferrocyanide solution, while Figure 5.25 b) shows that the GFs can still be effective at nanomolar concentrations in aqueous solutions.

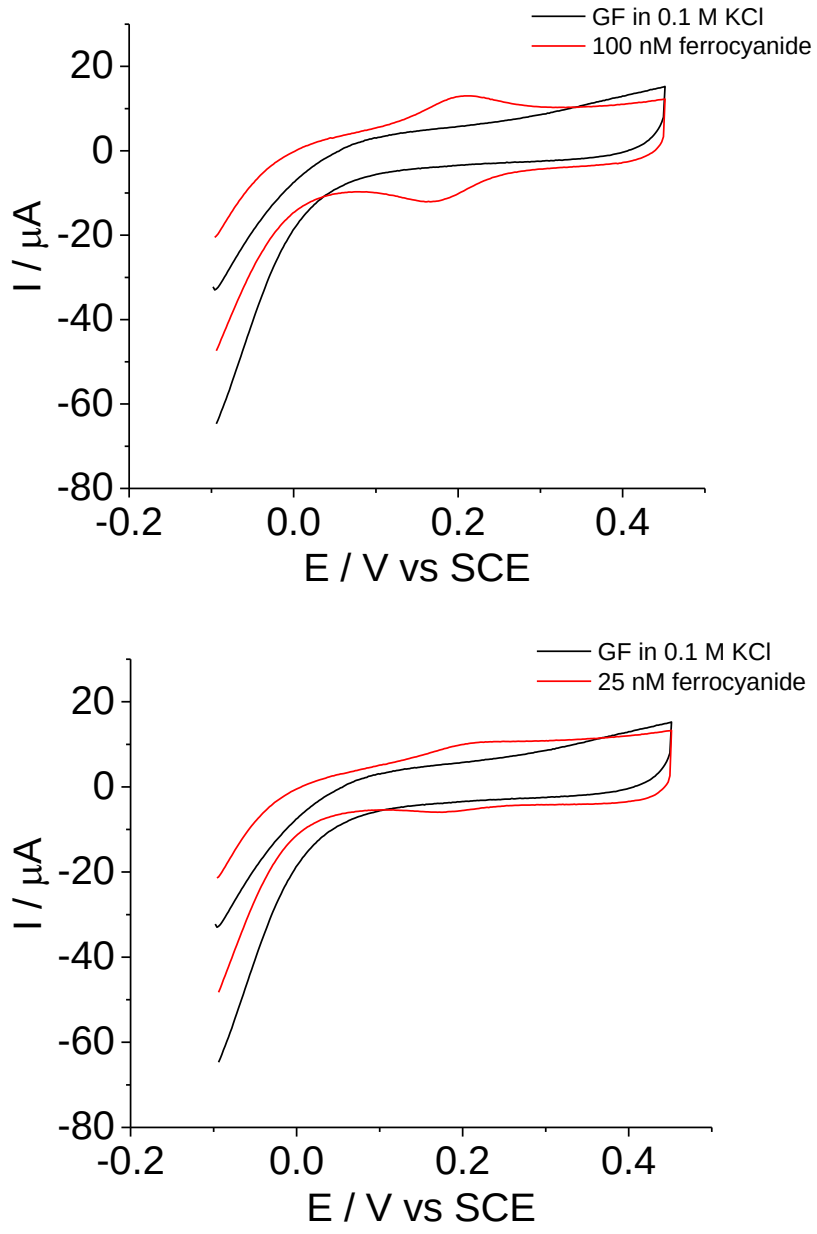

Figure 5.25: Cyclic voltammograms of a GF in a) 100 nM and b) 25 nM ferrocyanide in 0.1 M KCl solution, versus the GF in 0.1 M KCl background electrolyte solution. All cyclic voltammograms measured at 50 mV s^{-1}.

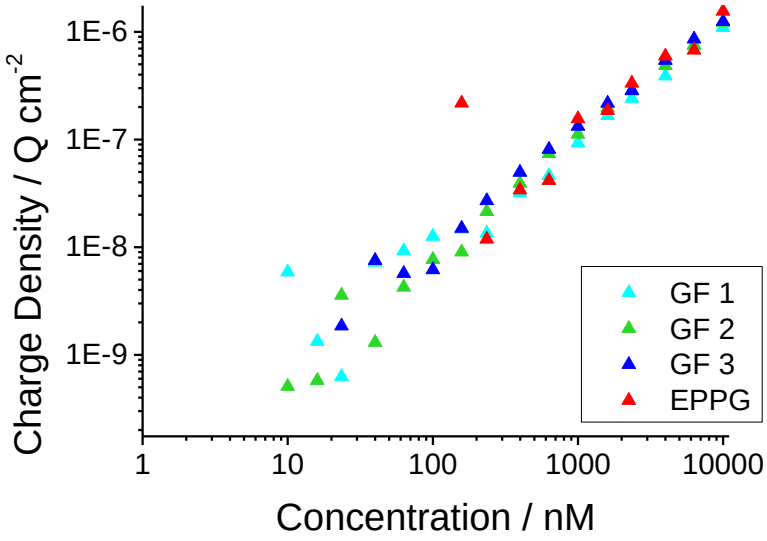

Figure 5.26: Charge density versus ferrocyanide concentration for GFs electrodes and an EPPG electrode.

The corresponding charge density / concentration relationship shown in Figure 5.26 suggests the GFs results become quantitatively unreliable just below 100 nM. In the linear region of 60 nM to 10 µM we do see a good degree of repeatability between the GF electrodes. Comparatively the EPPG electrode performed better for the aqueous system than in the non-aqueous, ferrocene system. In this aqueous system the EPPG maintains a linear relationship down to around 400 nM ferrocyanide in contrast to 3 µM for ferrocene. The GF LoQ is largely unchanged in the non-aqueous system. Following the charge/concentration profile Figure 5.26 the linear relationship breaks down below 100 nM, between 60 and 80 nM. When compared to the 60 nM ferrocene LoQ found previously this suggests the GFs ability to detect small concentrations is not severely affected by solution solvent. The LoD for the GFs in aqueous ferrocyanide solutions must again be very low, an analyte signal was detected as low as 10 nM, suggesting it is possible to detect a signal at a concentration below this. The 3σ statistical analysis returns a LoD of 68 nM and the 10σ analysis, a LoQ of 0.2 µM, both of which compare well to the non-aqueous system.

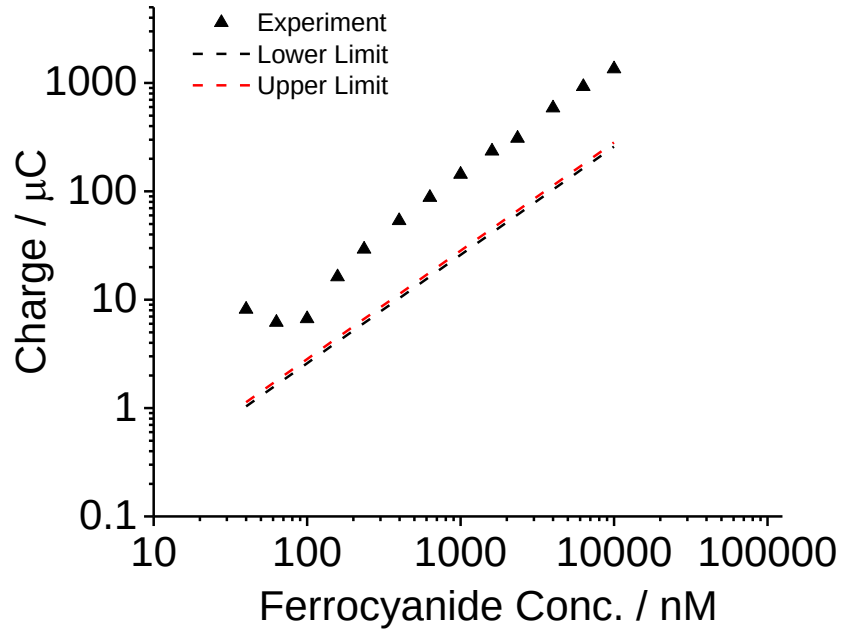

Figure 5.27: Charge density versus ferrocene concentration for a GF electrode. Also shown at the theoretical upper and lower charge limits.

As with the non-aqueous system, the charge passed by the GF at each ferrocyanide concentration was determined by integration and then plotted alongside the theoretical upper and lower limits of expected charge in Figure 5.27. Unlike the non-aqueous system however, the resulting charge measure from the ferrocyanide system is higher than the theoretical value predicted. Although a definitive cause was not discovered during the course of this work, this result could relate to interactions between the aqueous system and the platinum wire used as part of the experimental set-up. To discover the exact reason of this unexpected charge would be part of the further work to be conducted in this area. Despite this the LoQ and concentration detection afforded by these electrodes, considering the relaxed experimental setup and financial cost of the felt electrode, is impressive.

5.6. Conclusions

The experimental method outlined in this study allows GF electrodes to be used in quiescent electrochemical experiments yielding well-defined voltammetric peak signals. When the resulting

experimental voltammograms are combined with simulations, several key properties of the GF can be determined. These include the electrochemical surface area, the average pore size and the k° values for a range of redox systems. Capacitance measurements reveal the chemical nature of the carbon surface. To fully exploit the electroanalytical applications of the GF electrodes, a more robust simulation method is required. This will involve generating a 1D model based on radial coordinates rather than the Cartesian coordinates used in the current software and modelling the GF electrode as an ensemble.

In the two classical redox systems presented, the GFs have shown a remarkable ability to detect low concentrations of analyte in different solvent systems. It has also been shown that comparatively, they are able to detect concentrations 10 – 100 times lower than those of a carbon planar disc electrode. Given the low cost and their disposable nature, the results presented in this chapter justify further work to develop this promising electrode material for use in electrochemical sensors. A popular area of research is the detection of ascorbic and uric acid samples, both as individual samples and in solution together. This would provide an excellent opportunity to investigate the electrochemical resolution of the GFs. Another area of investigation would be to look at an array of voltammetric methods, other than cyclic voltammetry. With methods such as pulse or square wave voltammetry, both the limits of quantification and detection may further be reduced.

5.7. References

[1] U.T. Austin, A.Z. Weber, M.M. Mench, J.P. Meyers, P.N. Ross, J.T. Gostick, Q. Liu, Redox Flow Batteries, a Review, Journal of Applied Electrochemistry 41(LBNL-5442E) (2011).
[2] P. Zhao, H. Zhang, H. Zhou, B. Yi, Nickel foam and carbon felt applications for sodium polysulfide/bromine redox flow battery electrodes, Electrochimica Acta 51(6) (2005) 1091-1098.
[3] T. Wu, K. Huang, S. Liu, S. Zhuang, D. Fang, S. Li, D. Lu, A. Su, Hydrothermal ammoniated treatment of PAN-graphite felt for vanadium redox flow battery, Journal of solid state electrochemistry 16(2) (2012) 579-585.
[4] A. Shah, M. Watt-Smith, F. Walsh, A dynamic performance model for redox-flow batteries involving soluble species, Electrochimica Acta 53(27) (2008) 8087-8100.

[5] A. Di Blasi, O. Di Blasi, N. Briguglio, A. Aricò, D. Sebastián, M. Lázaro, G. Monforte, V. Antonucci, Investigation of several graphite-based electrodes for vanadium redox flow cell, Journal of Power Sources 227 (2013) 15-23.

[6] M.H. Chakrabarti, N.P. Brandon, S.A. Hajimolana, E. Tariq, V. Yufit, M.A. Hashim, M.A. Hussain, C.T.J. Low, P.V. Aravind, Application of carbon materials in redox flow batteries, Journal of Power Sources 253 (2014) 150-166.

[7] N. Vatistas, P. Marconi, M. Bartolozzi, Mass-transfer study of the carbon felt electrode, Electrochimica acta 36(2) (1991) 339-343.

[8] D. You, H. Zhang, J. Chen, A simple model for the vanadium redox battery, Electrochimica Acta 54(27) (2009) 6827-6836.

[9] Q. Xu, T. Zhao, Determination of the mass-transport properties of vanadium ions through the porous electrodes of vanadium redox flow batteries, Physical Chemistry Chemical Physics 15(26) (2013) 10841-10848.

[10] W. Wang, X. Wang, Investigation of Ir-modified carbon felt as the positive electrode of an all-vanadium redox flow battery, Electrochimica Acta 52(24) (2007) 6755-6762.

[11] X.-g. Li, K.-l. Huang, S.-Q. Liu, T. Ning, L.-q. Chen, Characteristics of graphite felt electrode electrochemically oxidized for vanadium redox battery application, Transactions of Nonferrous Metals Society of China 17(1) (2007) 195-199.

[12] W. Zhang, J. Xi, Z. Li, H. Zhou, L. Liu, Z. Wu, X. Qiu, Electrochemical activation of graphite felt electrode for VO 2+/VO 2+ redox couple application, Electrochimica Acta 89 (2013) 429-435.

[13] D.A. Brownson, L.C. Figueiredo-Filho, X. Ji, M. Gómez-Mingot, J. Iniesta, O. Fatibello-Filho, D.K. Kampouris, C.E. Banks, Freestanding three-dimensional graphene foam gives rise to beneficial electrochemical signatures within non-aqueous media, Journal of Materials Chemistry A 1(19) (2013) 5962-5972.

[14] B. Delanghe, S. Tellier, M. Astruc, Mass transfer to a carbon or graphite felt electrode, Electrochimica Acta 35(9) (1990) 1369-1376.

[15] K. Kinoshita, S. Leach, Mass-Transfer Study of Carbon Felt, Flow-Through Electrode, Journal of The Electrochemical Society 129(9) (1982) 1993-1997.

[16] N. Parikh, J. Allen, R. Yassar, Microstructure of gas diffusion layers for PEM fuel cells, Fuel Cells 12(3) (2012) 382-390.

[17] C. Amatore, J.M. Savéant, D. Tessier, Charge transfer at partially blocked surfaces: A model for the case of microscopic active and inactive sites, Journal of electroanalytical chemistry and interfacial electrochemistry 147(1-2) (1983) 39-51.

[18] M. Rudolph, D.P. Reddy, S.W. Feldberg, A simulator for cyclic voltammetric responses, Analytical chemistry 66(10) (1994) 589A-600A.
[19] A. Bard, L. Faulkner, Electrochemical Methods: Fundamentals and applications, 2nd ed., Wiley, New York, (2000).
[20] T.J. Davies, R.G. Compton, The cyclic and linear sweep voltammetry of regular and random arrays of microdisc electrodes: Theory, Journal of Electroanalytical Chemistry 585(1) (2005) 63-82.
[21] T.J. Davies, S. Ward-Jones, C.E. Banks, J. del Campo, R. Mas, F.X. Munoz, R.G. Compton, The cyclic and linear sweep voltammetry of regular arrays of microdisc electrodes: fitting of experimental data, Journal of Electroanalytical Chemistry 585(1) (2005) 51-62.
[22] B.A. Brookes, T.J. Davies, A.C. Fisher, R.G. Evans, S.J. Wilkins, K. Yunus, J.D. Wadhawan, R.G. Compton, Computational and experimental study of the cyclic voltammetry response of partially blocked electrodes. Part 1. Nonoverlapping, uniformly distributed blocking systems, The Journal of Physical Chemistry B 107(7) (2003) 1616-1627.
[23] T.J. Davies, B.A. Brookes, A.C. Fisher, K. Yunus, S.J. Wilkins, P.R. Greene, J.D. Wadhawan, R.G. Compton, A computational and experimental study of the cyclic voltammetry response of partially blocked electrodes. Part II: Randomly distributed and overlapping blocking systems, The Journal of Physical Chemistry B 107(26) (2003) 6431-6444.
[24] R.L. McCreery, Carbon Electrodes: Structural Effects on Electron Transfer Kinetics, in: A.J. Bard (Ed.), Electroanalytical Chemistry: A Series of Advances, CRC Press (1990).
[25] A. Baars, M. Sluytersrehbach, J.H. Sluyters, Application of the dropping mercury microelectrode (DM-MU-E) in electrode-kinetics and electroanalysis, Journal of Electroanalytical Chemistry 364(1-2) (1994) 189-197.
[26] N.J. Freeman, R. Sultana, N. Reza, H. Woodvine, J.G. Terry, A.J. Walton, C.L. Brady, I. Schmueser, A.R. Mount, Comparison of the performance of an array of nanoband electrodes with a macro electrode with similar overall area, Physical Chemistry Chemical Physics 15(21) (2013) 8112-8118.
[27] M.C. Henstridge, R.G. Compton, Mass Transport to micro- and nanoelectrodes and their arrays: a review, Chemical Record 12(1) (2012) 63-71.
[28] K. Dawson, A. Wahl, R. Murphy, A. O'Riordan, Electroanalysis at Single Gold Nanowire Electrodes, Journal of Physical Chemistry C 116(27) (2012) 14665-14673.
[29] R.E.G. Smith, T.J. Davies, N.D. Baynes, R.J. Nichols, The electrochemical characterisation of graphite felts, Journal of Electroanalytical Chemistry 747 (2015) 29-38.
[30] Nomenclature, symbols, units and their usage in spectrochemical analysis—II. data interpretation Analytical chemistry division, Spectrochimica Acta Part B: Atomic Spectroscopy 33(6) (1978) 241-245.

[31] J. Mocak, A.M. Bond, S. Mitchell, G. Scollary, A statistical overview of standard (IUPAC and ACS) and new procedures for determining the limits of detection and quantification: Application to voltammetric and stripping techniques (technical report), Pure and Applied Chemistry 69(2) (1997) 297-328.

Chapter 6:

Investigation into the Electrochemical Modification of Carbon Surfaces via an Aryl Radical Mechanism.

Contents

6.1 Introduction:

Carbon materials are employed in numerous application, from mechanical components to biomedical devices, neutron moderators in nuclear engineering, to electrochemical electrodes and charge transfer devices. In many cases, the properties of the carbon surface, are key to its effective use. By having the ability to control the surface of a material, we are better able to fit that material to a specific requirement. It has been shown that for catalysing oxidation reactions, the presence of nitrogen containing surface groups are crucial to the carbons activity, and for electrocatalysis, oxygen groups on the carbon surface are essential [1]. Two of the most important reactions within a PEFC fuel cell, the oxidation of $H_{2(g)}$ and the $O_{2(g)}$ reduction reaction are heavily reliant on the surface of the electrode (often platinum on a carbon support). The electronic properties of a carbon surface can also be modified by the addition of chemisorbed or physisorbed molecules with electron acceptor or donor groups [2-4]. The ability to adapt the carbon surface to such a vast array of applications has created significant academic and commercial interest in advancing existing functionalisation techniques and developing new ones. The electrochemical attachment of an organic molecule to a conductive material, such as carbon, is often called electrografting. The aim of this chapter was to investigate the modification of surfaces, of both graphitic felt (GF) and gold, by the electrografting of diazonium molecules to the surface. Finding a reliable method of altering the surface layer of the GF would allow the 'tuning' of the surface, by altering the surface molecule, to the particular goal of improving the carbon-POM interaction in the advanced CRRC fuel cells. It could also open up new possibilities for the use of GF's in sensing applications.

6.2 Results and Discussion

6.2.1 Modification of glassy carbon electrode

Initially modification work was carried out on a glassy carbon electrode using the 4-nitroanaline solution to produce a 4-nitrophenyl surface layer. This was carried out as described in chapter 4, with a 3-electrode configuration using a saturated calomel reference electrode (SCE) and a platinum mesh

counter electrode alongside the glassy carbon (GC) working electrode. The surface layer was grafted using the potentiostatic technique at 0.7 V for 10 minutes in the grafting solution. 10 mM ferricyanide in 1 M KCl (pH 5.5) was used as a redox probe to determine how successful the grafting had been. The 4-nitrophenyl modified electrode was placed in the ferricyanide solution and cycled between -0.2 V and 0.6 V across a range of scan rates.

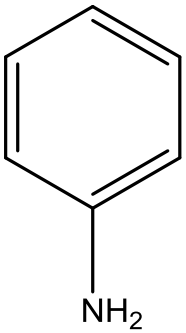

Figure 6.1: Structure of 4-nitroanaline molecule.

It is clear from Figure 6.2 that the surface is effectively passivated by the 4-nitrophenyl surface layer [5]. Whilst only the 10 mVs^{-1} scan rate is shown, the effect is similar across the scan rates used up to 1 V/s. Using the simulation method described in chapter 5 to discern the electron transfer rate constant, k^o = 0.0035 cm s^{-1} for the unmodified GC electrode, which is in agreement with previous work [6]. The lack of discernible peaks prevented the value of k^o for the modified.

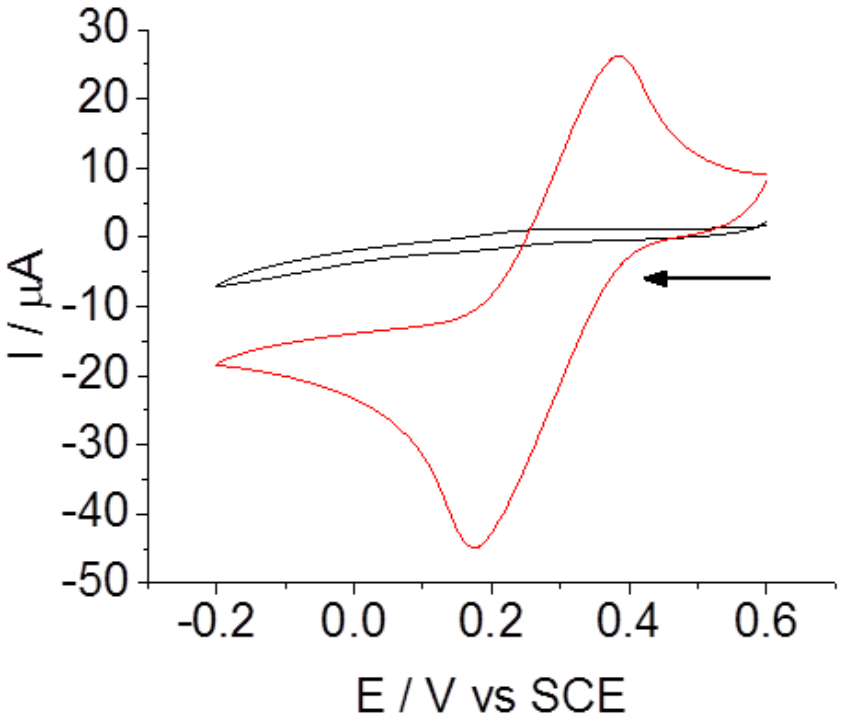

Figure 6.2: Voltammograms of Glassy Carbon electrode with (black) and without (red) a nitrobenzene surface layer in 10 mM ferricyanide, 1 M KCl at 10 mV s^{-1}.

6.2.2 Electrodes; Glassy Carbon versus Edge Plane Pyrolytic Graphite

The structure of glassy carbon (GC) contains a mixture of both edge and basal plane in the form of interconnected graphite ribbons [7]. In comparison edge plane graphite contains (EPPG) sheets of graphite orientated with the graphite's edge plane at the electrodes surface. Whilst the edge plane electrode is less representative of the carbon electrodes used in the fuel cell, due to the relatively small amount of basal plane graphite, it is widely believed to more active, giving a better cyclic voltammogram signal compared to than GC, as shown in chapter 3. To compare, both electrodes were polished and cleaned before being used to measure the CV of 10 mM ferricyanide solution. Figure 6.3 shows the edge plane electrode has a peak to peak separation of 57 mV rather than the GC separation of 85 mV. This suggests the solution is electrochemically reversible on the EPPG, displaying faster kinetics k^{o}= 0.004 cm s^{-1} (determined by the simulation method used in Chapter 5) than on the GC,

where the ferrocyanide is only quasi-reversible. For these reasons the edge plane electrode is used as the main electrode in the rest of this chapter [8].

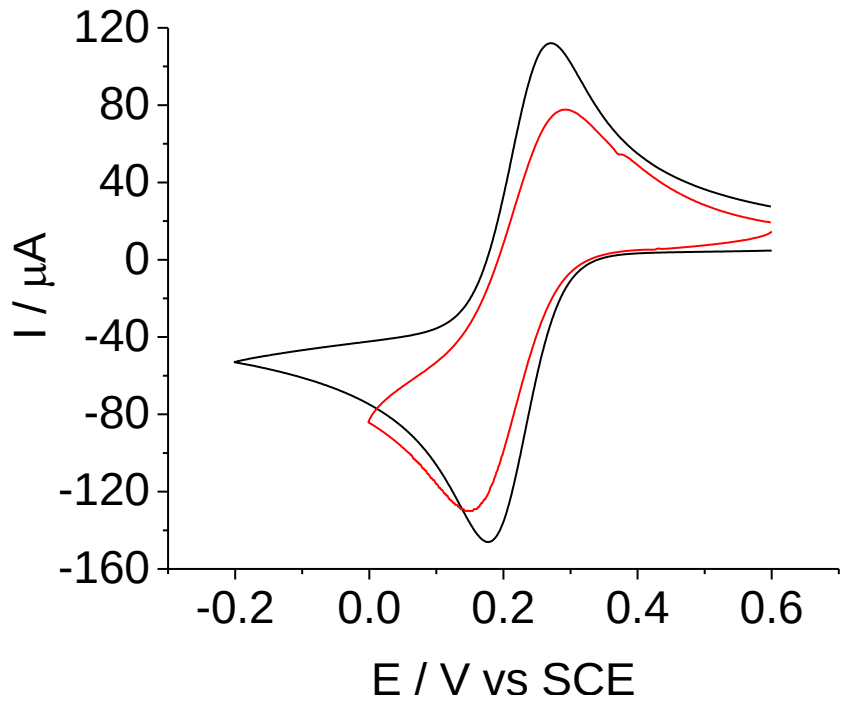

Figure 6.3: Comparison of the second scans of Glassy Carbon (red) and Edge Plane Pyrolytic Graphite (black) electrodes in 10 mM ferricyanide solution at 10 mV s^{-1}.

6.2.3 V1 Polyoxometalate

After using the ferricyanide solution to determine the baseline for both the clean carbon electrodes and the electrodes post-grafting, a similar set of experiments were run using V1 POM electrolyte. After polishing and cleaning, the EPPG electrode was placed in a cell containing 0.3 M V1 POM (pH 0) and cycled between 0.9 – 0.1 V at a range of scan rates. Figure 6.4 shows the cyclic voltammogram of this experiment. The initial redox peaks at approximately 0.5 V relates to the reduction/oxidation of vanadium in the Keggin, whereas the peaks around 0.2 V are due to the reduction/oxidation of molybdenum in the Keggin [9]. For the simulation of k^o, only the initial pair of peaks relating to the redox of the vanadium are used. After achieving CVs for the naked/unmodified EPPG electrode (Figure 6.4), experiments then examined the effect of deposition potential and time on layer

thickness. For the V1 POM shown in figure 6.4 k^{o}= 6.0 x 10^{-3} cm s^{-1} was determined, with a diffusion coefficient of 3.2 x 10^{-6} cm^2 s^{-1}.

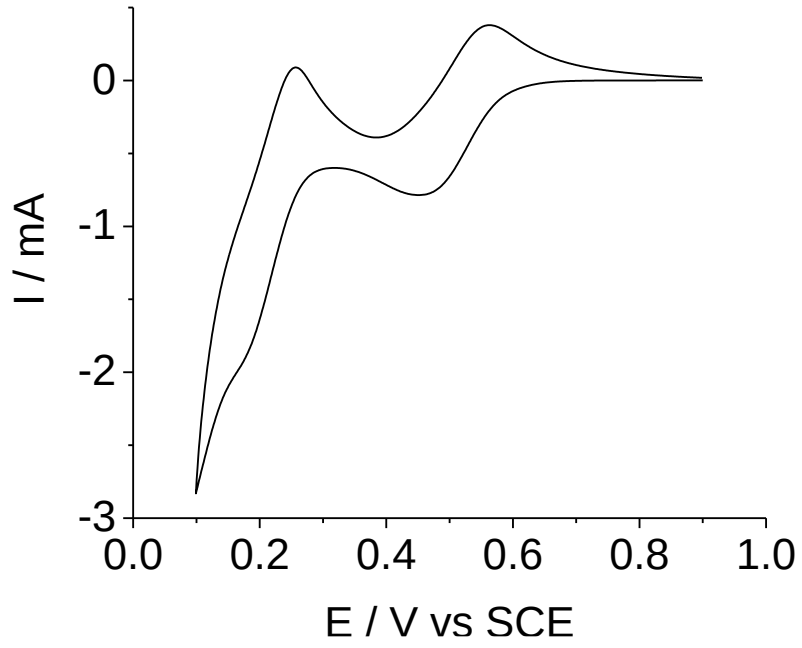

Figure 6.4: Voltammogram of clean EPPG electrode in 0.3M V1 POM at 10mVs^{-1} (no solution resistance compensation).

6.2.4 Positive Grafting Potentials

Literature indicated that a positive grafting potential, specifically 0.3 V, would be the optimum potential for grafting of 4-aminophenyl on carbon surfaces [10]. To investigate this, the previous setup for grafting was used and a range of positive potentials trialled. After grafting at a range of potentials for 600 s, the modified electrode was rinsed and transferred to a solution of 0.3 M V1 POM and cycled between 0.9 V and 0.1 V. There is a clear decrease in current between grafting at 0.5 V and 0.3 V as seen in Figure 6.5, whereas k^{o} changes from the 6.0 x 10^{-3} cm s^{-1} for the clean electrode to 5.5 x 10^{-3} cm s^{-1} for both the 0.7 V and 0.5 V grafting potentials, suggesting that the surface has been affected, although the lack of significant signal blocking would suggest very little, if any of the diazonium salt

grafted to the surface. For the other lower potentials, the lack of peak definition prevented k^o from being determined

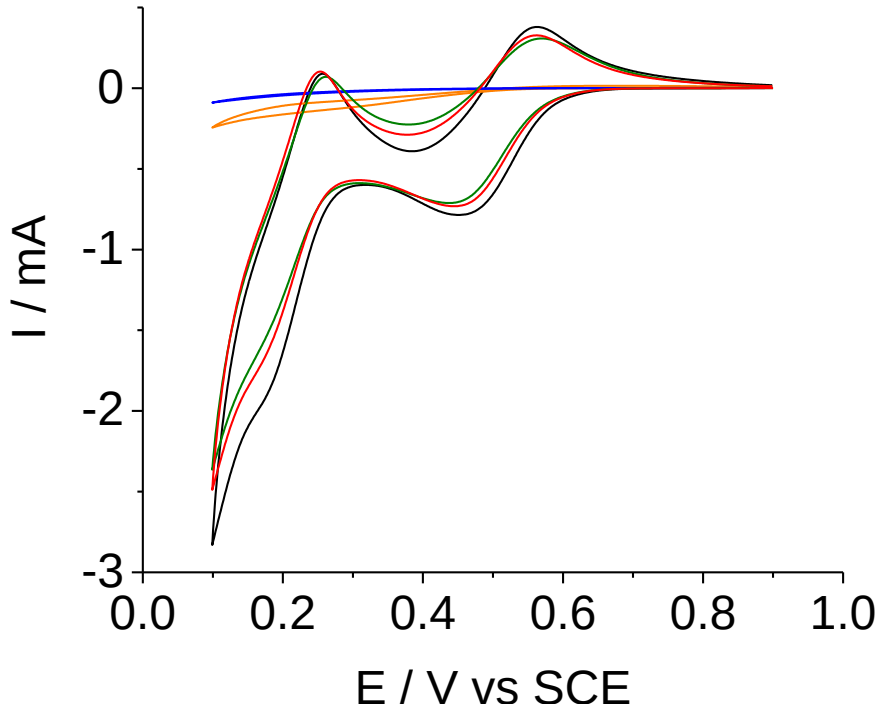

Figure 6.5: Comparison of positive grafting potentials against a clean EPPG electrode in 0.3 M V1 POM at 10 mV s^{-1}. Clean electrode (black) versus NB grafting at potentials of: 0.1 V (blue), 0.3 V (orange), 0.5 V (green) and 0.7 V (red).

However, when these results are compared to more negative grafting potentials produced using the same procedure but at grafting potentials of 0.1 V, -0.1 V and -0.3 V (Figure 6.6), it can be seen that thicker multilayers are formed at negative potentials, as indicated by the decreased amount of current. This is consistent with the proposed grafting mechanism; i.e. lower grafting potentials lead to an increased rate of diazonium reduction producing more phenyl radicals.

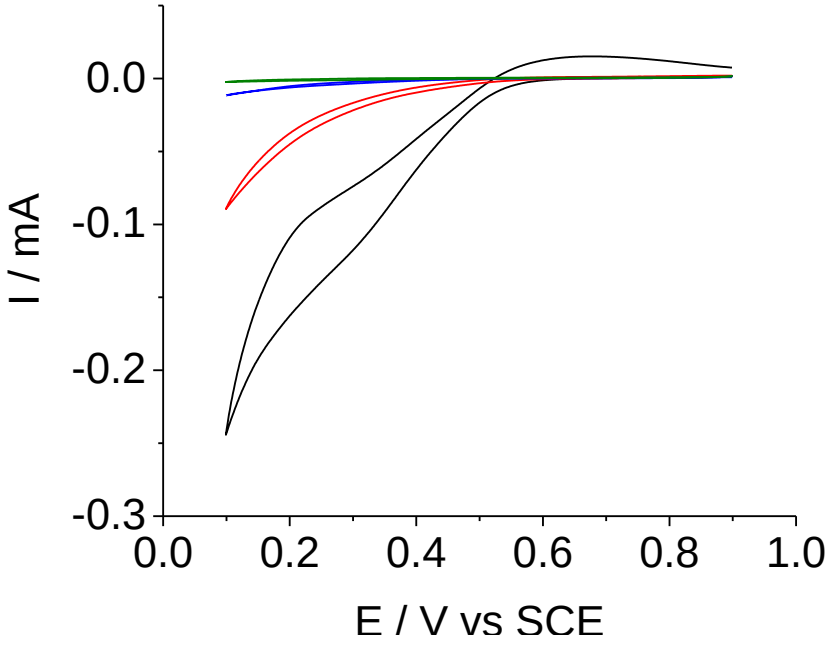

Figure 6.6: Comparison of potential of grafting potentials on an EPPG electrode in 0.3 M V1 POM at 10 mVs^{-1}. Potentials of 0.1 V (red), 0.3 V (black), -0.1 V (blue) and -0.3 V (green).

6.2.5 Grafting Time

The next experiments examined how time played a factor in the type of layer formed. The grafting of the electrode was carried out using the potentiostatic grafting method as described previously, whilst varying the time held at -0.3 V. A dip coated electrode was also tested as a baseline measurement; this involved the electrode sitting in the grafting solution for 10 minutes before being transferred to the V1 POM solution and measured.

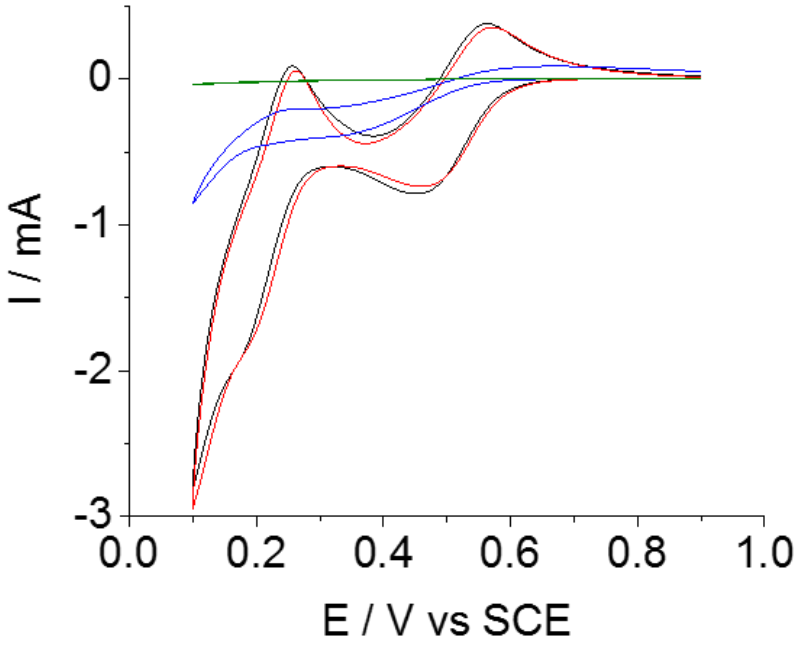

Figure 6.7: Comparison of effect of grafting time at -0.3 V, in 0.3 M V1 POM at 10 mVs^{-1}. Bare electrode (black), dip coated (red), 60 s (blue) and 300 s (green).

Figure 6.7 shows the expected result that a shorter grafting time results in a thinner or patchy surface layer allowing higher current to pass, including no reduction in current when using a dip coat. For the dip coated measurement, k^o = 6.2 x 10^{-3} cm s^{-1}, with an almost overlapping curve when compared to the bare electrode. Overall, it is clear that the potentiostatic method of grafting, even over very short time periods is producing a significant surface multilayer coverage, but significantly reducing current. An alternate approach was applied to attempt to gain greater control on the deposition of the diazonium where the deposition potential is not static, but cycled.

6.2.6 Cyclic Grafting

Using the same experimental setup as that of the potentiostatic method, the clean EPPG electrode was instead cycled between 0 V and -0.7 V over several scans, as seen in Figure 6.8. On the initial scan, there is clearly significant deposition from -0.4 V, which causes a reduction in current over subsequent

scans as the surface layer becomes thicker. This method suggests that a significant surface layer can be formed with only a single scan.

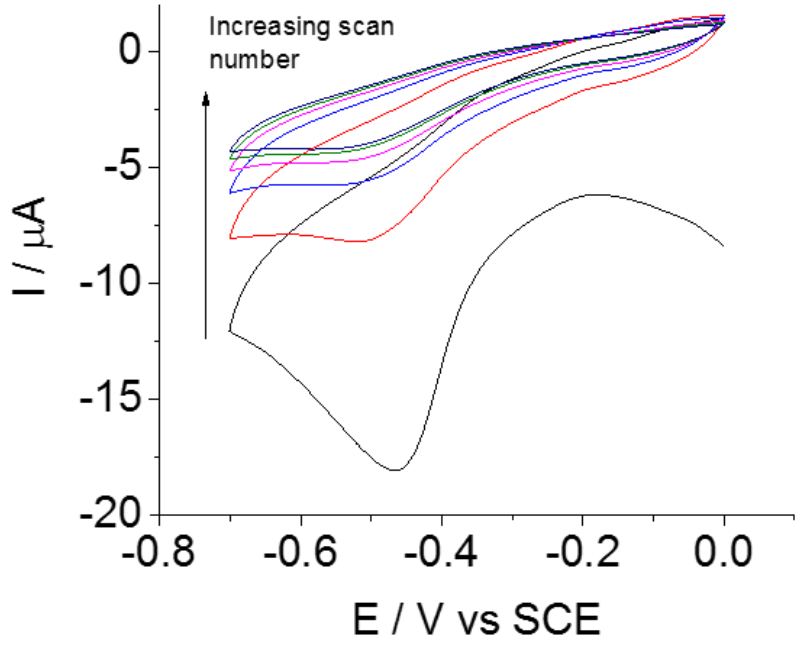

Figure 6.8: Cyclic grafting of 5 mM nitrobenzene on a bare EPPG electrode, scans 1-6 at 10 mV s^{-1}.

This technique is further preferable to the potentiostatic technique, as by determining the area under the curve, the charge and the surface coverage can be found. Note this makes two important assumptions, firstly that every electron passed reduces a diazonium salt to form the radical site, and secondly that every phenyl radical produced from the diazonium salt reduction attaches to the electrode-multilayer surface. These are difficult assumptions to make as dimerization of the radical diazonium is a very possible outcome.

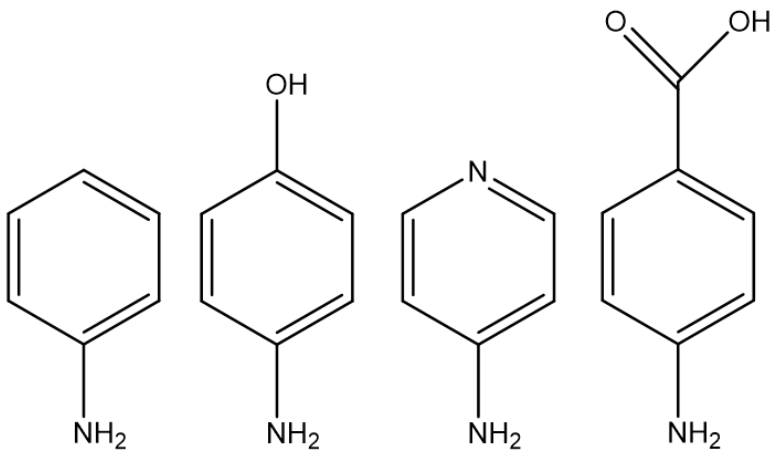

Figure 6.9: Structures of, from left to right; 4-nitroanaline, 4-aminophenol, 4-aminopyridine and 4-aminobenzoic acid.

This technique was applied to the original nitrobenzene (NB) diazonium salt, as well as 3 further salts; 4-aminobenzoic acid (ABA), 4-aminophenol (AP) and aminopyridine (APy), as shown in Figure 6.9. For each of these compounds it is important to determine the amount of reacted diazonium for each scan to determine the degree of reactivity of each structure. By integrating the area under both the forward and backward scan and multiplying the result by the scan rate the charge (Q) passed can be evaluated. Using the equation below it is then possible to find the number of moles of reacted diazonium, assuming that each electron passed reduces the diazonium by one electron.

$$mol = \frac{Q}{F} \qquad (6.1)$$

Where F is the Faraday constant. Literature cites a value of $\Gamma = 12.5 \times 10^{-10}$ mol cm^{-2} for the closest packing of 4-phenyl nitro groups on a carbon surface [11]. The 3 mm diameter electrodes have a surface area of 0.0707 cm^2, which would result in 8.84×10^{-11} mol of grafted diazonium to cover the surface, assuming that every diazonium radical attacks the surface. The results for the coverage as number of monolayers per scan are presented in Figure 6.10.

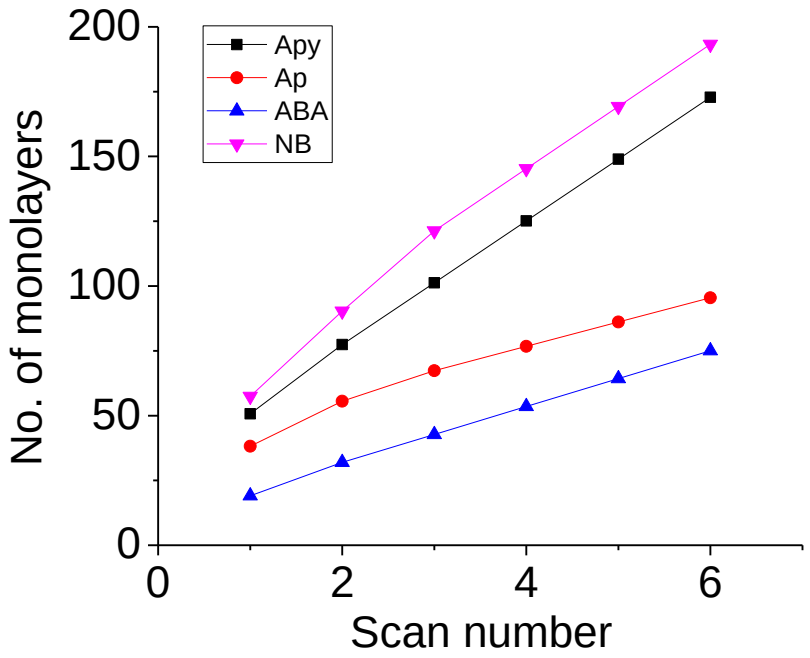

Figure 6.10: Comparison of surface layer thickness with increasing scan number of different diazonium surface graftings: ABA (blue), NB (green), AP (red) and APy (black).

In reality, it is unlikely that every diazonium radical attack will form a covalent bond to the electrode surface. A degree of the radicals will dimerize but not attach to the surface layer, contributing to charge passed but not surface coverage. Figure 6.10 shows that right from the initial scan enough charge has been passed to result in tens of multilayers forming. From the above Figure, it would appear that the nitrobenzene is able to react the greatest amount, most likely due to the complete lack of steric hindrance from preventing multilayer formation through radical attack at the 2 and 6 positions of the phenyl ring. Whilst dimerization will be ever present, it is interesting to note that while each subsequent scan sees a reduction in charge, over the 6 scans charge is still able to flow. This could be explained in one of two ways; the surface attachment of diazonium is incomplete, leaving some of the electrode surface free to pass charge, or that the surface coverage is complete yet the conjugated nature of the phenyl ring leaves the surface layers somewhat conductive allowing for the reduction of diazonium to continue. It is clearly still difficult to control the grafting of the diazonium to the surface.

The difficulty in controlling the deposition of diazonium salt led to multilayer formation, and the preferred monolayer remained elusive. Following the work of Y. Leroux and P. Hapiot, protected diazonium salts are used to prepare a single monolayer on a carbon surface [12-14]. By including a bulky silyl terminal group on the diazonium, in theory multilayer formation should be sterically prevented. This technique should not only achieve a monolayer; it has the added convenience of further functionalisation. The silyl terminal group can be cleaved post-grafting to leave a highly active alkyne. This leads to a large number of possible terminal groups allowing the surface to be modified as desired. Following on from the characterisation of the graphitic felts in chapter 4 the functionalisation focusses on GFs, rather than planar disc electrodes. This chapter also discusses the effects of grafting protected diazonium salts onto GFs and the functionalisations possible post-grafting. The protected diazonium precursors used within this chapter were provided by Dr Ross Davidson (Durham University) as part of a collaborative project with the group of Professor Andrew Beeby (Durham University) to investigate the possibility of functionalising graphene using the diazonium grafting process presented within this chapter.

The initial investigation into the feasibility of a protected diazonium monolayer involved the molecule designated Protected Diazonium 1 (PD1) shown in Figure 6.11(Inset). The molecule was electrochemically grafted to the surface of the GF using the method described in chapter 4. Shown in Figure 6.11 is the cyclic voltammogram of the grafting of PD1. The reductive peak at -1.0 V is distinctive of the one electron reduction of the diazonium group, allowing radical attack of the carbon surface. The reaction is also irreversible, another factor in determining this as the diazonium reaction.

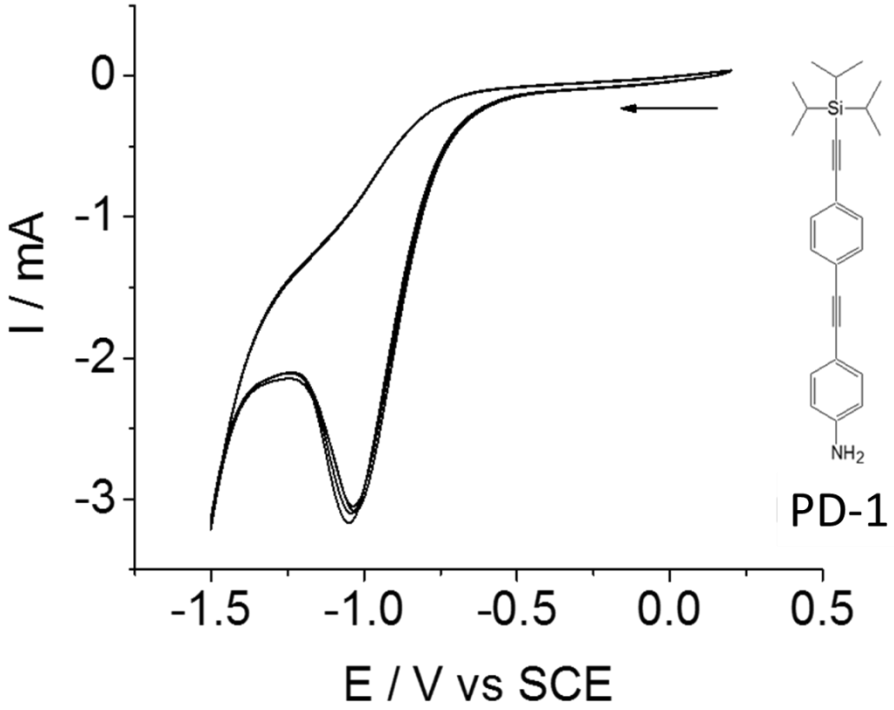

Figure 6.11: Cyclic voltammogram for the grafting of PD1 (molecular diagram inset) to a GF electrode. Scan at 30 mV s^{-1}, in a solution of 5 mM PD1, four sweeps are shown.

Whilst the current of successive scans does slowly decrease, it would be expected that a fully protected monolayer would prevent the majority of current flow. This leaves a few possible explanations as to why the current does not completely disappear in Figure 6.11. Firstly; that a complete monolayer has not yet been formed due to the length and bulk of the molecule. Deposition is slower due to the steric hindrance for molecules approaching the surface in the correct orientation. While there is a possibility of an incomplete surface coverage, the expectation would be that as the surface grafting began, the current of subsequent scans would be reduced by a blocking effect. The conjugated structure of PD1 leaves several sites on the aromatic rings open to attack by other free radical PD1 molecules. This could lead to the formation of multilayers, which may remain electrically conductive, again due to the conjugated nature of the molecules. This is turn would allow charge to continue to pass over several scans, generating a thicker surface layer. The most likely cause is a combination of multilayer formation and the dimerization of the molecule in solution. Due again to its length and highly conjugated structure, the molecule itself is a prime target for radical

attack. While the bulky silyl group offers a degree of protection from radical attack to the 2 and 6 positions of the first benzene ring, the length of the molecule from dual benzene rings leaves the 3 and 4 positions of the first benzene and 2 and 6 positions of the second ring, vulnerable. This would account for the large peak current. Figure 6.12 shows the cyclic voltammograms of an edge plane pyrolytic graphite (EPPG) planar disc electrode before and after the grafting of PD1, in a 1 mM ferrocyanide solution. Note that once the grafting has taken place, there is an almost complete drop in current suggesting a blocking surface layer has been deposited.

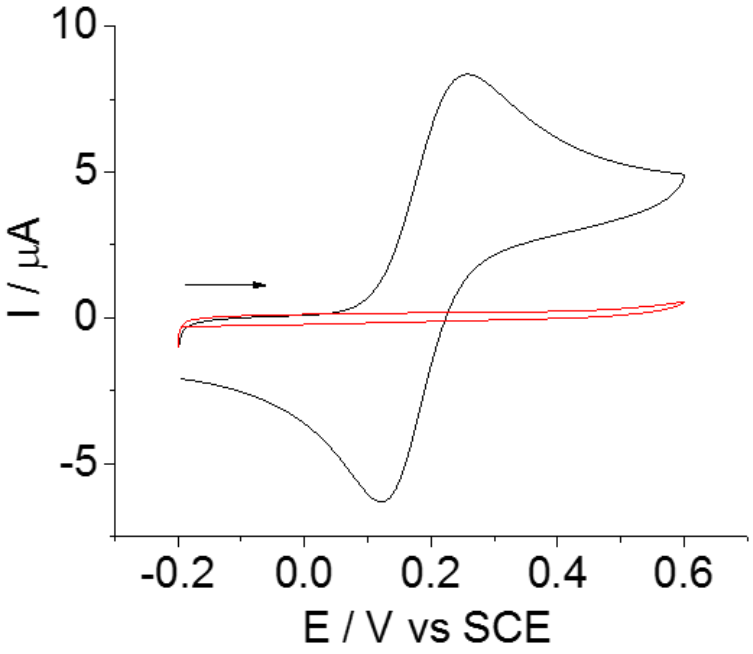

Figure 6.12: Cyclic voltammogram of a clean EPPG electrode (black) and a PD1 surface grafted EPPG electrode (red) in a 1 mM ferrocyanide in 0.1 M KCl solution at 50 mV s^{-1}.

One of the major difficulties faced when attaching organic groups to the GFs is producing evidence of the surface grafting and quantification of the layer thickness. The fibrous nature of the felts makes many forms of investigations (such as STM) difficult, as the strands of the fibre are not fixed but able to move. To determine whether or not the functionalisation had been successful, a different approach was taken. Following the cleaving of the protecting group using the method given in

Chapter 4, a thioacetate group was attached to the terminal alkyne to investigate the potential for functionalisation. The thioacetate modified Protected Diazonium is referred to as PD1-TA. This would allow the subsequent attachment of 20 nm gold nanoparticles, and allow SEM to judge the success of the technique. Not only do gold nanoparticles form bonds with thiol groups [15], literature also suggests they are able to attach to alkyne groups also [16]. This allows the comparison of each step in the grafting process.

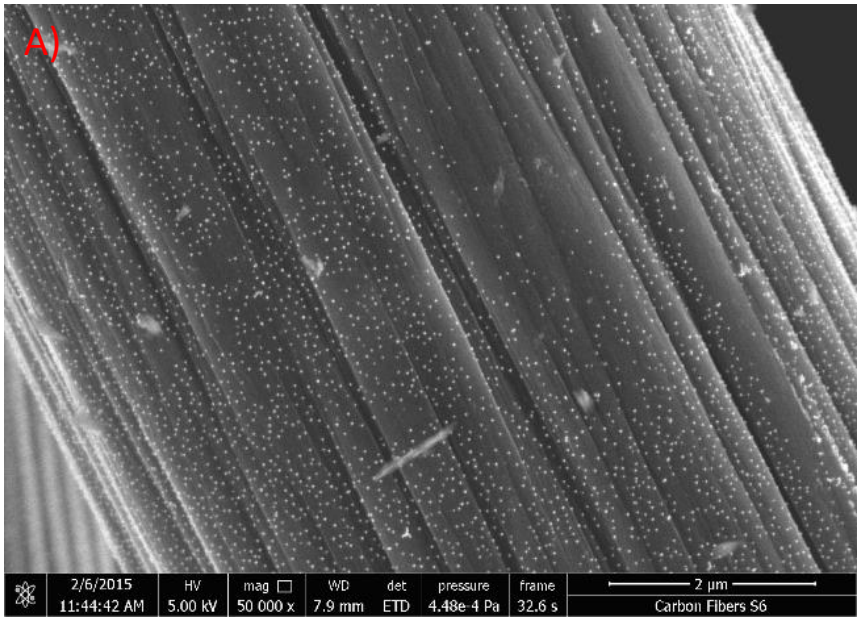

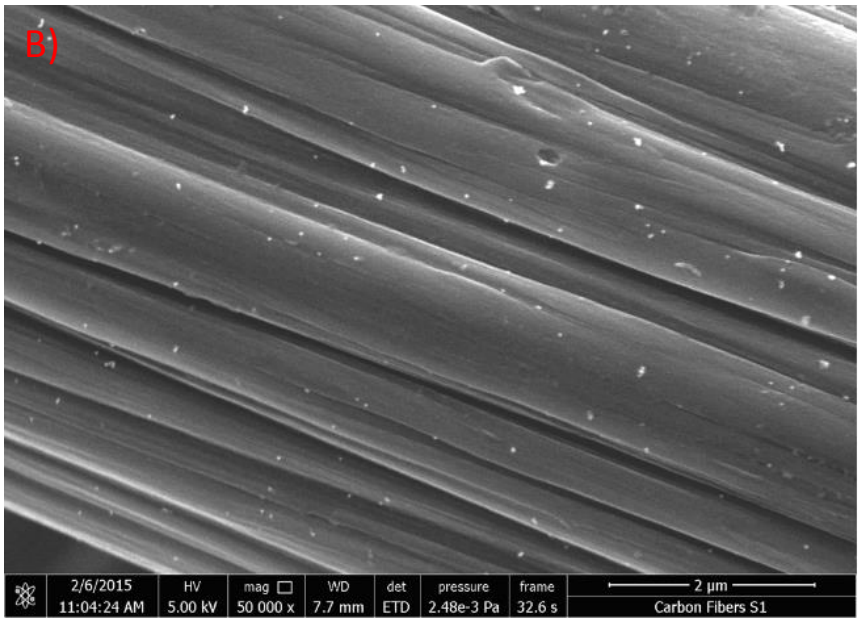

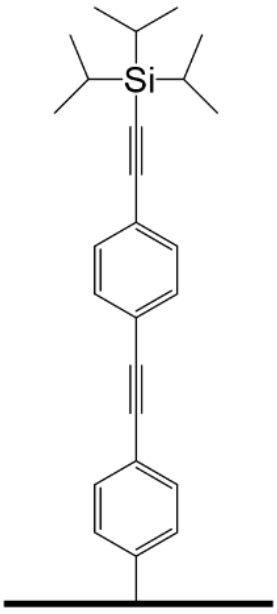

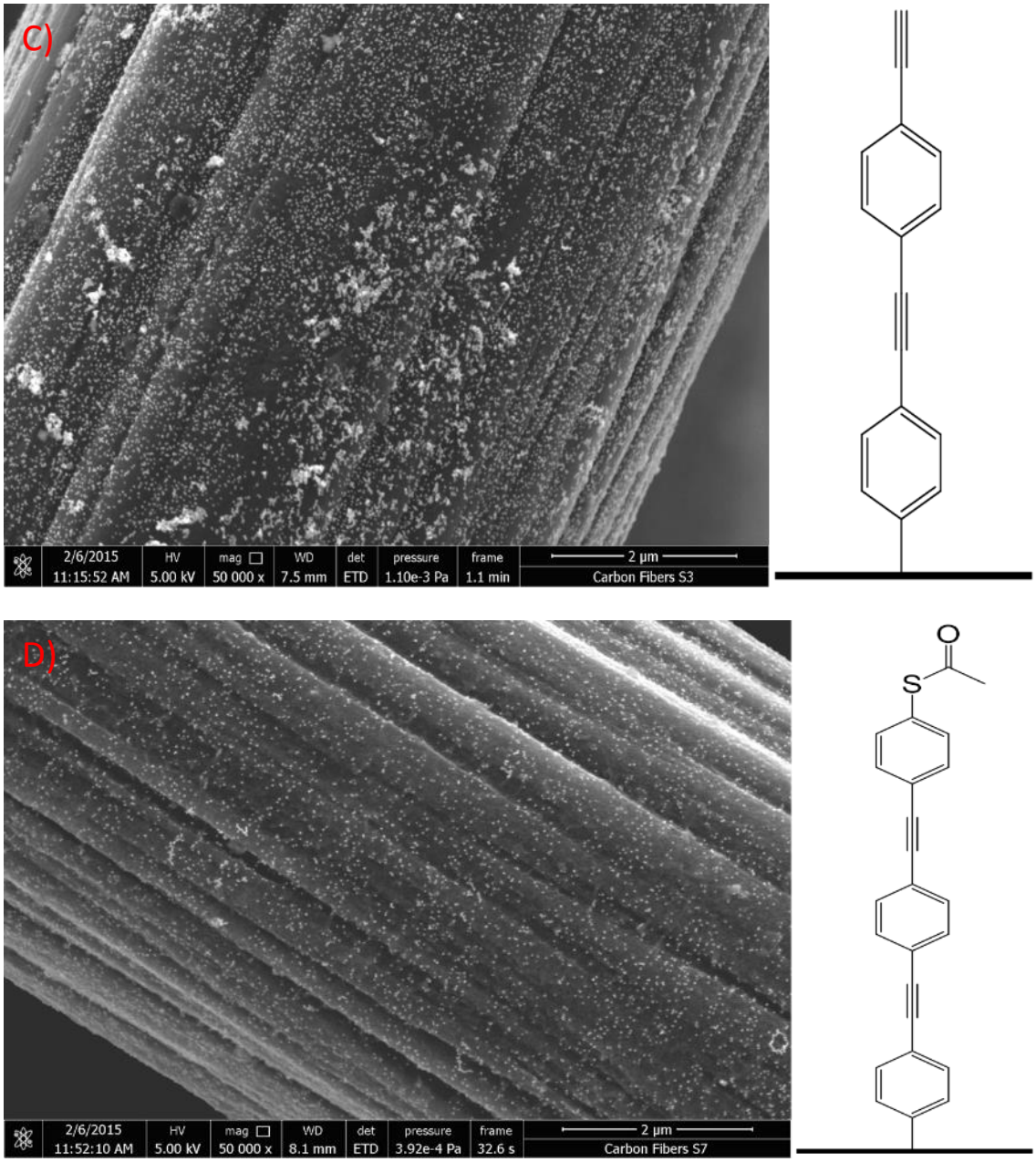

Figure 6.13: SEM images of GF surfaces a) clean, b) PD1 grafted surface, c) deprotected PD1 grafted surface and d) thioacetate modified PD1 grafted surface. Images taken after GFs have been immersed for 24 hours in 20 nm gold nanoparticle solution.

Figure 6.13 shows SEM images for GFs at different stages of functionalisation. A) shows a clean, unmodified felt, B) has had PD1 grafted to the surface, C) shows the felt after the silyl group has been cleaved to leave the terminal alkyne and for D) a thioacetate group has been added to the

alkyne using click chemistry (PD1-TA). Each of the 4 GFs spent 24 hours in a solution of 20 nM AuNPs (Sigma Aldrich), after which it was rinsed with ultra-pure water and left to dry at room temperature.

Where there is no prior functionalisation on the GF surface, as in Figure 6.13 A), the AuNPs have become attached to the carbon surface, likely through a range of physisorbed bonds to the wealth of carbon/oxygen groups across the surface. However, upon grafting PD1 to the GF and creating a multilayer, the AuNPs are unable to find appropriate sites to attach to, leading to the greatly reduced number of NPs visible in Figure 6.13 B).

Previous literature suggests that AuNPs find terminal alkynes to be a favourable site for adsorption [16]. This is clearly visible in Figure 6.13 C) where a significant increase of AuNPs decorating the surface of the GF. For Figure 6.13 D), two points can be noted; firstly there appears to be fewer AuNPs than on the alkyne image C), secondly that the GF itself has 'fuzzier' ridgelines, appearing less pristine than the previous samples. Both of these points can be explained by the process by which the thioacetate group is added to the monolayer. The chemistry involves stirring the GF in a harsh solution for several hours at 55 °C. The surface bound terminal alkynes, from the deprotected grafted layers, are highly active and liable to react with any nearby molecules, not just the thioacetate groups, reducing the amount of thioacetate attaching to the grafted layer. This in turn will lead to a reduced number of active binding sites for the AuNPs, resulting in fewer AuNPs visible in the SEM. Secondly, the conditions under which the functionalisation take place could be sufficient to roughen the GF surface. Although from the images it is unclear whether the GF surface has been roughened or if the ill-defined ridge lines are a product of the surface monolayer. While not a true analytical technique, the addition of AuNPs to the surface and the positive results point towards a successful grafting and modification procedure.

6.2.6. Grafting and Functionalisation of Au (111)

The fibrous nature of the GF electrodes makes it very difficult to study the surface using spectroscopic techniques. Some techniques would require destruction of the electrode, whilst others would find it difficult to measure anything other than an abundance of carbon, or require a more stable surface to view the grafting on. A collaborative project with the groups of Professor Richard Nichols (University of Liverpool), Professor Bingwei Mao (Xiamen University), Professor Andrew Beeby (Durham University) and Professor Paul Low (University of Western Australia) began to study the grafting using both STM and RAMAN spectroscopy [17]. In order to better investigate the chemistry of the functionalisation, the same method of grafting and functionalisation was followed, but with the subject being a gold coated glass side rather than a GF electrode, allowing STM and Raman/SHINERS measurements to be recorded for the functionalised gold electrodes. The initial investigation, grafting, functionalisation and electrochemical experiments were carried out by the author as part of the investigation into the grafting process. The post-grafting/functionalisation STM and Raman/SHINERS measurements and analysis were conducted by Dr Jinghong Liang at Xiamen University, China, as part of the collaboration, with band assignments following literature values [18-20]. The following Raman spectra, tables of absorbance bands and STM image have all been graciously provided by Dr Jinghong Liang [17].

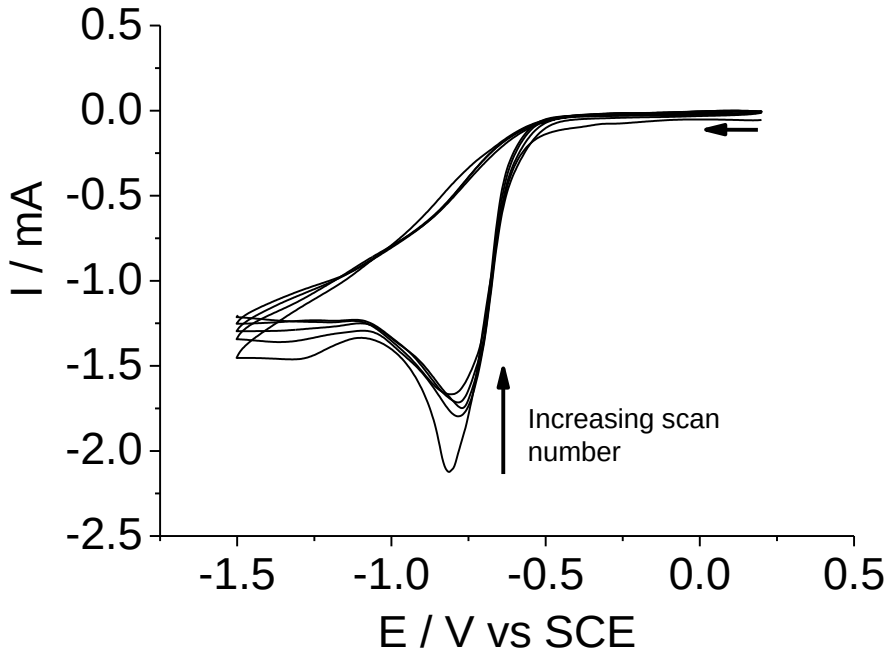

Figure 6.14: Cyclic voltammogram for the grafting of PD1 to a Au(111) electrode. Scan at 30 mV s^{-1}, in a solution of 5 mM PD1, five sweeps are shown.

Figure 6.14 shows cyclic voltammograms for the grafting of PD1 onto the gold surface at a scan rate of 30 mV s^{-1} in an acetonitrile solution containing 5 mM PD1, 5 mM $NaNO_2$, 10 mM $HClO_4$ and 0.1 M TBAB. TBAB served as the supporting electrolyte, a platinum mesh as the counter electrode, and SCE as the reference electrode. Figure 6.15 shows the cyclic voltammograms of the gold slide before and after grafting in a solution of 1 mM $K_4Fe(CN)_6$ and 0.1 M KCl, where the electrochemical blocking of the grafted electrode is clear to see. Figure 6.16 shows both the STM and SEM images of the grafted gold electrode after it has been submerged in gold nanoparticles in the same way as the carbon felts previously.

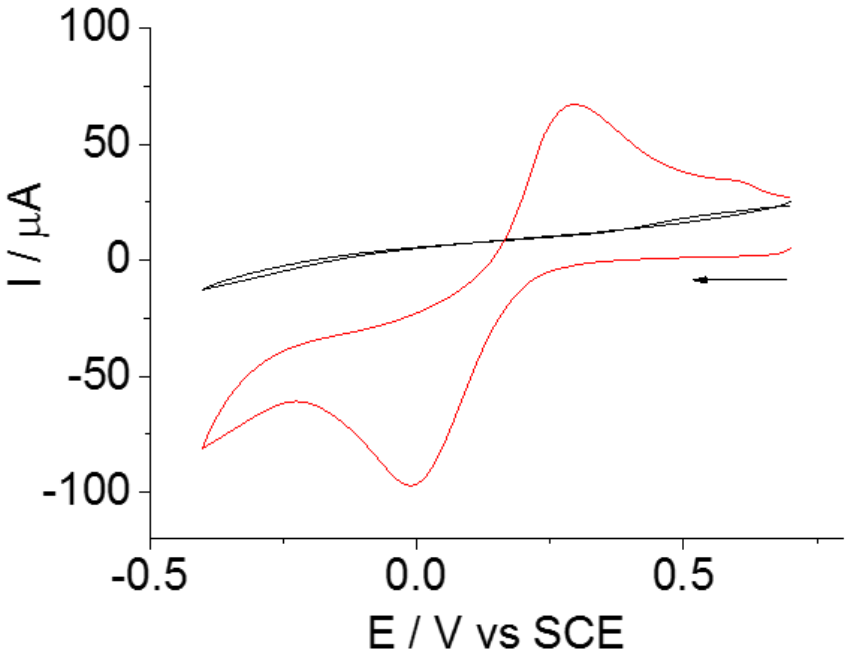

Figure 6.15: Cyclic voltammograms of a Au(111) electrode in 1 mM $K_4Fe(CN)_6$ and 0.1 M KCl before (red line) and after (black line) grafting, scan rate at 50 mV/s.

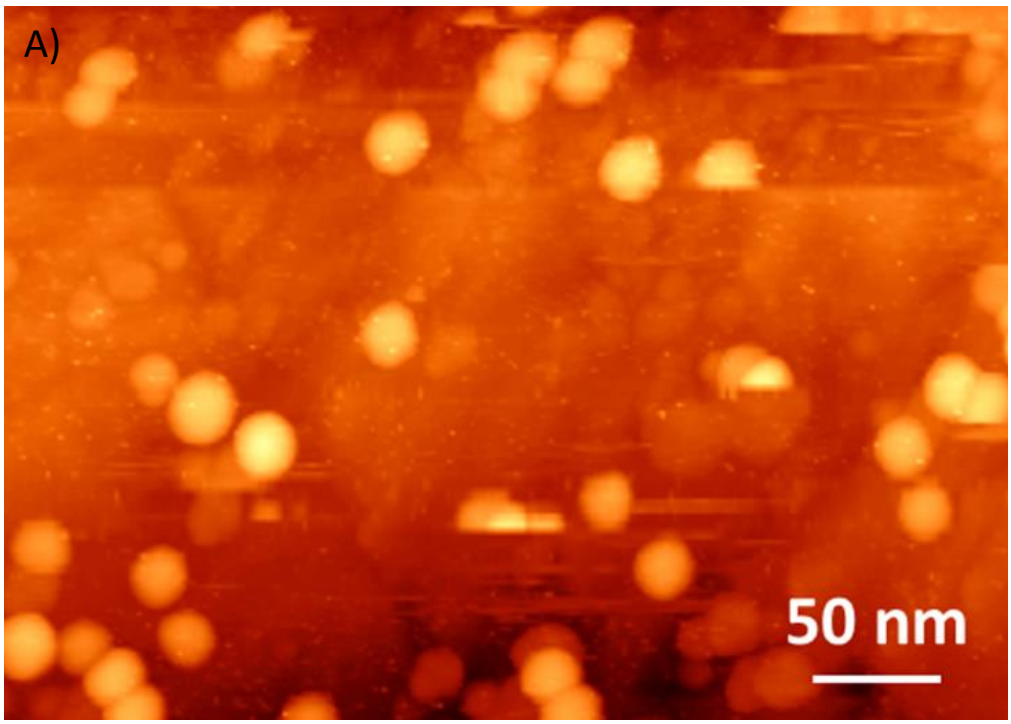

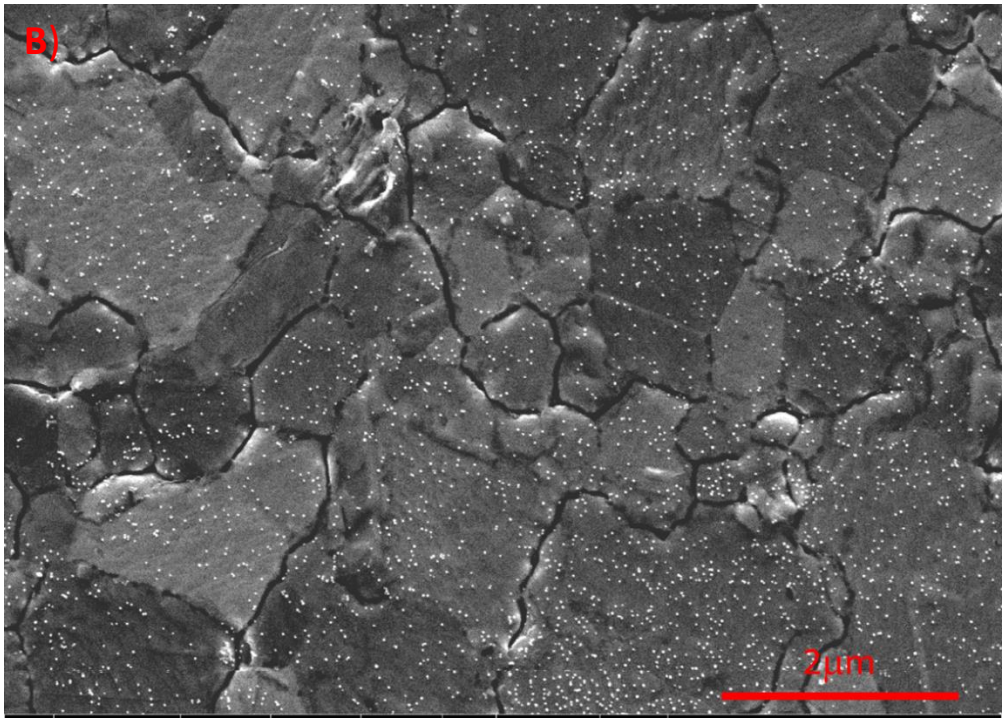

Figure 6.16: A) STM and B) SEM image of PD1-TA decorated by 20 nm gold nanoparticles.

Unlike with GF, grafting onto gold slides allows molecular characterisation of the surface and functionalisation steps with Raman spectroscopy. Figure 6.17 shows an illustration of the gap-mode and SHINERS methods used. The gap mode method relies on the adsorption of gold nanoparticles directly onto of the monolayer under investigation, while SHINERS (shell-isolated nanoparticle-enhanced Raman spectroscopy) employs gold nanoparticles with a thin SiO_2 shell [21-23]. Spectra were recorded with 633 nm laser excitation. A laser power of 0.15 mW was used for recording conventional Raman spectra of PD1 in solution and also gap mode Raman experiments, while 1.5 mW power was used for SHINERS experiments. In all cases spectral collecting time was 10 seconds. Control experiments were also undertaken for the gold nanoparticles on a clean gold substrate.

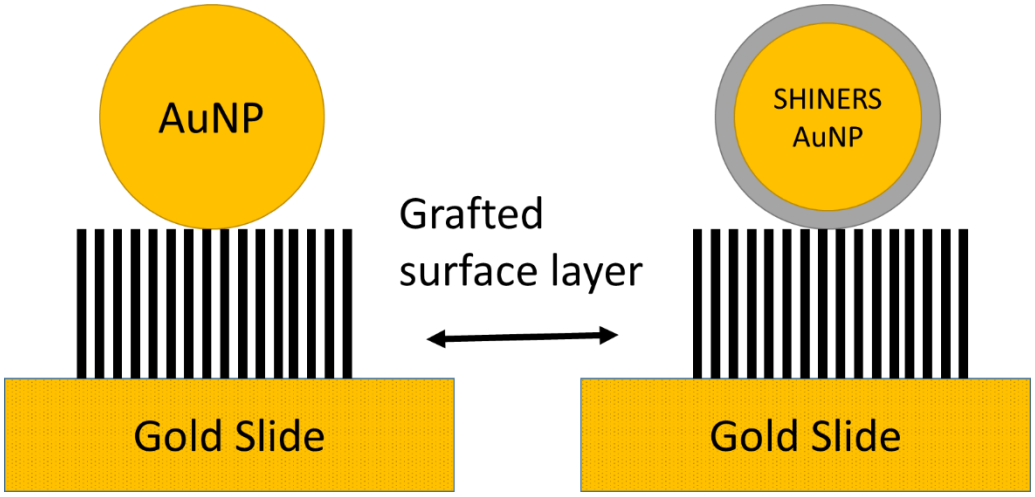

Figure 6.17: A schematic illustration of gap-mode SERS (left) and SHINERS (right) nanoparticles particles on a molecular functionalised Au(111) surface [17].

The Raman spectra of the surface grafted PD1 is compared against the spectra of PD1-TA in Figure 6.18. Also included for control experiments are the spectra of the unmodified gold electrode and PD1 in solution. Table 6.1 shows there is clear agreement between the spectral bands of the original, PD1 solution and both of the surface bound molecules. Both the surface bound molecules present a stretching mode corresponding to the Au-C surface binding at ~400 cm^{-1}, which is clearly absent in the solution based PD1 spectrum. There are also visible differences between the two surface bound molecules, with PD1-TA showing additional bands (1058 cm^{-1} and 1078 cm^{-1}) relating to the phenyl ring stretches and a thioacetate bending mode (481 cm^{-1}) clearly indicating the attachment of a thioacetate group [17]. The functionalization of PD1 to PD1-TA is further supported by the SHINERS spectra in Figure 6.19 and Table 6.2 with additional phenyl ring mode related to the thioacetate moiety following the Sonogashira reaction.

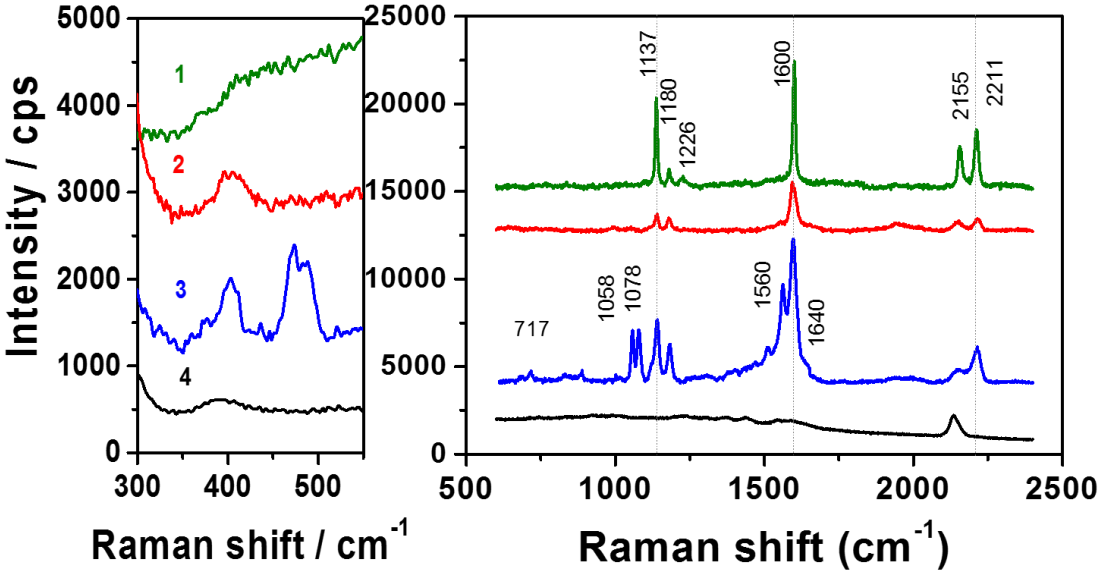

Figure 6.18: Gap-mode Raman spectra of 1) PD1 in solution, 2) surface bound PD1, 3) PD1-TA and 4) clean Au(111) electrode. Reproduced from ref. [17].

Table 6.1: Key gap-mode Raman spectral bands of solution PD1, surface bound PD1 and PD1-TA

Mode / cm^{-1}	PD1 – Solution	PD1 – Au Surface	PD1-TA – Au Surface
v(C≡C)	2211 2155	2214 2148	2214 2148
Benzene ring stretching	1600	1592	1597 1560
=C-NH_2 Stretch	1226		
Ring modes	1180 1137	1180 1137	1180 1139
Ring modes			1078 1058
Thioacetate bending mode			481
v(Au-C)		404	402

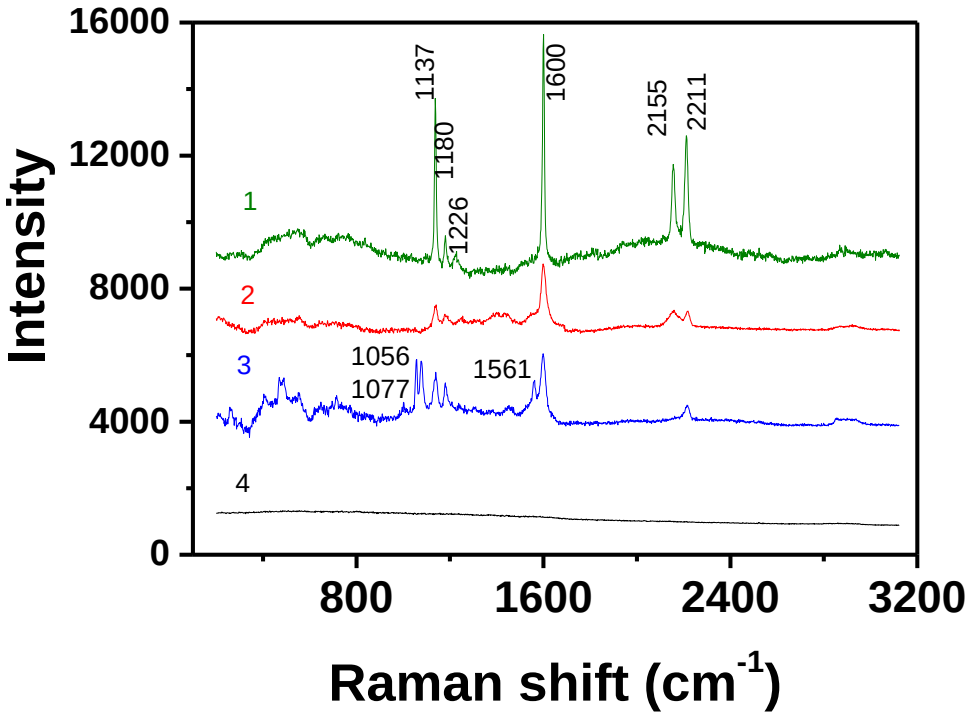

Figure 6.19: SHINERS Raman spectra of 1) solution PD1, 2) surface bound PD1, 3) PD1-TA and 4) a clean Au(111) electrode. Reproduced from ref. [17].

Table 6.2: Key SHINERS Raman spectral bands of solution PD1, surface bound PD1 and PD1-TA

Mode / cm^{-1}	PD1 – Solution	PD1 – Au Surface	PD1-TA – Au Surface
v(C≡C)	2211 2155	2216 2157	2214
Benzene ring stretch	1600	1600	1600 1561
=C-NH_2 Stretch	1226		
Ring modes	1180 1137	1182 1140	1178 1139
Ring modes			1077 1056

For the following single molecule measurements using STM, the PD1-TA was used. The molecule is connected to the gold plate electrode via a C-Au bond formed by the diazonium grafting, and to the gold STM tip by a spontaneously formed, Au-S bond. The method used in these experiments, called the *I*(*s*) method has been thoroughly described in literature. It involves lowering the STM tip to the electrode surface, applying a bias voltage and then retracting the tip while measuring the current decay vs retraction distance [24]. Some of these tip-surface interaction lead to the attachment of the tip to the deposited thioacetate moiety, when the retraction occurs a plateau, characteristic to a particular single molecule conductance, is visible in the *I*(*s*) trace as the tip is further withdrawn from the surface, the molecular junction is severed, presumably between the tip and the surface grafted molecule.

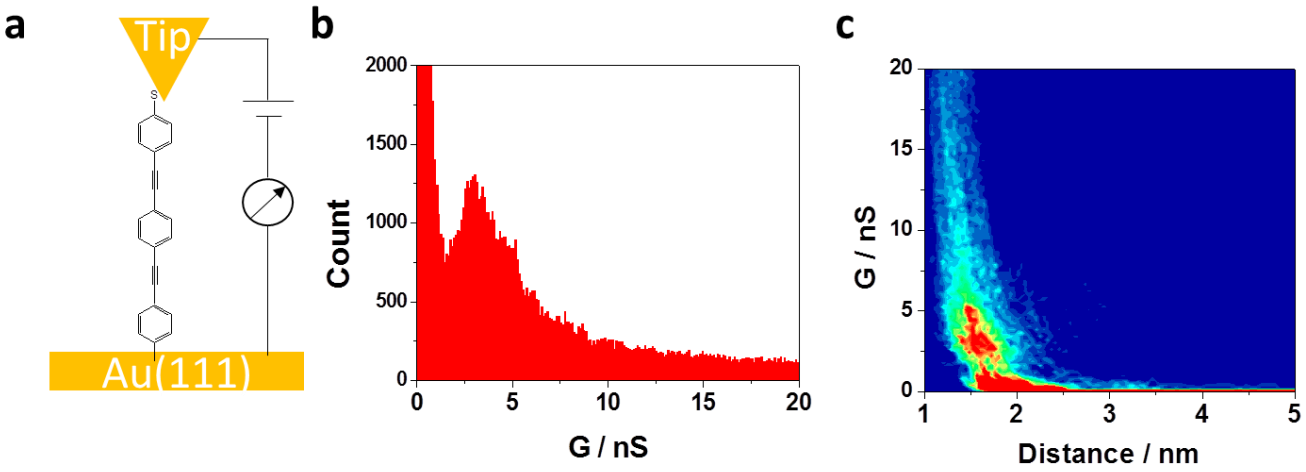

Figure 6.20: Thioacetate modified PD1 a) Diagram of STM experimental set up, b) 1D conductance histograms showing a peak at 3.0 nS and c) 2D conductance and distance histograms with a 1.7 nm break-off distance. Reproduced from ref. [17]

The histogram in Figure 6.20b, showing the collection of all plateau containing traces of the PD1-TA, has a definite peak at 3.0 nS. Previous literature shows a similar molecular wire, containing three phenyl rings, gave a conductance of 2.0 nS [25]. Unlike the PD1-TA, this wire has a Au-S attachment at both ends as well as additional moieties on the middle phenyl ring. Other similar molecular wires with triple phenyl rings and amine terminations give a broad histogram peak with conductance values of around 2.5 nS [26]. The higher conductance value recorded for PD1-TA is expected due to the increased stability of the Au-C diazonium grafting, opposed to molecular wires with dual, chemisorbed Au-S connections [27]. Overall, these studies lend further support to the successful surface grafting, and post-grafting functionalisation of the protected diazonium molecules.

6.2.7. 2nd Generation Blocking Molecules

Following the experiments using PD1 and the difficulty in forming a single monolayer on the GF, due to the length of the molecule, a second set of molecules were investigated. Designated Protected Diazonium 2 (PD2) and Protected Diazonium 3 (PD3), see Figure 6.21, these were again grafted onto GFs to further investigate surface chemical engineering on these materials.

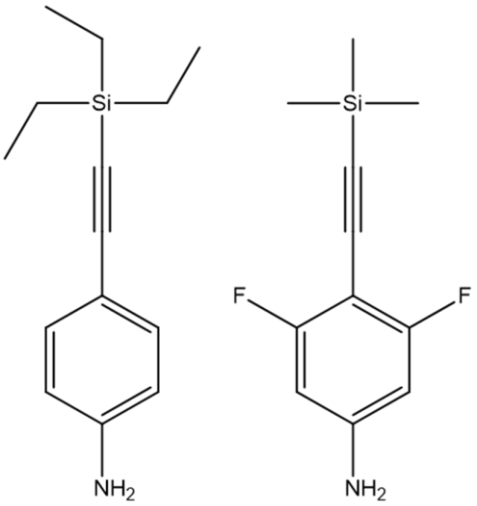

PD-2 PD-3

Figure 6.21: Diagram of PD2 and PD3 molecules

These molecules were designed to overcome the issue of multilayer formation by firstly being shorter than PD1, but also PD3 has fluoride groups in the 2 and 6 positions on the benzene ring, preventing any form of attachment at these points.

6.2.7.1 Grafting and Functionalisation on Graphitic Felts

The grafting of the diazonium to the surface followed the same Sonogashira procedure as described previously and the resulting cyclic voltammograms are presented in Figure 6.22. Note that unlike the PD1 sample, after the initial scan the current drops dramatically. This is consistent with the formation of a single, blocking monolayer. By integrating the area under the scan, as previously shown, it is possible to determine the number of electrons exchanged through the electrochemical reaction when certain assumptions are made. For this calculation the percentage coverage ($\Gamma^0 = 12.5x10^{-10}$ mol cm^{-2}) as described previously is used again here.

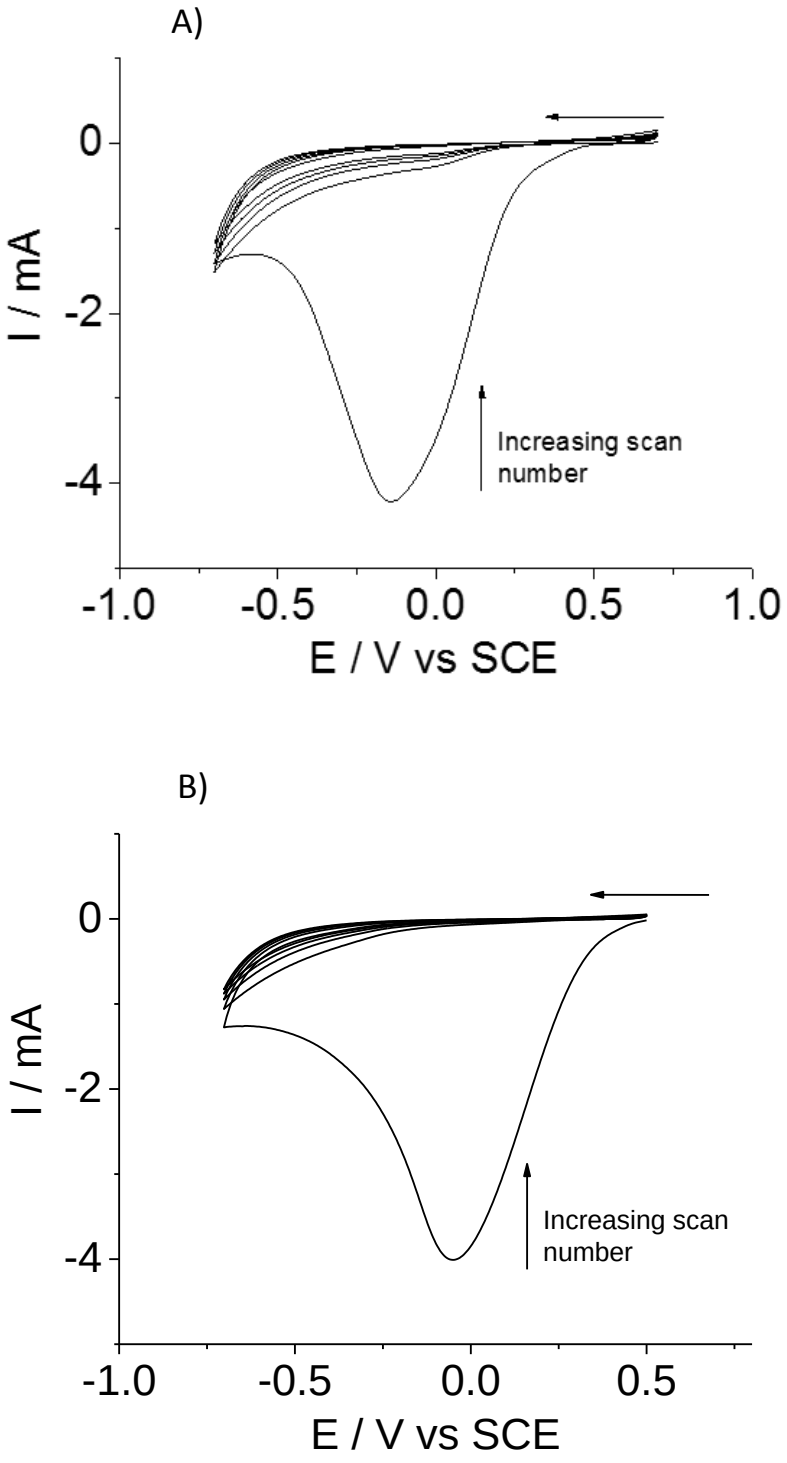

Figure 6.22: Cyclic voltammograms of GF grafting at 30 mV s^{-1} in 5 mM a) PD2 and b) PD3. Five scans are shown.

Table 6.3: Results of surface grafting charge integration.

Surface molecule	Q / C	Mols reacted	Coverage (%)
PD2	1.479	1.53×10^{-5}	223
PD3	0.804	8.33×10^{-6}	121

As mentioned, the large peak seen during the initial grafting scans in Figure 6.15a and b (-1.0 to -0.5 V), followed by an immediate drop in current on subsequent scans would suggest that the entire surface has been effectively covered with a layer of the protected diazonium molecule. Whilst the pronounced current drop after the first scan indicates that it is likely that the surface has been entirely covered, not all of the radical attacks will result in a covalent bond to the electrode surface. Instead, some radical attacks will lead to the dimerization of the protected diazonium compound in solution, rather than to those bound to the surface. It is interesting to note that while the fraction of expected coverage is expectedly high for both compounds, the charge consumed indicates that for PD2 almost double the quantity of diazonium reacts. This could be due to the blocking of the 2 and 6 positions of the phenyl ring of PD3 by fluorine substituents, preventing radical attacks at these positions. This reduces the chance of the diazonium molecules reacting with themselves (dimerising) or attaching to pre-grafted material due to the 2 and 6 positions being blocked. This could explain the reduced grafting charge and consequently the computed total number of moles reacting for the fluorine-substituted analogue.

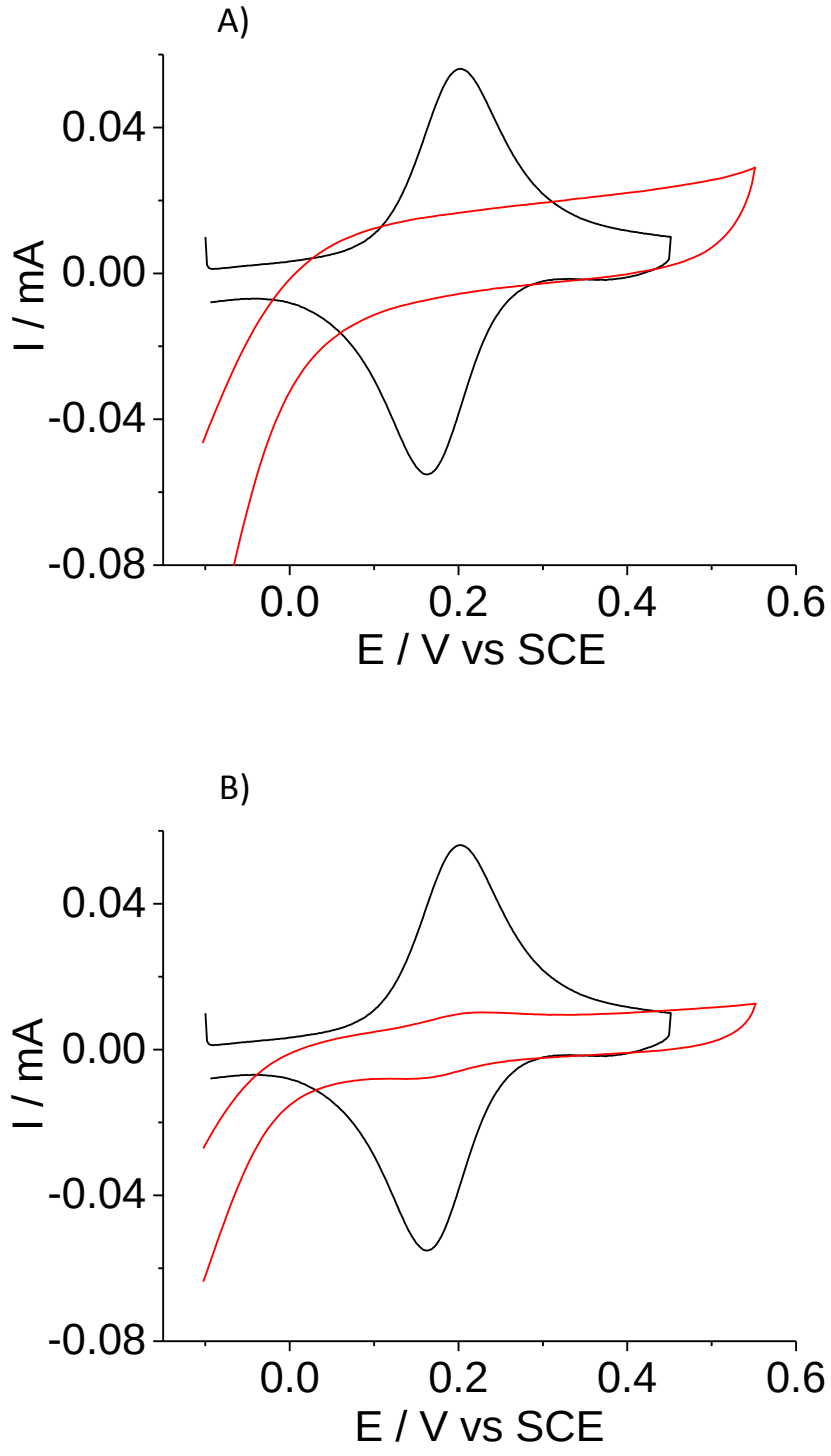

Figure 6.23: Cyclic voltammograms of clean GF (black) and GF after A) PD2 and B) PD3 surface grafting (red) in 1 μM ferrocyanide solution at 50 mV s^{-1}.

Figure 6.23 shows a GF before and after deposition of a) PD2 and b) PD3 surface layers, in a 1 μM ferrocyanide in 0.1 M KCl solution at 50 mV s^{-1}. In much the same way as for PD1 (Figure 6.12) it is

clear that a highly blocking surface layer has been deposited. Interestingly, for the PD3 sample (Figure 6.23b) there are still visible redox peaks for the ferrocyanide system after the surface has been coated. Ferrocyanide is an inner sphere redox probe that is very sensitive to the electrode surface, especially to the proportion of surface carbon-oxygen groups.[28] Whilst the significantly reduced current would suggest the surface has a significant level of PD3 coverage, the presence of ferrocyanide redox peaks, even small ones, suggests there may be exposed carbon surface.

6.2.7.2 Functionalisation with Ferrocene

One attractive functionality selected to investigate was a terminal ferrocene, as this provides an electrochemical probe of the surface modification. Following the same procedure as the previous post-grafting functionalisation, a bromoferrocene derivative was selected in place of the thioacetate functionalisation in the Sonogashira step. This would allow the ferrocene moiety to attach to the exposed alkyne of the cleaved protecting monolayer, with the aim that it remains sufficiently electroactive to serve as a direct electrochemical probe of the surface modification. The protected diazonium surfaces that have been cleaved and then functionalised with ferrocene are given the '-F' notations, for example PD2-F.

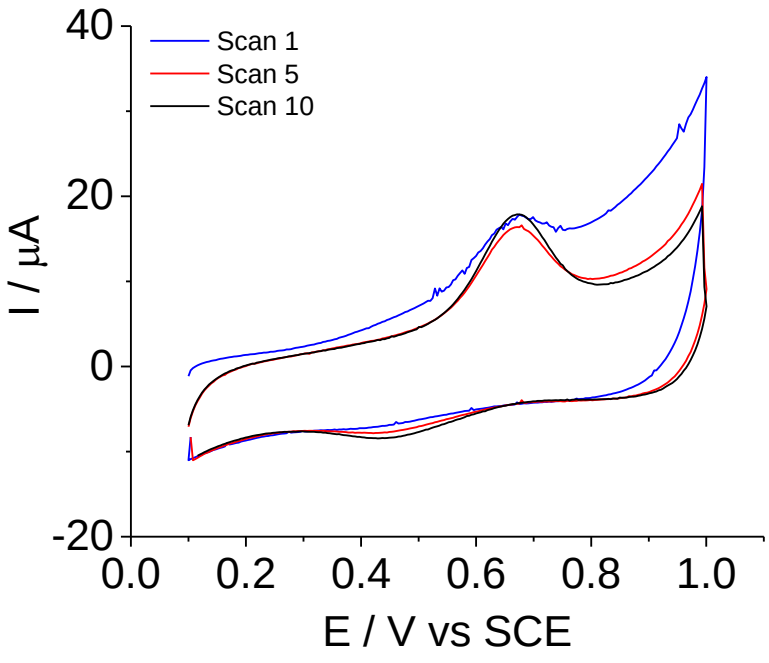

Figure 6.24: Cyclic voltammograms of a PD2-F GF at 50 mV s^{-1} in a solution of 0.1 M TBAP/Acetonitrile background electrolyte.

Figure 6.24 shows the first, fifth and tenth scan for a PD2-F GF. The measurements are taken at 50 mV s^{-1} in a solution of 0.1 M TBAP/Acetonitrile background electrolyte. The ferrocene redox system gives an oxidation peak at 0.65 V and a reduction peak at 0.45 V. Whilst these values are at a higher potential than would normally be associated with ferrocene, is entirely plausible due to the surface bound nature of the group. The peak-to-peak separation of almost 200 mV would suggest that this surface process is surprisingly slow on this grafted monolayer.

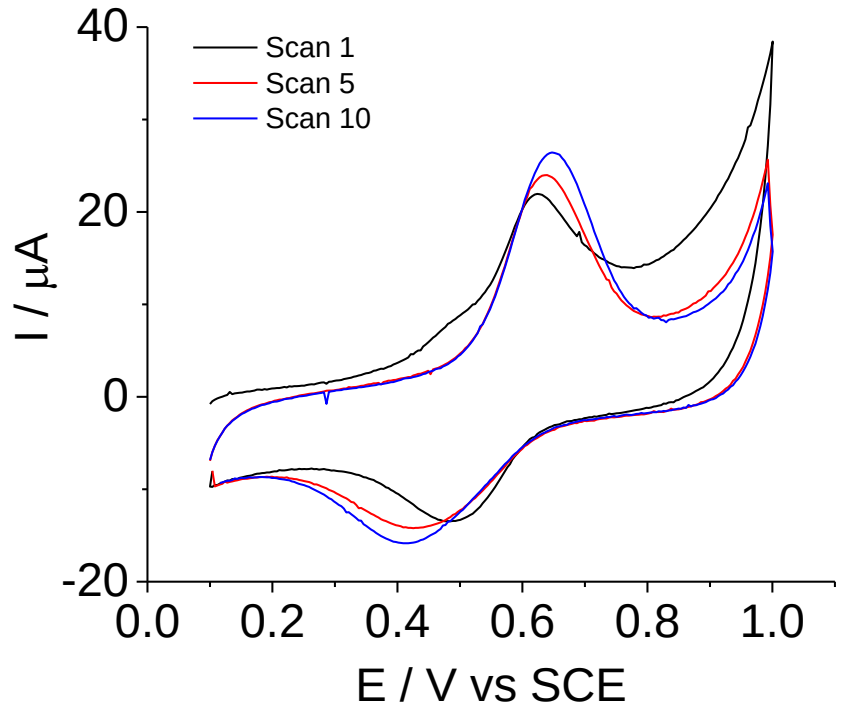

Figure 6.25: Cyclic voltammograms of a PD3-F GF at 50 mV s^{-1} in a solution of 0.1 M TBAP/Acetonitrile background electrolyte.

A similar result can be seen in Figure 6.25 with the surface grafting of PD3. The large peak separation deviates strongly from what would be expected from ideal monolayer voltammetry with a reversible redox couple like ferrocene. Looking at the charge passed for the oxidative peak for each of the two surface grafted electrodes (Figure 6.26), after 10 repeat scans in the background electrolyte, the

PD3-F surface has more than twice the charge of the PD2-F surface. Comparing the charge of the tenth scan for each surface to the expected number of mols in a single monolayer (68.8 nM) gives an insight into the degree of ferrocene functionalisation, assuming that the oxidative peak is entirely due to surface-bound ferrocene. For the PD2 surface only 0.43% of a monolayer has been functionalised, whereas for PD3 this value is 0.88%. Whilst these values suggest that the surface functionalisation has not been successful across the entire grafted surface, this is not entirely unexpected from the harsh conditions of the cleaving and functionalisation process, possibly leaving many surface sites unreceptive to the ferrocene.

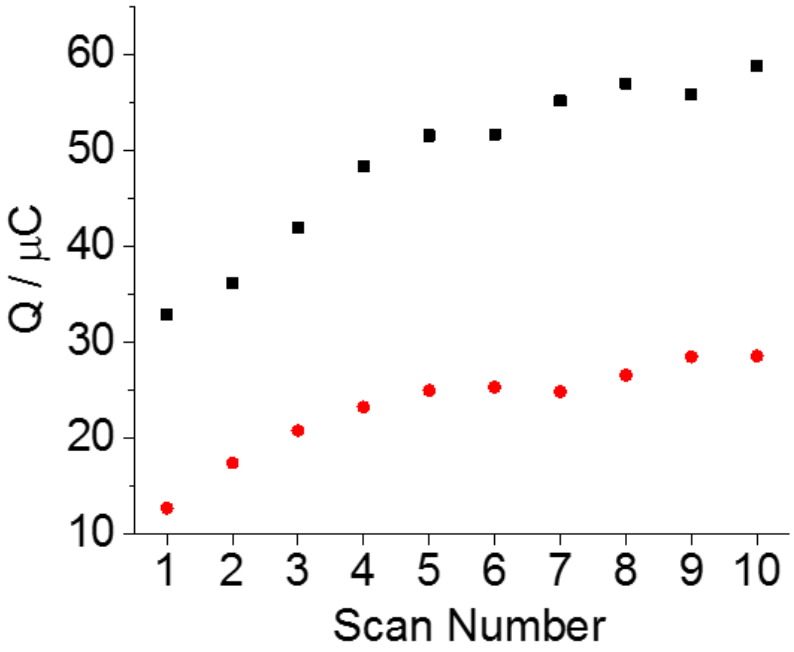

Figure 6.26: Chart of integrated charge vs scan number for PD2-F (red) and PD3-F (black)

The two questions that remain difficult to answer are; why does the oxidative current increase with scan number, and secondly why is the behaviour of the reductive peak so far from ideal. The possible answer to both question could lie in the stability of the surface-bound ferrocene, and whether the high switching potential of 1 V could be oxidatively cleaving either the ferrocene, the entire surface molecule, or something in-between, off the carbon surface. To investigate this a series

of measurements were taken on the same modified GF electrode. These are shown in Figure 6.27 A), B) and C) below.

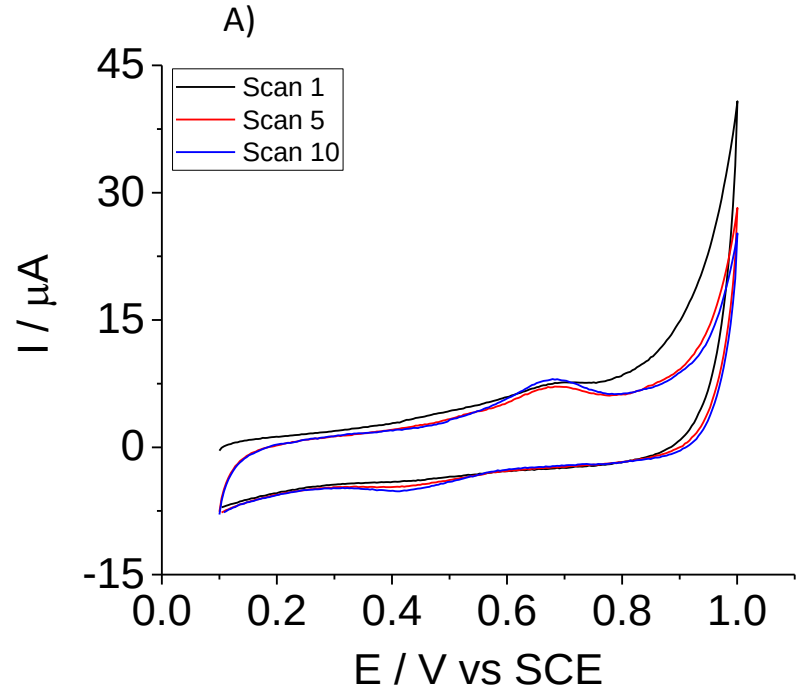

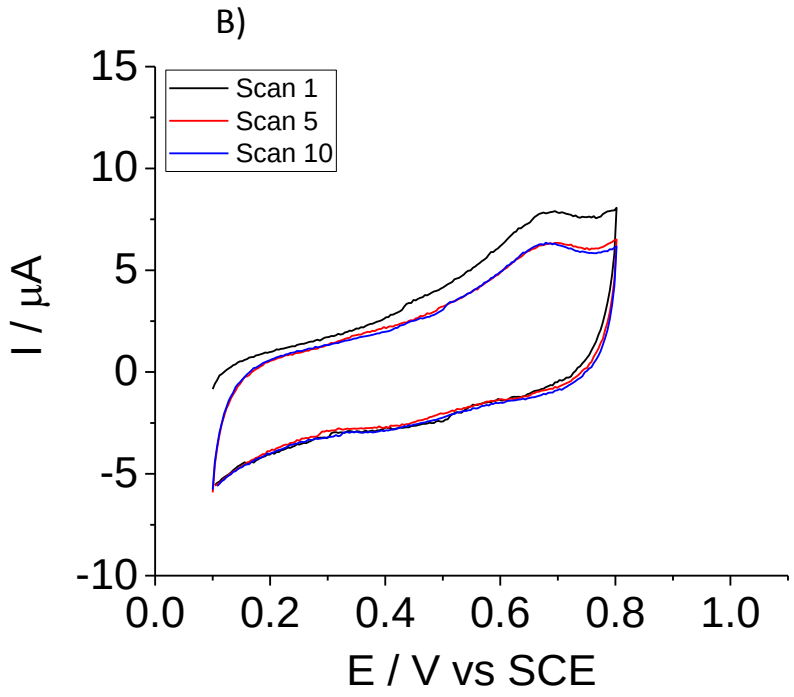

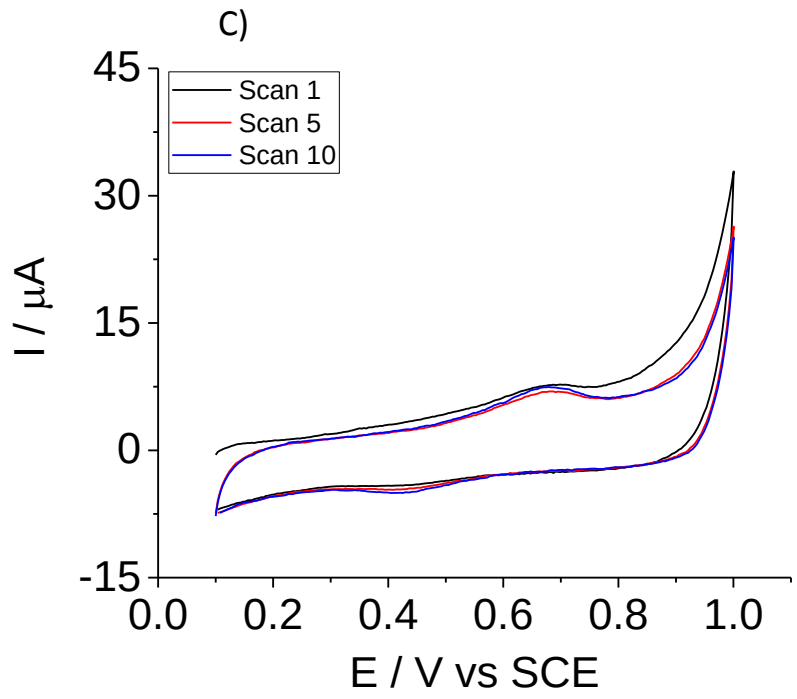

Figure 6.27: Cyclic voltammograms for a PD2-F GF at 50 mV s^{-1} in 0.1 M TBAP/Acetonitrile background electrolyte. Scans 1, 5 and 10 are shown for a) 0.1 V to 1.0 V, b) 0.1 V to 0.8 V and c) repeat of (a).

Figure 6.27 A) shows the first, fifth and tenth scans for the ferrocene modified GF, with an upper scan potential limit of 1 V. It can be noted that again with each subsequent scan, there is an increase in the oxidative peak height. Figure 6.27 B) shows the same GF, but the oxidative sweep of the experiment now stops at 0.8 V rather than 1 V. Now there appears to be no further increase in peak height and the scans now appear repeatable. Figure 6.27 C) shows a repeat of Figure 6.27 A) in order to determine if the change seen between the voltammograms of A) and B) was reversible. In C) the peak height does indeed begin to increase with scan number. This indicates that the high oxidative potential is having an effect on the surface. However, it is difficult to determine whether this amounts to a "negative effect" with molecules being oxidised off the surface, or a "positive effect", in which the higher potential leads so some reordering or activation of the surface allowing more of the attached ferrocene to display visible redox active.

In order to further investigate the grafting a series of control experiments were devised with both modified and unmodified electrodes. These are summarised in the following table:

Table 6.4: Summary of control experiments.

Electrode	Grafted with PD2	Deprotected with TBAF	Bromoferrocene present in Sonogashira reaction.
GF *Control 1*	No	Yes	Yes
GF *Control 2*	Yes	Yes	No
GF Standard	Yes	Yes	Yes

Control 1 was used to investigate whether products used and generated during the post-grafting procedure led to the redox signals seen previously, rather these peaks arising from surface bound ferrocene. *Control 2* was used to elucidate whether the voltammetric signals observed on the other electrodes are due to bromoferrocene being the active moiety and not due to any additional surface groups produced from the highly active alkyne group in the Sonogashira process. The GF Standard electrode follows the established procedure to produce a ferrocene terminated monolayer to provide a reference by which to judge the control experiment.

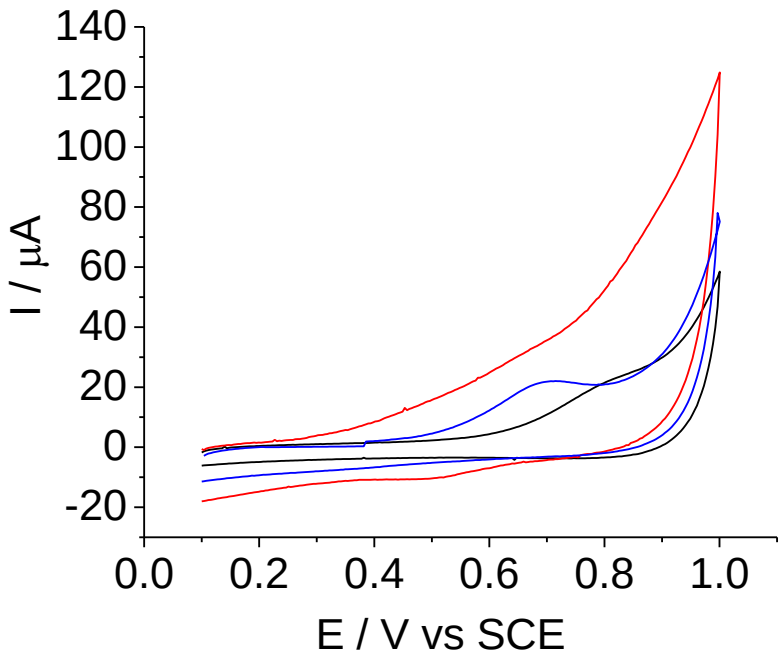

Figure 6.28: Cyclic voltammograms for control experiments GF *Control 1* (black), GF *Control 2* (red) and GF Standard (blue) at 50 mV s^{-1} in 0.1 M TBAP/acetonitrile.

Figure 6.28 shows cyclic voltammograms for the various control electrodes measured in 0.1 M TBAP/acetonitrile. The Standard electrode again shows an oxidative peak in the region expected for the ferrocene attachment. In contrast, *Control 2*, where no ferrocene was introduced to the surface, shows a complete lack of oxidative peak. The higher capacitive current for this electrode may be due to the, now chaotically terminated, monolayer. With no bromoferrocene present, the highly active alkyne group will react with a wide range of groups, leading to a more heterogeneous monolayer. The CV for *Control 1* does show an oxidative peak of sorts in the form of a shoulder at 0.8 V. This indicates that some ferrocene has been transferred from the Sonogashira reaction to the electrochemical measurements. This could be as a physisorbed species and may point to a lack of sufficient washing post-functionalisation. A more likely explanation may be physiosorption of the ferrocene on the unmodified carbon surface, as the presence of residual ferrocene on the modified surface due to inadequate washing might be expected to lead to a much broader signal on the GF Standard electrode.

6.2.8. Investigation of Ascorbic Acid

The electrochemical behaviour of ascorbic acid was selected for investigation at this point owing to its popularity as a target for electrochemical sensor detection. Whilst this obviously moves away from the initial aims of the project, it was of interest due to the emerging ability of using the GF electrodes as electrochemical sensors in their own right. (L-)Ascorbic acid (AA) also known as Vitamin C is one of the most important nutrients for humans, it's health benefits include the

prevention of scurvy, and high concentrations of AA are found in immune cells [29, 30]. Although their role in the immune system is unclear, it is consumed during periods of infection. There is a wide selection of literature on the study of AA by electrochemical methods due to its importance in the human body. It is also of interest as it is a well-documented chemically irreversible reaction that is sensitive to the electrode surface conditions [31]. A CV is shown in Figure 6.29 A) for an unmodified or 'blank' GF in the phosphate buffer background electrolyte solution and B) the blank GF's first, fifth and tenth scan in 0.1 mM ascorbic acid solution. At first it would appear, from Figure 6.29 B), that there is a degree of reversibility of the ascorbic acid oxidation, with a small reductive peak at 0.05 V. Upon closer inspection of the GF in the background electrolyte, it is clear that this reductive process is separate from the AA oxidation process. This could be due to some reaction between the carbon surface and the PBS system, or possibly contamination of the PBS system, as no reductive peak is normally seen at this potential [4]. When these voltammograms are overlaid in Figure 6.30 below, it becomes clear that there are two separate electrochemical processes, which at first glance had given the appearance of a complete redox system.

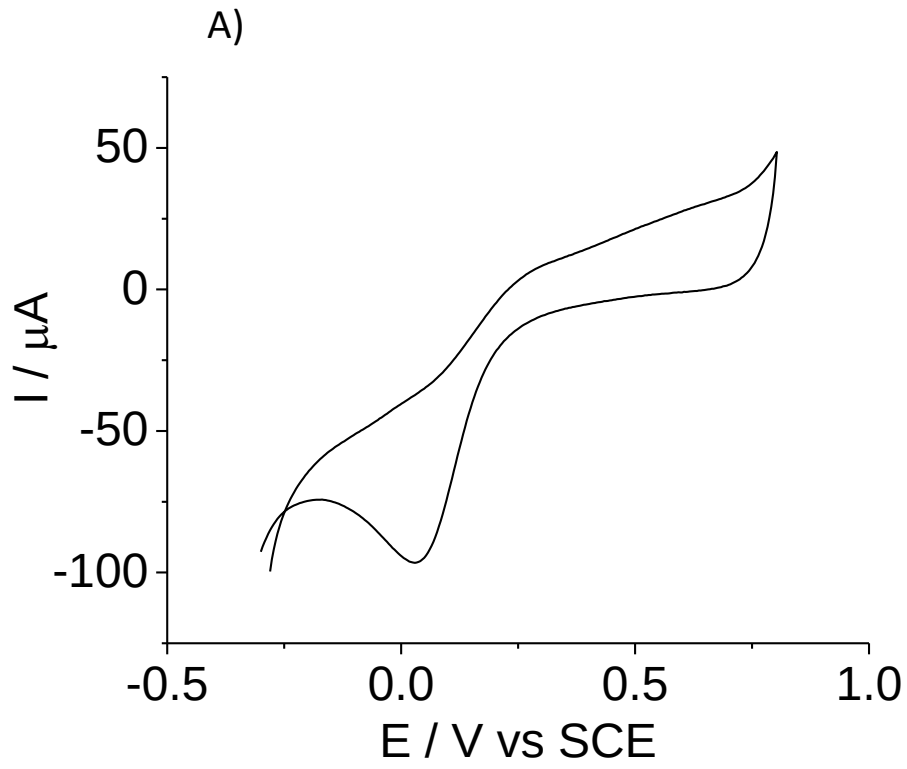

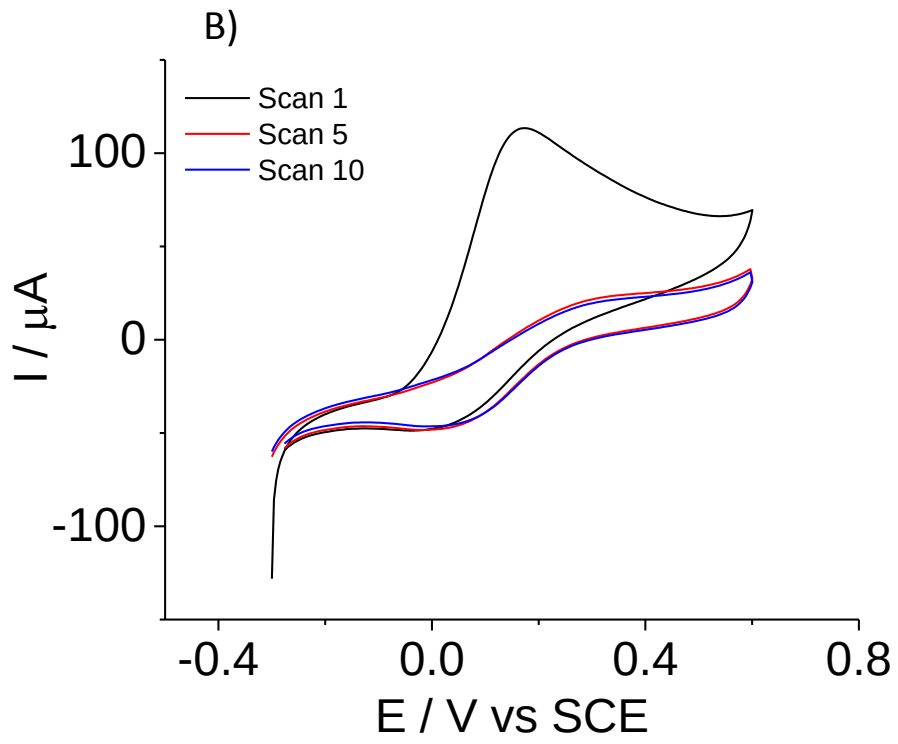

Figure 6.29: Cyclic voltammogram of a clean GF in a) 0.1 M pH 7 phosphate buffer solution (PBS) and b) 0.1 mM ascorbic acid in 0.1 M phosphate buffer solution at 50 mV s^{-1}.

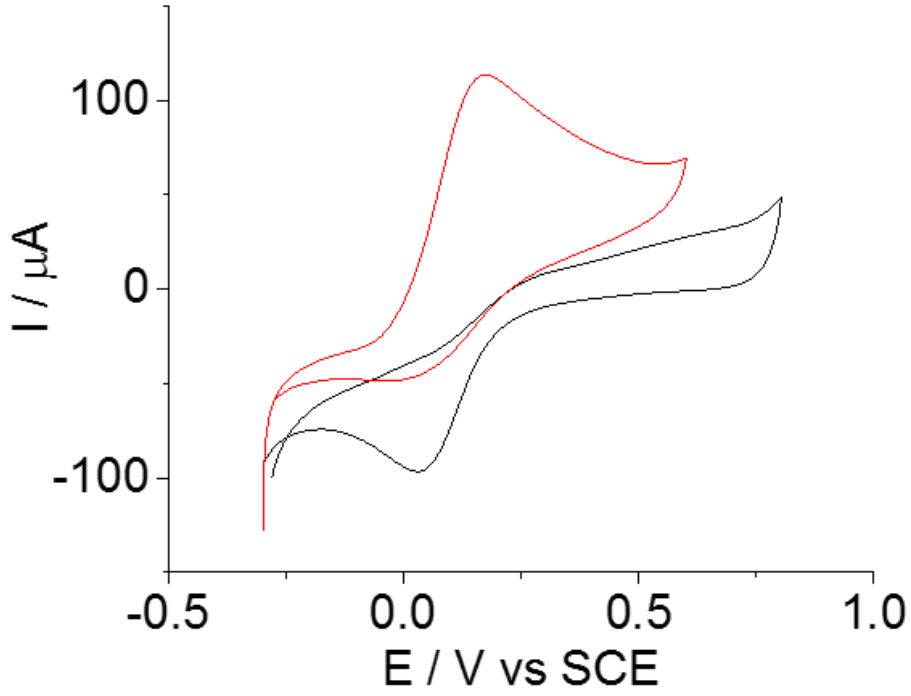

Figure 6.30: Overlaid cyclic voltammogram of a clean GF in 0.1 M PBS (black) and scan 1 of 0.1 mM ascorbic acid in 0.1 M PBS (red) at 50 mV s^{-1}.

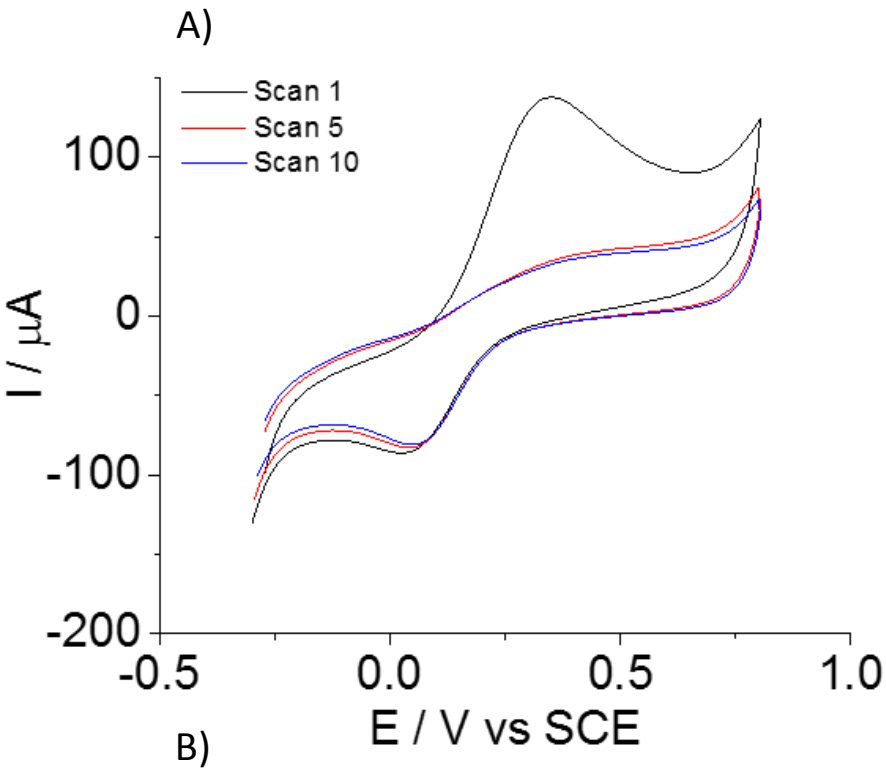

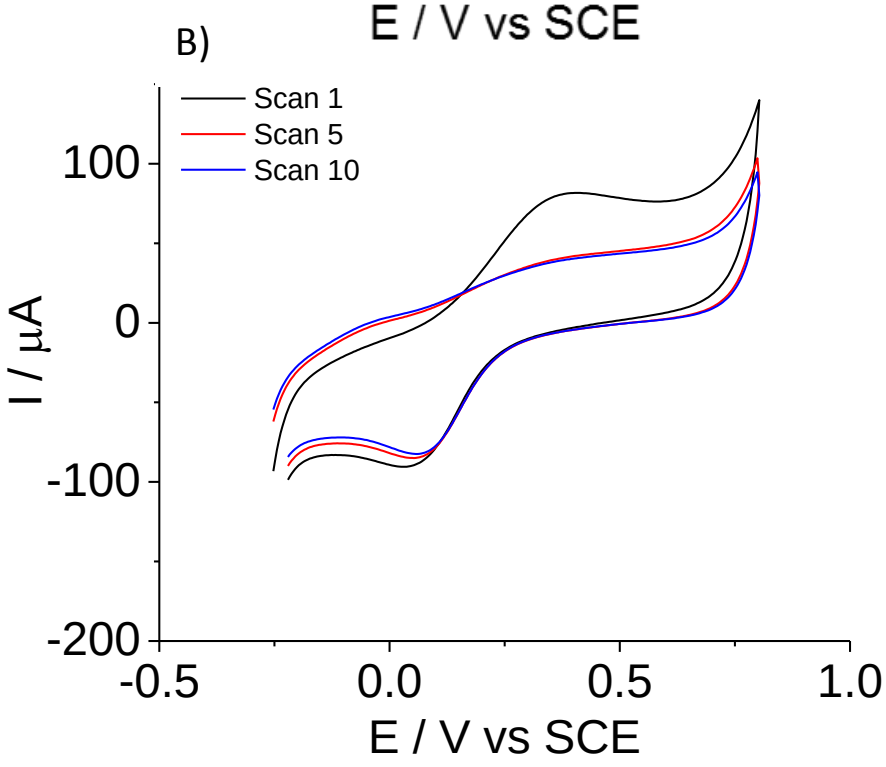

Figure 6.30: Cyclic voltammograms of the first, fifth and tenth scans for a) PD2 and b) PD3 surface grafted GF in 0.1 mM ascorbic acid in 0.1 M PBS at 50 mV s^{-1}.

After studying the solutions using clean GFs, the GFs were modified with the PD2 and PD3 protecting layers, using the same techniques presented earlier in the chapter. The following voltammograms in Figure 6.31 shows the first, fifth and tenth scans for the modified electrodes in 0.1 M ascorbic acid solution. While both electrodes have a clear oxidative peak for the ascorbic acid system, the peak is larger and better defined for the PD2 coating. It is also interesting that after the initial scan, this oxidative peak all but disappears, leaving only the reductive peak in the phosphate buffer, as seen with the bare GF electrode previously.

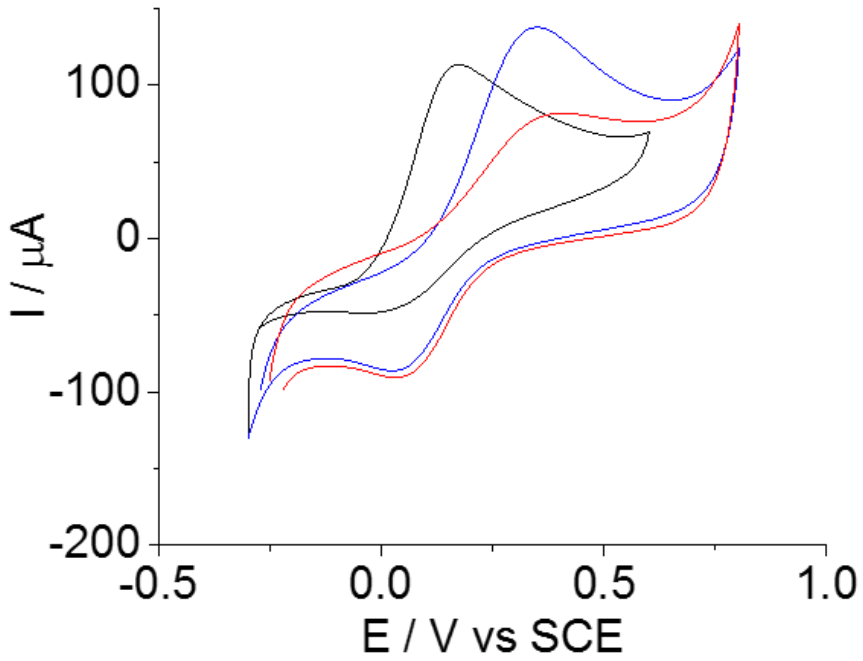

Figure 6.32: Overlaid cyclic voltammograms of scan 1 from a clean GF (black), PD2 (blue) and PD3 (red) surface grafted GF, in 0.1 mM ascorbic acid in 0.1 M PBS at 50 mV s^{-1}.

Comparing the first scan for both the PD2, PD3 and blank electrodes, in Figure 6.32 above, provides an interesting insight. For both the PD2 and PD3 surface layers, relative to the blank electrode, the oxidative peak for the ascorbic acid has shifted positively by approximately 0.2 V. This is a significant shift and suggests that the oxidative process is now hindered, for example by the modified surface layer increasing the distance of closest approach for the ascorbate ions. The most interesting part of

this, is that while the surface has been previously shown to have a large blocking effect on the electro-oxidation of ferrocyanide solutions, the oxidation of the ascorbic acid species is still possible.

6.3 Conclusions

Diazonium salts have been shown to be an effective method of surface modifications. They provide a strong surface bond, and have been shown to reliably block the POM from the electrode surface. Through adaptation of the grafting method from potentiostatic to cyclic, the grafting has become more controllable, but a repeatable method to functionalise the carbon surface with a single monolayer is still a challenge. Using this method to modify the surface of a graphite felt electrode, for use in a fuel cell, would be unfeasible. The surface layer is not stable and the production of multilayers would significantly reduce both the active surface area and the internal volume of the felts. This in turn reduces the efficiency of the electrodes. For these reasons depositing a single monolayer is preferable, it would also allow the effects of different diazonium terminal moieties to be seen, rather than being lost to the blocking effect of large multilayers. Work by Leroux et al suggested a method of grafting a single monolayer by using diazonium salts with large, terminal blocking groups [14]. The steric hindrance of these large groups prevents the radical diazonium salts in solution from reacting with those already grafted to the surface. The blocking groups can be removed later and replaced by different functionalities, making it a very versatile technique.

This chapter has presented a method of preparing a carbon surface, namely graphitic felt, with a surface layer coverage of covalently bound diazonium derivatives. Once these phenyl layers have been attached to the surface, the process for altering their terminal moieties using the Sonogashira reaction has also be shown. While it is still difficult to determine the thickness of the surface layers using the techniques presented, it is entirely possible, due to the steric hindrance provided by the blocking groups of PD2 and PD3, that a monolayer or small number of layers has been formed. Furthermore, by instead preforming the surface modification on a Au(111) surface, additional investigative techniques, in the form of STM and Raman spectroscopy became available. The

spectroscopy in particular facilitated a molecular level examination of the compounds once surface bound. They provide evidence for the success of the post-grafting modification procedures, being able to remove the blocking group and then to attach a new functional group to the terminal alkyne. The interactions of these modified surfaces with ascorbic acid are also examined by cyclic voltammetry. The complex nature of these surfaces makes it difficult to draw any definitive conclusions and further investigation is required.

In closing, it is the authors hope that this chapter provides insight into many of the exciting routes further research in this subject area could take. Further surface investigation techniques, such as AFM, could provide information on the thickness of the grafted surface layer, although this may have to be deployed with model carbon surface such as HOPG or edge plane samples. There is a plethora of combinations of blocking groups that could be synthesised to help control and eventually reduce the formation of multilayers, and an equally large number of possible post-grafting surface modifications. These routes may lead to more versatile carbon surfaces with properties tuned by the surface modification. Numerous applications may be foreseen, especially in connection with the aim of this PhD in the fuel cell industry, where carbon electrodes are either deployed as catalyst supports or directly as electrodes in redox flow systems.

6.5 References

[1] P. Serp, J.L. Figueiredo, Carbon materials for catalysis, John Wiley & Sons (2009).
[2] F.M. Koehler, N.A. Luechinger, D. Ziegler, E.K. Athanassiou, R.N. Grass, A. Rossi, C. Hierold, A. Stemmer, W.J. Stark, Permanent Pattern-Resolved Adjustment of the Surface Potential of Graphene-Like Carbon through Chemical Functionalization, Angewandte Chemie International Edition 48(1) (2009) 224-227.
[3] Y. Nosho, Y. Ohno, S. Kishimoto, T. Mizutani, The effects of chemical doping with F4TCNQ in carbon nanotube field-effect transistors studied by the transmission-line-model technique, Nanotechnology 18(41) (2007) 415202.

[4] K.S. Ngai, W.T. Tan, Z. Zainal, R.M. Zawawi, M. Zidan, Voltammetry Detection of Ascorbic Acid at Glassy Carbon Electrode Modified by Single-Walled Carbon Nanotube/Zinc Oxide, International Journal of Electrochemical Science 8(8) (2013) 10557-10567.
[5] H.G. Hong, M.D. Porter, Signal enhancement for electrochemical detection at glassy carbon electrode modified with phenyl layer, Journal of Electroanalytical Chemistry 578(1) (2005) 113-119.
[6] R.E.G. Smith, T.J. Davies, N.D. Baynes, R.J. Nichols, The electrochemical characterisation of graphite felts, Journal of Electroanalytical Chemistry 747 (2015) 29-38.
[7] G.M. Jenkins, K. Kawamura, Structure of glassy carbon, Nature 231(5299) (1971) 175-&.
[8] M. Gross, J. Jordan, Voltammerty at glassy-carbon electrodes, Pure and Applied Chemistry 56(8) (1984) 1095-1129.
[9] R. Murugesan, P. Sami, T. Jeyabalan, A. Shunmugasundaram, Synthesis, spectroscopic characterization and redox properties of titanium and vanadium substituted Keggin-type heteropolyanions, Transition Metal Chemistry 23(5) (1998) 583-588.
[10] W. Richard, D. Evrard, P. Gros, New insight into 4-nitrobenzene diazonium reduction process: Evidence for a grafting step distinct from NO2 electrochemical reactivity, Journal of Electroanalytical Chemistry 685 (2012) 109-115.
[11] P. Allongue, M. Delamar, B. Desbat, O. Fagebaume, R. Hitmi, J. Pinson, J.M. Saveant, Covalent modification of carbon surfaces by aryl radicals generated from the electrochemical reduction of diazonium salts, Journal of the American Chemical Society 119(1) (1997) 201-207.
[12] Y.R. Leroux, H. Fei, J.M. Noel, C. Roux, P. Hapiot, Efficient Covalent Modification of a Carbon Surface: Use of a Silyl Protecting Group To Form an Active Monolayer, Journal of the American Chemical Society 132(40) (2010) 14039-14041.
[13] Y.R. Leroux, F. Hui, P. Hapiot, A protecting-deprotecting strategy for structuring robust functional films using aryldiazonium electroreduction, Journal of Electroanalytical Chemistry 688 (2013) 298-303.
[14] Y.R. Leroux, P. Hapiot, Nanostructured Monolayers on Carbon Substrates Prepared by Electrografting of Protected Aryldiazonium Salts, Chemistry of Materials 25(3) (2013) 489-495.
[15] Y.K. Kang, D.J. Won, S.R. Kim, K.J. Seo, H.S. Choi, G.H. Lee, Z.S. Noh, T.S. Lee, C.J. Lee, Self-assembled monolayer of the aromatic thioacetate on the gold surface, Materials Science & Engineering C-Biomimetic and Supramolecular Systems 24(1-2) (2004) 43-46.
[16] J.S. Dewar, A review of the Pi-complex theory, Bulletin De La Societe Chimique De France 18(3-4) (1951) C71-C79.

[17] J. Liang, R.E.G. Smith, A. Vezzoli, L. Xie, D.C. Milan, R. Davidson, A. Beeby, P.J. Low, S.J. Higgins, B. Mao, R.J. Nichols, Electrochemically grafted single molecule junctions exploiting a chemical protection strategy, Electrochimica Acta Publication (2016).

[18] J.G. Kushmerick, J. Lazorcik, C.H. Patterson, R. Shashidhar, D.S. Seferos, G.C. Bazan, Vibronic Contributions to Charge Transport Across Molecular Junctions, Nano Letters 4(4) (2004) 639-642.

[19] Z. Liu, X. Wang, K. Dai, S. Jin, Z.-C. Zeng, M.-D. Zhuang, Z.-L. Yang, D.-Y. Wu, B. Ren, Z.-Q. Tian, Tip-enhanced Raman spectroscopy for investigating adsorbed nonresonant molecules on single-crystal surfaces: tip regeneration, probe molecule, and enhancement effect, Journal of Raman Spectroscopy 40(10) (2009) 1400-1406.

[20] M. Fletcher, D.M. Alexson, S. Prokes, O. Glembocki, A. Vivoni, C. Hosten, Surface-enhanced Raman scattering of a Ag/oligo(phenyleneethynylene)/Ag sandwich, Spectrochimica Acta Part A: Molecular and Biomolecular Spectroscopy 78(2) (2011) 706-711.

[21] J.F. Li, Y.F. Huang, Y. Ding, Z.L. Yang, S.B. Li, X.S. Zhou, F.R. Fan, W. Zhang, Z.Y. Zhou, D.Y. Wu, B. Ren, Z.L. Wang, Z.Q. Tian, Shell-isolated nanoparticle-enhanced Raman spectroscopy, Nature 464(7287) (2010) 392-395.

[22] J.R. Anema, J.-F. Li, Z.-L. Yang, B. Ren, Z.-Q. Tian, Shell-Isolated Nanoparticle-Enhanced Raman Spectroscopy: Expanding the Versatility of Surface-Enhanced Raman Scattering, in: R.G. Cooks, E.S. Yeung (Eds.), Annual Review of Analytical Chemistry, Vol 4 (2011), 129-150.

[23] J.F. Li, X.D. Tian, S.B. Li, J.R. Anema, Z.L. Yang, Y. Ding, Y.F. Wu, Y.M. Zeng, Q.Z. Chen, B. Ren, Z.L. Wang, Z.Q. Tian, Surface analysis using shell-isolated nanoparticle-enhanced Raman spectroscopy, Nature Protocols 8(1) (2013) 52-65.

[24] W.J. Hong, H. Li, S.X. Liu, Y.C. Fu, J.F. Li, V. Kaliginedi, S. Decurtins, T. Wandlowski, Trimethylsilyl-Terminated Oligo(phenylene ethynylene)s: An Approach to Single-Molecule Junctions with Covalent Au-C sigma-Bonds, Journal of the American Chemical Society 134(47) (2012) 19425-19431.

[25] W. Haiss, C.S. Wang, I. Grace, A.S. Batsanov, D.J. Schiffrin, S.J. Higgins, M.R. Bryce, C.J. Lambert, R.J. Nichols, Precision control of single-molecule electrical junctions, Nature Materials 5(12) (2006) 995-1002.

[26] M.T. Gonzalez, X.T. Zhao, D.Z. Manrique, D. Miguel, E. Leary, M. Gulcur, A.S. Batsanov, G. Rubio-Bollinger, C.J. Lambert, M.R. Bryce, N. Agrait, Structural versus Electrical Functionalization of Oligo(phenylene ethynylene) Diamine Molecular Junctions, Journal of Physical Chemistry C 118(37) (2014) 21655-21662.

[27] T. Hines, I. Díez-Pérez, H. Nakamura, T. Shimazaki, Y. Asai, N. Tao, Controlling Formation of Single-Molecule Junctions by Electrochemical Reduction of Diazonium Terminal Groups, Journal of the American Chemical Society 135(9) (2013) 3319-3322.

[28] D.A.C. Brownson, C.E. Banks, The Electrochemistry of Graphene, The Handbook of Graphene Electrochemistry, Springer London, London, (2014), 79-126.
[29] T.Z. Attia, Simultaneous determination of rutin and ascorbic acid mixture in their pure forms and combined dosage form, Spectrochimica Acta Part a-Molecular and Biomolecular Spectroscopy 169 (2016) 82-86.
[30] B. van't Land, G. Boehm, J. Garssen, Breast Milk: Components with Immune Modulating Potential and Their Possible Role in Immune Mediated Disease Resistance, in: R.R. Watson, S. Zibadi, V.R. Preedy (Eds.), Dietary Components and Immune Function, Humana Press, Totowa, NJ, (2010), 25-41.
[31] D.E. Hughes, Irreversible reaction-kinetics of the aerobic oxidation of ascorbic-acid, Analytical Chemistry 57(2) (1985) 555-558.

Overall Conclusions and Future Work.

This thesis has shown the development of fundamental techniques in the preparation of graphitic felts for use in a stationary electrochemical cell, as well as novel methods for interpreting the data to determine structural information relating to pore size within the material. Simulations also reveal important electrochemical information, such as the diffusion coefficient and the electron transfer rate constant for the analytes under investigation. Future work in this area will need to develop a more robust simulation method. The current one-dimensional method relies on Cartesian coordinates, but a one-dimensional model using radial coordinates would give a more representative view of the environment within a felt electrode.

The limit of detection work begun in this thesis showed graphite felts have great potential as electrochemical sensors, bucking the trend of using smaller, micro-electrodes to detect minute concentrations. Low concentrations of metals could be studied using anodic stripping voltammetry. This could have particular applications in the food and drink industry to detect toxic metals such as cadmium and mercury. Graphite felt electrodes may be able to detect low concentrations of trace metals without introducing additional mercury into the test environment.

The difficulties in using potential or time controls to reliably graft a uniform layer of diazonium molecules to the surface of the carbon electrode have been shown. The future of this route of surface modification relies directly on the second generation of diazonium molecules that contain a bulky blocking group to prevent multilayer formation. Whilst the technique itself was developed elsewhere, the application of this to a 3D structured electrode, such as graphite felt, is novel, and allows for future work to refine the technique and build upon its applications. Surface investigation techniques, such as AFM, could provide information on the thickness of the grafted surface layer, although this may have to be deployed with model carbon surfaces such as HOPG or edge plane samples. There is a plethora of combinations of blocking groups that could be synthesised to help control and eventually reduce the formation of multilayers, and an equally large number of possible

post-grafting surface modifications. These routes may lead to more versatile carbon surfaces with properties tuned by the surface modification. Numerous applications may be foreseen, especially in connection with the aim of this PhD in the fuel cell industry, where carbon electrodes are either deployed as catalyst supports or directly as electrodes in redox flow systems. In addition this thesis has shown how this technique is also applicable to a metal surface, such as gold. The post-grafting modification will provide a range of terminal moieties for the study of molecular junctions via AFM as initiated in this work.

Overall in terms of meeting the initial objectives of this thesis this project has had success and setbacks. The study of graphite felt and its use as a stationary electrode was very successful and the work regarding this has now been published. Work relating to the graphite felts potential in an electrochemical sensing application is still on going at time of writing. Unfortunately, the modified graphitic felts were not able to be tested in a working fuel cell due to complications arising outside the scope of this project. Despite this, the modification of graphite felts with a thin layer of blocked diazonium, followed by the post –grafting modification of this layer was achieved successfully.